ENVIRONMENTAL ISSUES AND IONS: THERMOCHEMISTRY AND STRUCTURES OF METAL POLLUTANTS COMPLEXED WITH WATER, SEQUESTERING AGENTS, AND AMINO ACIDS

by

Theresa Elizabeth Cooper

A dissertation submitted to the faculty of
The University of Utah
in partial fulfillment of the requirements for the degree of

Doctor of Philosophy

Department of Chemistry

The University of Utah

August 2012

THE UNIVERSITY OF UTAH GRADUATE SCHOOL

STATEMENT OF DISSERTATION APPROVAL

The dissertation of **Theresa Elizabeth Cooper**

has been approved by the following supervisory committee members:

Peter B. Armentrout	, Chair	**5/3/11** Date Approved
Charles A. Wight	, Member	**5/3/11** Date Approved
John C. Conboy	, Member	**5/3/11** Date Approved
Michael D. Morse	, Member	**5/3/11** Date Approved
P. K. Andrew Hong	, Member	**5/3/11** Date Approved

and by **Henry S. White** , Chair of the Department of **Chemistry**

and by Charles A. Wight, Dean of The Graduate School.

ABSTRACT

The fundamental interactions between two biologically and environmentally relevant metals, Zn^{2+} and Cd^{2+}, complexed with water, crown ethers, and histidine are examined using a variety of experimental methods and quantum chemical calculations. Chapters 3 and 6 detail the first experimentally determined hydration energies for $n = 6 – 10$ for $Zn^{2+}(H_2O)_n$ and $n = 3 – 11$ for $Cd^{2+}(H_2O)_n$ measured using threshold collision-induced dissociation in a guided ion beam mass spectrometer. Kinetic energy dependent cross sections are obtained for each reactant and analyzed to yield 0 K threshold measurements for loss of one, two, and three water ligands after accounting for multiple collisions, kinetic shifts, and energy distributions. The threshold measurements are converted from 0 K to 298 K values to give the hydration enthalpies and free energies for sequentially losing one water from each complex. Theoretical geometry optimizations and single point energy calculations are performed on reactant and product complexes using several levels of theory and basis sets to obtain thermochemistry for comparison to experiment. The charge separation process, $M^{2+}(H_2O)_n \rightarrow MOH^+(H_2O)_m + H^+(H_2O)_{n-m-1}$, is also observed, analyzed, and discussed in detail in both Chapters 4 and 6 for M = Zn and Cd. In Chapter 5, complexes of $Zn^{2+}(H_2O)_n$, where $n = 6 – 12$, are also examined using infrared multiple photon dissociation (IRMPD) spectroscopy, blackbody infrared radiative dissociation (BIRD), and theory for experimental determination of the

coordination behavior of Zn^{2+}. IRMPD spectroscopy experiments and theoretical calculations are also used in Chapter 7 to gain conformational insight into host-guest systems, namely Zn^{2+} and Cd^{2+} complexed with crown ethers (12-crown-4, 15-crown-5, and 18-crown-6). Finally, Chapter 8 examines the gas-phase structures of singly and doubly-charged complexes involving Zn and Cd with the amino acid histidine (His) as well as de-protonated His (His–H) using IRMPD spectroscopy.

For a great scientist, my biggest supporter, and the best father:

for my Dad

TABLE OF CONTENTS

ACKNOWLEDGEMENTS

The work presented in this dissertation would not have been possible without the help of many great individuals. Above all, I would like to thank the best advisor I could have ever asked for, Dr. Peter B. Armentrout. Over my years at the University of Utah Peter has given me guidance, support, so many great opportunities, and self-confidence. His intelligence, passion, and dedication to his students and his work is obvious and I hope I can embody these qualities and be as inspiring to others as he is to me.

I would also like to thank all the past and present Armentrout group members. Specifically, Dr's. Damon Carl, Bob Moision, and Murat Citir, who were instrumental in my development as a scientist through their assistance, useful discussions, and friendship.

The staff of the chemistry department have also selflessly helped me throughout my graduate research career. Specifically, Dale Heisler and Ron Jones of the electronics shop as well as Dennis Romney and Jeff Welch of the machine shop. All of whom have helped me problem solve issues in the lab as they arise. A big thank you to Ms. Deborah Olson, she greatly helped me through my endeavors during my time as the chair of the chemistry student advisory committee and continues to be a friend and confidant.

On a personal note, Mr. Ryan Hofstetter helped me tremendously through his unwavering love and support and his encouraging words in all my highest highs and lowest lows. I truly could not have done it without you. My parents, Margo and David Cooper, led by example and inspired me from a young age to do what I love and to do it

well. Among other things, they instilled in me a strong work ethic and competitive drive, which will continue to help me throughout my career and life. Finally, to little Cooper Hofstetter, you were with me the day I defended this thesis and I already loved you even though it would be a eight more months before we met you.

Lastly, the National Science Foundation generously provided funding for the work presented in this dissertation.

CHAPTER 1

INTRODUCTION AND OVERVIEW

Introduction

Heavy metals are used extensively in industrialized countries and their contamination of water resources has caused a widespread concern over the pollution of food resources, drinking water, and eventually the atmosphere. These metals are one of the most hazardous classes of pollutants and pose a serious health concern because of their nonbiodegradablity, toxicity, and carcinogenic properties.[1] An accurate and complete understanding of the thermochemical properties, reaction pathways, and structure of hydrated heavy metals is necessary for the efficient removal of metal pollutants from aqueous systems. The heavy metal ions of interest chosen in this work are Zn^{2+} and Cd^{2+}. Zinc is an essential nutrient, found as the metal center in several important proteins and enzymes, however, its high anthropogenic usage has caused levels of this metal to reach the point of contamination.[1-4] The hydration of Cd^{2+} is especially interesting because cadmium is highly toxic and environmentally hazardous. Cadmium is particularly dangerous to human health because it is a known carcinogen, nonbiodegradable, and can replace zinc in many biological systems resulting in deactivation of the biological moiety.[1]

Over the past several decades a large amount of work has been accomplished looking into the hydration of many different singly and doubly charge metals using a variety of experimental and theoretical techniques, as outlined in the forthcoming chapters. Despite this work, the experimental thermochemistry of hydrated zinc and cadmium dications is presently unknown. To address this lack of thermochemical information, we examine the dissociation behavior of $M^{2+}(H_2O)_n$ complexes, where M = Zn and Cd and $n = 6 - 10$ for Zn and $n = 3 - 11$ for Cd. In all cases, the dominant process observed is reaction 1.1,

$$M^{2+}(H_2O)_n \rightarrow M^{2+}(H_2O)_{n-1} + H_2O \qquad (1.1)$$

followed by sequential loss of additional water molecules, although particular sized complexes also undergo a charge separation process, reaction 1.2.

$$M^{2+}(H_2O)_n \rightarrow MOH^{+}(H_2O)_m + H^{+}(H_2O)_{n-m-1} \qquad (1.2)$$

Analysis of the kinetic energy dependence of these collision-induced reactions provides the first experimental determination of the hydration energies for zinc and cadmium dication-water complexes. These energetics are measured experimentally using threshold collision-induced dissociation (TCID) in a guided ion beam tandem mass spectrometer coupled with a thermal electrospray ionization source (ESI-GIBMS) and are subsequently compared to theoretical calculations.

The thermochemical investigation of these hydrated dications has led to a variety of other studies also presented in this dissertation. The structural coordination behavior of $Zn^{2+}(H_2O)_n$, where $n = 6 - 12$, was investigated using infrared multiple photon

dissociation (IRMPD) spectroscopy and blackbody infrared radiative dissociation (BIRD). In addition to investigating hydrated Zn^{2+} and Cd^{2+}, IRMPD spectroscopy was used to gain structural insight into complexes of these metals bound to different sequestering agents as well as small biological ligands (i.e., amino acids). All spectroscopy experiments were performed in a collaborative effort with two other research institutions and utilized a Fourier-transform ion cyclotron resonance mass spectrometer (FT-ICR) coupled to the beamline of a tunable IR laser. For structural determination the spectra generated are compared to linear absorption spectra predicted by quantum chemical calculations.

Overview

Chapter 2 presents a brief description of the ESI-GIBMS experimental setup and procedures. Additionally, the process of data reduction and analysis is also outlined. Analyses of the data are described for single, competitive, and sequential dissociations of $M^{2+}(H_2O)_n$; fitting the data to these models results in themochemical information for the endothermic reactions presented in Chapters 3, 4, and 6.

Chapter 3 details the collision-induced dissociation experiments for $Zn^{2+}(H_2O)_n$, where $n = 6 – 10$, resulting in the first experimentally determined sequential bond dissociation energies (BDEs) of these complexes. A detailed theoretical study into the structures and predicted BDEs of the low-energy $Zn^{2+}(H_2O)_n$ complexes is also presented using several levels of theory for comparison to experiment. Different levels of theory disagree on the ground state (GS) conformation leading to potential ambiguities in the final thermochemical values. These questions are addressed and answered with spectroscopic studies in Chapter 5. The work in Chapter 3 has been published: Cooper,

Theresa E.; Carl, D. R.; Armentrout, P. B. Journal of Physical Chemistry A, **2009**, *113*, 13727 – 13741.

Chapter 4 examines the competition between reactions 1.1 and 1.2 for $Zn^{2+}(H_2O)_n$ in great detail. Results from this study are sufficient to establish a new, more precise definition of the "critical size" for charge separation. Calculated rate-limiting transition states for reaction 1.2 are also compared to experimental threshold measurements Finally, a complete reaction coordinate is calculated, outlining a possible pathway for reaction 1.2 to occur for the dissociation of $Zn^{2+}(H_2O)_7$. This work has been published: Cooper, Theresa E.; Armentrout, P. B. Journal of Physical Chemistry A, **2009**, *113*, 13742 – 13751.

Chapter 5 answers questions posed in Chapter 3 through IRMPD spectroscopy and BIRD experiments. Coordination behavior of $Zn^{2+}(H_2O)_n$, where $n = 6 – 12$, is discussed, resulting in a more definitive assignment of the experimental and theoretical thermochemical values of the hydrated zinc dication. This work was the first in a new collaboration with the Williams group at the University of California, Berkeley and was published: Cooper, Theresa E.; O'Brien, J. T.; Williams, E. R.; Armentrout, P.B. Journal of Physical Chemistry A, **2010**, *114*, 12646 – 12655.

Chapter 6 presents the complete experimental and theoretical investigation of the hydration energies of $Cd^{2+}(H_2O)_n$ complexes, $n = 3 – 11$. The competition between reactions 1.1 and 1.2 is also examined and rate-limiting transition states for the charge separation process are calculated and compared to experimental threshold measurements of the reaction barrier height. This chapter encompasses two publications: Cooper, Theresa E.; Armentrout, P. B. Chemical Physics Letters (Invited Frontiers Article) **2010**,

486, 1 – 6 and Cooper, Theresa E.; Armentrout, P. B. Journal of Chemical Physics, **2011**, *134*, 114308.

Chapter 7 introduces IRMPD spectroscopy work done in a collaborative effort with the FOM Institute for Plasma Physics "Rijnhuizen", a user facility in the Netherlands. The gas-phase structures of Zn^{2+} and Cd^{2+} complexed with varying sized crown ethers, 12-crown-4 (12c4), 15-crown-5 (15c5), and 18-crown-6 (18c6), are investigated and the spectra are compared to those predicted by quantum chemical calculations. The experimental work was done in collaboration with Drs. Jos Oomens and Jeffrey Steill at the FOM and has been published: Cooper, Theresa E.; Carl D. R.; Oomens, J.; Steill, J. D.; Armentrout, P. B. Journal of Physical Chemistry A, **2011**, *115*, 5408 – 5422.

Chapter 8 continues the collaboration with the FOM Institute, gaining conformational insight into biologically important complexes of histidine with Zn and Cd using IRMPD spectroscopy. Comparisons are made between the experimentally observed spectra and the calculated linear absorption spectra to determine likely contributing gas-phase conformations. This work has been published: Hofstetter, Theresa E.; Howder, C.; Berden, G.; Oomens, J.; Armentrout, P. B. Journal of Physical Chemistry B, **2011**, *115*, 12648 – 12661.

References

(1) Richens, D. T. *The Chemistry of Aqua Ions*; John Wiley and Sons, Inc: New York, 1997.

(2) Spiro, T. G. *Zinc enzymes*; J. Wiley: New York, 1983.

(3) Kimura, E. *Pure & Appl. Chem.* **1993**, *65*, 355.

(4) Nriagu, J. O. *Zinc in the Environment*; Wiley: New York, 1980.

CHAPTER 2

IN-HOUSE EXPERIMENTAL TECHNIQUES AND DATA ANALYSES

Guided Ion Beam Mass Spectrometer with an Electrospray Ionization Source

Experimental procedures. The experiments described in Chapters 3, 4, and 6 on hydrated metal dications, $M^{2+}(H_2O)_n$, were performed using a guided ion beam mass spectrometer with an electrospray ionization source (ESI-GIBMS), which has been described in detail previously.[1-3] There are four main regions in the GIMS shown in Figure 2.1: ESI source, magnetic momentum analyzer, octopole ion guide and reaction cell, and a quadrupole mass filter and Daly detector. The $M^{2+}(H_2O)_n$ complexes were generated using an ESI source,[3] comprising a stainless steel electrospray needle, a heated capillary, an 88 plate ion funnel, and a hexapole ion guide where the ions undergo sufficient thermalizing collisions to bring them to a Maxwell Boltzmann distribution at ambient temperatures. $M^{2+}(H_2O)_n$, where M = Zn or Cd, clusters are formed by passing a dilute solution of $M(NO_3)_2$, 10^{-4} M in water, through the electrospray needle at a low flow rate of 0.02 - 0.10 mL/hr with a high voltage applied to the needle, typically 2.0 - 2.2 kV. The capillary following the spray is heated to 80 °C to promote desolvation of large droplets and has a small applied potential, typically <15 V. The ion funnel[4] collects

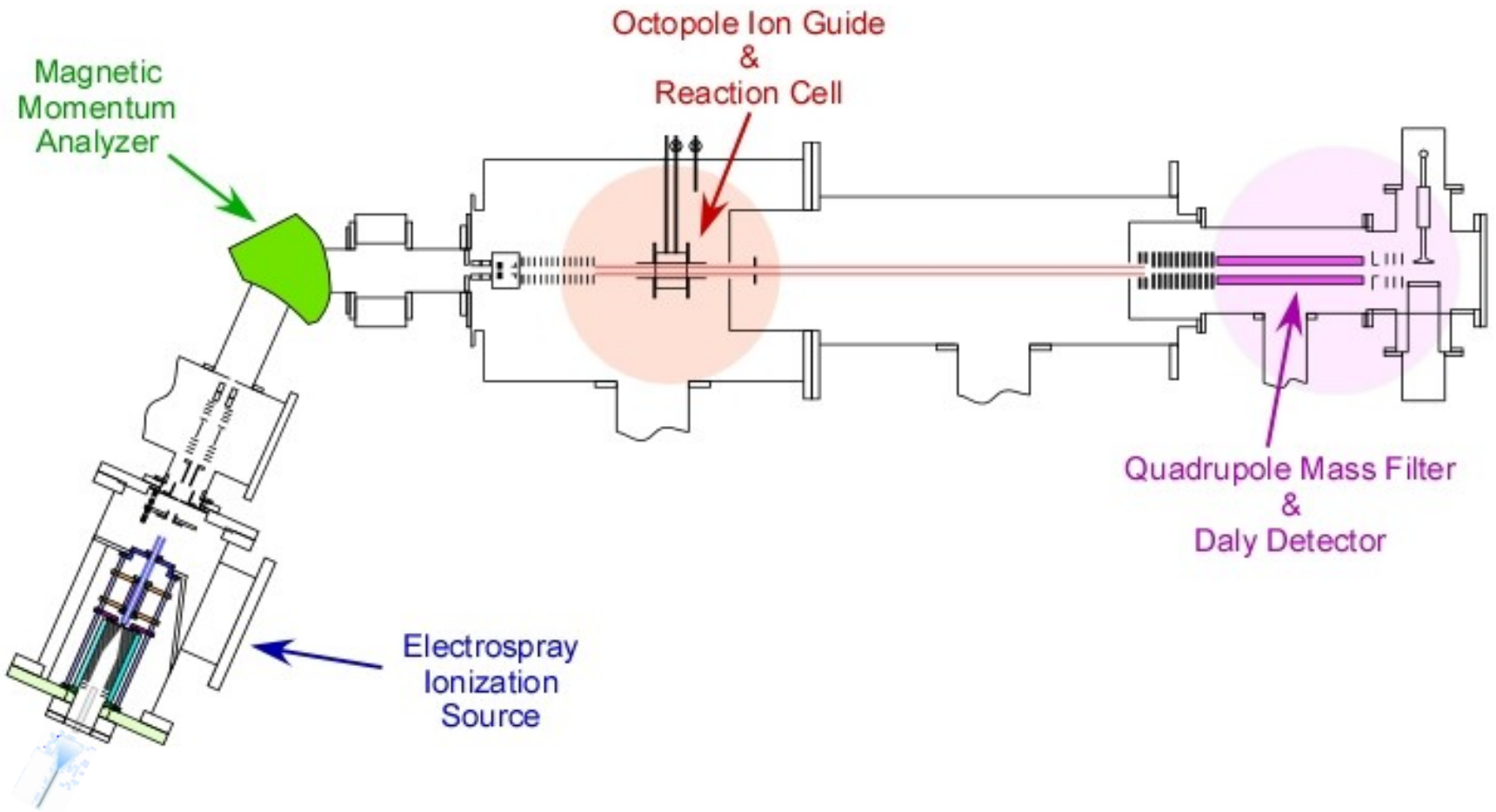

Figure 2.1. Schematic of the ESI-GIBMS

the ions emitted from the capillary thereby increasing signal intensity.[5,6] The ions are pulled through the funnel by a gentle DC gradient, typically 5 - 8 V, and undergo multiple collisions with the ambient gas. Compared to previous settings used with this ESI source, the conditions needed to generate $Zn^{2+}(H_2O)_n$ and $Cd^{2+}(H_2O)_n$ complexes are unusually gentle because of the propensity of these ions to dissociate via the charge separation pathway, reaction 1.2, into metal hydroxide and protonated water complexes. The radio frequency (rf) hexapole ion guide/collision cell traps the ions in the radial direction using an rf amplitude typically set between 200 – 250 V peak to peak. Here, the ions undergo $>10^4$ collisions with the ambient gas as they drift through the hexapole, such that the emerging ions are thermalized, as shown previously[3,7-9] and in work performed in this dissertation. Thermal ions are assumed to be in their ground vibrational and rotational states such that they can be described by a Maxwell Boltzmann distribution at 300 K. Increasing the voltage to the DC fin electrodes, an in source fragmentation technique described in more detail elsewhere,[10] tends to form smaller metal hydrate complexes; this technique was used to form certain complex sizes of $M^{2+}(H_2O)_n$ as explicitly outlined in Chapters 3 and 6 for Zn and Cd.

The ions generated, as described above, are focused and accelerated into a magnetic momentum analyzer, which selects the desired reactant by its mass-to-charge ratio (m/z). The selected reactant is decelerated to a known potential relative to the hexapole in the ion source, V_{Lab}, and focused into an rf octopole ion guide where the ion is trapped radially. A collision gas cell surrounds part of the octopole and contains xenon, which is introduced to the collision cell at pressures varying between 0.05 and 0.20 mTorr. Xenon makes an excellent choice for inducing dissociation as it is heavy,

monatomic, chemically unreactive, and polarizable, thereby providing efficient kinetic to internal energy transfer upon collision.[11,12] After collision, reactant and product ions drift to the end of the octopole guide, where they are focused into a quadrupole mass filter for mass analysis and then detected utilizing a Daly detector,[13] which is capable of single ion counting. This process is repeated at varying collision energies, V_{Lab}, until the kinetic energy dependent intensities of all parent and product ions are recorded over the energy range of interest.

Data Reduction and Analyses

Raw data conversion. As described elsewhere,[1] ion intensities are converted to absolute cross sections, which corresponds to the probability of a reaction to occur, using a Beer's Law relationship, eqs 2.1 and 2.2.

$$I = I_0 \exp(-\sigma_{tot}\rho l) \tag{2.1}$$

$$\sigma_P = \sigma_{tot}\left(\frac{I_P}{\sum I_P}\right) \tag{2.2}$$

Here, I is the ion intensity of the transmitted ion beam, I_0 is the sum of all ion intensities, σ_{tot} is the total cross section, ρ is the gas density of xenon in the reaction cell, l is the effective gas cell path length, σ_P is a product cross section with transmitted intensity I_P. Absolute cross sections have an uncertainty of ±20%.

In addition, V_{Lab} is converted to the relative kinetic energy in the center-of-mass (CM) frame using $E_{CM} = 2\ V_{Lab}\ m/(m + M)$, where m is the mass of the neutral collision gas, M is the mass of the ionic reactant, and the factor of two accounts for the charge on the reactant complexes. The absolute energy zero and kinetic energy distribution of the

reactant ions are determined using a retarding potential technique.[1] The derivative of the normalized ion intensities is fit to a Gaussian distribution, with a full width at half maximum (FWHM) in V_{Lab} that ranges in these experiments from 0.08 - 0.15 eV. The absolute uncertainty in V_{Lab} is 0.05 eV.

Threshold modeling. In order to extract accurate thermochemical results from analysis of the kinetic energy dependent cross sections, several factors must be considered. Experiments were performed at three different pressures of Xe (typically about 0.05, 0.10, and 0.20 mTorr) and the resulting cross sections extrapolated to a zero pressure cross section to ensure single collision conditions.[14,15] This rigorously removes effects arising from multiple collisions, which are particularly significant in the present system for higher order water losses and the charge separation channels. Using this zero pressure cross section, the loss of a single water molecule from a reactant $M^{2+}(H_2O)_n$ complex is modeled using eq 2.3

$$\sigma(E) = \sigma_0 \Sigma\, g_i\, (E + E_i - E_0)^N / E \qquad (2.3)$$

In this modified line-of-centers expression, σ_0 is an energy independent scaling factor, E is the relative translational energy of the reactants, E_0 is the reaction threshold at 0 K, and N is an adjustable fitting parameter that characterizes the energy deposition during collision.[2] The summation is over the rovibrational states of the reactants having excitation energies E_i and populations g_i, where $\sum g_i = 1$. The number of rovibrational states is directly counted using the Beyer-Swinehart Stein-Rabinovitch algorithm[16-19] and a Maxwell-Boltzmann distribution is used to describe the populations g_i. Before

comparison with the data, the model is also convoluted over the kinetic energy distributions of the reactants.[1]

The complexes examined in the present study are sufficiently large that their dissociation lifetime near the dissociation threshold is comparable to the experimental time of flight, $\tau \approx 5 \times 10^{-4}$ s in this apparatus. This behavior can give rise to a kinetic shift that can be estimated by incorporating Rice-Ramsperger-Kassel-Marcus (RRKM) theory[19,20] into eq. 2.3, as discussed in detail elsewhere.[21-23] Competition between multiple dissociation pathways can be modeled statistically, as discussed elsewhere,[24] for an individual reaction channel, *j*. When both of these effects are explicitly considered, eq 2.3 is modified to eq. 2.4,

$$\sigma_j(E) = \frac{N\sigma_{0,j}}{E}\sum_i g_i \int_{E_{0,j}-E_i}^{E} \frac{k_j(E^*)}{k_{tot}(E^*)} P_{D1}(E-\varepsilon)^{N-1} d\varepsilon \qquad (2.4)$$

where ε is the energy transferred into the reactant ion by the collision such that the energy available for dissociation is $E^* = \varepsilon + E_i$. $P_{D1} = 1 - \exp[-k_{tot}(E^*)\tau]$ is the probability of dissociation of the energized molecule, EM.

Theoretical results discussed in Chapter 3 show that a distribution of different reactant and product isomers are possible. Modeling using eq 2.4 is necessary to account for the competition between these multiple dissociation pathways, which in this case yield product ions having the same mass. In Chapters 4 and 6 eq 2.4 is used to account for the competition between the water loss and charge separation dissociations of $M^{2+}(H_2O)_n$, which should be taken into account for the most accurate thermochemistry of the system. Explicit consideration of both dissociation channels is necessary because the higher energy pathway can be inhibited in such a way that its detection may only be

possible at higher energies than its actual 0 K threshold, yielding an energetic difference known as the "competitive shift".

Should the unimolecular rate constant be sufficiently fast for complete dissociation, eq 2.4 reduces to eq 2.3 for a single channel. The RRKM unimolecular rate constants for dissociation are given by eq 2.5,

$$k_{tot}(E^*) = \Sigma\, k_j(E^*) = \Sigma s_j\, N^{\dagger}_{vr,j}(E^* - E_{0,j}) \,/\, h\rho_{vr}(E^*) \qquad (2.5)$$

where s_j is the reaction degeneracy for channel j given by the ratio of the rotational symmetry numbers (reactant/products),[19] $N^{\dagger}_{vr,j}$ is the number of ro-vibrational states of the transition state (TS) for channel j at an energy $E^* - E_{0,j}$ above the reaction barrier, and $\rho_{vr}(E^*)$ is the density of states for the ro-vibrational levels of the EM. The rotational constants and vibrational frequencies of the EM and TSs are taken from quantum chemical calculations (detailed in Chapters 3, 4, and 6).

For water loss channels, the transition state is loose as the bond cleavage is heterolytic with all the charge remaining on the complex containing the metal ion.[25] The TS for water loss is treated at the phase space limit (PSL) in which the transitional modes are treated as rotors.[23] In this limit, the TS is product-like such that its molecular parameters are taken from quantum chemical calculations of the products. Additionally, there is no other energetic barrier associated with the reaction beyond its endothermicity. As such, $E_{0,j}$ represents the experimental bond dissociation energy (BDE) for water loss from a $M^{2+}(H_2O)_n$ reactant. Because the charge separation process produces two singly charged species, there must be a Coulombic barrier along the reactant coordinate for this dissociation channel, such that the appropriate TS is tight. Molecular parameters for

these TSs are taken from calculations described in Chapters 4 and 6. Here, $E_{0,j}$ represents the barrier height associated with the charge separation reaction, which corresponds to the energetic difference between the rate-limiting TS and the reactant ground state.

Sequential modeling is used in Chapters 3, 4, and 6 in order to obtain thermochemical information on smaller complexes not directly accessible from the ESI source due to the energetic favorability of the charge separation process at certain smaller complex sizes. Accordingly, thresholds for secondary dissociation are modeled in conjunction with modeling the single water loss channel. The "sequential BDE" is derived from the difference between the primary and secondary thresholds. A statistical approach to modeling sequential dissociation has recently been developed and proven to provide accurate thresholds for singly charged systems,[26] as well as work performed on the doubly charge systems in this dissertation. This model makes statistical assumptions regarding the energy deposition in the products of the initial CID reaction. Ultimately, the model assigns a probability for further dissociation of the product of reaction 1.1 using eq 2.6,

$$P_{D2} = 1 - \exp[-k_2(E_2^*)\,\tau] \tag{2.6}$$

where E_2^* is the internal energy of the product ion undergoing secondary dissociation. This energy is determined by energy conservation, i.e., $E_2^* = E^* - E_0 - T_1 - E_L$, where T_1 is the translational energy of the primary products and E_L is the internal energy of the neutral product. Statistical assumptions are used to assign the distributions of each of these quantities, thereby allowing calculation of the secondary dissociation rate constant, k_2. Because of the complexity of the sequential dissociation model, its use is presently

limited to single primary product channels such that no designation of the individual reaction channel *j* is included in eq 2.6.

Analysis of the data involves using eqs 2.3, 2.4, or 2.6 to reproduce the data over extended energy and magnitude ranges, using a least squares criterion for optimizing the fitting parameters, $\sigma_{0,j}$, $E_{0,j}$, and N. The uncertainties in these parameters include variations associated with modeling several independent experimental cross sections, scaling the theoretical vibrational frequencies by ±10%, varying the N value by ±0.1, scaling the experimental time of flight up and down by a factor of two, and the uncertainty in the absolute energy scale. As a note, sequential BDEs are relative values; therefore the uncertainty is typically lower than the calculated absolute uncertainty for primary and secondary thresholds because several contributions to the uncertainty in the energy cancel.

References

(1) Ervin, K. M.; Armentrout, P. B. *J. Chem. Phys.* **1985**, *83*, 166.

(2) Muntean, F.; Armentrout, P. B. *J. Chem. Phys.* **2001**, *115*, 1213.

(3) Moision, R. M.; Armentrout, P. B. *J. Am. Soc. Mass Spectrom.* **2007**, *18*, 1124.

(4) Kim, T.; Udseth, H. R.; Smith, R. D. *Anal. Chem.* **2000**, *72*, 5014.

(5) Shaffer, S. A.; Prior, D. C.; Anderson, G. A.; Udseth, H. R.; Smith, R. D. *Anal. Chem.* **1998**, *70*, 4111.

(6) Shaffer, S. A.; Tolmachev, A.; Prior, D. C.; Anderson, G. A.; Udseth, H. R.; Smith, R. D. *Anal. Chem.* **1999**, *71*, 2957.

(7) Carl, D. R.; Moision, R. M.; Armentrout, P. B. *Int. J. Mass Spectrom.* **2007**, *265*, 308.

(8) Carl, D. R.; Chatterjee, B. K.; Armentrout, P. B. *J. Chem. Phys.* **2010**, *132*, 044303.

(9) Carl, D. R.; Moision, R. M.; Armentrout, P. B. *J. Am Soc. Mass Spectrom.* **2009**, *20*, 2312.

(10) Carl, D. R.; Moision, R. M.; Armentrout, P. B. *J. Am. Soc. Mass Spectrom.* **2009**.

(11) Dalleska, N. F.; Honma, K.; Sunderlin, L. S.; Armentrout, P. B. *J. Am. Chem. Soc.* **1994**, *116*, 3519.

(12) Aristov, N.; Armentrout, P. B. *J. Phys. Chem.* **1986**, *70*, 4111.

(13) Daly, N. R. *Rev. Sci. Instrum.* **1960**, *31*, 264.

(14) Hales, D. A.; Lian, L.; Armentrout, P. B. *Int. J. Mass Spectrom. Ion Process.* **1990**, *102*, 269.

(15) Schultz, R. H.; Crellin, K. C.; Armentrout, P. B. *J. Am. Chem. Soc.* **1991**, *113*, 8590.

(16) Stein, S. E.; Rabinovich, B. S. *Chem. Phys. Lett.* **1977**, *49*, 1883.

(17) Beyer, T. S.; Swinehart, D. F. *Comm. Assoc. Comput. Mach.* **1973**, *16*, 379.

(18) Stein, S. E.; Rabinovich, B. S. *J. Chem. Phys.* **1973**, *58*, 2438.

(19) Gilbert, R. G.; Smith, S. C. *Theory of Unimolecular and Recombination Reactions*; Blackwell Scientific: Oxford, 1990.

(20) Holbrook, K. A.; Pilling, M. J.; Robertson, S. H. *Unimolecular Reactions*; Wiley: New York, 1996.

(21) Loh, S. K.; Hales, D. A.; Lian, L.; Armentrout, P. B. *J. Chem. Phys.* **1989**, *90*, 5466.

(22) Khan, F. A.; Clemmer, D. E.; Schultz, R. H.; Armentrout, P. B. *J. Phys. Chem.* **1993**, *97*, 7979.

(23) Rodgers, M. T.; Ervin, K. M.; Armentrout, P. B. *J. Chem. Phys.* **1997**, *106*, 4499.

(24) Rodgers, M. T.; Armentrout, P. B. *J. Chem. Phys.* **1998**, *109*, 1787.

(25) Armentrout, P. B.; Simons, J. *J. Am. Chem. Soc.* **1992**, *114*, 8627.

(26) Armentrout, P. B. *J. Chem. Phys.* **2007**, *126*, 234302.

CHAPTER 3

HYDRATION ENERGIES OF ZINC (II): THRESHOLD COLLISION-INDUCED DISSOCIATION EXPERIMENTS AND THEORETICAL STUDIES

Abstract

The first experimentally determined sequential bond dissociation energies of $Zn^{2+}(H_2O)_n$ complexes, where $n = 6 – 10$, are measured using threshold collision-induced dissociation in a guided ion beam tandem mass spectrometer coupled with an electrospray ionization source. Kinetic energy dependent cross sections are obtained and analyzed to yield 0 K threshold measurements for loss of one and two water ligands after accounting for multiple collisions, kinetic shifts, and energy distributions. The threshold measurements are then converted from 0 K to 298 K values to give the hydration energies for sequentially losing one water from each parent complex. Theoretical geometry optimizations and single point energy calculations are performed using several levels of theory for comparison to experiment. Although different levels of theory disagree on the ground state conformation of most complexes examined here leading to potential ambiguities in the final thermochemical values, calculations at the MP2(full) level provide the best agreement with experiment. On this basis, the present experiments are

Adapted with permission from Cooper, T. E.; Carl, D. R.; Armentrout, P. B., *J. Phys. Chem. A*, **2009**, *113*, 13727.

most consistent with the inner solvent shell of Zn^{2+} being five waters, except for $Zn^{2+}(H_2O)_6$ where all waters bind directly to the metal ion. The charge separation process, $Zn^{2+}(H_2O)_n \rightarrow ZnOH^+(H_2O)_m + H^+(H_2O)_{n-m-1}$, which is in competition with the loss of water from the parent complex, is also observed for $n = 6 - 8$. These processes are analyzed in detail in the following chapter.

Introduction

Zinc solvation and coordination behavior is of paramount importance in the fields of biochemistry and bioinorganic chemistry as the zinc ion is required for the activation of certain proteins and metalloenzymes.[1-3] Thus, zinc is biologically important and not toxic. In addition, zinc metal consumption ranks fourth in the world among all metals.[4] The most common uses are to galvanize steel, as a component in brass, and as an additive in rubbers and paints.[4] Such high usage implies large discharges to the environment, such that zinc is quickly infiltrating aqueous systems, thereby making its way into the food chain, drinking water, and eventually the atmosphere.

Zinc coordination behavior has previously been studied using a variety of experimental methods including Raman spectroscopy on aqueous $Zn^{2+}(ClO_4)_2$,[5] ion equilibria using a variety of ligands (but not water),[6-8] collision-induced dissociation (CID) mass spectrometry of the hydrated ion,[9,10] and X-ray absorption fine structure studies of the ion in aqueous media.[11] Despite this activity, experimental thermochemistry for the hydration of zinc cations is presently unknown. Because of the lack of experimental bond energies, a host of theoretical work has been performed utilizing a variety of quantum chemical and Monte Carlo calculations including density functional theory (DFT), Hartree Fock (HF), and molecular dynamics simulations.[5-9,11-18]

Neither experiment nor theory has yet established definitively the number of waters in the inner solvent shell surrounding the zinc cation in $Zn^{2+}(H_2O)_n$ complexes. X-ray, Raman, and near-IR spectroscopy report a coordination number of six forming an octahedral inner shell, which until recently has been the commonly accepted configuration.[3,5,11,19] Using quantum chemical calculations, several studies found the differences in energies between inner solvent shells of four, five, and six water molecules to be very small.[14,15,18] Indeed, the lowest energy complex switches between an inner shell of four or six depending on the level of theory used. An inner shell of six is favored by MP2 calculations, whereas B3LYP theory has a slight preference for an inner shell of four.[14-16,18] Pavlov et al.[18] theorized that calculations of larger clusters ($n > 12$) are needed to accurately represent the dilute solutions explored by X-ray scattering, Raman, and near-IR experiments. However, such conclusions are clearly influenced by the basis set size, as demonstrated by Peschke et al.[8] for the Zn^{2+} ion interacting with acetone ligands. They found large energy differences when geometries were calculated using B3LYP/6-311++G(d,p) compared to the values given in the B3LYP/LANL2DZ calculations reported by Pavlov et al.[18]

To address the lack of thermochemical information on the hydration energies of the zinc cation, the present study examines the dissociation behavior of $Zn^{2+}(H_2O)_n$ complexes where $n = 7 – 10$. In all cases, the dominant process observed is reaction 3.1,

$$Zn^{2+}(H_2O)_n \rightarrow Zn^{2+}(H_2O)_{n-1} + H_2O \qquad (3.1)$$

followed by sequential loss of additional water molecules. Analysis of the kinetic energy dependence of these reactions provides the first experimental determinations of the

hydration energies of zinc cation-water complexes. These values are compared to previous and present theoretical calculations, which also examine the issue of the size of the inner solvent shell.

In addition, particular sized complexes are found to undergo a charge separation process, reaction 3.2, which is discussed in detail in the Chapter 4 of this dissertation.

$$Zn^{2+}(H_2O)_n \rightarrow ZnOH^{+}(H_2O)_m + H^{+}(H_2O)_{n-m-1} \quad (3.2)$$

One result from the analysis in Chapter 4 that is important here is that competition between reactions 3.1 and 3.2 does influence the experimental thresholds for reaction 3.1 with $n \leq 7$ and this effect is included in the thermochemistry reported here. Finally, we note that because the threshold for charge separation is below the threshold for water loss for $n = 7$, electrospray ionization (ESI) sources are generally limited to producing $Zn^{2+}(H_2O)_7$ and larger complexes.

Theoretical and Experimental Section

Computational details. Because there is a debate in the literature regarding the calculated ground state of the $Zn^{2+}(H_2O)_n$ complexes, a simulated annealing procedure using the AMBER (Version 8) program[20] was used to generate all possible low-lying isomers. Annealing procedures were followed three independent times for inner hydration shells of four, five, or six water ligands. To constrain the inner shell to these sizes, an energetic barrier was used to prevent waters from moving too far from the metal ion, and applied to the second shell waters (when applicable) preventing these ligands from entering into the first shell. Each isomer was then optimized using a low level of ab initio theory, HF/3-21G.[21,22] Using the Gaussian03 package,[23] further geometry

optimizations were performed on the lowest lying isomers generated from the annealing process (about 50 structures for the larger complexes). These structures were first optimized at the B3LYP/6-31G(d) level[24-26] in a "loose" geometry optimization, which utilizes a large step size (0.01 au) and RMS force constant (0.0017) to give a rapid geometry convergence. The lowest energy structures (about 25) were further optimized with a larger basis set, B3LYP/6-311+G(d,p). This level of theory was used for the final geometry optimizations as well as providing vibrational frequencies and rotational constants.

These calculated frequencies and rotational constants were used in the RRKM thermochemical analysis discussed below, as well as for zero point energy (ZPE) conversions of theoretical bond dissociation energies to 0 K thermochemical values. The vibrational frequencies were each scaled by 0.989[27] before being used in these analyses. Using these geometries, single point energy (SPE) calculations were performed using the B3LYP, B3P86,[28] and MP2(full)[29] levels of theory with a 6-311+G(2d,2p) basis set. As will be seen below, conflicting results are provided by these two DFT levels versus the MP2(full) calculations. To explore which set of results is more likely to be accurate, a third DFT calculation was performed using the M06[30,31] functional, which was developed specifically for noncovalent interactions found in ion solvation and hydration. Accordingly, additional SPE energies were calculated using the M06 level with a 6-311+G(2d,2p) basis set. Diffuse functions were used in the geometry optimization, frequency calculation, and SPE calculations because of their importance for describing the hydrogen bonding of the zinc water clusters. Previous works have discussed this importance in both zinc hydration and solvation.[8,18] Basis set superposition errors

(BSSE) were also calculated for dissociation of the lowest energy structures at each level of theory in the full counterpoise (cp) limit.[32,33] The BSSE corrections found for all three DFT calculations were relatively small, ≤5 kJ/mol, and slightly larger for the MP2(full) level, 8 – 10 kJ/mol depending on the size of the complex. For simplicity purposes, when these four levels of theory are discussed the B3LYP and B3P86 levels will be abbreviated together as "Bx" and the M06 and MP2(full) will be abbreviated together as "Mx". In addition to the Bx and Mx results, we also performed BHandHLYP[34]/6-311++G(2d,2p)//BHandHLYP/6-311++G(d,p) calculations (which were shown in a previous study[35] to be able to describe hydrogen bonding in amino acids as well as or better than computationally more expensive methods) for the lowest energy complexes of the four, five, and six water inner shells of $Zn^{2+}(H_2O)_6$. (Identical geometries were obtained using the 6-311+G(d,p) basis set.) Results show that the six water inner shell is the lowest energy structure, but the other two complexes are ~2 kJ/mol above the ground state, similar to the MP2(full) level discussed in more detail below.

In addition to the B3LYP and BHandHLYP geometry optimizations performed, we also calculated MP2(full)/6-311+G(d,p) geometries for $Zn^{2+}(H_2O)_n$ for n = 5 – 9, M06/6-311+G(d,p) geometries for n = 6 – 10, and B3LYP/6-311++G(d,p) geometries for n = 6 and 9, along with their corresponding SPEs at the same three levels of theory used above. No discernible differences in the geometries and energetics were found using these more expensive approaches. Hence, results from the B3LYP/6-311+G(d,p) geometry optimizations are used exclusively in the discussion below.

Experimental procedures. The experimental methods used to form the $Zn^{2+}(H_2O)_n$ complexes and obtain the kinetic energy dependent cross sections for the

collision-induced dissociation are described in detail in Chapter 2. Unique to this work, the DC fin electrodes, an in source fragmentation technique described in more detail elsewhere,[36] were used to increase the amount of the $Zn^{2+}(H_2O)_7$ complex produced by our ESI. Increasing the voltage on the fins tends to form smaller metal hydrate complexes as described by Carl et al.,[36] however, for the case of zinc hydration increasing the fin voltage past the intensity peak for the $n = 7$ complex generated charge separation products and no complexes smaller than $n = 7$ were observed from our source.

Results and Discussion

Theoretical geometries of zinc water clusters. As described above, geometry optimizations and frequency calculations were performed at the B3LYP/6-311+G(d,p) level of theory. Although experimental data for the $Zn^{2+}(H_2O)_n$ complexes where $n = 1 – 5$ are not accessible at this time, for completeness, these structures were also optimized and SPEs calculated at the same theoretical levels designated above.

In agreement with previous theoretical results performed on these smaller complexes,[5,8,15-18] all waters bind directly to the zinc metal ion for $n = 1 – 4$. In all four species, the water ligands are distributed to maximize the distance between ligands, such that the oxygen atoms are located in linear, distorted trigonal planar, and near-tetrahedral geometries for $n = 2 – 4$, respectively. Key structural parameters for these smaller complexes are provided in Table 3.1.

For larger clusters sizes, $n \geq 5$, there is a debate as to the number of waters in the inner shell of the ground state structure. Both Hartmann et al. and Lee et al. examined the possibility of having an inner shell of 3 water ligands at the $n = 4$ and 5 complexes and both studies found that these structures were very high in energy.[15,16] In the present

work, several isomers of the $n = 5 – 10$ clusters (excluding the 3 water inner shell) were explored theoretically, with energy differences for low-energy isomers presented in Table 3.2. The lowest energy structures having inner solvent shells of 4, 5, and 6 water ligands are shown in Figures 3.1 – 3.3 for the $n = 6 – 8$ complexes. In most cases, when a second shell water ligand forms two hydrogen bonds to the inner shell (indicated by an AA designation), the structure is lower in energy than if there is only one hydrogen bond to the inner shell (indicated by A). A number of additional higher energy isomers were also calculated for all inner shell sizes of the $n = 6 – 10$ complexes. Because of the large number of isomers investigated, their geometries and relative energetics are not included here.

For $n = 5$, the present results find that the $Zn^{2+}(H_2O)_4(H_2O)_1$ or (4,1)_AA structure has a distorted tetrahedral inner solvent shell with the fifth water forming two hydrogen bonds to the inner shell. The nomenclature used here for these complexes specifies the number of inner shell waters x and second shell water ligands y by (x,y) augmented with the designation of the hydrogen bonding motif of the complex. The (4,1)_AA structure is slightly more stable at the Bx levels (B3LYP and B3P86) than the $Zn^{2+}(H_2O)_5$ or (5,0) structure with all five waters in the inner solvent shell forming a square pyramidal shape, but Mx results (M06 and MP2(full)) find the opposite result, Table 3.2. The Bx results are in agreement with earlier DFT theoretical work performed on this size complex,[15,18] as are the MP2 results with analogous earlier calculations.[14,16] Alternate isomers include the (4,1)_A structure, which has the second shell water singly hydrogen bonded to the inner shell and lies 1 – 15 kJ/mol higher than (4,1)_AA. Because the torsional motion of the outer water molecule is now much looser (nearly a free rotor),

Table 3.1. B3LYP/6-311+G(d,p) geometry optimized structures for ground state $Zn^{2+}(H_2O)_{1-4}$[a]

Complex	Symmetry	r(ZnO) (Å)	∠OZnO (°)	∠ZnOH (°)	r(OH) (Å)	∠HOH (°)
H_2O	C_{2v}				0.962 (2)	105.1
$Zn^{2+}(H_2O)$	C_{2v}	1.881		125.3 (2)	0.984 (2)	109.5
$Zn^{2+}(H_2O)_2$	D_{2d}	1.876 (2)	180.0	125.6 (4)	0.979 (4)	108.8 (2)
$Zn^{2+}(H_2O)_3$	C_2	1.944 (2), 1.953	120.0 (3)	125.3 (2), 126.8 (2) 126.4 (2)	0.974 (4) 0.979 (2)	107.9 (2) 107.2
$Zn^{2+}(H_2O)_4$	S_4	2.002 (4)	105.1 (2), 111.7 (4)	126.0 (4), 126.3 (4)	0.970 (8)	107.6 (4)

[a] Values in parentheses indicate degeneracies.

Table 3.2. Relative calculated enthalpy (ΔH_0) and free energies (ΔG_{298})[a] (kJ/mol) of $Zn^{2+}(H_2O)_x(H_2O)_y$ where x is the number of waters in the inner solvent shell and y is the number of waters in the second shell.[b]

Complex (x,y)		Present work				Literature			
		B3LYP// B3LYP	B3P86// B3LYP	M06// B3LYP	MP2(full)// B3LYP	B3LYP// B3LYP[c]	B3LYP// B3LYP[d]	MP2(FC)// RHF[e]	MP2// HF[f]
$Zn^{2+}(H_2O)_5$	(4,1)_AA	0.0 (2.6)	0.0 (2.9)	6.5 (8.2)	3.3 (4.3)	0.0	0.0	2.5	3.8 (0.0)
	(4,1)_A	1.1 (0.0)	0.8 (0.0)	14.9 (12.9)	8.4 (5.7)				
	(5,0)	4.2 (5.8)	4.6 (6.4)	0.0 (0.6)	0.0 (0.0)	4.2	1.7	0.0	0.0 (0.4)
	(5,0)_switch	5.8 (5.4)	6.0 (5.8)	1.4 (0.0)	2.4 (0.3)				
$Zn^{2+}(H_2O)_6$	(4,2)_2AA	0.0 (0.0)	0.0 (0.0)	13.1 (12.8)	3.8 (7.5)	0.0	0.0	0.0	18.8 (12.6)
	(5,1)_A_aA_b	8.2 (0.3)	8.6 (0.6)	12.2 (4.1)	4.2 (0.0)	20.5	4.2	1.5	16.7 (3.8)
	(5,1)_A_a	17.1 (3.1)	17.4 (3.3)	26.6 (12.3)	16.9 (6.6)	15.5			26.4 (11.3)
	(6,0)	13.7 (14.0)	14.6 (14.8)	0.0 (0.0)	0.0 (3.9)	14.2	4.6	0.6	0.0 (0.0)
$Zn^{2+}(H_2O)_7$	(4,3)_3D,DD_2AA,A	0.0 (6.5)	0.0 (6.5)	14.9 (9.6)	10.8 (5.5)				
	(4,3)_2D,DD_AA,2A	4.1 (0.0)	4.1 (0.0)	23.6 (7.7)	18.0 (2.1)				
	(4,3)_2D,2DD_3AA	10.1 (23.0)	10.2 (23.0)	17.9 (18.9)	18.1 (19.1)				
	(5,2)_4D_2A_bA_b	0.2 (12.0)	0.1 (12.0)	0.0 (0.0)	0.0 (0.0)		0.0		
	(6,1)_AA	18.4 (31.3)	18.7 (31.6)	3.2 (4.3)	8.7 (9.7)		20.1		

Table 3.2. continued

Complex (x,y)		Present Work				Literature			
		B3LYP// B3LYP	B3P86// B3LYP	M06// B3LYP	MP2(full)//B 3LYP	B3LYP//B 3LYP[c]	B3LYP//B 3LYP[d]	MP2(FC)// RHF[e]	MP2// HF[f]
$Zn^{2+}(H_2O)_8$	(4,4)_2D,2DD_2AA,2A	1.8 (0.0)	2.4 (0.1)	21.4 (12.5)	14.9 (6.1)				
	(5,3)_3AA	0.0 (7.1)	0.0 (6.6)	0.0 (0.0)	0.0 (0.0)				
	(6,2)_2D,DD_2AA	16.8 (23.5)	17.7 (23.9)	2.1 (1.7)	6.7 (6.3)				
	(6,2)_4D_2AA	17.7 (25.0)	17.8 (24.6)	2.0 (2.2)	7.3 (7.5)				
$Zn^{2+}(H_2O)_9$	(4,5)_D,3DD_2AA,3A	5.8 (0.0)	6.3 (0.0)	30.7 (14.6)	22.1 (6.0)				
	(5,4)_4A_bA_b	0.0 (10.3)	0.0 (9.8)	0.0 (0.0)	0.0 (0.0)				
	(6,3)_6D_3AA	13.5 (27.9)	13.1 (26.9)	2.8 (7.0)	3.9 (8.0)				
	(6,3)_4D,DD_3AA	16.9 (26.0)	16.7 (25.3)	4.5 (3.3)	7.2 (6.0)				
$Zn^{2+}(H_2O)_{10}$	(4,6)_2AA,4A	3.5 (0.0)	4.4 (0.0)	26.9 (16.3)	18.6 (8.0)				
	(5,5)_4A_bA_b,A_a	0.0 (7.1)	0.0 (6.2)	0.0 (0.0)	0.0 (0.0)				
	(6,4)_4D,2DD_4AA	18.1 (35.5)	16.9 (33.5)	0.0 (10.3)	5.5 (15.9)				

[a] ΔG_{298} values given in parentheses. [b] Values are single point energies calculated at the level shown using a 6-311+G(2d,2p) basis set with geometries calculated at the B3LYP/6-311+G(d,p) level. Zero point energy corrections are included. [c] Values reported by Pavlov et al.[18] using a B3LYP/6-311+G(2d,2p)//B3LYP/LANL2DZ level of theory. [d] Values reported by Hartmann et al.[15] using a B3LYP/SHA1//B3LYP/SHA3 level of theory. [e] Values reported by Bock et al.[14] using a MP2(FC)/HUZSP*//RHF/HUZSP* level of theory. [f] Values reported by Lee et al.[16] using a MP2/TZ2P//HF/TZ2P level of theory.

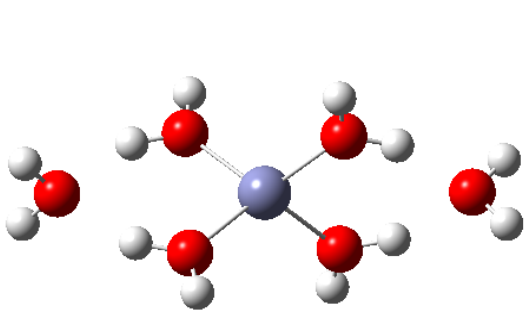

$Zn^{2+}(H_2O)_4(H_2O)_2$ - (4,2)_2AA

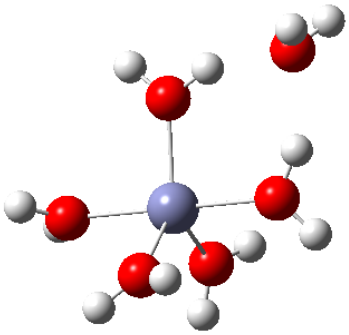

$Zn^{2+}(H_2O)_5(H_2O)$ - (5,1)_A_aA_b

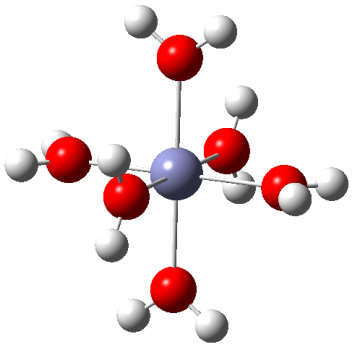

$Zn^{2+}(H_2O)_6$ - (6,0)

Figure 3.1. Low energy isomers of $Zn^{2+}(H_2O)_6$ calculated at the B3LYP/6-311+G(d,p) level of theory.

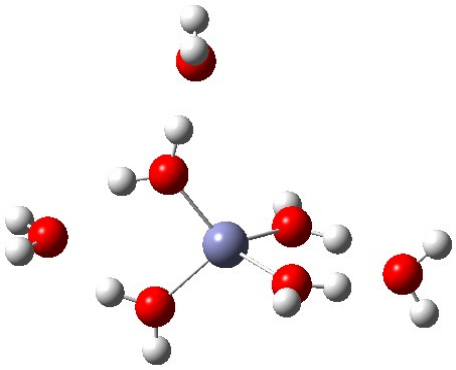

$Zn^{2+}(H_2O)_4(H_2O)_3$ -
(4,3)_3D,DD_2AA,A

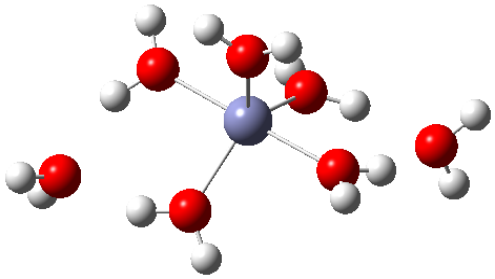

$Zn^{2+}(H_2O)_5(H_2O)_2$ -
(5,2)_4D_2A_bA_b

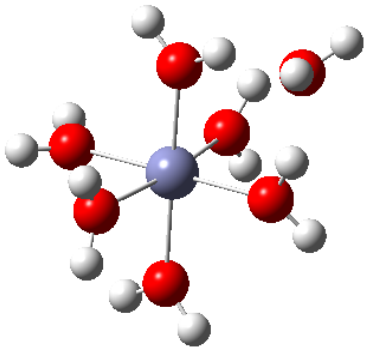

$Zn^{2+}(H_2O)_6(H_2O)$ - (6,1)_AA

Figure 3.2. Low energy isomers of $Zn^{2+}(H_2O)_7$ calculated at the B3LYP/6-311+G(d,p) level of theory.

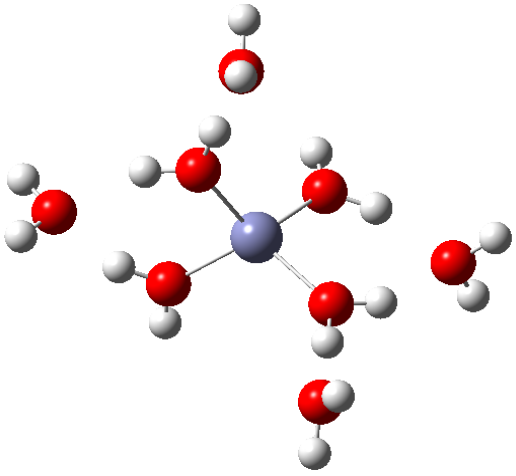

$Zn^{2+}(H_2O)_4(H_2O)_4$ -
(4,4)_2D,2DD_2AA,2A

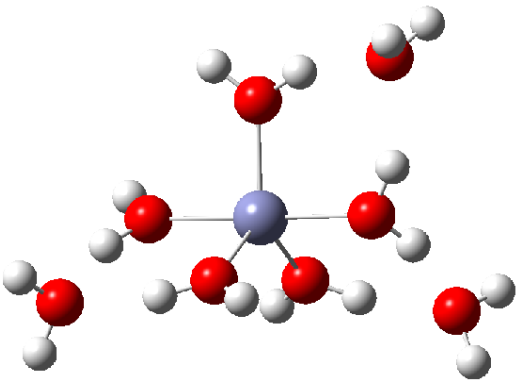

$Zn^{2+}(H_2O)_5(H_2O)_3$ -
(5,3)_3AA

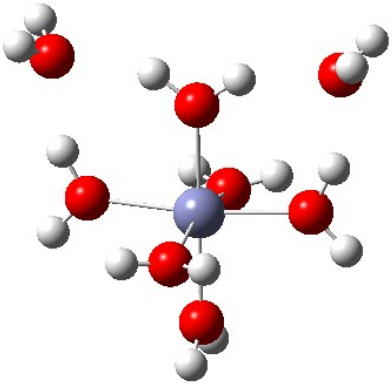

$Zn^{2+}(H_2O)_6(H_2O)_2$ -
(6,2)_2D,DD_2AA

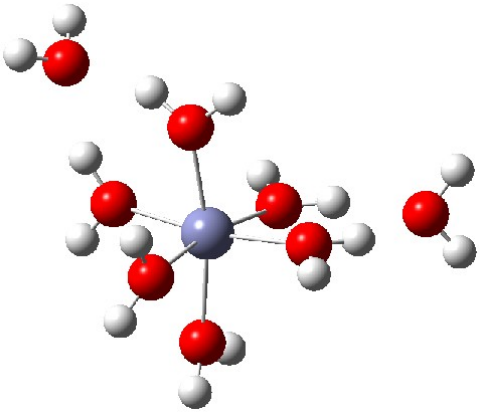

$Zn^{2+}(H_2O)_6(H_2O)_2$ -
(6,2)_4D_2AA

Figure 3.3. Low energy isomers of $Zn^{2+}(H_2O)_8$ calculated at the B3LYP/6-311+G(d,p) level of theory.

this structure has a lower 298 K free energy than (4,1)_AA at the Bx levels. Compared to the (5,0) structure, (5,0)_switch decreases the ∠OZnO bond angle of the two waters whose hydrogen atoms are pointing vertical to the base of the square pyramid, whereas ∠OZnO increases for the waters whose hydrogens are in the plane of the base.

For n = 6, there are now three options for the size of the inner shell with (4,2), (5,1), and (6,0) configurations, where the latter has all six water ligands in the inner solvent shell in a pseudo-octahedral geometry. These optimized structures are shown in Figure 3.1 and are comparable to geometries in previous reports.[14-18] Bock et al. performed geometry optimizations and SPE calculations using a MP2(FC)/HUZSP*//RHF/HUZSP* level and found that the energy difference between (4,2)_2AA, (5,1)_AA, and (6,0) was less than 2 kJ/mol, Table 3.2.[14] In contrast, Lee et al. found a larger energetic difference favoring the (6,0) structure by almost 17 kJ/mol over the (4,2)_2AA and (5,1)_AA structure using MP2/TZ2P//HF/TZ2P calculations.[16] As for the n = 5 complex, B3LYP results provide a much different ordering. Pavlov et al. found a flexible coordination calculating the preference for (4,2)_2AA to be about 14 – 21 kJ/mol whereas the (5,1)_AA and (6,0) differ from each other by about 1 kJ/mol using a B3LYP/6-311+G(2d,2p)//B3LYP/LANL2DZ level of theory.[18] Hartmann et al. used a B3LYP/SHA3//B3LYP/SHA1 level of theory and found a preference toward the (4,2)_2AA complex by 4 – 5 kJ/mol over (5,1)_AA and (6,0).[15] Pavlov et al. and Lee et al. also included an alternative (5,1)_A geometry, which was found to be about 5 kJ/mol lower in energy than (5,1)_AA at the B3LYP level[18] but about 10 kJ/mol higher than (5,1)_AA at the MP2 level.[16]

As for these previous results, we find energy differences among the three possible structures of the $n = 6$ complex calculated here to be relatively small, <14 kJ/mol, with the ground state changing from (4,2)_2AA for Bx to (6,0) for Mx calculations, Table 3.2. In the lowest energy (4,2)_2AA isomer, both second solvent shell water molecules bind to the inner solvent shell through two hydrogen bonds, Figure 3.1. The (5,1)_A_aA_b structure binds the outer shell water molecule to the apex water and one water in the base, abbreviated with the "a" and "b" subscripts, respectively. This arrangement necessitates rotation of one of the base water molecules, which disrupts some of the hydrogen bonding found in the (5,0) and (5,0)_switch structures. The (5,1)_A_a isomer has the sixth water singly hydrogen bound to the apex water of the square pyramid inner shell, such that it lies 9 – 14 kJ/mol above (5,1)_A_aA_b at 0 K, in contrast to the results of Pavlov et al. At 298 K, this excitation energy drops to 3 – 8 kJ/mol and the MP2(full) GS becomes the (5,1)_A_aA_b complex, whereas (6,0) becomes the M06 ground state, Table 3.2. The (4,2)_2AA remains the GS for the Bx calculations at 298 K.

Larger complexes, $n = 7 – 10$, were optimized using the same basic inner shell shapes. As many of these complexes have similar hydrogen bonding in the second solvation shell, our nomenclature includes terms "D" or "DD" to describe an inner shell water that donates to a second shell water with one or two hydrogen bonds, respectively. For the $n = 7$ complex, the 4- and 5-coordinate zinc ion structures are isoenergetic with each other at the two Bx levels of theory, whereas Mx calculations favor the 5-coordinate inner shell. These structures are shown in Figure 3.2. In the (4,3)_3D,DD_2AA,A complex, the seventh water is added to the (4,2)_2AA complex such that it forms only one hydrogen bond to the inner shell, which is much weaker than the two hydrogen bonds

formed for the second shell ligands in the (4,2)_2AA and (5,2)_4D_2A_bA_b complexes, as discussed further below. The (4,3) complex forms three higher energy isomers. Among these, the (4,3)_2D,DD_AA,2A, has two singly hydrogen-bound waters in the outer shell, where one of these is bound to an inner shell water that also binds the bridging second shell water. Although this complex is 4 – 9 kJ/mol higher in energy than (4,3)_3D,DD_2AA,A at 0 K, it has a lower free energy at 298 K by 2 – 7 kJ/mol. Interestingly, the (4,3)_2D,2DD_3AA isomer is highest in energy even though all three second shell waters form two hydrogen bonds to the inner shell. This is because the pseudo-tetrahedral inner shell must distort severely to allow the third second shell water to hydrogen bond to inner shell waters already binding the other second shell water ligands. The (5,2)_4D_2A_bA_b structure of the $n = 7$ complex has both second shell waters doubly bound across from each other to the base of the square pyramid and is comparable in geometry to the complex reported by Hartmann et al.[15] No high energy isomers for the (6,1)_AA structure were investigated in the present work, as Pavlov et al. reported a slight preference for the seventh water being doubly hydrogen bonded to the octahedral inner shell instead of a single hydrogen bond, with these two isomers being very close in energy (<1 kJ/mol).[18] A (7,0) complex was investigated here, but in agreement with the work of Hartmann et al.,[15] the (7,0) structure would always rearrange to the (6,1)_AA during optimization. Both of these previous studies neglected calculations of the (4,3) complexes.

In the $Zn^{2+}(H_2O)_8$ complex, for which previous theoretical results are not available, the tetrahedral 4-coordinate structure rises in energy at 0 K and the square pyramidal 5-coordinate inner shell is the lowest energy structure at all four levels of

theory, Table 3.2. This transition results from both distortions in the tetrahedral inner shell that result as the eighth water is added and to the fact that the eighth water must be singly hydrogen bonded whereas the (5,3)_3AA and (6,2)_2D,DD_2AA structures allow the eighth water to form two hydrogen bonds, Figure 3.3, thereby lowering the energies of these structures. The (4,4)_2D,2DD_2AA,2A structure adds two singly hydrogen bonded water molecules to (4,2)_2AA. At 298 K, these two singly bound second shell water ligands raise the entropy of this complex, such that this 4-coordinate structure is lowest in free energy at the Bx levels. Three (5,3) isomers were located with the lowest energy 0 K structure, (5,3)_3AA, having all three second shell waters doubly hydrogen bonded to the inner shell waters, with two connected to opposite pairs of base inner shell waters and the third connecting the apex water with a base water. This structure is also lowest in free energy at the Mx levels. The (6,2)_2D,DD_2AA and (6,2)_4D_2AA structures differ by less than 1 kJ/mol in energy, Table 3.2. Both have two second shell waters doubly hydrogen bonded to the inner shell, but in the lower energy structure, one of the inner shell waters is shared by the second shell waters, whereas in (6,2)_4D_2AA, they use two different pairs of inner shell waters, Figure 3.3. The former structure allows for the retention of more hydrogen bonding interactions among the inner shell waters. At 298 K, Bx calculations predict the six coordinate complexes to be much higher in free energy (23 – 25 kJ/mol), however, Mx calculations predict both (6,2) complexes to be only 2 – 7 kJ/mol higher in free energy.

In $Zn^{2+}(H_2O)_9$, the tetrahedral 4-coordinate structure again rises in energy relative to the (5,4)_$4A_bA_b$, which is the ground state geometry at all four levels of theory. The (6,3)_6D_3AA structure also lowers slightly in energy as the ninth water doubly

hydrogen bonds to the inner shell forming a complex with D_3 symmetry. The lowest 4-coordinate isomer found, (4,5)_D,3DD_2AA,3A, has two second shell waters doubly hydrogen bonded with the other three waters all singly hydrogen bonded to inner shell waters. While the lowest 5-coordinate complex is the (5,4)_$4A_bA_b$ with all 4 second shell waters forming two hydrogen bonds to the base of the square pyramid inner shell. Although this (5,4) structure is lowest in enthalpy at 0 K, its 298 K free energy is 10 kJ/mol higher than the (4,5) at the Bx levels (6 and 15 kJ/mol lower at MP2 and M06, respectively). The (6,3)_6D_3AA maximizes the distance between the second solvent shell waters such that no inner shell water is bound to two different second shell waters. The (6,3)_4D,DD_3AA complex is ~2 – 3 kJ/mol higher in energy than (6,3)_6D_3AA because one inner shell water is shared between two second shell waters. At 298 K, (6,3)_4D,DD_3AA is now lower in free energy by about 2 – 4 kJ/mol because one inner shell water is not constrained by a H bound to a second shell water.

For the $Zn^{2+}(H_2O)_{10}$ complex, again the 5-coordinate inner shell structure, (5,5)_$4A_bA_b,A_a$ is lowest in energy and can be formed by adding the tenth water singly hydrogen bonded to the apex water of the symmetric (5,4)_$4A_bA_b$ structure. However, the tetrahedral (4,6)_2AA,4A structure is relatively low in energy, has D_{2d} symmetry, and can be formed by singly hydrogen bonding four second shell waters to the inner solvent shell of the (4,2)_2AA structure. In (6,4)_4D,2DD_4AA, which has C_2 symmetry, the second shell is orientated in such a way that two inner solvent shell water ligands must each share two different second shell waters, i.e., the binding motif illustrated in the (6,2)_2D,DD_2AA complex, Figure 3.3.

Comparison to calcium water clusters. In contrast to the ambiguity of the inner coordination shell of Zn^{2+}, our previous studies of Ca^{2+} hydration[37] indicate that the 6-coordinate inner shell is the clear ground state configuration, being lower in energy by 10 – 23 kJ/mol compared to the 5-coordinate and lower by 24 – 47 kJ/mol compared to the 4-coordinate, depending on the level of theory for the $n = 6$ complexes. This assignment has now been confirmed by recent spectroscopic studies.[38] The 6-coordinate structures remain the ground states for larger $Ca^{2+}(H_2O)_n$ complexes (up to $n = 11$) with structures similar to the lowest energy structures found here. The (6,2)_2D,DD_2AA and (6,2)_4D_2AA isomers are similar to the two lowest energy structures discussed previously for $Ca^{2+}(H_2O)_8$, although there the (6,2)_4D_2AA structure is lower in energy by 2.2 – 2.6 kJ/mol. Also, the (6,3)_ 6D_3AA structure was found to be the ground state structure of $Ca^{2+}(H_2O)_9$.

Interestingly, the calculated distances from the metal ion to the inner shell oxygens are 0.2 to 0.4 Å larger for Ca^{2+} compared to Zn^{2+} for all complex sizes. This difference directly reflects the relative ionic radii of Ca^{2+} versus Zn^{2+}, 1.05 and 0.78 Å, respectively,[39] which can be attributed to the higher nuclear charge of Zn^{2+} with the additional ten electrons added to the 3d core orbitals. Compared to Ca^{2+}, which has a rare gas electron configuration, the ambiguity of the most stable inner shell for zinc can be understood in part by the 18 e^- rule, which is satisfied by $Zn^{2+}(H_2O)_4$, lending this inner shell enhanced stability compared to those where more waters are directly bonded to the metal ion.

CID cross sections. Experimental cross sections for collision-induced dissociation with Xe were acquired for $Zn^{2+}(H_2O)_n$ where $n = 7$ - 10, as shown in Figure

3.4. In all cases, the dominant reactions are the loss of a single water molecule, reaction 3.1, followed by loss of additional water molecules as the translational energy increases. The smallest zinc water complex observed was $Zn^{2+}(H_2O)_3$, Figures 3.4b and 3.4c, which has a cross section that is considerably smaller than that of the $Zn^{2+}(H_2O)_4$ product. In addition, the energy gap between the onsets of these two product ions is considerably larger than between any other pair of sequential products. These observations suggest that the $Zn^{2+}(H_2O)_4$ complex is particularly stable and may provide a clue as to the inner solvent shell of Zn^{2+}, as discussed further below. $ZnOH^+(H_2O)_n$ and $H^+(H_2O)_m$ products are also observed and shown as the total "charge separation" cross section in Figures 3.4a – d. These processes are discussed in detail in the following chapter. For the purposes of the present work, it is important to note that the $Zn^{2+}(H_2O)_7$ complex dissociates by charge separation in reaction 3.3 at lower energies than loss of a water molecule in reaction 3.1.

$$Zn^{2+}(H_2O)_7 + Xe \rightarrow ZnOH^+(H_2O)_3 + H^+(H_2O)_3 + Xe \qquad (3.3)$$

Because the charge separation process 3.3 is energetically more favorable than the competing water loss reaction, competition between these channels shifts the apparent water loss threshold to higher energies. Including this competition for $n \leq 7$ is necessary when extracting accurate threshold energies, as discussed in detail in Chapter 4.

Thermochemical results. Cross sections for the primary and secondary dissociation products were analyzed using eqs 2.3 and 2.4 and the sequential dissociation model (eq. 2.6) in several ways, with Table 3.3 summarizing the average modeling parameters used.

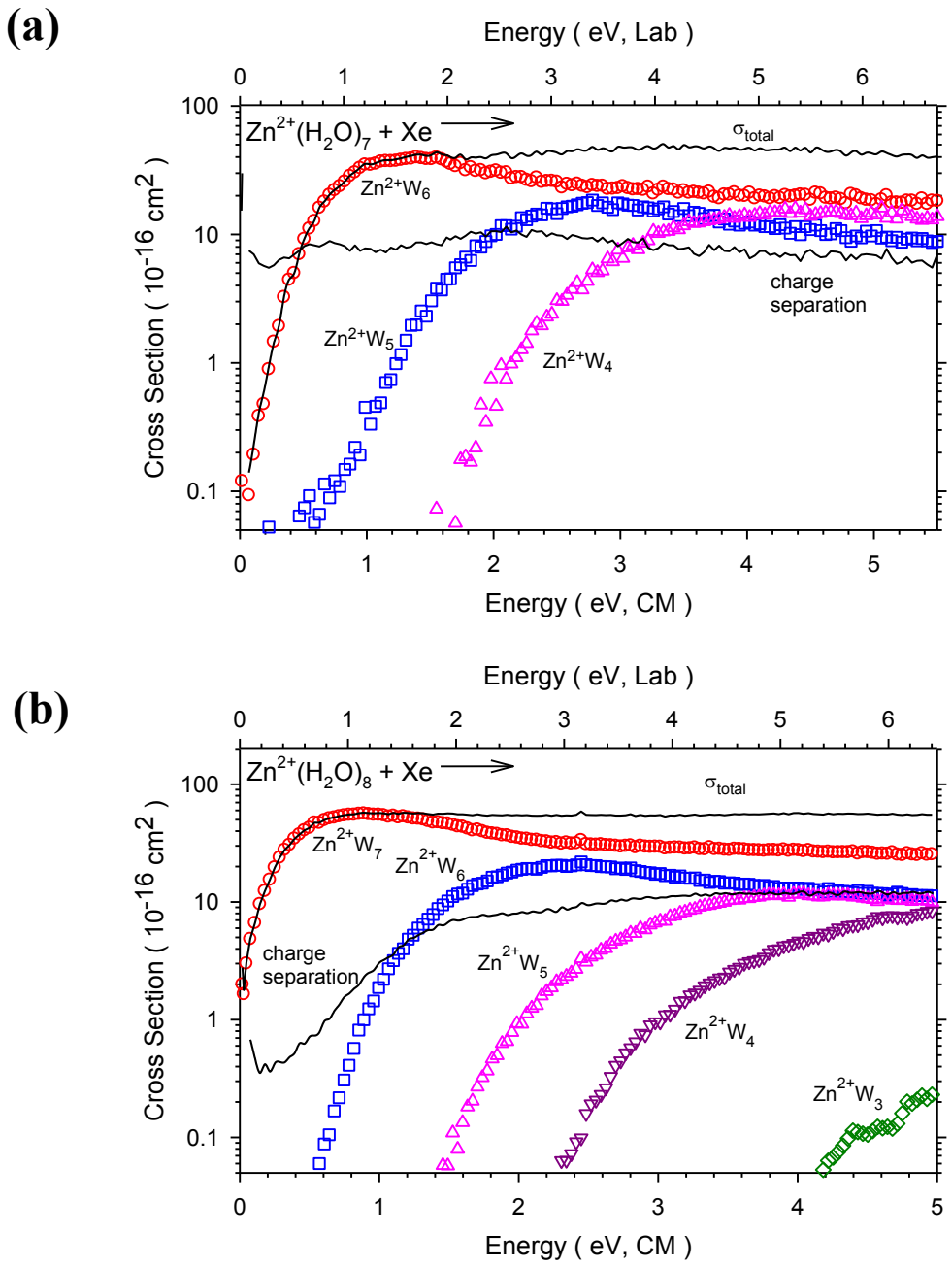

Figure 3.4. CID cross sections for the sequential water loss (open symbols) and charge separation processes (line) for $Zn^{2+}W_n$ where n = 7 – 10 and W = H_2O (parts a – d, respectively) colliding with Xe at 0.2 mTorr as a function of energy in the laboratory (upper x-axis) and center of mass (lower x-axis) frames.

(c)

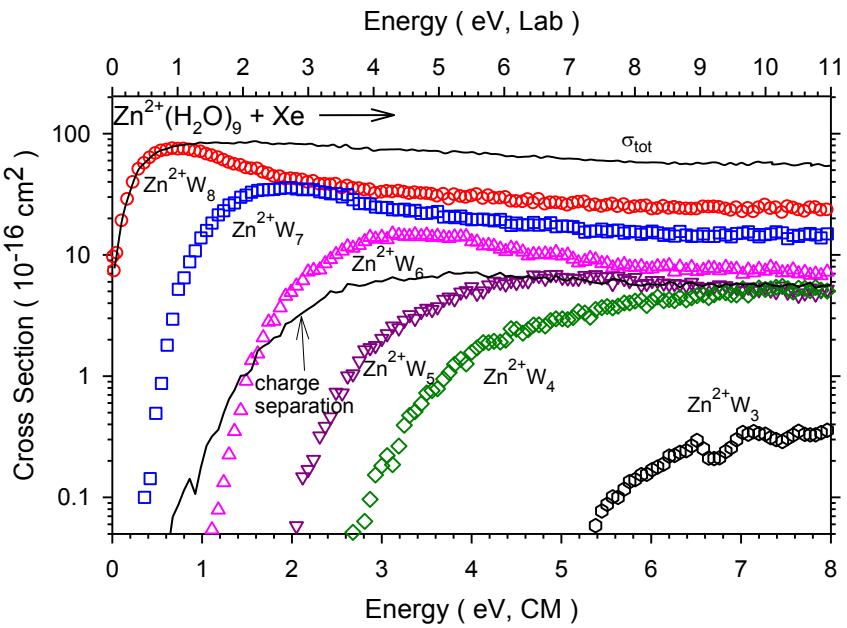

(d)

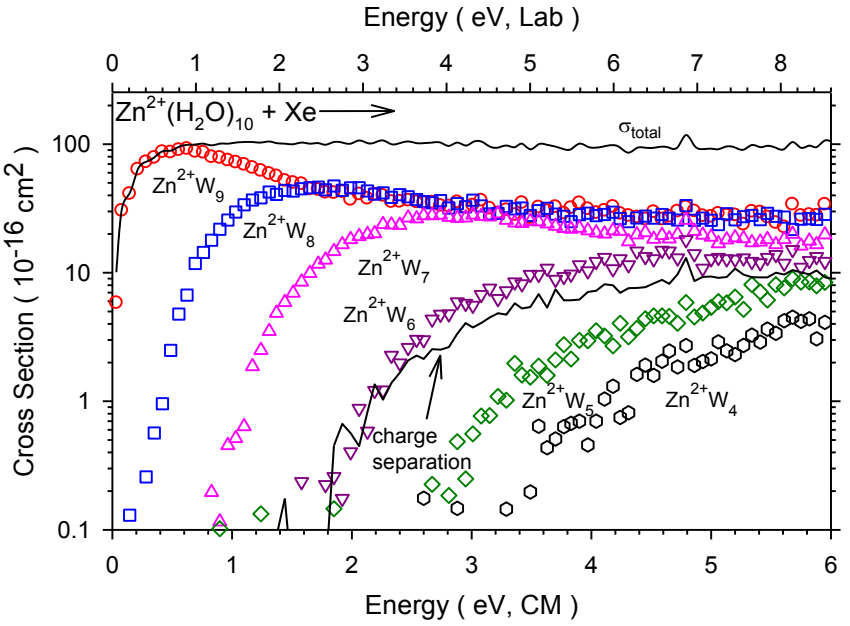

Figure 3.4. continued

Threshold E_0 values were determined for the primary dissociation of each complex from modeling with (eq 2.4) and without (eq 2.3) including RRKM theory. The difference between these results is the kinetic shift, which is appreciable for all complexes. The kinetic shifts for the water loss channels gradually increase as the complex gets larger. Notably, cross sections could not be reproduced with fidelity in the threshold region when fitting the water loss channels with eq 2.3, whereas including RRKM theory in eq 2.4 allows the kinetic energy dependence of the cross sections to be modeled accurately over a wide range of energies.

One complication with the analyses conducted here is that the results depend on the isomers assumed for the reactants and products. It should be realized that these changes in the threshold values are not a result of experimental error, but of the ambiguity in the theoretical calculations regarding the GS structures of the reactant and product complexes. Because theory provides ambiguous guidance about which isomers are favored, the analyses summarized in Table 3.3 include all pertinent permutations of the predicted EMs and TSs, as discussed below for each complex.

n = 9 and 10. For $Zn^{2+}(H_2O)_{10}$ and $Zn^{2+}(H_2O)_9$, there are no charge separation processes competing with either the primary or secondary water loss channels, Figure 3.4. For both complexes, the primary water loss dissociation is modeled simply by using eq 2.4 and the secondary water loss is modeled by introducing the sequential dissociation model using eq 2.6. A representative model is shown in Figure 3.5a for the sequential dissociation of $Zn^{2+}(H_2O)_9$, assumed to have the (5,4)_$4A_bA_b$ ground state geometry, or (5,4) (from this point forward we abbreviate our naming scheme to (*x*,*y*) for the lowest

Table 3.3. Optimized parameters of eqs. 2.3, 2.4, and 2.6 from analysis of CID cross sections [a]

n	Reactant	Product	σ_0	*N*	Kinetic Shift (eV)	E_0 (PSL, eV)	$\Delta S^{\dagger}_{1000\ K}$ (J/mol K)
10	(5,5)	(5,4)[b]	103 (3)	1.0 (0.1)	0.58 (0.04)	0.44 (0.03)	12 (4)
	(5,5)	(5,4)[c]	102 (4)	1.1 (0.1)	0.58 (0.07)	0.44 (0.06)	12 (4)
		(5,3)[c]	83 (5)	1.1 (0.1)		1.17 (0.03)	
	(5,5)	(5,4)[d]	103 (4)	1.0 (0.1)	0.58 (0.04)	0.44 (0.03)	12 (4)
		(6,3)[d,e]	103 (4)	1.0 (0.1)		0.48	10 (4)
	(5,5)	(5,4)[d]	103 (3)	1.0 (0.1)	0.58 (0.04)	0.44 (0.03)	12 (4)
		(4,5)[d,f]	103 (3)	1.0 (0.1)		0.50	80 (4)
	(5,5)	(4,5)[c]	101 (4)	1.1 (0.1)	0.55 (0.07)	0.47 (0.06)	79 (4)
		(5,3)[c]	84 (5)	1.1 (0.1)		1.14 (0.03)	
	(5,5)	(4,5)[c]	101 (4)	1.1 (0.1)	0.55 (0.07)	0.47 (0.06)	79 (4)
		(4,4)[c]	84 (5)	1.1 (0.1)		1.13 (0.03)	
	(4,6)	(5,4)[d]	103 (3)	1.0 (0.1)	0.64 (0.04)	0.38 (0.03)	-50 (4)
		(4,5)[d,f]	103 (3)	1.0 (0.1)		0.44	16 (4)
9	(5,4)	(5,3)[b]	92 (8)	0.9 (0.2)	0.42 (0.10)	0.55 (0.08)	54 (8)
	(5,4)	(5,3)[c]	92 (6)	0.9 (0.2)	0.40 (0.08)	0.57 (0.06)	57 (8)
		(4,3)[c]	58 (17)	0.9 (0.2)		1.31 (0.09)	
	(5,4)	(5,3)[c]	93 (6)	0.9 (0.2)	0.39 (0.08)	0.58 (0.06)	56 (8)
		(5,2)[c]	58 (17)	0.9 (0.2)		1.30 (0.09)	
	(5,4)	(5,3)[d]	92 (8)	0.9 (0.2)	0.42 (0.10)	0.55 (0.08)	54 (8)
		(6,2)[d,e]	92 (8)	0.9 (0.2)		0.62	75 (8)
	(5,4)	(5,3)[d]	92 (8)	0.9 (0.2)	0.42 (0.10)	0.55 (0.08)	54 (8)
		(4,4)[d,f]	92 (8)	0.9 (0.2)		0.57	90 (8)
	(4,5)	(5,3)[d]	91 (8)	0.9 (0.2)	0.50 (0.10)	0.47 (0.08)	-8 (8)
		(4,4)[d,f]	92 (8)	0.9 (0.2)		0.49	28 (8)
	(4,5)	(4,4)[b]	91 (8)	0.9 (0.2)	0.48 (0.10)	0.49 (0.08)	23 (8)

Table 3.3. continued

n	Reactant	Product	σ_0	N	Kinetic Shift (eV)	E_0 (PSL, eV)	$\Delta S^{\dagger}_{1000\ K}$ (J/mol K)
8	(5,3)	(4,3) [b]	67 (6)	0.8 (0.2)	0.34 (0.09)	0.71 (0.07)	65 (8)
	(5,3)	(4,3) [c]	68 (5)	0.8 (0.2)	0.33 (0.08)	0.72 (0.06)	67 (9)
		(4,2) [c]	48 (5)	0.8 (0.2)		1.68 (0.06)	
	(5,3)	(5,2) [d]	66 (6)	0.8 (0.2)	0.37 (0.09)	0.68 (0.07)	55 (8)
		(4,3) [d,e]	66 (6)	0.8 (0.2)		0.79	65 (8)
	(5,3)	(4,3) [d]	67 (6)	0.8 (0.2)	0.34 (0.09)	0.71 (0.07)	65 (8)
		(5,2) [d,f]	67 (6)	0.8 (0.2)		0.71	54 (8)
	(4,4)	(4,3) [d]	66 (6)	0.8 (0.2)	0.39 (0.09)	0.66 (0.07)	22 (8)
		(5,2) [d,f]	66 (6)	0.8 (0.2)		0.66	11 (8)
	(4,4)	(5,2) [b]	65 (6)	0.8 (0.2)	0.44 (0.09)	0.62 (0.07)	17 (8)
7	(4,3)	(4,2) [b]	58 (5)	0.7 (0.2)	0.20 (0.10)	0.89 (0.06)	18 (7)
	(4,3)	(4,2) [c]	58 (7)	0.8 (0.2)	0.21 (0.11)	0.88 (0.07)	19 (10)
		(4,1) [c]	37 (10)	0.8 (0.2)		2.02 (0.09)	
	(5,2)	(6,0) [c]	58 (7)	0.8 (0.2)	0.19 (0.11)	0.90 (0.07)	63 (10)
		(5,0) [c]	37 (10)	0.8 (0.2)		2.00 (0.09)	
	(5,2)	(5,1) [c]	58 (7)	0.8 (0.2)	0.14 (0.11)	0.95 (0.07)	76 (10)
		(5,0) [c]	37 (10)	0.8 (0.2)		1.98 (0.09)	
	(5,2)	(6,0) [d]	58 (5)	0.7 (0.2)	0.18 (0.10)	0.91 (0.06)	62 (7)
		(4,2) [d,e]	58 (5)	0.7 (0.2)		0.95	28 (7)
	(5,2)	(6,0) [d]	57 (5)	0.7 (0.2)	0.16 (0.10)	0.92 (0.06)	62 (7)
		(5,1) [d,e]	57 (5)	0.7 (0.2)		0.96	73 (7)
	(4,3)	(4,2) [d]	58 (5)	0.7 (0.2)	0.20 (0.10)	0.89 (0.06)	18 (7)
		(5,1) [d,f]	58 (5)	0.7 (0.2)		0.98	67 (7)
	(4,3)_ [g]	(4,2) [d]	58 (5)	0.7 (0.2)	0.28 (0.10)	0.81 (0.06)	-29 (7)
		(5,1) [d,f]	58 (5)	0.7 (0.2)		0.90	18 (7)

[a] Uncertainties in parentheses. [b] Single channel modeling using eq 2.4. [c] Sequential dissociation modeling using eqs 2.4 and 2.6. [d] Composite modeling using eq 2.4.

[e] Difference between the higher and lower energy threshold is given by MP2(full) results for respective complex sizes. [f] Difference between the higher and lower energy threshold is given by Bx results for respective complex sizes. [g] (4,3)_2D,DD_AA,2A isomer.

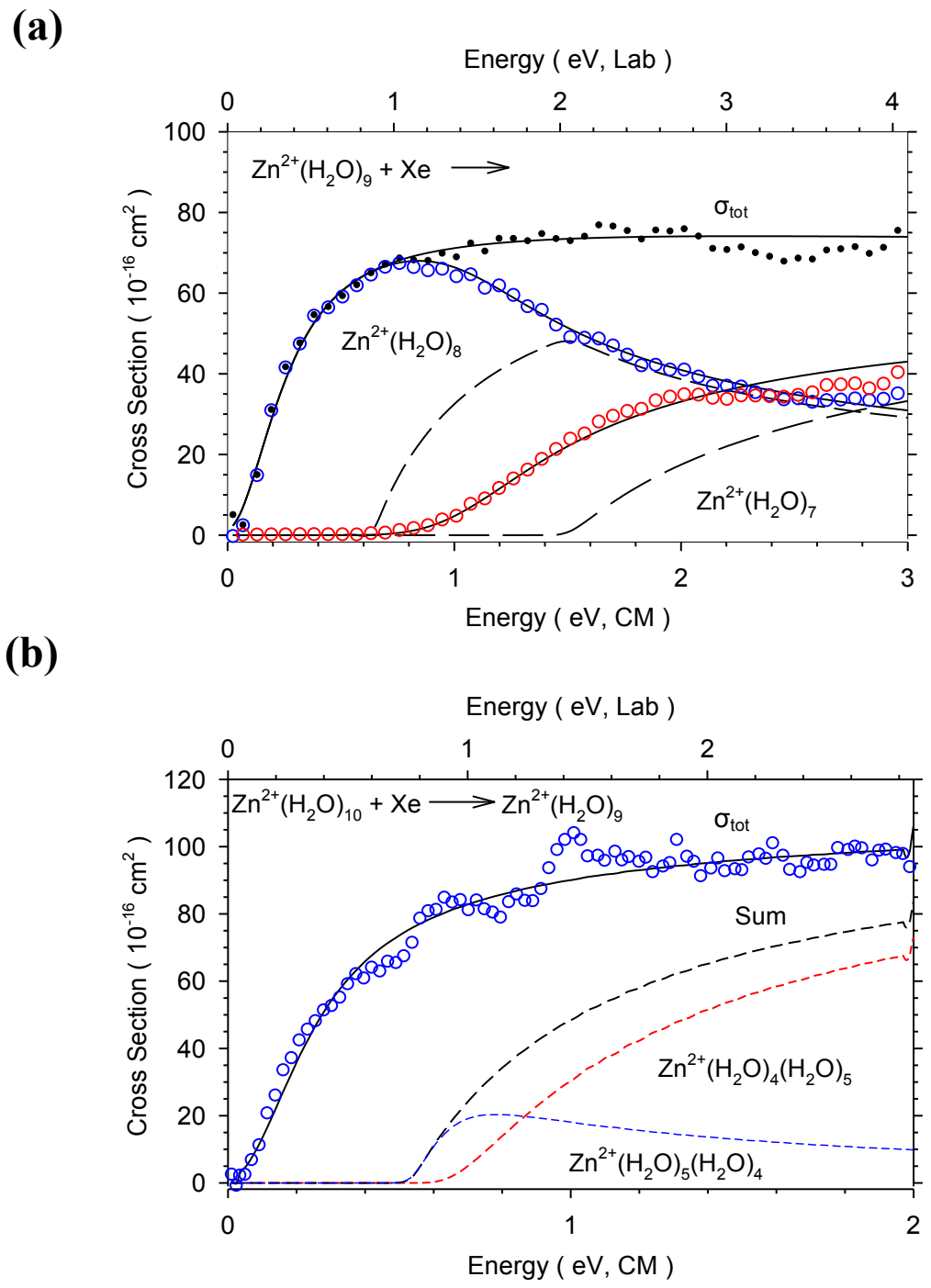

Figure 3.5. Zero pressure extrapolated cross sections for the CID of $Zn^{2+}(H_2O)_9$ (part a) and $Zn^{2+}(H_2O)_{10}$ (part b) with Xe. Solid lines show the best fits to both the primary and secondary water loss using eqs 2.4 and 2.6 convoluted over the kinetic and internal energy distributions of the neutral and ion. Dashed lines show the absence of experimental kinetic energy broadening for reactions with an internal energy of 0 K. In part b, the relative energy between the (5,4) and (4,5) products is set to the 0.06 eV value from Bx calculations. Optimized parameters for these fits are found in Table 3.3.

energy isomer of each inner solvent shell). We find that the primary thresholds obtained are independent of whether the sequential dissociation channel is included in the modeling or not, Table 3.3. However, small differences are observed depending on the isomers assumed for the reactants and products. If the $Zn^{2+}(H_2O)_{10}$ data are analyzed using molecular parameters appropriate for the (5,5) isomer dissociating to (5,4) + H_2O, then the threshold is 0.44 ± 0.03 eV, whereas dissociation to (4,5) + H_2O yields a slightly higher threshold of 0.47 ± 0.06 eV, and a (4,6) → (5,4) + H_2O dissociation gives a lower threshold by 0.06 eV. Likewise, analysis of $Zn^{2+}(H_2O)_9$ data assuming a (4,5) reactant has a threshold that is 0.08 eV lower than the (5,4) reactant, Table 3.3. These changes in measured thresholds are the result of differing kinetic shifts in all cases. When the reactants have four inner shell water ligands, there are more outer shell waters with lower torsional frequencies, which leads to a higher density of states and a much lower entropy of activation (by 60 J/mol K, Table 3.3) than when the reactants have a five water inner shell. Because of this restriction, the rates of dissociation decrease thereby increasing the kinetic shift and lowering the 0 K threshold for the four water inner shell complexes. Overall, there is no experimental means of ascertaining which interpretation of the data is preferred, so multiple values are discussed below in comparison to theoretical bond energies.

In the analyses discussed above, it was assumed that a single reactant isomer dissociates to a single product isomer, whereas several product isomers could conceivably be formed from any reactant. To consider this, we analyzed the data assuming that a single EM could dissociate to multiple product channels, such that

several dissociation channels (each leading to a product having the same mass) compete, as modeled using eq 2.4. In these "composite" models, the energy difference between product channels was fixed at the theoretical difference calculated at either the Bx (an average of B3LYP and B3P86) or MP2(full) levels. This method of analysis may better describe changes in the kinetic shift resulting from different entropies and densities of states of each product channel. A representative model is shown in Figure 3.5b for the composite fitting of (5,5) dissociating to both (5,4) + H_2O and (4,5) + H_2O using the Bx predicted relative energy of 0.06 eV between these two product channels. Dissociation to (5,4) is the lowest energy pathway; however, above about 0.85 eV, the (4,5) product dominates, Figure 3.5b, because it has a larger number of states resulting from the singly hydrogen bonded outer shell water ligand. Thus, the (5,5) → (4,5) + H_2O dissociation is faster according to RRKM rate theory and will have a smaller kinetic shift than the (5,5) → (5,4) + H_2O dissociation. Although the (4,5) product channel does not directly affect the threshold, it controls the high energy shape of the cross section, potentially influencing the *N* value in eq 2.4 used to reproduce the data, which could indirectly shift the measured threshold. In practice, we find that such composite fits of the data do not lead to significant shifts in the *N* values or measured thresholds (in all cases, changes in E_0 of less than 0.01 eV, Table 3.3). Thus, composite fits may very well be more accurate representations of the dissociation phenomena occurring but do not influence the thermochemistry derived.

In our analysis of the $Zn^{2+}(H_2O)_{10}$ data, the difference between the primary and secondary thresholds is 0.73 ± 0.03 eV when treated as (5,5) → (5,4) + H_2O → (5,3) + 2 H_2O, 0.67 ± 0.03 eV when treated as (5,5) → (4,5) + H_2O → (5,3) + 2 H_2O, and 0.66 ±

0.03 eV when treated as (5,5) → (4,5) + H_2O → (4,4) + 2 H_2O. Analysis of the $Zn^{2+}(H_2O)_9$ data yields a primary – secondary threshold difference of 0.74 ± 0.09 eV when treated as (5,4) → (5,3) + H_2O → (4,3) + 2 H_2O. These threshold energy differences are more precise than the differences in the absolute threshold energies listed in Table 3.3 because several systematic uncertainties cancel. The latter value of 0.74 ± 0.09 eV agrees well with that obtained from the 0.71 ± 0.07 eV threshold for the primary dissociation processes, reaction 3.1 modeled as (5,3) → (4,3) + H_2O. In contrast, the primary-secondary threshold difference for n = 10 of 0.73 ± 0.03 eV is higher in energy than the 0.55 ± 0.08 eV value given by the primary dissociation of n = 9, reaction 3.1 modeled as (5,4) → (5,3) + H_2O. Likewise, the 0.67 ± 0.03 and 0.66 ± 0.03 eV threshold differences are similarly higher than the primary threshold when modeled in a self-consistent manner, namely as (4,5) → (5,3) + H_2O and (4,5) → (4,4) + H_2O, respectively. This result is discussed further below.

n = 7 and 8. Analysis of the primary reaction pathways of $Zn^{2+}(H_2O)_8$ and $Zn^{2+}(H_2O)_7$ considering various reactant and product isomers yields similar results as the n = 9 and 10 complexes. The (4,4) → (4,3) + H_2O dissociation yields an E_0 value that is 0.05 eV lower than the (5,3) → (4,3) + H_2O dissociation, which has a threshold of 0.71 ± 0.07 eV. As for the larger complexes, this increase is a result of the larger number of low torsional frequencies of the (4,4) compared to the (5,3) reactant, such that the entropy of activation decreases by 40 J/mol K, Table 3.3. We also find that a (5,3) → (5,2) + H_2O pathway has a lower threshold than (5,3) → (4,3) + H_2O by 0.03 eV, because the former product is more constrained than the latter (with a change in the entropy of activation of only 10 J/K mol). Similarly, the (4,4) → (5,2) + H_2O dissociation has the lowest

threshold and entropy of activation of 0.62 ± 0.07 eV and 17 ± 8 J/mol K, respectively, because this dissociation involves the loosest reactant dissociating to the most constrained product.

More dissociation pathways were analyzed for the dissociation of $Zn^{2+}(H_2O)_7$ because theory predicts multiple low energy structures of the reactant and product. Comparing the (4,3) → (4,2) + H_2O dissociation, which has an E_0 value of 0.89 ± 0.06 eV, (5,2) → (6,0) + H_2O is only 0.01 – 0.03 eV higher in energy (depending on whether a composite analysis is used and what the higher energy channel is), well within experimental uncertainty. Lower in energy is the dissociation of (4,3)_2D,DD_AA,2A to the (4,2) complex having an E_0 value of 0.81 ± 0.06 eV, a difference of 0.08 eV. This shift is relatively large because two of the three second shell waters are singly hydrogen bonded in (4,3)_2D,DD_AA,2A, whereas only one of them is in (4,3). This leads to a change in the entropy of activation of about 50 J/mol K.

For sequential dissociation of $Zn^{2+}(H_2O)_8$, modeled as (5,3) → (4,3) + H_2O → (4,2) + $2H_2O$, the difference between the primary and secondary thresholds yield 0.96 ± 0.06 for the dissociation energy of $Zn^{2+}(H_2O)_6$-H_2O. This value agrees with the threshold value obtained from the primary dissociation process of $Zn^{2+}(H_2O)_7$ modeled as (4,3) → (4,2) + H_2O, 0.89 ± 0.06 eV. In this system, derivation of accurate thermochemistry requires that the modeling should take into account the competition between the water loss and charge separation processes using eq 2.4. This is described fully in the following chapter.

In our analysis of the sequential dissociation of $Zn^{2+}(H_2O)_7$, a number of reactant and product isomers were again considered. When modeled as (4,3) → (4,2) + H_2O →

(4,1) + $2H_2O$, the difference between the primary and secondary thresholds is 1.13 ± 0.05 eV. When modeled as (5,2) → (6,0) + H_2O → (5,0) + $2H_2O$, the difference between the primary and secondary E_0 values is 1.10 ± 0.05 eV, within experimental uncertainty. However, the difference between the primary and secondary thresholds is 1.03 ± 0.05 eV, 0.10 eV lower in energy, when the data are analyzed assuming (5,2) → (5,1) + H_2O → (5,0) + $2H_2O$. Examination of Table 3.3 shows that this difference is a result of small changes in both the absolute primary (by 0.07 eV) and secondary (by 0.04 eV) thresholds. In both cases, the differences in the thresholds can be traced to changes in the kinetic shifts associated with the varying reactant and product isomers. For this secondary threshold, no primary threshold for the dissociation of $Zn^{2+}(H_2O)_6$ is available for the comparison as charge separation limits the size of the reactants to $n \geq 7$.

Experimental bond enthalpies: primary and secondary values. Table 3.4 lists experimental 0 K hydration energies that are equated with the primary threshold energies and differences between the secondary and primary threshold energies, all taken from Table 3.3. Theoretical 0 K hydration energies calculated here at three levels of theory and from the literature are shown for comparison. The reactant and product isomers chosen for comparison in Table 3.4 are based on the relative 298 K free energies and 0 K enthalpies given in Table 3.2. For a primary threshold energy, the reactant isomer is assumed to be the 298 K GS (as this species should have the dominant population in a thermally equilibrated source) and the product isomer is the 0 K GS (as our threshold analysis is dominated by the lowest 0 K enthalpy species, Figure 3.5b). In contrast, the secondary thresholds correspond to the 0 K primary product GS isomer dissociating to the 0 K product GS isomer for each level of theory. Because Bx and Mx calculations

Table 3.4. Comparison of experimental 0 K bond energies (kJ/mol) to theoretical values. Values in bold highlight the experimental threshold energies interpreted on the basis of the corresponding theoretical value.

n	Reactant	Product	Experiment	B3LYP// B3LYP[a]	B3P86// B3LYP[a]	M06// B3LYP[a]	MP2(full)// B3LYP[a]	MP2(FC)// RHF[b]	B3LYP// B3LYP[c]	B3LYP// B3LYP[d]	MP2// HF[e]
6	(4,2)	(4,1)	**98.4[f,g] (3.9)**	**97.0**	**100.6**	103.7	95.7		101.3	100.8[h]	95.0
			109.0[g] (4.8)								
	(6,0)	(5,0)	**94.6[f,g] (3.9)**	87.1	90.1	**110.2**	**93.6**	123.1[h]	91.2		110.9
			105.8[g] (4.8)								
7	(4,3)	(4,2)	78.2[f] (4.8)	79.8	82.5	78.3	76.5				
			92.6[g] (5.8)								
	(4,3)_[i]	(4,2)	**71.4[f] (4.8)**	**75.7**	**78.4**	69.6	69.3				
	(5,2)	(6,0)	**79.2[f] (4.8)**	93.5	97.0	**81.7**	**83.3**				
	(6,1)	(6,0)		75.1					76.6		
	(5,2)	(4,2)		79.7						87.9	
8	(4,4)	(4,3)	**63.7[f] (5.8)**	**74.8**	**77.0**	76.4	72.7				
	(5,3)	(4,3)	70.4[f] (5.8)	**75.8**	**78.6**	96.3	86.3				
			71.4[g] (8.7)								
	(5,3)	(5,2)	**67.5[f] (5.8)**	76.0	78.8	**81.4**	**75.4**				

Table 3.4. continued

n	Reactant	Product	Experiment	B3LYP// B3LYP[a]	B3P86// B3LYP[a]	M06// B3LYP[a]	MP2(full)// B3LYP[a]	MP2(FC)// RHF[b]	B3LYP// B3LYP[c]	B3LYP// B3LYP[d]	MP2// HF[e]
			69.5[g] (8.7)								
9	(4,5)	(5,3)	**45.3[j] (7.7)**	**65.6**	**66.8**	49.5	50.9				
			64.6[g] (2.9)								
	(5,4)	(5,3)	**53.1[j] (7.7)**	**70.8**	**72.5**	**79.4**	**71.6**				
			70.4[g] (2.9)								
10	(4,6)	(5,4)	**36.7[j] (2.9)**	**57.2**	**58.1**	34.3	40.2				
	(5,5)	(5,4)	**42.5[j] (2.9)**	60.6	62.4	**61.5**	**59.0**				

[a] Geometry optimizations calculated using a B3LYP/6-311+G(d,p) level and SPE values calculated with a 6-311+G(2d,2p) basis set for each level. ZPE and cp corrected. [b] Values reported by Bock et al. using MP2(FC)/HUZSP*//RHF/HUZSP*.[14] [c] Values reported by Pavlov et al. using B3LYP/6-311+G(2d,2p)//B3LYP/ LANL2DZ.[18] [d] Values reported by Hartmann et al.[15] using B3LYP/SHA1//B3LYP/SHA3. [e] Values reported by Lee et al.[16] using MP2/TZ2P//HF/TZ2P. [f] Values including competitive shift reported in Chapter 4. [g] Sequential dissociation model using eqs 2.4 and 2.6. [h] No counterpoise correction. [i] (4,3)_2D,DD_AA,2A isomer. [j] Single channel model using eq 2.4.

interpretation of the data. In Table 3.4, values in bold highlight the experimental threshold energy and its corresponding theoretical value.

For the n = 6 bond enthalpies, which can only be obtained from secondary thresholds for dissociation of $Zn^{2+}(H_2O)_7$ dissociating to $Zn^{2+}(H_2O)_5 + 2H_2O$, values were obtained including competition with the charge separation process, as accounted for and explained in the following chapter, and ignoring this competition. For both possible reactant isomers, (4,2) and (6,0), the value that includes this competition is lower, ranging from 94 – 99 kJ/mol, and is our best measurement of the n = 6 hydration energy. The energy difference between the values with and without competition is nearly constant, 10 – 11 kJ/mol for the two isomers, and is a measure of the competitive shift in this case.

Similar to the n = 6 complexes, the n = 7 complex exhibits a competitive shift of ~14 kJ/mol for the (4,3) → (4,2) + H_2O dissociation pathway, Table 3.4. (Although not explicitly examined, it is expected that similar shifts would occur for any of the other combinations of reactant/product isomers for the n = 7 complex, as was observed for the n = 6 system.) Note that the sequential energy listed for $Zn^{2+}(H_2O)_8$ dissociating to $Zn^{2+}(H_2O)_6 + 2H_2O$, 0.96 ± 0.06 eV, agrees within experimental uncertainty with the primary dissociation threshold of $Zn^{2+}(H_2O)_7$ that does not account for competition, 0.89 ± 0.06 eV, Table 3.3. In both measurements, competition with charge separation has shifted the thresholds to higher energies. As for the n = 6 complex, our best experimental hydration energies for n = 7 are those obtained from the analyses that include competition, here the primary thresholds. These range from 71 – 79 kJ/mol, Table 3.4, depending on the various reactant and product isomers assumed in the analysis.

The water loss dissociation channel of the $n = 8$ complex is not affected significantly by competition with the charge separation channel that occurs at this complex size. Accordingly, the difference between 0 K hydration energies obtained from the primary and secondary dissociation channels are within 1 – 2 kJ/mol, well within experimental uncertainty. These values range from 63 – 72 kJ/mol, Table 3.4, depending on reactant and product isomers.

For the $n = 9$ complex, there is no charge separation channel competing with dehydration. We measure a difference between the primary and secondary E_0 values for the (5,5) → (5,4) + H_2O → (5,3) + $2H_2O$ process as 0.73 ± 0.03 eV, whereas the primary E_0 value for (5,4) → (5,3) + H_2O is lower, 0.55 ± 0.08 eV, Table 3.3. The difference between these two measurements (0.18 eV) is outside of experimental uncertainty (0.11 eV), and alternate isomer assumptions, (4,5) → (5,3) + H_2O, yield similar results (see above). One possible explanation for this difference hypothesizes that we are producing a distribution of isomers of these larger complexes in our ESI source. For instance, isomers of the $n = 8 – 10$ complexes having a 4-coordinate inner hydration shell are calculated to lie 15, 22, and 19 kJ/mol, respectively, above the 5-coordinate GSs at the MP2(full) level of theory, Table 3.2. According to the free energies of these species calculated at the MP2(full) level, a Boltzmann distribution at 298 K predicts the (4,5) structure to be 8% abundant. The presence of these higher energy isomers in our reactant ion beams could lead to primary dissociation thresholds that are low by amounts up to these excitation energies. However, using this example, if the $n = 9$ cross section is modeled assuming 92% (5,4) and 8% (4,5) isomers are present with an energy gap of 22 kJ/mol (0.23 eV) between them, the 0 K threshold determined changes by only 0.03 –

0.04 eV from analysis where only the (5,4) reactant is present. Notably, the relative Bx free energies of the (5,4) and (4,5) are reversed compared to the Mx energies, such that the (4,5) species would be calculated to comprise 98% of the reactant beam. In this case, virtually no change in threshold would occur if 2% excited isomers in the reactant ions were included in the analysis.

Unlike the primary dissociations, we don't believe that the sequential energies are influenced by alternate isomers in the reactant beam. This is because even if the reactant ions have a distribution of isomers, the primary and secondary thresholds are lowered by the same amount of energy, such that the relative measurement is unaffected. It can also be noted that a distribution of primary product isomers, such as that shown in Figure 3.5b, will not influence the absolute secondary threshold because the thermodynamics cannot be dependent on the pathway used to produce the secondary product from reactant ions. From an experimental point of view, neither the primary threshold of 0.55 ± 0.08 eV nor the secondary threshold of 0.73 ± 0.03 eV can be discounted as a valid measurement for the (5,4) → (5,3) + H_2O process.

Comparison of experimental and theoretical bond energies. Figures 3.6a and 3.6b are direct comparisons of experimental and theoretical 0 K hydration energies from Table 3.4. Figure 3.6a has experimental data interpreted using Bx predicted GS isomers compared to Bx theoretical hydration energies and Figure 3.6b compares the values obtained from Mx predicted isomers. As discussed above, there is no primary value for $n = 6$ as this complex cannot be formed in the ESI source because of the charge separation process, and there is no secondary value for $n = 7$ because competition with the charge separation process cannot be included in the analysis. Good agreement with theory is

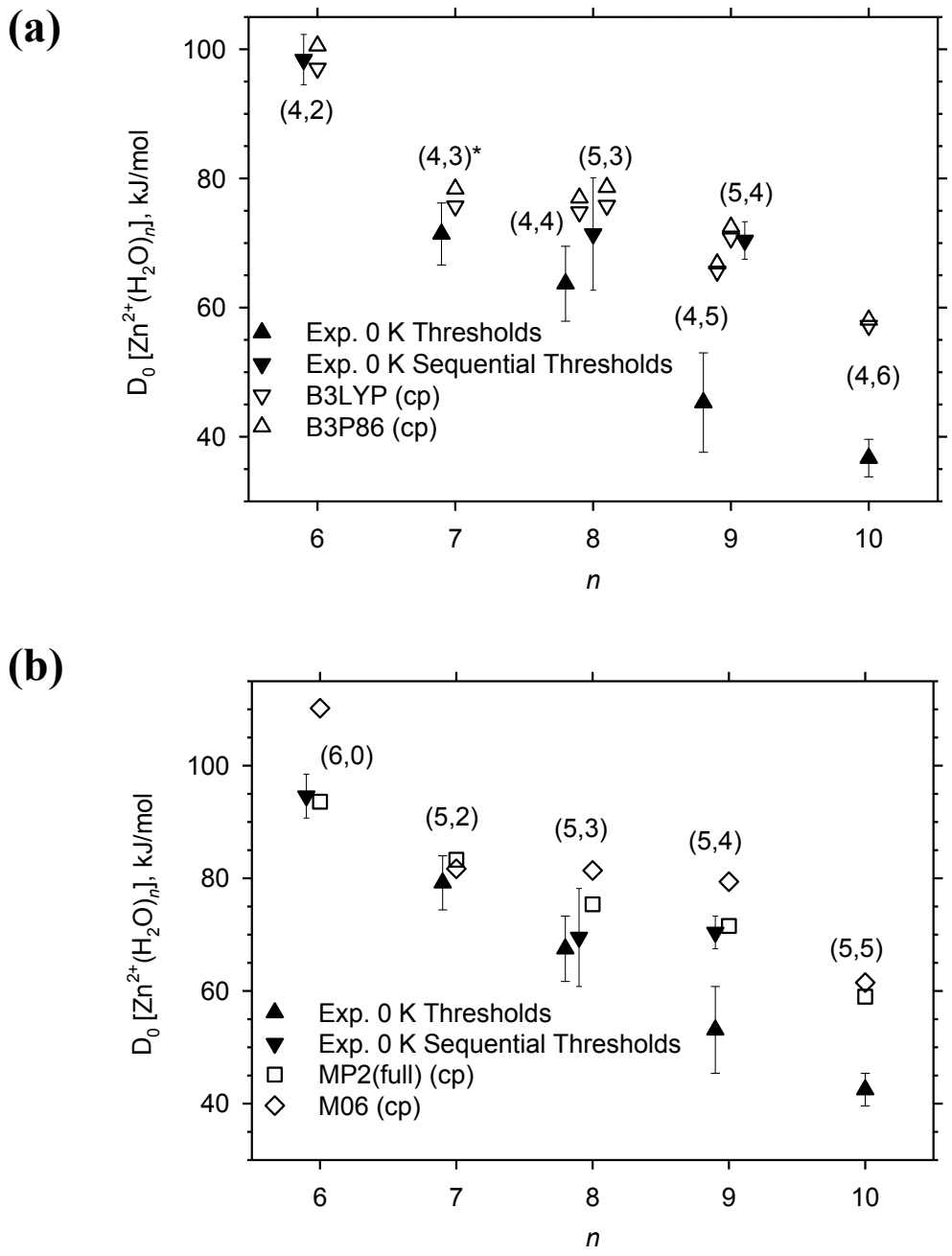

Figure 3.6. Comparison of experimental (solid symbols) and theoretical (open symbols) hydration enthalpies at 0 K for Bx (part a) and Mx (part b) results. All theoretical results shown are counterpoise corrected. The (4,3)* isomer corresponds to (4,3)_2D,DD_AA,2A.

found for $n = 6$, for all reactant and product isomers, but only when the effects of competition are included, Table 3.4, which verifies the importance of including the competitive shifts as analyzed in Chapter 4. This more sophisticated modeling is necessary to obtain accurate hydration energies for this complex size, yielding 98.4 ± 3.9 kJ/mol using the Bx predicted (4,2) isomer and 94.6 ± 3.9 kJ/mol for the Mx predicted (6,0) reactant. Both methods of data analysis give excellent agreement to their respective levels of theory with MADs (mean absolute deviations) between experiment and three of the four levels of theory: 1.8 kJ/mol for the Bx (4,2) isomer and 1.0 kJ/mol for the MP2(full) (6,0) reactant. In contrast, the M06 level predicts a binding energy for (6,0) that is 15.6 kJ/mol higher in energy than experiment and 16.6 kJ/mol higher than MP2(full). Overall, neither theory nor the precision of the data analysis allows an unambiguous determination of which isomer is the true ground state. Therefore, we show both individual dissociation pathways in Figures 3.6a and 3.6b.

Similar to the $n = 6$ dissociation, the experimental 0 K hydration energies for the different isomers of $n = 7$ vary between the (4,3)_2D,DD_AA,2A and (5,2) reactant species predicted by Bx and Mx, respectively. The (4,3)_2D,DD_AA,2A dissociation is lower by 8 kJ/mol, compared to the (5,2) dissociation, a difference that is attributed to a change in the kinetic shift as discussed above. The (4,3)_2D,DD_AA,2A dissociation gives reasonable agreement with Bx theory, MAD of 5.7 kJ/mol, Figure 3.6a. Threshold results interpreting the data using the (5,2) reactant also gives excellent agreement to Mx theory with a MAD of 3.3 kJ/mol, Figure 3.6b, within experimental uncertainty.

As for the $n = 7$ results, the 0 K hydration energies for the various isomers of $n = 8$ remain within experimental uncertainty of each other. Here more dissociation

pathways are considered because the primary process is assumed as the lowest 298 K free energy reactant dissociating to the lowest 0 K product, but the secondary process is the lowest energy 0 K dissociation. In this case, Bx results predict a (4,4) → (4,3) + H_2O primary process and a (5,3) → (4,3) + H_2O secondary process with MADs of 12.2 and 5.8 kJ/mol, respectively. The Mx GS structure results are less ambiguous at the larger complex sizes, predicting the (5,3) → (5,2) + H_2O for both the primary and secondary processes, Figure 3.6b. The differences in these thresholds from MP2(full) theory are 7.9 and 5.9 kJ/mol, respectively, and increase to 13.9 and 11.9 kJ/mol for M06 theory, respectively. Overall, neither theory nor experiment are able to definitively ascertain which reactants or dissociations are truly active.

For the larger n = 9 and 10 water complexes, experimental E_0 values obtained using eq 2.4 assuming a five-water inner solvent shell for the reactants differ from theoretical results by 16 – 26 kJ/mol depending on the level of theory used to interpret the data. However, when the data are analyzed assuming a (5,5) → (5,4) + H_2O → (5,3) + $2H_2O$ dissociation pathway, predicted by both Bx and Mx, the relative secondary threshold obtained yields a binding energy for n = 9 that is in excellent agreement with theory, with a MAD of only 4.3 kJ/mol. This is in much better agreement with theory than the primary values. The primary value predicted by Bx is the (4,5) → (5,3) + H_2O dissociation, with a MAD of 20.9 kJ/mol, Figure 3.6a. The Mx levels again predict the primary process as the 5-coordinate dissociation. Although this is the same isomeric dissociation seen in the secondary value above, the primary process has a MAD of 22.5 kJ/mol lower than the energy predicted by theory, Figure 3.6b. Obviously the sequential value is in much better agreement with all three levels of theory. These deviations have

several possible explanations. As discussed above, higher energy isomers could be present in the reactant ion beams, leading to primary dissociation thresholds that are lower than the calculated bond energies for the GSs. In particular for these larger complexes, it seems possible that rehydration of smaller complexes in the hexapole region of the source could place a water ligand in a more weakly bound outer solvent shell, e.g., (5,3,1). As demonstrated in Chapter 4, there can be appreciable barriers to rearrangement of such outer shell water molecules moving to more stable inner shell positions. Another possible explanation is that thermalization of these larger complexes is not as complete as the smaller, more strongly bound complexes. Indeed, analysis indicates that the primary threshold would agree with that derived from the secondary threshold if the $n = 9$ reactant had a temperature of 500 K. However, such an analysis also necessitates lowering the N value such that the model no longer reproduces the data nearly as well, thereby discounting this hypothesis. Furthermore, a temperature of 500 K seems extraordinarily high for a source that has previously shown to produce thermalized ions.[37,40-42] The third explanation is that theory is not accurately accounting for the partially filled second solvent shell seen in the 8 – 10 water complexes. Rudolph et al. believed that the second hydration shell around Zn^{2+} is filled at $n = 18$ with an inner shell of 6, and any smaller structure with a partially filled second shell yielded a calculated binding enthalpy that would account for only 62 - 69% of the experimentally found single ion hydration enthalpy.[5] However, the study by Rudolph et al. only performed calculations using HF and MP2 levels of theory (with a variety of smaller basis sets compared to those used here) on the $n = 1 – 6$ and 18 complexes. On the basis of the calculations performed here, an inner solvent shell of six is consistently higher in energy

than inner solvent shells of five and four for complexes up to $n = 10$, with the exception of the Mx results for the (6,0) complex. Pavlov et al. also addressed the importance of a filled second solvent shell for accurate binding energies and inner shell size prediction. They concluded that larger cluster sizes of at least $n > 12$ were necessary to represent the dilute solutions found in spectroscopy experiments.[18] The importance of the second hydration sphere in the calculation of both frequencies and SPEs is seen both in the literature and in the work presented here for $n \geq 8$. Investigations are ongoing as to whether an alternate basis set or theoretical approach will more accurately account for this partially filled second shell.

For the $n = 10$ complexes, the primary processes are again much lower in energy than theory. If the data are interpreted as a 4-coordinate reactant dissociating to a 5-coordinate product (as predicted by Bx), the threshold, 36.7 ± 2.9 kJ/mol, has a MAD from theory of 20.9 kJ/mol, Figure 3.6a. This value actually agrees within experimental uncertainty with values calculated at the Mx levels of theory, however, this level of theory strongly supports the 5-coordinate GSs, leading to internal inconsistency. Similarly, the $(5,5) \rightarrow (5,4) + H_2O$ process supported by Mx has a threshold of 42.5 ± 2.9 kJ/mol, with a MAD compared to theory of 17.8 kJ/mol, Figure 3.6b. If a temperature of 500 K for the reactant is used in the analysis, the threshold increases to 50.3 kJ/mol giving a MAD of 10.0 kJ/mol. However, raising the temperature of the reactant means that the model fails to reproduce the data well and gives a threshold for $n = 10$ that is still lower in energy than that predicted by theory. Because primary thresholds for both $n = 9$ and 10 are low compared to theory, and the sequential value for $n = 9$ agrees, we do not believe these primary thresholds represent our best experimental values.

Conversion from 0 K to 298 K thermodynamics. Using the vibrational frequencies and rotational constants of the zinc water clusters calculated at the B3LYP/6-311+G(d,p) level of theory discussed above, a rigid rotor/harmonic oscillator approximation was applied to convert the 0 K bond energies to 298 K hydration enthalpies, Table 3.5. The uncertainties in these conversions are found by scaling the vibrational frequencies up and down by 10%. This approximation may not be suitable for all cases because of the low frequency torsional motions. Nevertheless, values appropriate for the GS species as determined from single point energies and free energies at both the Bx and Mx levels of theory were considered, as discussed above. When looking at the different reaction pathways in Table 3.5, it can be noted that changes in the $T\Delta S_{298}$ values are inversely related to changes in the kinetic shift from Table 3.3. As the kinetic shift increases, the hydration energy decreases and both the entropy of activation and dissociation also decrease.

Comparing the dissociation pathways selected for Figure 3.6a (those predicted by Bx), the free energy values (ΔG_{298}) decrease as the complex gets larger. For the predicted primary dissociation pathways, the relative entropies of dissociation, $T\Delta S_{298}$, change as (4,2) > (4,3)_2D,DD_AA,2A < (4,4) > (4,5) > (4,6), whereas the sequential secondary dissociations vary as (4,2) > (4,3) < (5,3) > (5,4) > (5,5). In general, the $T\Delta S_{298}$ value will increase as the relative number of states of the products increases or the number of states of the reactant decreases. Because the $T\Delta S_{298}$ values are calculated as the difference in the entropies of the product GS + H_2O and reactant GS, variations in the entropies of dissociation are largely dependent on the vibrational frequencies. If the

Table 3.5. Conversion of 0 K thresholds to 298 K enthalpies and free energies for water loss from $Zn^{2+}(H_2O)_n$. All values in kJ/mol with uncertainties in parentheses.

n	Dissociation	ΔH_0[a]	$\Delta H_{298} - \Delta H_0$[b]	ΔH_{298}	$T\Delta S_{298}$[b]	ΔG_{298}
6	(4,2) → (4,1)	98.4 (3.9)	4.7 (0.4)	103.1 (3.9)	46.6 (1.0)	56.5 (4.1)
	(6,0) → (5,0)	94.6 (3.9)	2.1 (0.5)	96.7 (3.9)	45.5 (1.4)	51.2 (4.1)
7	(4,3)_[c]→ (4,2)	71.4 (4.8)	-1.0 (0.3)	70.4 (4.8)	17.9 (1.4)	52.5 (5.0)
	(5,2) → (6,0)	79.2 (4.8)	6.2 (0.3)	85.4 (4.8)	39.1 (1.2)	46.3 (4.9)
8	(4,4) → (4,3)	63.7 (5.8)	1.1 (0.3)	64.8 (5.8)	34.6 (1.6)	30.2 (6.0)
	(4,4) → (5,2)	59.8 (5.8)	1.6 (0.2)	61.4 (5.8)	30.0 (1.1)	31.4 (5.9)
	(5,3) → (4,3)	71.4 (5.8)	3.6 (0.6)	75.0 (5.8)	46.0 (1.2)	29.0 (5.9)
	(5,3) → (5,2)	67.5 (5.8)	4.2 (0.4)	71.7 (5.8)	41.2 (1.1)	30.5 (5.9)
9	(4,5) → (5,3)	45.3 (7.7)	-1.4 (0.1)	43.9 (7.7)	20.7 (1.6)	23.2 (7.9)
	(5,4) → (5,3)	53.1 (7.7)	2.6 (0.4)	55.7 (6.8)	40.6 (1.1)	15.1 (7.8)
10	(4,6) → (5,4)	36.7 (2.9)	-3.2 (0.04)	33.5 (2.9)	10.9 (1.4)	22.6 (3.2)
	(5,5) → (5,4)	42.5 (2.9)	1.1 (0.3)	43.6 (2.9)	29.2 (1.0)	14.4 (3.1)

[a] Experimental values from Table 3.4. [b] Values calculated from the vibrations and rotations calculated at the B3LYP/6-311+G(d,p) level. Uncertainties found by scaling the frequencies up and down by 10%. [c] (4,3)_2D,DD_AA,2A isomer.

reactant has more loose torsional frequencies compared to the product, the entropy of dissociation decreases. An example of this is seen in the large decrease (28.7 kJ/mol) from the (4,2) to (4,3)_2D,DD_AA,2A dissociations. Here the (4,3)_2D,DD_AA,2A has two single acceptor waters, "A", in the second solvent shell and thereby has more low torsional frequencies than the (4,2) complex where both second shell waters form "AA" H-bonds. Overall, the patterns in dissociation entropies parallel those for the entropy of activation (discussed above for $n = 7 – 10$). Although the entropy of activation values are evaluated at 1000 K and do depend on details of the RRKM analysis, the variation in their values is also largely dependent on the changes in the vibrational frequencies of the EM and TS associated with solvent shell rearrangements.

Now looking at the dissociations predicted by the Mx levels of theory found in Figure 3.6b, the trend in $T\Delta S_{298}$ values can be explained using similar reasoning as that applied to the Bx predicted dissociations. Because the inner solvent shell remains constant at five waters, the relative entropies of dissociation remain fairly constant with values varying as (6,0) > (5,2) ~ (5,3) ~ (5,4) > (5,5). There is only a small decrease in the $T\Delta S_{298}$ from the (6,0) to (5,2) reactants. The latter complex undergoes an inner solvent shell rearrangement upon dissociation, which can have a more drastic affect on the $T\Delta S_{298}$ value, as seen above. However, both the (5,2) and (6,0) complexes have all water ligands bound relatively tightly with no singly hydrogen bound waters in the second shell, unlike the (4,3)_2D,DD_AA,2A complex.

Obviously, the $\Delta S^{\dagger}$, $T\Delta S_{298}$, and $\Delta\Delta G_{298}$ values (difference between the ΔG_{298} values of $Zn^{2+}(H_2O)_n$ and $Zn^{2+}(H_2O)_{n-1}$) of the water loss products are directly dependant on the GS structure chosen and will vary based on the inner solvent shell size and second

shell bonding. This emphasizes the need for careful analysis of all reaction dissociation pathways because of the ambiguous results of the theoretical calculations, especially in the cases where alternate isomers lead to changes in the kinetic shift large enough to alter the hydration energy.

Conclusion

The energy dependent cross sections of the collision-induced dissociation of $Zn^{2+}(H_2O)_7$, $Zn^{2+}(H_2O)_8$, $Zn^{2+}(H_2O)_9$, and $Zn^{2+}(H_2O)_{10}$ are determined using guided ion beam mass spectrometry. Experimental and theoretical bond dissociation energies for the $Zn^{2+}(H_2O)_n$ (n = 6 - 10) show a steady increase in energy as each water is removed agreeing with an intuitive understanding of metal ion hydration. Although the ESI source is limited to producing complexes of $n \geq 7$, our sequential dissociation model is able to provide additional thermochemical information for n = 6. Also, work has been performed analyzing the affect of the competition of the charge separation on the water loss thresholds, specifically those for the n = 7 and 6 binding energies (Chapter 4).

An exhaustive and thorough search into the low energy structures of $Zn^{2+}(H_2O)_n$, where n = 1 – 10, is reported and examines inner shell sizes of 4, 5, and 6. We find B3LYP and B3P86 calculations predict a GS with an inner shell of 4 up to n = 8 where the GS switches to an inner shell of 5. This transition to a larger inner shell is a result of distortions in the tetrahedral inner shell and the need to bind outer shell water ligands to the inner shell via single hydrogen bonds, both of which raise the energy of the 4-coordinate structure relative to the 5-coordinate. The average of the MADs between experiment and Bx theory reported in Figure 3.6a is 9.8 kJ/mol. In contrast, M06 and MP2(full) calculations show a preference of an inner shell of 5 for n = 5 and 7 – 10, and

of 6 for $n = 6$. The average of the MADs between experiment and Mx theory in Figure 3.6b is 11.0 kJ/mol. This larger MAD is primarily because the M06 calculations generally overestimate the binding enthalpies, whereas the MAD between experiment and MP2(full) theory is 8.0 kJ/mol. Thus, it appears that MP2(full) gives the best agreement between experiment and theory for the water loss dissociation energies. For most values of *n*, both DFT and MP2 calculations show that all three inner shell sizes are close in energy and a distribution of all isomers is experimentally possible. Because of this ambiguity, analysis of all dissociation pathways of the varying structures predicted by both levels of theory is carefully considered. Changes in the structures of the EM and TS lead to changes in the kinetic shift of the dissociation. Scrutiny of Figures 3.6a and 3.6b shows that Bx and MP2(full) theory provide similar agreement with experiment for the $n = 6$ and 7 complexes, but the Bx theoretical predictions of (4,4) and (4,5) GSs for $n = 8$ and 9 are inconsistent with the data. In contrast, the MP2 predictions of (5,3) and (5,4) GSs are in good agreement with our experimental results for $n = 8$ and 9. Although not definitive at this point, these comparisons suggest that the structural predictions of MP2 theory are more reliable. This means that most zinc complexes studied here have a 5-coordinate inner hydration shell, with the exception being $Zn^{2+}(H_2O)_6$ where all ligands are bonded directly to the metal ion. Future work will look into the isomer distributions produced via ESI via a spectroscopic investigation of these complexes, which may better describe the binding energies of second solvent shell waters.

References

(1) Spiro, T. G. *Zinc enzymes*; J. Wiley: New York, 1983.

(2) Kimura, E. *Pure & Appl. Chem.* **1993**, *65*, 355.

(3) Richens, D. T. *The Chemistry of Aqua Ions*; John Wiley and Sons, Inc: New York, 1997.

(4) Nriagu, J. O. *Zinc in the Environment*; Wiley: New York, 1980.

(5) Rudolph, W. W.; Pye, C. C. *Phys. Chem. Chem. Phys.* **1999**, *1*, 4583.

(6) Peschke, M.; Blades, A. T.; Kebarle, P. *Int. J. Mass Spectrom.* **1999**, *187*, 685.

(7) Peschke, M.; Blades, A. T.; Kebarle, P. *J. Am. Chem. Soc.* **2000**, *122*, 1492.

(8) Peschke, M.; Blades, A. T.; Kebarle, P. *J. Am. Chem. Soc.* **2000**, *122*, 10440.

(9) Shvartsburg, A. A.; Siu, K. W. M. *J. Am. Chem. Soc.* **2001**, *123*, 10071.

(10) Blades, A. T.; Jayaweera, P.; Ikonomou, M. G.; Kebarle, P. *Int. J. Mass Spectrom. Ion Processes* **1990**, *102*, 251.

(11) Chillemi, G.; D'Angelo, P.; Pavel, N. V.; Sanna, N.; Barone, V. *J. Am. Chem. Soc.* **2002**, *124*, 1968.

(12) D'Angelo, P.; Barone, V.; Chillemi, G.; Sanna, N.; Meyer-Klaucke, W.; Pavel, N. V. *J. Am. Chem. Soc.* **2002**, *124*, 1958.

(13) Pappalardo, R. R.; Marcos, E. S. *J. Phys. Chem.* **1993**, *97*, 4500.

(14) Bock, C. W.; Katz, A. K.; Glusker, J. P. *J. Am. Chem. Soc.* **1994**, *117*, 3754.

(15) Hartmann, M.; Clark, T.; vanEldik, R. *J. Mol. Model.* **1996**, *2*, 354.

(16) Lee, S.; Kim, J.; Park, J. K.; Kim, K. S. *J. Phys. Chem.* **1996**, *100*, 14329.

(17) Hartmann, M.; Clark, T.; vanEldik, R. *J. Amer. Chem. Soc.* **1997**, *119*, 7843.

(18) Pavlov, M.; Siegbahn, P. E. M.; Sandstrom, M. *J. Phys. Chem. A* **1998**, *102*, 219.

(19) Wakita, H.; Johansson, G.; Sandstrom, M.; Goggin, P. L.; Hitotshi, O. J. *J. Solution Chem.* **1991**, *20*, 642.

(20) Moision, R. M.; Armentrout, P. B. *J. Phys. Chem. A.* **2006**, *110*, 3933.

(21) Roothan, C. C. J. *Rev. Mod. Phys.* **1954**, *23*, 69.

(22) Binkley, J. S.; Pople, J. A.; Hehre, W. J. *J. Am. Chem. Soc.* **1951**, *102*, 939.

(23) Frisch, M. J.; Trucks, G. W.; Schlegel, H. B.; Scuseria, G. E.; Robb, M. A.; Cheeseman, J. R.; Montgomery, J., J. A. ; Vreven, T.; Kudin, K. N.; Burant, J. C.; Millam, J. M.; Iyengar, S. S.; Tomasi, J.; Barone, V.; Mennucci, B.; Cossi, M.; Scalmani, G.; Rega, N.; Petersson, G. A.; Nakatsuji, H.; Hada, M.; Ehara, M.; Toyota, K.; Fukuda, R.; Hasegawa, J.; Ishida, M.; Nakajima, T.; Honda, Y.; Kitao, O.; Nakai, H.; Klene, M.; Li, X.; Knox, J. E.; Hratchian, H. P.; Cross, J. B.; Bakken, V.; Adamo, C.; Jaramillo, J.; Gomperts, R.; Stratmann, R. E.; Yazyev, O.; Austin, A. J.; Cammi, R.; Pomelli, C.; Ochterski, J. W.; Ayala, P. Y.; Morokuma, K.; Voth, G. A.; Salvador, P.; Dannenberg, J. J.; Zakrzewski, V. G.; Dapprich, S.; Daniels, A. D.; Strain, M. C.; Farkas, O.; Malick, D. K.; Rabuck, A. D.; Raghavachari, K.; Foresman, J. B.; Ortiz, J. V.; Cui, Q.; Baboul, A. G.; Clifford, S.; Cioslowski, J.; Stefanov, B. B.; Liu, G.; Liashenko, A.; Piskorz, P.; Komaromi, I.; Martin, R. L.; Fox, D. J.; Keith, T.; Al-Laham, M. A.; Peng, C. Y.; Nanayakkara, A.; Challacombe, M.; Gill, P. M. W.; Johnson, B.; Chen, W.; Wong, M. W.; Gonzalez, C.; Pople, J. A. Gaussian 03, Revision D.01; Gaussian, Inc.: Pittsburgh, PA, 2005.

(24) Becke, A. D. *J. Chem. Phys.* **1993**, *98*, 5648.

(25) Lee, C.; Yang, W.; Parr, R. G. *Phys. Rev. B* **1988**, *37*, 785.

(26) Ditchfield, R.; Hehre, W. J.; Pople, J. A. *J. Chem. Phys.* **1971**, *72*, 5639.

(27) Bauschlicher Jr., C. W.; Partridge, H. *J. Chem. Phys.* **1995**, *103*, 1788.

(28) Perdew, J. P. *Phys. Rev. B* **1986**, *33*, 8822.

(29) Moller, C.; Plesset, M. S. *Phys. Rev.* **1934**, *46*, 618.

(30) Zhao, Y.; Truhlar, D. G. *Theor. Chem. Acc.* **2008**, *120*, 215.

(31) Zhao, Y.; Truhlar, D. G. *Acc. Chem. Res.* **2008**, *41*, 157.

(32) Boys, S. F.; Bernardi, R. *Mol. Phys.* **1970**, *19*, 553.

(33) van Duijneveldt, F. B.; van Duijneveldt, J. G. C. M.; van Lenthe, J. H. *Chem. Rev.* **1994**, *94*, 1873.

(34) Becke, A. D. *J. Chem. Phys.* **1993**, *98*, 1372.

(35) Yu, W.; Liang, L.; Lin, Z.; Ling, S.; Haranczyk, M.; Gutowski, M. *J. Comput. Chem.* **2008**, *30*, 589.

(36) Carl, D. R.; Moision, R. M.; Armentrout, P. B. *J. Am. Soc. Mass Spectrom.* **2009**.

(37) Carl, D. R.; Moision, R. M.; Armentrout, P. B. *Int. J. Mass Spectrom.* **2007**, *265*, 308.

(38) Bush, M. F.; Saykally, R. J.; Williams, E. R. *ChemPhysChem* **2007**, *8*, 2245.

(39) Wilson, R. G.; Brewer, G. R. *Ion Beams with Applications to Ion Implantation*; Wiley: New York, 1973.

(40) Moision, R. M.; Armentrout, P. B. *J. Am. Soc. Mass Spectrom.* **2007**, *18*, 1124.

(41) Carl, D. R.; Chatterjee, B. K.; Armentrout, P. B. *J. Chem. Phys.* **2010**, *132*, 044303.

(42) Carl, D. R.; Moision, R. M.; Armentrout, P. B. *J. Am Soc. Mass Spectrom.* **2009**, *20*, 2312.

CHAPTER 4

AN EXPERIMENTAL AND THEORETICAL INVESTIGATION OF THE CHARGE SEPARATION ENERGIES OF HYDRATED ZINC (II): REDEFNITION OF THE CRITICAL SIZE

Abstract

In the preceding chapter, the hydration energies of $Zn^{2+}(H_2O)_n$ complexes, where $n = 6 – 10$, were measured using threshold collision-induced dissociation (CID) in a guided ion beam tandem mass spectrometer (GIBMS) coupled with an electrospray ionization (ESI) source. The present investigation explores the charge separation processes observed, $Zn^{2+}(H_2O)_n \rightarrow ZnOH^+(H_2O)_m + H^+(H_2O)_{n-m-1}$, and the competition between this process and the loss of water. The results demonstrate that charge separation processes occur at variable complex sizes of $n = 6$, 7, and 8, prompting a redefinition of the "critical" size for charge separation. Experimental kinetic energy dependent cross sections are analyzed to yield 0 K threshold energies for the charge separation products and the effects of competition with this channel on the energies for losing one and two water ligands after accounting for multiple collisions, kinetic shifts, and energy distributions. A complete reaction coordinate is calculated for the $n = 7$ complex dissociating into $ZnOH^+(H_2O)_3 + H^+(H_2O)_3$. Calculated rate-limiting transition

Adapted with permission from Cooper, T. E.; Armentrout P.B., *J. Phys. Chem. A* **2009**, *113*, 13742.

states for n = 6 - 8 are also compared to experimental threshold measurements for the charge separation processes.

Introduction

As detailed in the preceding chapter (Chapter 3), the zinc ion is required for the activation of certain proteins and metalloenzymes[1-3] and is used heavily in industry as well.[4] Because of its heavy usage, zinc is quickly infiltrating aqueous environments such that a complete understanding of the hydration of zinc(II) cations is essential to understand their behavior in aqueous environments. Zinc coordination and hydration behavior has previously been studied using a variety of experimental and theoretical methods,[5-18] as detailed in Chapter 3.

In Chapter 3, the dissociation behavior of $Zn^{2+}(H_2O)_n$ complexes where n = 7 – 10 was examined using guided ion beam tandem mass spectrometry (GIBMS). In all cases, the dominant process observed is reaction 4.1,

$$Zn^{2+}(H_2O)_n \rightarrow Zn^{2+}(H_2O)_{n-1} + H_2O \qquad (4.1)$$

followed by sequential loss of additional water molecules. Analysis of the kinetic energy dependence of these reactions provides the first experimental determinations of the hydration energies of zinc cation-water complexes. Chapter 3 shows that accurate thermochemistry relies on including consideration of different isomers, specifically how many inner shell (x) versus outer shell (y) water ligands are present in the reactants and products. These isomers are indicated by (x, y) nomenclature. Competing with reaction 4.1 is the charge separation process, reaction 4.2.

$$Zn^{2+}(H_2O)_n \rightarrow ZnOH^{+}(H_2O)_m + H^{+}(H_2O)_{n-m-1} \quad (4.2)$$

This phenomenon has previously been examined using tandem mass spectrometry by Shvartsburg and Siu, who defined the critical size, n_{crit}, as "the maximum number of ligands at which dissociative charge transfer is competitive with simple ligand loss."[9] They found a lower limit to the critical size of Zn^{2+} complexes of $n_{crit} = 6$, whereas Blades et al. found $n_{crit} = 5$, also using CID studies.[10] Both reports suggest that the critical size depends directly on the second ionization energy of the metal. In related work, Peschke et al. found that when NH_3 vapor was added to $Zn^{2+}(H_2O)_n$ (n = 8 and 9), proton transfer to NH_3 and the formation of $ZnOH^{+}(H_2O)_m$ occurred with a dominant product of m = 4. Further addition of NH_3 vapor results in the formation of $ZnOH^{+}(NH_3)_m$ via ligand exchange.[6]

In the present work, the competition between reactions 4.1 and 4.2 is examined, thereby providing more accurate thermodynamic information for both channels. Interestingly, we find that the charge separation process, reaction 4.2, is observed for complexes of n = 6, 7, and 8, which to our knowledge, is the first time such a variable critical size has been observed for any metal. Given this ambiguity, we suggest that the energetics for reaction 4.2 can be used to provide a more exact definition of the critical size.

Experimental and Theoretical Section

Experimental procedures. The experimental methods used to form $Zn^{2+}(H_2O)_n$ complexes and obtain their kinetic energy dependent cross sections for collision-induced dissociation are described in detail in Chapters 2 and 3.

Computational details. Using the Gaussian03 package,[19] vibrational frequencies, rotational constants, and energies were calculated for all reaction species. The tight transition states (TSs) of the charge separation processes were found through a series of relaxed potential energy scans along the likely reaction coordinate at a B3LYP/6-31G(d) level.[20-22] Geometry optimizations and frequency calculations of the TSs and intermediates (INTs) were performed at a B3LYLP/6-311+G(d,p) level. Here the vibrational frequencies of the TSs were found to have only one imaginary frequency, and all INTs were determined to be vibrationally stable. These calculated frequencies and rotational constants were used in the RRKM thermochemical analysis discussed above, as well as for zero point energy (ZPE) conversions of theoretical bond dissociation energies to 0 K thermochemical values. The vibrational frequencies were scaled by 0.989[23] before being used in these analyses. Using these geometries, single point energy (SPE) calculations were performed using the B3LYP, B3P86,[24] and MP2(full)[25] levels with a 6-311+G(2d,2p) basis set.

Because of the importance of proton bound water clusters in the present study, the computational procedure used here was tested by comparison with results from a previous experimental study of the solvation enthalpies of protonated water clusters, $H^+(H_2O)_z \rightarrow H^+(H_2O)_{z-1} + H_2O$.[26] For $z = 3$, the 0 K bond enthalpies calculated at the B3LYP, B3P86, and MP2(full) levels of theory are 86.1, 87.8, and 88.0 kJ/mol, respectively, which are in close agreement with the experimentally determined value of 85.8 ± 5.4 kJ/mol. For $z = 2$, the calculated 0 K enthalpies are 143.8, 149.2, and 138.7 kJ/mol, respectively, where the MP2(full) value is in best agreement with the experimental value of 135.6 ± 5.4 kJ/mol.

The ground states (GS) of the reactant zinc water complexes are taken from Chapter 3, which explored all possible low lying isomers of $Zn^{2+}(H_2O)_x(H_2O)_y$, where x = 1 – 4 and y = 0, x = 4 and y = 1 – 6, x = 5 and y = 0 – 5, and x = 6 and y = 0 – 4.

Results and Discussion

CID cross sections. Experimental cross sections for collision-induced dissociation of $Zn^{2+}(H_2O)_n$, where n = 7 – 10, with Xe are shown in Figure 4.1a – d and acquired as detailed in Chapter 3. In all cases, the loss of a single water molecule, reaction 4.1, is the dominant process, followed by loss of additional water molecules as the translational energy increases. There are three independent charge separation processes that complicate the dissociation of $Zn^{2+}(H_2O)_6$, $Zn^{2+}(H_2O)_7$, and $Zn^{2+}(H_2O)_8$.

Figure 4.1a shows that the $Zn^{2+}(H_2O)_7$ complex dissociates by charge separation in reaction 4.3 at lower energies than loss of a water molecule in reaction 4.1.

$$Zn^{2+}(H_2O)_7 + Xe \rightarrow ZnOH^{+}(H_2O)_3 + H^{+}(H_2O)_3 + Xe \qquad (4.3)$$

However, despite having a lower apparent threshold, this process has a smaller cross section compared to that for water loss above about 0.4 eV. On the basis of the magnitudes of the two cross sections, charge separation is an entropically disfavored reaction by a factor of about 6 near 1 eV. This is consistent with the need to pass over the tight TS corresponding to the Coulombic barrier, whereas water loss involves a loose TS, as described in Chapter 2. The cross section for reaction 4.3 initially decreases with energy and then rises near 0.2 eV. This behavior indicates that reaction 4.3 is endothermic by less than reaction 4.1 and that there is sufficient internal energy available

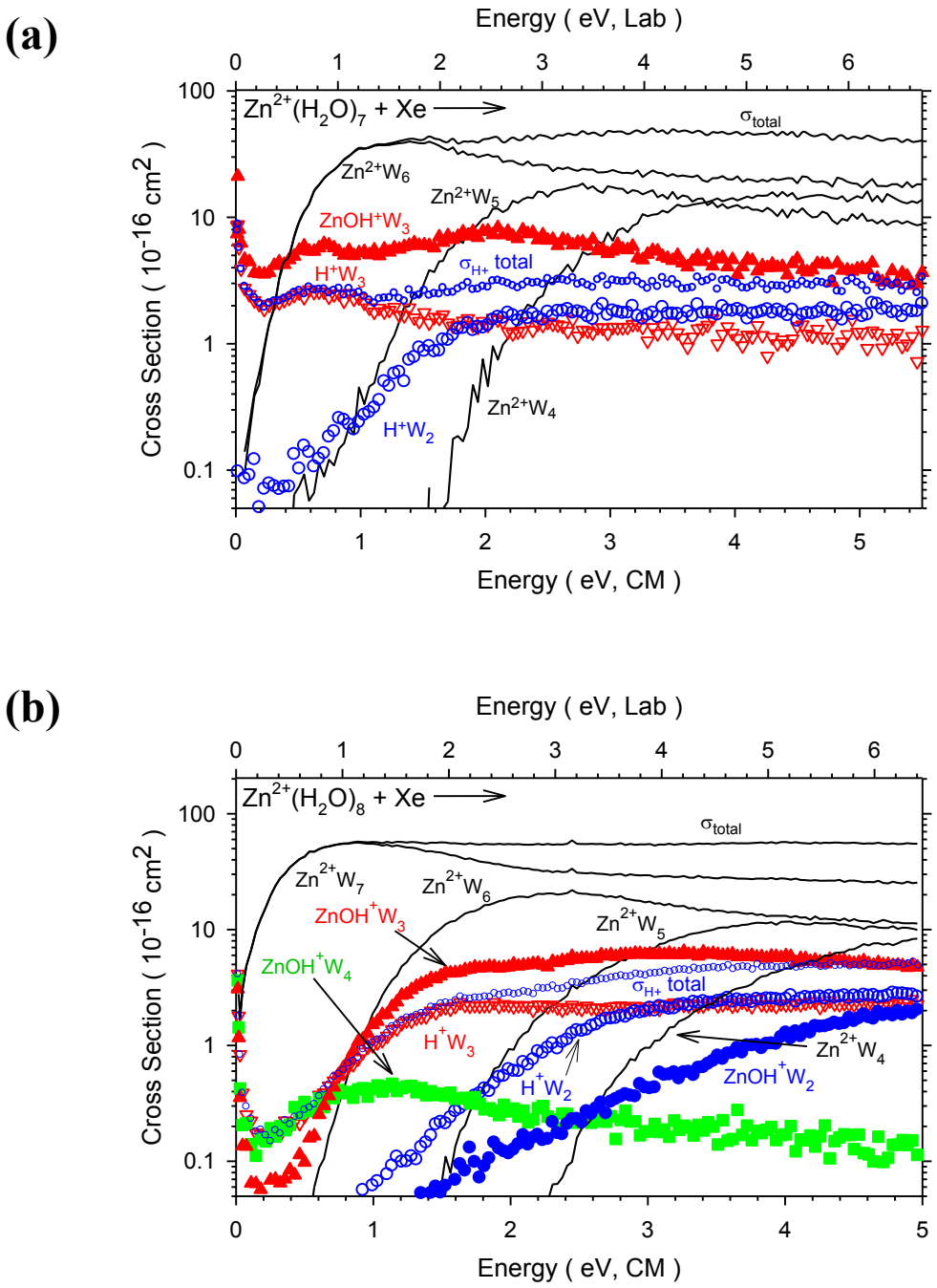

Figure 4.1. CID cross sections for the sequential water loss (lines) and charge separation processes (symbols) for $Zn^{2+}W_n$ where n = 7 - 10 and W = H_2O (parts a - d, respectively) colliding with Xe at 0.2 mTorr as a function of energy in the laboratory (upper x-axis) and center of mass (lower x-axis) frames. Hydrated zinc hydroxide ion products are shown by solid symbols and protonated water complex products by open symbols.

(c)

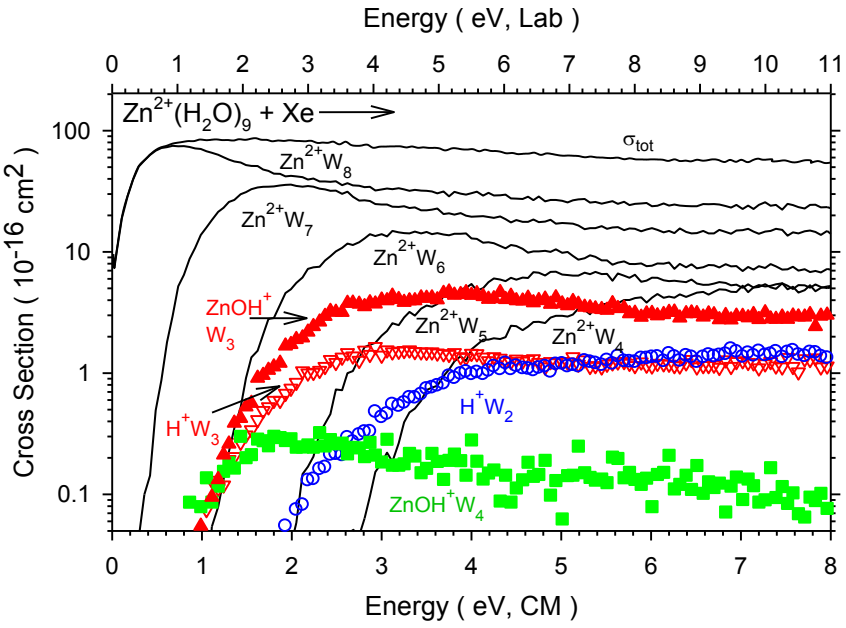

(d)

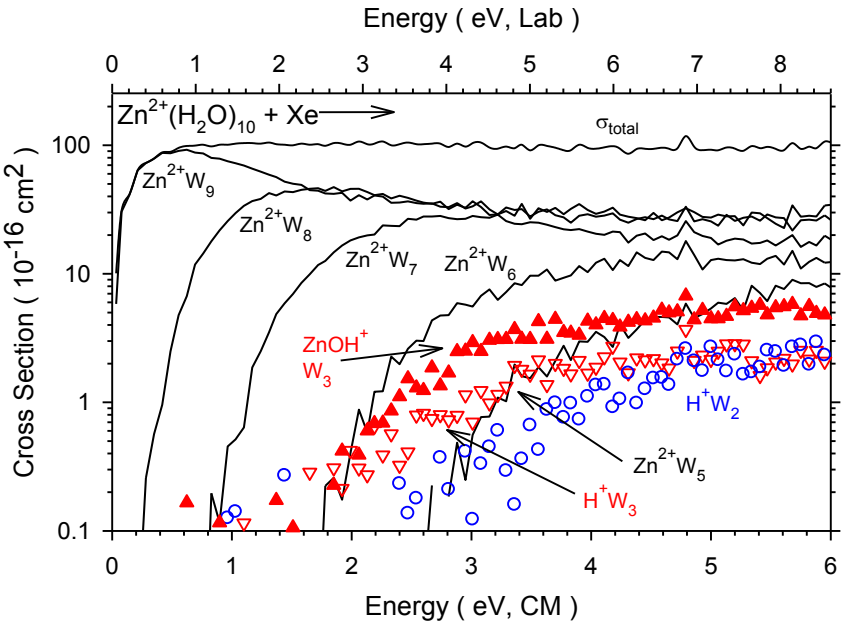

Figure 4.1. continued

in the $Zn^{2+}(H_2O)_7$ reactant that a fraction of the complexes dissociate readily at very low collision energies. The magnitudes of the cross sections for the two charge separated products should be identical, but that for the protonated water cluster is smaller than for the hydrated zinc hydroxide, a result observed in most of the systems examined here and for other hydrated metal dications examined in our laboratory. These differences must be a result of lower collection efficiency of the lighter product ion, which is particularly problematic in these systems because the charge separation products have appreciable kinetic energies resulting from the Coulombic repulsion once they pass over the Coulomb barrier. Because the momentum of the two products must be equal, the lighter product has a higher energy by a factor corresponding to the mass ratio of the two products. This has been qualitatively confirmed for the charge separation of $Ca^{2+}(H_2O)_2$ by verifying that the ratio of the two singly charged products is sensitive to the focusing and transmission characteristics past the reaction region. (Of course, in our apparatus as well as all others, there is no guarantee that the collection of all products is 100%, but the rf octopole surrounding the reaction region and the subsequent focusing optics have proven to efficiently transmit products in the majority of systems we have examined over several decades of experiments. The discussion here points out that the light ion in the charge separation pair is particularly susceptible to losses because of its large kinetic energy release. Indeed, the transmission studies performed on the $Ca^{2+}(H_2O)_2$ system find that the magnitudes of the cross sections for water loss are invariant with focusing, those for the hydroxide ion product are affected slightly (by less than the 20% uncertainty in the absolute cross section magnitudes), whereas those for the hydrated hydronium ion products can change appreciably (factors of two). Indeed the ratio of the two products

observed here is substantially closer to unity than in previously published work on analogous systems.[9,10])

In the dissociation of $Zn^{2+}(H_2O)_8$, the lowest energy charge separation process observed is reaction 4.4.

$$Zn^{2+}(H_2O)_8 + Xe \rightarrow ZnOH^{+}(H_2O)_4 + H^{+}(H_2O)_3 + Xe \qquad (4.4)$$

Here the cross sections for both ionic products agree in magnitude up to about 0.5 eV, Figure 4.1b. The apparent threshold for this reaction is higher in energy than the apparent threshold for simple water loss in reaction 4.1, a result that can also be observed in Figure 4.1c. The $ZnOH^{+}(H_2O)_4$ product was not collected for $Zn^{2+}(H_2O)_{10}$ (Figure 4.1d) because of its very low intensity, near the detection limit. The exothermic tail observed for the $ZnOH^{+}(H_2O)_4$ and $H^{+}(H_2O)_3$ product channels in Figure 4.1b is a result of multiple collisions and disappears once these cross sections are extrapolated to zero pressure (as demonstrated in a later section). Because reaction 4.4 is now both thermodynamically and entropically disfavored compared with reaction 4.1, the magnitude of its cross sections is less than 1% of the magnitude of that for reaction 4.1, much smaller than the relative magnitudes of the corresponding products in Figure 4.1a. Above about 0.5 eV, the $H^{+}(H_2O)_3$ cross section increases relative to the $ZnOH^{+}(H_2O)_4$ cross section, Figure 4.1b. This increase in the $H^{+}(H_2O)_3$ cross section matches the appearance of the $ZnOH^{+}(H_2O)_3$ product, indicating the onset of reaction 4.3, the charge separation reaction from the primary $Zn^{2+}(H_2O)_7$ product, which is much more efficient than reaction 4.4. The relative thresholds for appearance of $Zn^{2+}(H_2O)_6$ and

$ZnOH^+(H_2O)_3$ make it very clear that reaction 4.3 does indeed have a lower threshold than the water loss channel, consistent with our conclusions above from Figure 4.1a.

The cross sections of the $ZnOH^+(H_2O)_3$ product ions in both Figures 4.1a and 4.1b exhibit a second feature at higher energies beginning near 1 and 2 eV, respectively. This increase is not mirrored in the $H^+(H_2O)_3$ cross sections, but is found in the sum of the $H^+(H_2O)_3$ and $H^+(H_2O)_2$ cross sections under all conditions and for all complex sizes. The appearance of these higher energy features is much more obvious when the cross sections are viewed on a linear scale. Multiple experiments were conducted to see whether these features might be an artifact, but no indications of this were found. Therefore, we conclude that this second feature is explained by the charge separation process, reaction 4.5.

$$Zn^{2+}(H_2O)_6 \rightarrow ZnOH^+(H_2O)_3 + H^+(H_2O)_2 \qquad (4.5)$$

The apparent threshold of this charge separation process is lower in energy than the water loss dissociation to form $Zn^{2+}(H_2O)_5$, Figure 4.1a and 4.1b, such that the magnitudes of the charge separated product cross sections are about 45% of that for water loss when comparing the respective maximum cross sections. Because both charge separation processes 4.3 and 4.5 are energetically more favorable than the competing water loss reactions, the question of why smaller $Zn^{2+}(H_2O)_n$ complexes are seen in CID arises. These smaller clusters are formed because the sequential water loss channels are entropically favored. The density of states is much higher for the water loss channels because of the loose water loss TS compared to the tight TS needed for charge separation. Because the threshold difference between the competing channels is relatively small, the

water loss channels are still a dominant process in the dissociation behavior even though energetically more costly.

The cross section for $ZnOH^+(H_2O)_2$ is seen in Figure 4.1b, but because of the small intensity of this product it was not collected for the other reactant ions in Figures 4.1a, 4.1c, and 4.1d. This cross section rises very slowly above about 1.0 eV, which makes it difficult to ascertain whether it originates from the charge separation process, reaction 4.6,

$$Zn^{2+}(H_2O)_5 \rightarrow ZnOH^+(H_2O)_2 + H^+(H_2O)_2 \qquad (4.6)$$

or from the sequential loss of a water ligand from the $ZnOH^+(H_2O)_3$ product formed in reactions 4.4 and 4.5. This process is investigated further using theoretical calculations, as discussed below.

Charge separation reactions observed in the dissociation of $Zn^{2+}(H_2O)_9$ and $Zn^{2+}(H_2O)_{10}$, Figures 4.1c and 4.1d, mirror the results found for the smaller complexes. As noted above, the results of Figure 4.1c clearly show that reaction 4.4 has a higher threshold energy than water loss from $Zn^{2+}(H_2O)_8$, whereas reaction 4.3 has a lower threshold energy than water loss from $Zn^{2+}(H_2O)_7$. In Figure 4.1d, only the most intense charge separation products, those from reactions 4.3 and 4.5 are now observed.

Thermochemical results. Cross sections for the primary and secondary dissociation products were analyzed using eq 2.4 or eqs 2.4 and 2.6 in several ways, with Table 4.1 summarizing the average modeling parameters used. Threshold E_0 values are given for the primary dissociation of each complex from modeling with eq 2.4, which includes lifetime effects. If lifetime effects are not included, the threshold obtained from

Table 4.1. Optimized parameters from analysis of CID cross sections for $Zn^{2+}(H_2O)_{7,8}$ [a]

Reactant	Product	σ_0	*N*	E_0 (eV)	$\Delta S^{\dagger}_{1000\ K}$ J/mol K
(5,3)	(4,3) [b,c]	67 (6)	0.8 (0.2)	0.71 (0.07)	65 (8)
	TS[4 + 3] [b]	0.52 (0.2)	0.6 (0.2)	0.94 (0.07)	96 (5)
	(4,3) [b,c]	68 (5)	0.8 (0.2)	0.72 (0.06)	67 (9)
	(4,2) [b,c]	48 (5)	0.8 (0.2)	1.68 (0.06)	96 (5)
	(4,3) [d]	76 (4)	0.8 (0.2)	0.73 (0.06)	65 (10)
	TS[4 + 3] [d]	0.03 (0.01)	0.8 (0.2)	**0.80 (0.05)**	96 (5)
	(4,3) [e]	75 (3)	0.7 (0.1)	0.76 (0.04)	68 (9)
	(4,2) [e]	59 (9)	0.7 (0.1)	1.75 (0.05)	
	TS[4 + 3] [e]	0.010 (0.003)	0.7 (0.1)	**0.78 (0.05)**	96 (5)
(5,3)	(5,2) [b,c]	66 (6)	0.8 (0.2)	0.68 (0.07)	55 (8)
	(5,2) [d]	75 (4)	0.8 (0.2)	0.70 (0.06)	54 (10)
	TS[4 + 3] [d]	0.01 (0.01)	0.8 (0.2)	**0.77 (0.05)**	96 (5)
(4,4)	(5,2) [b,c]	65 (6)	0.8 (0.2)	0.62 (0.07)	17 (8)
	TS[4 + 3] [b]	0.5 (0.2)	0.7 (0.2)	0.88 (0.07)	53 (5)
	(5,2) [d]	73 (4)	0.9 (0.2)	0.62 (0.06)	18 (10)
	TS[4 + 3] [d]	0.01 (0.01)	0.9 (0.2)	**0.69 (0.05)**	53 (5)
(4,4)	(4,3) [b,c]	66 (6)	0.8 (0.2)	0.66 (0.07)	22 (8)
	(4,3) [d]	76 (4)	0.9 (0.2)	0.66 (0.06)	65 (10)
	TS[4 + 3] [d]	0.03 (0.01)	0.9 (0.2)	**0.73 (0.05)**	53 (5)
(4,3)	(4,2) [b,c]	58 (5)	0.7 (0.2)	0.89 (0.06)	18 (7)
	TS[3 + 3] [b]	7 (1)	0.9 (0.2)	0.69 (0.05)	110 (5)
	(4,2) [b, c]	58 (7)	0.8 (0.2)	0.88 (0.07)	19 (10)
	(4,1) [b, c]	37 (10)	0.8 (0.2)	2.02 (0.09)	

Table 4.1. continued

Reactant	Product	σ_0	N	E_0 (eV)	$\Delta S^{\dagger}_{1000\ K}$ J/mol K
	(4,2) [d]	63 (6)	0.9 (0.3)	**0.81 (0.05)**	17 (7)
	TS[3 + 3][d]	7E-6 (5E-6)	0.9 (0.3)	0.69 (0.06)	110 (5)
	(4,2) [e]	67 (4)	0.9 (0.1)	**0.82 (0.05)**	17 (9)
	(4,1) [e]	21 (12)	0.9 (0.1)	**1.84 (0.08)**	
	TS[3 + 3][e]	4E-6 (3E-6)	0.9 (0.1)	0.69 (0.05)	110 (5)
(4,3)_2D,DD _AA,2A	(4,2) [b,c]	58 (5)	0.7 (0.2)	0.81 (0.06)	-29 (7)
	TS[3 + 3][b]	7 (1)	0.9 (0.2)	0.66 (0.06)	62 (5)
	(4,2) [d]	61 (6)	0.9 (0.3)	**0.74 (0.05)**	-29 (7)
	TS[3 + 3] [d]	7E-6 (5E-6)	0.9 (0.3)	0.66 (0.06)	62 (5)
(5,2)	(6,0) [b,c]	58 (7)	0.8 (0.2)	0.90 (0.07)	63 (10)
	(5,0) [b,c]	37 (10)	0.8 (0.2)	2.00 (0.09)	
	TS[3 + 3] [b]	7 (1)	0.9 (0.2)	0.70 (0.05)	115 (5)
	(6,0)[e]	65 (4)	1.0 (0.1)	**0.82 (0.05)**	61 (9)
	(5,0)[e]	22 (12)	1.0 (0.1)	**1.80 (0.08)**	
	TS[3 + 3][e]	6E-6 (3E-6)	1.0 (0.1)	0.69 (0.05)	115 (5)
(5,2)	(5,1) [b,c]	58 (7)	0.8 (0.2)	0.95 (0.07)	76 (10)
	(5,0) [b,c]	37 (10)	0.8 (0.2)	1.98 (0.09)	
	(5,1)[e]	65 (4)	1.0 (0.1)	**0.85 (0.05)**	74 (9)
	(5,0)[e]	20 (12)	1.0 (0.1)	**1.79 (0.08)**	
	TS[3 + 3][e]	9E-6 (3E-6)	1.0 (0.1)	0.73 (0.05)	115 (5)

[a] Uncertainties in parentheses. Values in bold provide the best values and highlight threshold energies that differ from less sophisticated modeling. [b] No competition included. [c] Values reported in Chapter 3.[d] Competitive dissociation modeling using eq 2.4. [e] Competitive and sequential dissociation modeling using eqs 2.4 and 2.6.

analysis is higher because of a kinetic shift. The kinetic shifts for the charge separation reactions 4.3 and 4.4 are both about 0.1 eV. Those for the water loss products are discussed in Chapter 3.

The energy dependent cross sections for the primary reaction pathways of $Zn^{2+}(H_2O)_8$ and $Zn^{2+}(H_2O)_7$ are influenced by the competition between the water loss and charge separation processes. Modeling of these competitive reactions using eq 2.4 can also include the sequential dissociation of the primary product of the water loss channel through the incorporation of eq 2.6, which then includes the effects of competition felt by the secondary water loss. Figures 4.2a and 4.2b show a representative model of the competitive dissociation of $Zn^{2+}(H_2O)_8$ when analyzed as a $Zn^{2+}(H_2O)_5(H_2O)_3$ or (5,3) complex competitively dissociating to (4,3) + H_2O products and $ZnOH^+(H_2O)_4$ + $H^+(H_2O)_3$ or TS[4 + 3], where the primary (4,3) product ion sequentially dissociates to (4,2) + H_2O products. (At present, the computational machinery used for our data analysis, the CRUNCH program, is not capable of performing a competitive analysis of a secondary dissociation product, such as $Zn^{2+}(H_2O)_8 \rightarrow Zn^{2+}(H_2O)_7 + H_2O \rightarrow Zn^{2+}(H_2O)_6 + 2H_2O$ competing with $Zn^{2+}(H_2O)_8 \rightarrow Zn^{2+}(H_2O)_7 + H_2O \rightarrow ZnOH^+(H_2O)_3 + H^+(H_2O)_3$.) In order to determine the competitive shift, the threshold values obtained in this work are compared to the values where competition is not accounted for, as reported in Chapter 3. In the competitive analyses, it is found that whichever process has the lower energy threshold is essentially unaffected by the competition regardless if the TS is loose (water loss) or tight (charge separation). Thus, reaction 4.1 for $Zn^{2+}(H_2O)_8$ has a threshold of 0.71 – 0.76 eV when modeled as a (5,3) $\rightarrow$ (4,3) + H_2O dissociation no matter if the cross section is fit independently or with competition, whereas the higher

(a)

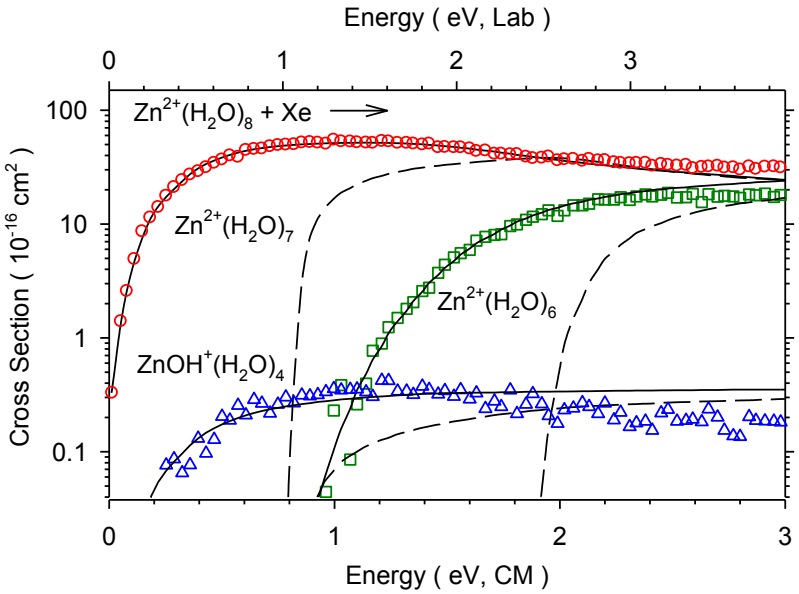

(b)

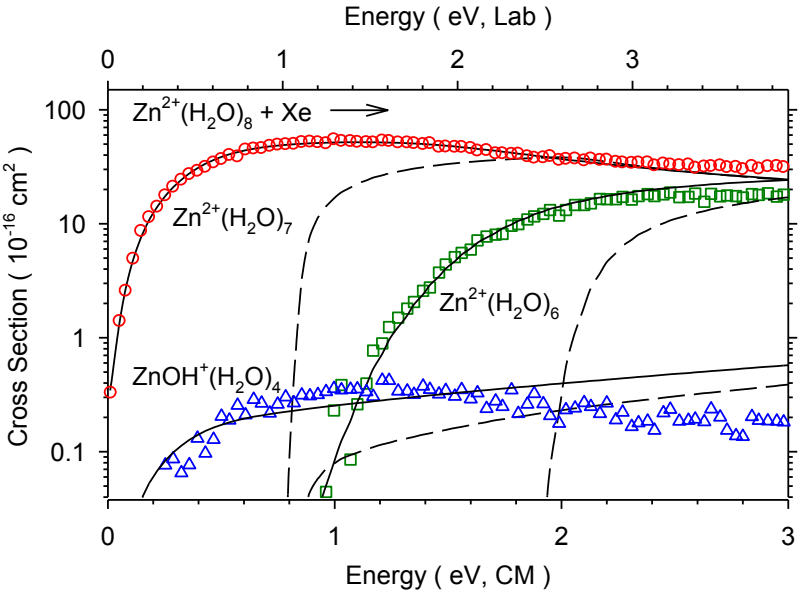

Figure 4.2. Parts a and b show the zero pressure extrapolated cross sections for the CID of $Zn^{2+}(H_2O)_8$ with Xe. Solid lines show the best fit to both the primary and secondary water loss and the competing charge separation product ion using eqs 2.4 and 2.6 convoluted over the kinetic and internal energy distributions of the neutral and ionic reactants. Dashed lines show the models in the absence of experimental kinetic energy broadening for reactants with an internal energy of 0 K. Optimized parameters for the fit in part a are found in Table 4.1, where the five vibrations of the product of reaction 4.2 were treated as rotational degrees of freedom during the analysis. Part b shows the fit where the five degrees of freedom were treated as vibrations and the high energy region is not described accurately.

energy charge separation channel shows a competitive shift of 0.14 – 0.16 eV. In contrast, analysis of $Zn^{2+}(H_2O)_7$ dissociation (when modeled as (4,3) → (4,2) + H_2O → (4,1) + $2H_2O$ competing with (4,3) → TS[3 + 3]) finds that the lower energy charge separation channel has a threshold of 0.69 eV for all modeling conditions, whereas the threshold for reaction 4.1 shifts down by about 0.06 eV when competition is included (and that for the secondary water loss channel shifts down by 0.18 eV).

As noted in Chapter 3, theory yields ambiguous results regarding the GS of the $Zn^{2+}(H_2O)_n$ complexes. Because a distribution of reactant and product GS isomers may be possible, the water loss dissociation pathways were analyzed with several assumed dissociation pathways (as described in detail in Chapter 3). Depending on the isomers chosen in the data analysis, the kinetic shift may change slightly leading to a change in the E_0 threshold for dissociation. Although the structures of the calculated charge separation tight TSs do not depend on the reactant isomer, the reactant isomer chosen for data analysis will affect the kinetic shift. As previously discussed in Chapter 3, complexes like (4,4), (4,3), and (4,3)_2D,DD_AA,2A have larger densities of states than their counterparts with more inner shell water molecules because the additional outer shell waters have lower torsional frequencies. Thus, these reactants increase the time for dissociation, which increases the kinetic shift (lowering E_0) compared to the more constrained 5- and 6-inner shell coordinate complexes. Although the E_0 values change according to the kinetic shift, the competitive shift between modeling with and without including competition remains fairly constant regardless of the reactant isomer. The charge separation process for the $Zn^{2+}(H_2O)_8$ complex has a competitive shift of 0.14 – 0.19 eV, whereas the water loss threshold remains constant within experimental

uncertainty with or without including competition, for all isomers. Likewise, the competitive shifts for the primary and secondary water loss dissociations for the $Zn^{2+}(H_2O)_7$ complexes are 0.06 – 0.10 eV and 0.18 – 0.20 eV, respectively.

As noted above, vibrational frequencies and rotational constants for the loose TSs associated with water loss were taken directly from the theoretical calculations in Chapter 3. Those for the tight charge separation TSs are calculated as described below. In each of these TSs, the lowest vibrational frequency (~4 cm^{-1}) corresponds to a torsion of the complex about the reaction coordinate. The next four vibrations (8 – 63 cm^{-1}) correspond to hindered rotations of the incipient $ZnOH^+(H_2O)_m$ and $H^+(H_2O)_{n-m-1}$ products at the TS. These five vibrations were treated as rotational degrees of freedom during the analysis. This treatment gave models that reproduced the energy dependence of the experimental cross sections, but also made this TS "looser", greatly decreasing the scaling factor, $\sigma_{0,j}$ needed in the competitive and competitive sequential fits (Table 4.1). Treatment of these five degrees of freedom as vibrations yielded scaling factors ($\sigma_{0,j}$) closer to unity, but the energy dependences were not described as accurately because the model deviates strongly from the data at higher energies, Figure 4.2b. The charge separation E_0 decreases because the product has fewer rotational degrees of freedom, which reduces the number of states at the transition state, thereby increasing the kinetic shift.

Theoretical results. Theoretical geometries and relative energetics of $Zn^{2+}(H_2O)_n$, where n = 1 – 10, for multiple isomers with inner solvent shell sizes of 4, 5 and 6 are presented in Chapter 3. Given the ground state structures of the zinc dication water complexes, the mechanism for the charge separation processes can be seen to be complex. For instance, formation of $ZnOH^+(H_2O)_3 + H^+(H_2O)_3$ from $Zn^{2+}(H_2O)_7$

requires that two of the outer shell waters in the (4,3)_2AA,A structure must move to create a third solvent shell (4,1,2)_AADD_2A, thus forming the $H^+(H_2O)_3$ leaving group. To investigate this charge separation process more thoroughly, a complete reaction coordinate path for this dissociation was investigated theoretically. As mentioned above, the path was first generated by scanning along the likely reaction coordinates at a B3LYP/6-31G(d) level, with the geometries and energies of the TSs and INTs further optimized at the B3LYP/6-311+G(2d,2p)//B3LYP/6-311+G(d,p) level. The surface generated describes the proton transfer mechanism and is shown in Figure 4.3 with energies listed in Table 4.2. In this mechanism, the singly bound second shell water ligand of the (4,3)_2AA,A GS moves forming TS1, 29.4 kJ/mol higher in energy, as it bridges between an inner and a second solvent shell water. INT1, (4,2,1)_AA,AAD_A, is then formed as this water molecule enters the third solvent shell. A more complex path is required to move the next water molecule, which is doubly hydrogen bonded in the second shell of the (4,3) GS and INT1. One of those hydrogen bonds must first be broken and then the water can move closer to the leaving group creating a series of shallow TSs and INTs. In TS5, 53.9 kJ/mol above the (4,3) GS and 30.0 kJ/mol above INT4, (4,2,1)_AAD,A_A, this water bridges the first and second solvent shell, explaining the similarity in energy relative to the 29.4 kJ/mol difference between TS1 and the (4,3) GS. Finally, the rate limiting step is TS7 = TS[3+3], 70.7 kJ/mol above the (4,3) GS, where the $H^+(H_2O)_3$ pulls away leaving $ZnOH^+(H_2O)_3$, which has a pseudo-tetrahedral geometry. Overall, this charge separation process is calculated to be exothermic by 68.9 kJ/mol at this level of theory, Table 4.2.

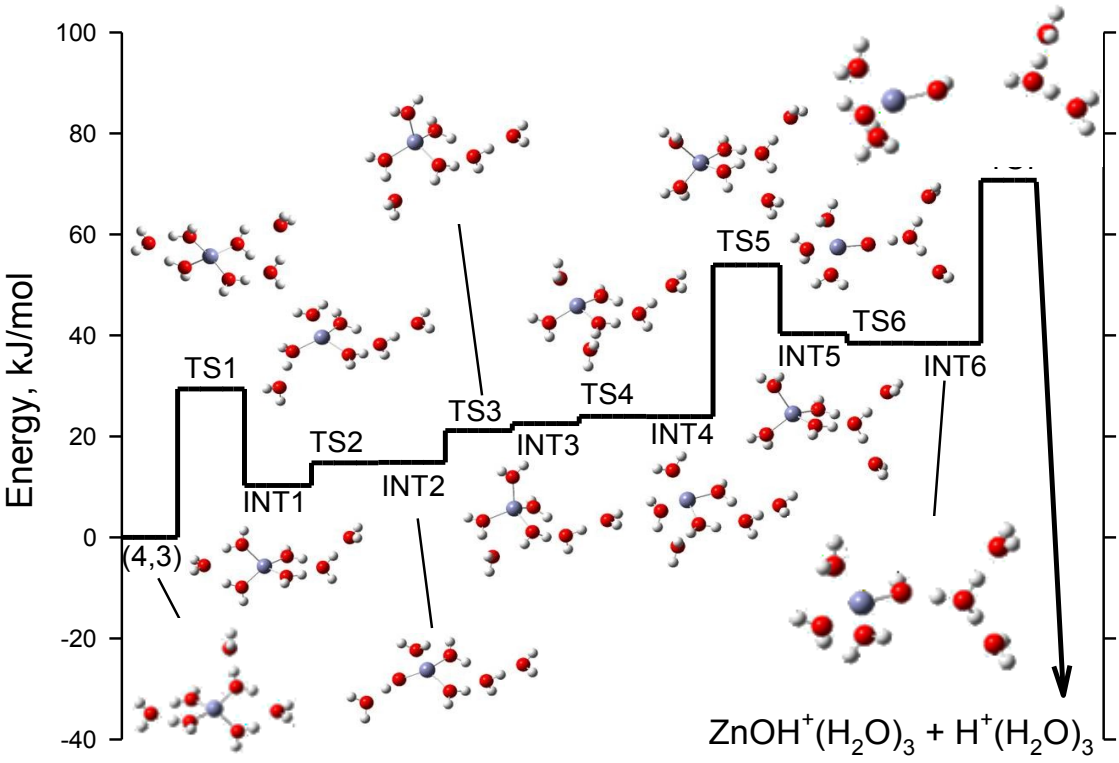

Figure 4.3. The complete reaction coordinate for $Zn^{2+}(H_2O)_7$ charge separating to $ZnOH^+(H_2O)_3 + H^+(H_2O)_3$ calculated at a B3LYP/6-311+G(2d,2p)//B3LYP/6-311+G(d,p) level of theory including zero point energy corrections. Optimized structures of the transition states (TSs) are shown above the surface and intermediates (INTs) are below.

Table 4.2. Relative energies (kJ/mol) for intermediates (INTs) and transition states (TSs) along the reaction coordinate for charge separation of $Zn^{2+}(H_2O)_{5\text{-}8}$ calculated at the B3LYP/6-311+G(2d,2p)//B3LYP/6-311+G(d,p) level.

species	relative energy
$Zn^{2+}(H_2O)_5$ (4,1)	0.0
TS [2 + 2]	72.6
$ZnOH^+(H_2O)_2$+ $H^+(H_2O)_2$	-77.4
$Zn^{2+}(H_2O)_6$ (4,2)	0.0
TS [3 + 2]	74.6
$ZnOH^+(H_2O)_3$+ $H^+(H_2O)_2$	-65.7
$Zn^{2+}(H_2O)_7$ (4,3)	0.0
TS1	29.4
INT1	10.3
TS2	14.8
INT2	14.9
TS3	21.1
INT3	22.5
TS4	24.0
INT4	23.9
TS5	53.9
INT5	40.3
TS6	38.5
INT6	38.4
TS7 = TS[3 + 3]	70.7
$ZnOH^+(H_2O)_3$+ $H^+(H_2O)_3$	-68.9
$Zn^{2+}(H_2O)_8$ (5,3)	0.0
TS [4 + 3]	99.4
$ZnOH^+(H_2O)_4$+ $H^+(H_2O)_3$	-56.3

Complete reaction coordinates for the n = 5, 6, and 8 charge separations were not fully optimized but must follow a similar pathway for proton transfer as the n = 7 charge separation. In all these cases, it is clear that the rate-limiting step needed for thermochemical analysis is the TS with $H^+(H_2O)_{n-m-1}$ pulling away from $ZnOH^+(H_2O)_m$, where m = 2 for n = 5, m = 3 for n = 6, and m = 4 for n = 8. The optimized tight TSs of the charge separation processes occurring for n = 5, 6, and 8 are shown in Figure 4.4. The structure of the $ZnOH^+(H_2O)_4$ complex is the GS at all three levels of theory and has the fourth water in the second shell forming three hydrogen bonds, one donor bond with the hydroxide group and two acceptor bonds with inner shell water molecules. Although $ZnOH^+(H_2O)_4$ has an overall single charge, its structure once again demonstrates the ability of the zinc dication to form stable structures at an inner shell size of four. A five coordinate $ZnOH^+(H_2O)_4$ was also investigated, where the inner shell forms a square pyramidal shape with the hydroxide group bonding to the Zn^{2+} at the base of the square pyramid. This is found to be higher in energy by 20 – 27 kJ/mol at all three levels of theory.

Energies for the rate-limiting TSs for n = 5, 6, and 8 are listed in Table 4.2, along with the respective exothermicities of the overall charge separation processes. Relative to the ground state reactant complexes, the energetic barriers for n = 5 – 7 are within 5 kJ/mol of each other (72.6, 74.6, and 70.7 kJ/mol, respectively), whereas that for n = 8 is higher at 99.4 kJ/mol. (Similar trends are found for both B3P86 and MP2(full) calculations, with B3P86 energies being very similar to the B3LYP energies and those for MP2(full) being 5 – 23 kJ/mol higher, Table 4.3.) This large change in the barrier may be explained by differences between the structure of the hydroxide complexes at the TS

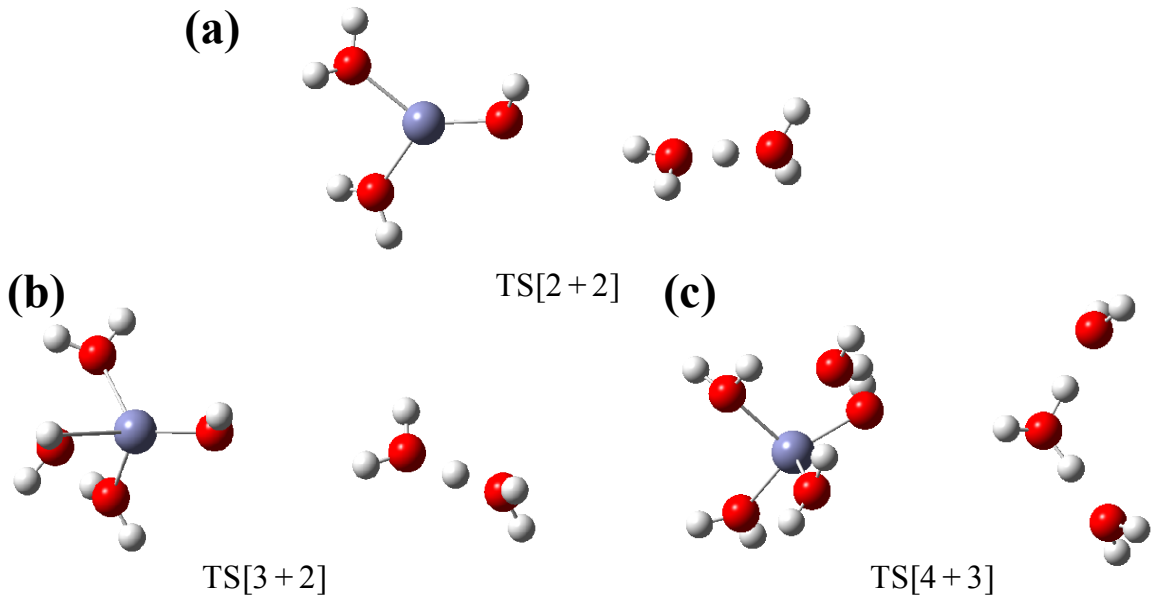

Figure 4.4. Optimized rate limiting transition states of the n = 5, 6, and 8 charge separation products $ZnOH^+(H_2O)_m + H^+(H_2O)_{n-m-1}$, where m = 2, 3 and 4 and n-m-1 = 2, 2, and 3 for parts a – c, respectively, calculated at the B3LYP/6-311+G(d,p) level of theory.

and in the GS products. The $ZnOH^+(H_2O)_2$ and $ZnOH^+(H_2O)_3$ moieties in the $n = 5 – 7$ TSs, Figures 4.3 and 4.4, are structurally close to their respective GS products thereby minimizing the energy of the TS. However, the additional water ligand in the $ZnOH^+(H_2O)_4$ complex is involved in three H-bonds as described above in order to stabilize the hydroxide group. Compared to the GS complex, each H-bond is much longer in TS[4+3], thereby increasing its energy. It can also be seen that the overall exothermicity of the charge separation processes roughly increases as *n* decreases: 77.4, 65.7, 68.9, and 56.3 kJ/mol for $n = 5 – 8$, respectively, such that the reverse Coulombic barrier increases as *n* decreases for $n = 5 – 7$: 150.0, 140.3, 139.6 kJ/mol, respectively. One potential reason for this increase is that as the complex gets smaller the dissociation is more like a pure electrostatic Coulomb repulsion. For example, in the charge separation of the $Zn^{2+}(H_2O)_5$ complex, there are fewer waters interacting with the two charge carriers in the TS and products, as shown in Figure 4.4. This trend changes in moving from $n = 7$ to 8 as the reverse Coulombic barrier is highest for $n = 8$, 155.7 kJ/mol, as rationalized by the structural changes in the hydroxide needed to form three H-bonds, as described above.

Experimental transition state energies and comparison to theory. Chapter 3 contains a detailed examination of the comparison between experimental and theoretical 0 K hydration energies. Excellent agreement with theory is found for $n = 6 – 8$, which verifies the importance of including the competitive shifts. Table 4.3 compares the experimental dissociation 0 K thresholds for charge separation, which include competitive shifts, to the values predicted by theory for these rate-limiting TSs. There is good agreement for all three reactant isomers at $n = 7$, although the MP2 values are

Table 4.3. Comparison of 0 K transition state energies to theory (kJ/mol)

n	Reactant	Product	Experiment	B3LYP[a]	B3P86[a]	MP2(full)[a]
5	(4,1)	TS[2 + 2]		72.6	74.3	90.1
		(4,0)		100.3	104.1	98.6
6	(4,2)	TS[3 + 2]		74.6	75.5	86.6
	(4,2)	(4,1)	98.4 (3.9) [b]	97.0	100.6	95.7
7	(4,3)	TS[3 + 3]	66.6 (5.8)[c]	70.7	72.2	82.9
		(4,2)	78.2 (4.8) [b]	79.8	82.5	76.5
	(4,3)_2D,DD _AA,2A	TS[3 + 3]	63.7 (5.8)[c]	66.6	68.1	75.8
		(4,2)	71.4 (4.8) [b]	75.7	78.4	69.3
	(5,2)	TS[3 + 3]	66.6 (4.8)[c]	70.6	72.1	93.8
		(6,0)	79.2 (4.8) [b]	93.5	97.0	83.3
8	(4,4)	TS[4 + 3]	68.5 (6.8)[c,d]	97.7	95.6	102.9
		(4,3)	63.7 (5.8) [b]	74.8	77.0	72.7
	(5,3)	TS[4 + 3]	74.3 (4.8)[c]	99.4	98.0	117.8
		(5,2)	68.5 (10.5)[b,d]	76.0	78.8	75.4

[a] Geometry optimizations calculated using B3LYP/6-311+G(d,p) and SPE values calculated with a 6-311+G(2d,2p) basis set at the level indicated. All values are ZPE corrected. [b] Values reported in Chapter 3. [c] Values taken from Table 4.1 using competitive modeling with eq 2.4. [d] Average of primary and sequential thresholds reported in Chapter 3.

somewhat high (by 12 – 27 kJ/mol). However, theory predicts an energy for the charge separation TS of the $n = 8$ complex that is 24 – 44 kJ/mol above the experimental value for both the (5,3) and (4,4) reactants. As discussed in Chapter 3, this is a further indication that there is a need for additional experimental and theoretical work at cluster sizes of $n \geq 8$.

In addition, Table 4.3 also compares both the experimental thresholds and theoretically predicted 0 K enthalpies required for charge separation versus water loss. Although no experimental dissociation energies are available for $n = 5$ as of yet, theory favors charge separation over water loss by 28 – 30 kJ/mol at the DFT levels and 9 kJ/mol at the MP2(full) level, in qualitative agreement with our observations for reaction 4.6. Likewise, for $n = 6$, theory predicts charge separation is favored by about 22 – 25 kJ/mol (DFT) or 9 kJ/mol (MP2), as observed for reaction 4.5. For a four coordinate $n = 7$ reactant, DFT predicts that the charge separation reaction 4.3 is favored by 9 – 10 kJ/mol, whereas MP2(full) finds that the water loss channel is favored by about 6 kJ/mol. For the (5,2) complex, DFT favors charge separation by 23 – 25 kJ/mol, however, MP2(full) again predicts that water loss is preferred, by 11 kJ/mol. The experimental results definitively show that charge separation is favored, with an average energy difference determined from competitive modeling of 11 ± 2 kJ/mol. Finally, for $n = 8$, experiment and theory agree that water loss is favored over the charge separation reaction 4.4, with an average threshold difference of 5 ± 2 kJ/mol, compared to the DFT prediction of about 19 – 23 kJ/mol and 30 – 42 kJ/mol for MP2(full). Clearly, the MP2(full)//B3LYP calculations are overestimating the energy barrier for charge separation. Because of this discrepancy, MP2(full) geometry optimizations were

performed on these TSs. Energies calculated at the MP2//MP2 level are 5 kJ/mol lower for the (4,1) GS and 3 kJ/mol higher for TS[2+2] than the MP2//B3LYP energies. Accordingly, the MP2//MP2 predicted barrier for the $n = 5$ charge separation is 8 kJ/mol higher in energy than the MP2//B3LYP barrier. Thus, this more computationally expensive procedure does not appear to give a better estimation for these charge separation barriers.

Using Coulomb's law to calculate the reverse barrier from the charge separation products to their TS, we find that the barriers are similar for all complex sizes, ranging from 188 – 210 kJ/mol, because the product separation at the TS (chosen as the separation between the two center of masses of each charged species) varies little, 6.58 – 7.35 Å. These electrostatic barriers are much higher in energy than the TS values given by either modeling the experimental results or the computed reaction coordinate, but the electrostatic barriers do not account for any covalent interactions between the two charged products at the optimized separation distance nor for any delocalization of the charge resulting from hydration.

Using the calculated frequencies and rotational constants of the tight transition states for charge separation, a rigid rotor/harmonic oscillator approximation was applied to convert the 0 K barrier heights of the $n = 7$ and 8 reactants to 298 K values in Table 4.4. The (4,3) and (5,3) reactants are selected as representative of these complexes. The uncertainties in these conversions are found by scaling the vibrational frequencies up and down by 10%. Because the conversion to 298 K depends on the vibrations and rotations of the complex, there are two possible conversion values for the charge separation TSs depending on whether the five low frequency torsions are treated as vibrations or rotors.

Table 4.4. Conversion of 0 K thresholds to 298 K enthalpies and free energies for the charge separation transition states for $Zn^{2+}(H2O)_{7,8}$. All values in kJ/mol with uncertainties in parentheses.

Complex	ΔH_0[a]	$\Delta H_{298} - \Delta H_0$[b]	ΔH_{298}	$T\Delta S_{298}$	ΔG_{298}
TS[3 + 3]	66.6 (5.8)	1.6 (0.1)[c]	68.2 (5.8)	41.6 (1.0)[c]	26.6 (5.9)
		7.0 (0.2)[d]	73.6 (5.8)	24.8 (1.0)[d]	48.8 (5.9)
TS[4 + 3]	74.3 (4.8)	-0.6 (0.4)[c]	73.7 (4.8)	39.5 (1.1)[c]	34.2 (4.9)
		4.6 (0.3)[d]	78.9 (4.8)	16.4 (1.0)[d]	62.5 (4.8)

[a] Experimental values from Table 4.3. [b] Values calculated from the vibrations and rotations calculated at the B3LYP/6-311+G(d,p) level. Uncertainties found by scaling the frequencies up and down by 10%. [c] Values calculated with the first 5 vibrations of the TS being treated as rotations. [d] Values calculated using all vibrations.

When treated as rotors, the 298 K enthalpies for the charge separation TSs at $n = 7$ and 8 are 68.2 and 73.7 kJ/mol, respectively, but rise to 73.6 and 78.9 kJ/mol, respectively, when vibrations are used for the low frequency torsions. Thus, the conversion values of the two different methods differ from each other by about 5 kJ/mol. The entropies of dissociation, $T\Delta S_{298}$, for the charge separation TSs are larger when the first five vibrations of the TS are treated as rotations because of the larger rotational entropy of the product. Thus, the ΔG_{298} values are smaller for the charge separation TSs when the first five vibrations of the TS are treated as rotations compared to results when all vibrations are used in the TS. Without a more thorough analysis of the potential energy surfaces involved, it is difficult to state with certainty whether the treatment of these degrees of freedom as vibrations or rotations is more correct. We are inclined to believe they should be treated as rotations and note that this model fits the charge separation data better at higher energies, as noted above.

Critical size. Previous studies have defined the critical size as the value of n where "the charge reduction reaction… becomes competitive with single ligand loss"[10] and equivalently as "the maximum number of ligands at which dissociative charge transfer is competitive with simple ligand loss."[9] Such a definition is an experimental one that is highly dependent on instrumental sensitivity and product collection (which is more difficult for the charge separation products because of the kinetic energy release). Furthermore, previous studies of the critical size have relied primarily on observations of the maximum size of the hydroxide ion products. Indeed, Blades et al.[10] assign all their critical sizes as the value of $m + 2$ in reaction 4.2, on the basis that the only protonated water cluster they observed with any intensity was H_3O^+. Thus, they assigned $n_{crit} = 5$ for

Zn^{2+} because the largest hydroxide complex they observed was $ZnOH^+(H_2O)_3$. Shvartsburg and Siu[9] also use their observation of "the largest singly charged hydrated metal ions" as the basis for assigning their critical values, but often get values larger by 1 compared to Blades et al., e.g., $n_{crit} = 6$ for Zn^{2+}. They suggest this is because their higher sensitivity allows them to see complexes corresponding to larger values of *m* and *n-m-1*. Notably, Shvartsburg and Siu also point out, quite correctly, that the n_{crit} values could be lower limits if for instance the hydrated metal hydroxide cation complexes partially dissociate before observation. They also point out that tandem mass spectrometry experiments are required, otherwise the largest hydrated metal hydroxide cation observed could be generated in the source by hydration of smaller complexes.

Ultimately, both of these studies focus on the observation of the product ion rather than the behavior of the reactant ion, which is what the definition of critical size is supposed to specify. Thus, any study that does not allow some means of identifying which $MOH^+(H_2O)_m$ product is formed simultaneously with which $H^+(H_2O)_{n-m-1}$ product will fail to identify the correct precursor *n* that undergoes the charge separation reaction 4.2. Thus, we observe that the $ZnOH^+(H_2O)_3$ complex is formed in greatest abundance, in agreement with the observations of Blades et al. who assign $n_{crit} = 5$. With greater sensitivity, however, the largest hydrated zinc hydroxide cation complex we observe is $ZnOH^+(H_2O)_4$, which if formed along with H_3O^+, would lead to assignment of $n_{crit} = 6$, in agreement with Shvartsburg and Siu. However, the kinetic-energy resolved studies performed here clearly show that the latter hydroxide complex is accompanied by the $H^+(H_2O)_3$ product ion, and therefore comes from dissociation of the $Zn^{2+}(H_2O)_8$ complex, which would lead to the assignment $n_{crit} = 8$. Fundamentally, the key observations in all

three studies are essentially the same, but the final results differ because of instrumental sensitivity and the ability to assign the true products of the charge separation reaction. Indeed, we find that three complexes of zinc definitely undergo charge separation, $n = 6 – 8$, and possibly 5, which according to a definition for n_{crit} that relies on the competitiveness of the charge reduction reaction with single ligand loss means that all three (possibly four) complexes have the "critical" size. Clearly, there is no singular "critical" size that differentiates when charge separation is observed and when it is not.

If a singular (truly critical) value for n_{crit} is needed, then the observations of the present study dictate the need for a different definition for the charge separation critical size. As noted above, the calculated barrier for charge separation for the $n = 5 - 7$ complexes remains fairly constant, whereas the hydration energies increase as the cluster gets smaller (Chapter 3). These trends demonstrate that there should be a maximum-sized cluster for which charge separation is energetically favored over the loss of one water ligand. We suggest that the critical size be equated with this size complex, which makes the definition of the critical size a thermodynamic one that depends solely on the relative energies of the barrier for charge separation versus that for loss of a water ligand. In general, for clusters larger than this critical size, charge separation is both energetically and entropically disfavored, such that this channel will be small (such as for $n = 8$ here) if observed at all. Note that the identification of n_{crit} as being less than 8 is verified by examination of the relative onsets of the products in Figure 4.1b, where the $ZnOH^+(H_2O)_4$ cross section has an apparent threshold that is clearly higher in energy than the competing water loss product forming $Zn^{2+}(H_2O)_7$. At the critical size, the favorable energy for charge separation will generally allow it to be observed experimentally unless

entropy effects disfavoring it are substantial. Because of these features, this proposed definition will often coincide with the previous experimental definition although the correct assignment of n_{crit} still relies on the sensitivity of the apparatus and the correlation between the protonated hydrate and hydrated metal hydroxide cation complexes formed in reaction 4.2. (The question of whether tunneling through the charge separation barrier might enhance the probability of observing charge separation even below its classical threshold energy has also arisen. We believe this is unlikely to be influential given that our calculations indicate that the rate limiting step for charge separation involves movements of the separating singly charged products away from one another. All proton motions susceptible to tunneling effects come before the rate limiting step.) Using the presently proposed definition, the critical size for zinc hydration is $n_{crit} = 7$ as confirmed by both experimental thresholds and theoretical results. Consistent with these more quantitative evaluations, examination of part a of Figure 4.1 clearly shows that the $ZnOH^+(H_2O)_3 + H^+(H_2O)_3$ products have apparent thresholds that are lower in energy than the threshold for the competing water loss forming $Zn^{2+}(H_2O)_6$. Thus, thermal ion sources (such as our ESI source) will ordinarily be unable to generate hydrated complexes smaller than n_{crit} because charge separation will occur instead of evaporation of additional ligands. As shown in analogous studies on Cu^{2+} hydration, such small complexes can be formed by utilizing either high-energy collisional-activated dissociation (CAD),[27] which takes advantage of the entropic favorability of the dehydration reactions compared to charge separation, or a pickup technique,[28] in which water molecules are condensed onto a beam of neutral copper atoms and then ionized using electron ionization.

Conclusion

Collision-induced dissociation cross sections for $Zn^{2+}(H_2O)_n$, where n = 7 – 10, are examined in detail with regard to the charge separation products, $ZnOH^+(H_2O)_m$ + $H^+(H_2O)_{n-m-1}$. The experimental cross sections show that charge separation occurs at n = 6 – 8 and possibly at n = 5, although the latter products might also be the result of sequential dissociation. Because a range of complex sizes are observed to undergo charge separation in competition with dehydration, the critical size for charge separation is redefined as the largest value of n at which the charge separation is energetically favored over the loss of one water ligand. For $Zn^{2+}(H_2O)_n$ complexes, this means that $n_{crit} = 7$.

A complete reaction coordinate for the charge separation dissociation at n = 7 is calculated and rate limiting transition states for n = 5, 6, and 8 are also evaluated. The molecular parameters for these TSs are used to analyze the cross sections for collision-induced dissociation of $Zn^{2+}(H_2O)_7$ and $Zn^{2+}(H_2O)_8$ including the competition between dehydration and charge separation reactions. As evaluated in Chapter 3, accounting for this competition is necessary for obtaining accurate hydration energies for n = 6 – 8. Although no experimental measurements are possible at this time for smaller complexes, theory indicates that the charge separation process at n = 5 and 6 is favored over water loss. Because the Coulomb barrier for the charge separation processes at n = 5 – 7 relative to the GS reactants are similar in energy, trends in the hydration energies indicate that the charge separation process should be energetically favored for all $Zn^{2+}(H_2O)_n$ complexes when $n \leq n_{crit}$. As a consequence, formation of these smaller complexes in an

ESI source will generally be limited and methods seeking to form them by dissociation should fail.

References

(1) Spiro, T. G. *Zinc enzymes*; J. Wiley: New York, 1983.

(2) Kimura, E. *Pure & Appl. Chem.* **1993**, *65*, 355.

(3) Richens, D. T. *The Chemistry of Aqua Ions*; John Wiley and Sons, Inc: New York, 1997.

(4) Nriagu, J. O. *Zinc in the Environment*; Wiley: New York, 1980.

(5) Rudolph, W. W.; Pye, C. C. *Phys. Chem. Chem. Phys.* **1999**, *1*, 4583.

(6) Peschke, M.; Blades, A. T.; Kebarle, P. *Int. J. Mass Spectrom.* **1999**, *187*, 685.

(7) Peschke, M.; Blades, A. T.; Kebarle, P. *J. Am. Chem. Soc.* **2000**, *122*, 1492.

(8) Peschke, M.; Blades, A. T.; Kebarle, P. *J. Am. Chem. Soc.* **2000**, *122*, 10440.

(9) Shvartsburg, A. A.; Siu, K. W. M. *J. Am. Chem. Soc.* **2001**, *123*, 10071.

(10) Blades, A. T.; Jayaweera, P.; Ikonomou, M. G.; Kebarle, P. *Int. J. Mass Spectrom. Ion Processes* **1990**, *102*, 251.

(11) Chillemi, G.; D'Angelo, P.; Pavel, N. V.; Sanna, N.; Barone, V. *J. Am. Chem. Soc.* **2002**, *124*, 1968.

(12) D'Angelo, P.; Barone, V.; Chillemi, G.; Sanna, N.; Meyer-Klaucke, W.; Pavel, N. V. *J. Am. Chem. Soc.* **2002**, *124*, 1958.

(13) Pappalardo, R. R.; Marcos, E. S. *J. Phys. Chem.* **1993**, *97*, 4500.

(14) Bock, C. W.; Katz, A. K.; Glusker, J. P. *J. Am. Chem. Soc.* **1994**, *117*, 3754.

(15) Hartmann, M.; Clark, T.; vanEldik, R. *J. Mol. Model.* **1996**, *2*, 354.

(16) Lee, S.; Kim, J.; Park, J. K.; Kim, K. S. *J. Phys. Chem.* **1996**, *100*, 14329.

(17) Hartmann, M.; Clark, T.; vanEldik, R. *J. Amer. Chem. Soc.* **1997**, *119*, 7843.

(18) Pavlov, M.; Siegbahn, P. E. M.; Sandstrom, M. *J. Phys. Chem. A* **1998**, *102*, 219.

(19) Frisch, M. J.; Trucks, G. W.; Schlegel, H. B.; Scuseria, G. E.; Robb, M. A.; Cheeseman, J. R.; Montgomery, J., J. A. ; Vreven, T.; Kudin, K. N.; Burant, J. C.; Millam, J. M.; Iyengar, S. S.; Tomasi, J.; Barone, V.; Mennucci, B.; Cossi, M.; Scalmani, G.; Rega, N.; Petersson, G. A.; Nakatsuji, H.; Hada, M.; Ehara, M.; Toyota, K.; Fukuda,

R.; Hasegawa, J.; Ishida, M.; Nakajima, T.; Honda, Y.; Kitao, O.; Nakai, H.; Klene, M.; Li, X.; Knox, J. E.; Hratchian, H. P.; Cross, J. B.; Bakken, V.; Adamo, C.; Jaramillo, J.; Gomperts, R.; Stratmann, R. E.; Yazyev, O.; Austin, A. J.; Cammi, R.; Pomelli, C.; Ochterski, J. W.; Ayala, P. Y.; Morokuma, K.; Voth, G. A.; Salvador, P.; Dannenberg, J. J.; Zakrzewski, V. G.; Dapprich, S.; Daniels, A. D.; Strain, M. C.; Farkas, O.; Malick, D. K.; Rabuck, A. D.; Raghavachari, K.; Foresman, J. B.; Ortiz, J. V.; Cui, Q.; Baboul, A. G.; Clifford, S.; Cioslowski, J.; Stefanov, B. B.; Liu, G.; Liashenko, A.; Piskorz, P.; Komaromi, I.; Martin, R. L.; Fox, D. J.; Keith, T.; Al-Laham, M. A.; Peng, C. Y.; Nanayakkara, A.; Challacombe, M.; Gill, P. M. W.; Johnson, B.; Chen, W.; Wong, M. W.; Gonzalez, C.; Pople, J. A. Gaussian 03, Revision D.01; Gaussian, Inc.: Pittsburgh, PA, 2005.

(20) Becke, A. D. *J. Chem. Phys.* **1993**, *98*, 5648.

(21) Lee, C.; Yang, W.; Parr, R. G. *Phys. Rev. B* **1988**, *37*, 785.

(22) Ditchfield, R.; Hehre, W. J.; Pople, J. A. *J. Chem. Phys.* **1971**, *72*, 5639.

(23) Bauschlicher Jr., C. W.; Partridge, H. *J. Chem. Phys.* **1995**, *103*, 1788.

(24) Perdew, J. P. *Phys. Rev. B* **1986**, *33*, 8822.

(25) Moller, C.; Plesset, M. S. *Phys. Rev.* **1934**, *46*, 618.

(26) Dalleska, N. F.; Honma, K.; Armentrout, P. B. *J. Am. Chem. Soc.* **1993**, *115*, 12125.

(27) O'Brien, J. T.; Williams, E. R. *J. Phys. Chem. A* **2008**, *112*, 5893.

(28) Duncombe, B. J.; Duale, K.; Buchanan-Smith, A.; Stace, A. J. *J. Phys. Chem. A* **2007**, *111*, 5158.

CHAPTER 5

ZN^{2+} HAS A PRIMARY HYDRATION SPHERE OF FIVE: IR ACTION SPECTROSCOPY AND THEORETICAL STUDIES OF HYDRATED ZN^{2+} COMPLEXES IN THE GAS-PHASE

Abstract

Complexes of $Zn^{2+}(H_2O)_n$, where n = 6 – 12, are examined using infrared multiple photon dissociation (IRMPD) spectroscopy, blackbody infrared radiative dissociation (BIRD), and theory. Geometry optimizations and frequency calculations are performed at the B3LYP/6-311+G(d,p) level along with single point energy calculations for relative energetics at the B3LYP, B3P86, and MP2(full) levels with a 6-311+G(2d,2p) basis set. The IRMPD spectrum of $Zn^{2+}(H_2O)_8$ is most consistent with the calculated spectrum of the 5-coordinate MP2(full) ground state (GS) species. Results from larger complexes also point toward a coordination number of five, although contributions from 6-coordinate species cannot be ruled out. For n = 6 and 7, comparisons of the individual IRMPD spectra with calculated spectra are less conclusive. However, in combination with the BIRD and laser photodissociation kinetics as well as a comparison to hydrated Cu^{2+} and Ca^{2+}, the presence of 5-coordinate species with some contribution from 6-coordinate species seems likely. Additionally, the BIRD rate constants show that $Zn^{2+}(H_2O)_6$ and $Zn^{2+}(H_2O)_7$ complexes are less stable than $Zn^{2+}(H_2O)_8$. This trend is

Adapted with permission from Cooper, T. E.; O'Brien, J.T; Williams, E. R.; Armentrout, P.B., *J. Phys. Chem. A* **2010**, *114*, 12655.

consistent with previous work that demonstrates the enthalpic favorability of the charge separation process forming singly charged hydrated metal hydroxide and protonated water complexes versus loss of a water molecule for complexes of $n \leq 7$. Overall, these results are most consistent with the lowest-energy structures calculated at the MP2(full) level of theory and disagree with those calculated at B3LYP and B3P86 levels.

Introduction

Zinc is required for the activation of certain proteins and metalloenzymes[1-3] and is used heavily in industry as well.[4] Because of such high usage, zinc is quickly infiltrating aqueous environments and has become a metal contaminant in many watersheds around the world. To understand biological transport of zinc and its impact in aqueous environments, a complete understanding of the hydration of zinc(II) cations is essential.

The solvated zinc(II) cation has been studied using ion equilibria with a variety of ligands (but not water)[5-7] and collision-induced dissociation (CID) mass spectrometry of the hydrated ion[8,9] (and more recently in Chapters 3 and 4 of this dissertation). For larger complexes, dissociation of hydrated Zn^{2+} complexes results in the loss of a water molecule, reaction 5.1,

$$Zn^{2+}(H_2O)_n \rightarrow Zn^{2+}(H_2O)_{n-1} + H_2O \qquad (5.1)$$

followed by sequential loss of additional water molecules as the available energy increases. For smaller hydration shells, the $Zn^{2+}(H_2O)_n$ complex undergoes a charge separation process, reaction 5.2,

$$Zn^{2+}(H_2O)_n \rightarrow ZnOH^{+}(H_2O)_m + H^{+}(H_2O)_{n-m-1} \quad (5.2)$$

In Chapter 4, it was determined that the largest value of n at which reaction 5.2 is energetically favored over reaction 5.1, otherwise known as the critical size (n_{crit}), is when $n = 7$ ($m = 3$). In addition, Chapter 3 reported the first experimental hydration energies of $Zn^{2+}(H_2O)_n$, where $n = 6 – 10$. In both of these preceding chapters, accurate thermochemistry relies on the explicit consideration of different low-energy isomers in their data analysis, specifically, how many inner shell versus outer shell water ligands are present in the calculated structures of the reactants and products.

Establishing the number of water molecules in the inner solvent shell for the hydrated zinc dication has been the subject of numerous computational and experimental studies,[3,7,9-16] as detailed in Chapter 3. Briefly, X-ray, Raman, and near-IR spectroscopy experiments report a coordination number (CN) of six, which until recently has been the commonly accepted configuration.[3,10-12] Quantum chemical calculations in this dissertation and in previous studies[13-15] have shown that the lowest-energy complex can have an inner shell of four, five, or six water molecules depending on the level of theory used and previous studies. These studies also found that the energetic differences between these structures are quite small. As discussed in Chapter 3, depending on complex size, an inner shell of five or six is favored by MP2 and M06 calculations, whereas B3LYP and B3P86 theory have a preference for an inner shell of either four or five.[13-16] The ambiguity in the theoretical results may be partially understood by how strongly different approaches weight the electronic stability imparted by the 18 electron rule, which is fulfilled at a CN of four, compared to having more water molecules

directly bound to the Zn^{2+}, which is sterically feasible. In Chapters 3 and 4, the interpretation of experimental thermochemical values for zinc hydration depends on the presumed ground state (GS) structures of the reactant and product. Therefore, in order to obtain accurate thermochemistry, these studies report multiple hydration energies for each complex size where theoretical results give two or more likely GS configurations (n = 6 – 10).

Infrared multiple photon dissociation (IRMPD) spectroscopy is a powerful tool for probing the structures and the CN of singly and doubly charged hydrated complexes in the gas phase.[17-30] The IRMPD spectra and blackbody infrared radiative dissociation (BIRD) kinetics on a number of hydrated doubly charged metals have been reported previously by Williams and coworkers.[18-21] Specifically, the spectra for $Cu^{2+}(H_2O)_n$ support a CN = 4 and exhibit evidence of the formation of a third solvent shell at $n \geq 10$.[20] Alkaline earth metals (Mg^{2+}, Ca^{2+}, and Ba^{2+}) show a CN = 6, with evidence of complexes with a CN = 7 for Ba^{2+} at small cluster size, but a CN = 8 for Ca^{2+} is more favorable at larger cluster size.[18,19,21] Here, similar comparisons of IRMPD spectra for $Zn^{2+}(H_2O)_n$, where n = 6 – 12, and BIRD experiments with calculated spectra at the B3LYP/6-311+G(d,p) level for species with relative energies determined at B3LYP, B3P86 and MP2(full) levels with a 6-311+G(2d,2p) basis set are used to give further insight to the CN and specific water binding motifs for Zn(II) in the gas phase.

Experimental and Theoretical Section

Experimental methods. Experiments were performed using a 2.7 T Fourier-transform ion cyclotron resonance mass spectrometer at University of California Berkeley.[18,31,32] Distributions of $Zn^{2+}(H_2O)_n$ were produced by nanoelectrospray

ionization (ESI) of 5 mM aqueous solution of $ZnCl_2$ using borosilicate capillaries pulled to an inner diameter of ~1 μm. These complexes were introduced into the mass spectrometer and were trapped in a cylindrical ion cell that is surrounded by a copper jacket cooled to 215 K by a regulated flow of liquid nitrogen.[33] The copper jacket was allowed to equilibrate for at least 8 h prior to the experiments. Ions were accumulated in the cell for 3 – 5 s during which time dry N_2 gas (~2×10^{-6} Torr) was pulsed into the vacuum chamber using a piezoelectric valve to enhance trapping and thermalization of the ions. A mechanical shutter was subsequently closed to prevent further ion accumulation and residual gases were pumped out for 5 – 8 s resulting in a base pressure of ~1×10^{-8} Torr prior to ion isolation.

$Zn^{2+}(H_2O)_7$ was the smallest complex observed directly by ESI, in agreement with zinc hydration work performed in Chapters 3 and 4 at University of Utah with the thermal ESI outlined in Chapter 2. Small amounts of $Zn^{2+}(H_2O)_6$ were formed by collisionally activated dissociation (CAD) of larger complexes using a frequency sweep or chirp excitation waveform (175 μs, 2000 Hz/μs, 200 $V_{pk\text{-}pk}$) that increased the average velocity of all trapped ions with $m/z > 94$. This excitation was repeated eight times with a 300 ms delay between each chirp to maximize the intensity of the $Zn^{2+}(H_2O)_6$. Dry N_2 was pulsed into the chamber (~10^{-6} Torr) during this time to enhance collisional activation, and residual gases were then pumped out for 8 s prior to isolation of this ion. In previous work,[20] similar methods were necessary to form $Cu^{2+}(H_2O)_6$ because hydrated Cu^{2+} is thought to undergo reaction 5.2 at similar values of n as hydrated Zn^{2+}. It is important to note that the minimum size formed directly by ESI or through the CAD

process is in no way related to the CN of the ion, but is instead related to the propensity for this complex to dissociate via reaction 5.2, as discussed in more detail below.

Complexes of interest were isolated using a stored waveform inverse Fourier transform. To obtain IR action spectra, the isolated complexes were irradiated using tunable IR light produced by an optical parametric oscillator/amplifier (OPO/OPA) system (LaserVision, Bellevue, WA) pumped by the fundamental of Nd:YAG laser (Continuum Surelight I-10, Santa Clara, CA) at 10 Hz repletion rate. Laser irradiation times were varied from 1 – 30 s to improve the dynamic range and the signal-to-noise of the IR spectrum. Typically, shorter irradiation times (1 – 5 s) were used for frequencies in the free-OH stretch region (3600 – 3750 cm^{-1}) of the IR spectrum; otherwise longer irradiation times (5 – 30 s) were used. From the abundances of the precursor and product ions, dissociation rates as a function of the IR laser frequency were obtained. These dissociation rates were corrected for the BIRD background dissociation, the differences in laser power at different frequencies, and the duration of laser irradiation. To obtain unimolecular dissociation rate constants for both laser photodissociation at a specific frequency and for BIRD,[34-36] ions were exposed to radiation for up to 50 s, and this data was fit to first-order kinetics. All data were acquired using a MIDAS[37] modular data system. Products from reaction 5.1 were observed only for the photodissociation of $n \geq 8$; however, $n = 6$ and 7 dissociated only via reaction 5.2, in line with the discussion above.

Computational methods. Quantum chemical results for $Zn^{2+}(H_2O)_n$ complexes, $n = 4 – 10$, used in this study have been described completely in Chapter 3. Similar procedures were used for the $Zn^{2+}(H_2O)_{11}$ and $Zn^{2+}(H_2O)_{12}$ complexes. Briefly,

complexes with a CN of four, five, and six were geometry optimized and their vibrational frequencies calculated at the B3LYP[38,39] level of theory with a 6-311+G(d,p) basis set using the *Gaussian03* package.[40] For comparison to experiment, the calculated vibrational frequencies are broadened using a Gaussian line shape with a 50 and 15 cm^{-1} full width at half maxima (FWHM) for the bonded and free-OH stretches, respectively. Gaussian line shapes with a 10, 15, and 20 cm^{-1} FWHM were all tried in the free-OH stretch region and the best agreement to experimental band shapes was found using 15 cm^{-1}, in agreement with a previous report on Cu^{2+} hydration.[20]

Theoretical frequencies are scaled by 0.956, which has been shown previously to provide good agreement with experimental IR spectra in the free-OH region.[20,41] This scaling factor corrects for the approximation of the electronic structure and the assumption of a harmonic potential energy surface[42] and can range from 0.8 – 1. In Chapter 3, we verified that results of geometry optimizations and vibrational frequency calculations performed at alternate levels of theory, including B3LYP/6-311++G(d,p), B3LYP/6-311+G(2d,2p), BHandHLYP/6-311+G(d,p), BHandHLYP/6-311++G(d,p), and MP2(full)/6-311+G(d,p), yielded geometries with no discernible differences and vibrational frequencies within 1% of the B3LYP/6-311+G(d,p) results used here.

Relative energies of different isomers are determined using single point energies (SPE) at the B3LYP, B3P86,[43] and MP2(full)[44] levels using a 6-311+G(2d,2p) basis set. The relative energetics include zero point energy (ZPE) corrections to yield 0 K values and thermal corrections to 215 K. These corrections use the calculated frequencies scaled by 0.989, a scaling factor determined by Bauschlicher Jr. and Partridge to give accurate ZPE corrections at the B3LYP level using a 6-311+G(3df,2p) basis set.[45] Use of

different scaling factors for vibrational frequencies versus zero point energy corrections is common.[46]

Results and Discussion

BIRD kinetics. Dissociation rate constants in the zero-pressure limit[47-49] were obtained from BIRD mass spectra as a function of reaction times up to 120 s at 215 K. The temperature of 215 K was chosen so that the lifetimes of larger zinc hydrate complexes are sufficiently long that IR action spectra can be readily measured, as reported for $Cu^{2+}(H_2O)_{6\text{-}12}$.[20] The dissociation rate constants increase with complex size for $n \geq 8$ as seen in Figure 5.1. This is a consequence of both a decrease in the water binding energy inherent to these larger metal hydrate complexes (Chapter 3) and to an increase in the rate of absorption of blackbody radiation. The $n = 7$ and 6 complexes are also progressively less stable than the $n = 8$ complex, although only a small change is seen between $n = 7$ and 8, in contrast to the sharp decrease in stability seen previously[20] for Cu^{2+} at these same complex sizes. This decrease in stability results from the lower barrier for reaction 5.2 compared to reaction 5.1 at and below the critical size of $n_{crit} = 7$. As discussed previously in Chapter 4, the barrier for reaction 5.2 remains relatively constant when $n \leq n_{crit}$, whereas the hydration energies of reaction 5.1 increase rapidly as the complex size decreases. The smaller change in stability from $n = 8$ to 7 for Zn^{2+} compared to Cu^{2+} may show that zinc has less propensity to charge separate at the $n = 7$ complex than copper. Copper has a larger second ionization energy compared to zinc (20.3 eV versus 18.0 eV)[50,51] and therefore could charge separate with greater efficiency.

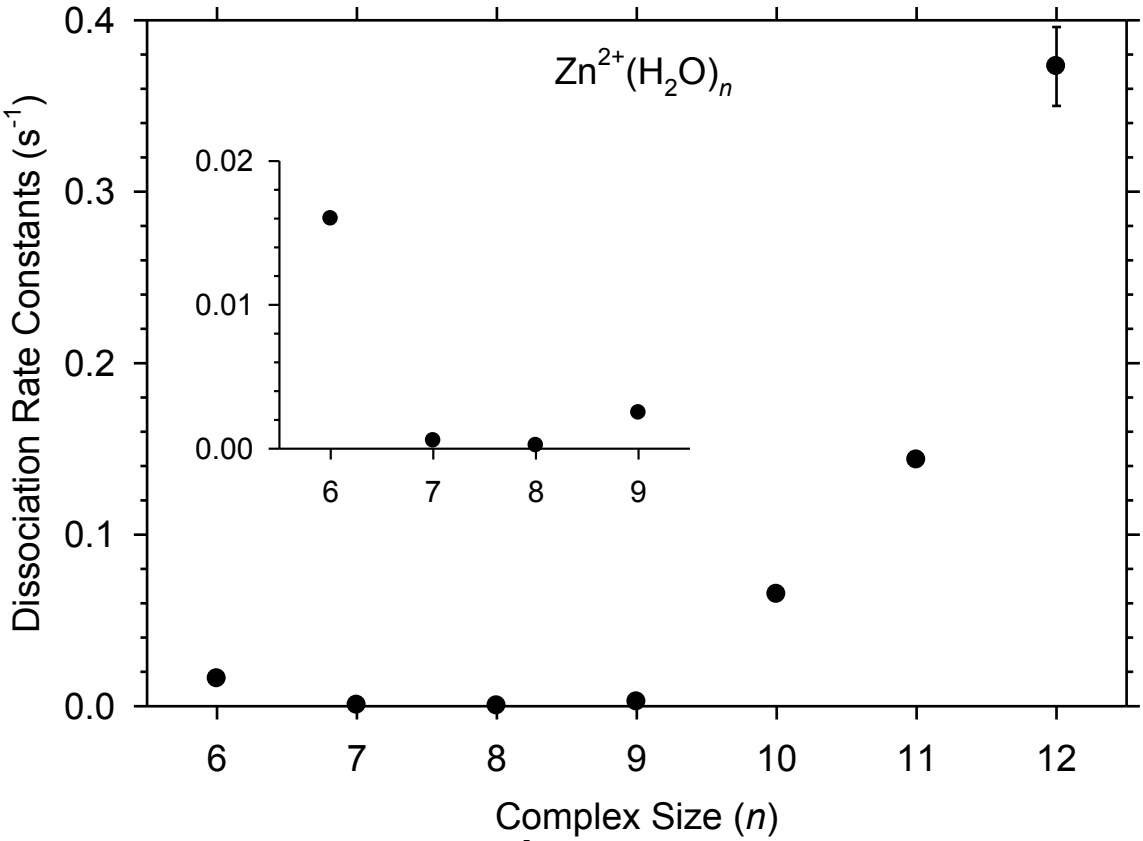

Figure 5.1. BIRD rate constants of $Zn^{2+}(H_2O)_n$, where $n = 6 – 12$, with a copper jacket temperature of 215 K. Uncertainties for each rate are shown but are smaller than the points for $n = 6 – 11$.

IR action spectra. Infrared photodissociation spectra from 2800 – 3800 cm^{-1} for $Zn^{2+}(H_2O)_n$, where n = 6 – 12, are shown in Figure 5.2. There are two obvious high frequency bands in the n = 6 – 9 spectra above ~3600 cm^{-1} in the free-OH region. The smaller of the two peaks, centered ~3600 cm^{-1}, is the symmetric (ν_{sym}) free-OH stretch of water molecules that do not donate any hydrogen bonds, whereas the larger peak (centered ~3670 cm^{-1}) is the asymmetric (ν_{asym}) stretch of these same water molecules. These bands for an isolated water molecule occur at 3657 and 3756 cm^{-1}, respectively.[52] The large red shift in these free-OH stretches can be explained by the partial electron transfer from the water molecules to the metal cation[23] and also a Stark effect.[53] A similar frequency shift of these free OH stretches is seen in other studies on complexes of $H_3O^+(H_2O)_{3-8}$,[24,29,54] $Cu^{2+}(H_2O)_{6-9}$,[20] $Ca^{2+}(H_2O)_{4-9}$,[18] $Ni^+(H_2O)_{1-5}$,[23] and $Cs^+(H_2O)_{1-5}$.[55] In agreement with trends observed with $Ca^{2+}(H_2O)_n$ and $Cu^{2+}(H_2O)_n$, these ν_{sym} and ν_{asym} peaks for $Zn^{2+}(H_2O)_n$ shift to the blue (i.e., a reduced red shift from that of isolated water) as n increases.

The spectra for n = 10 – 12 have up to four unique bands in this high frequency region, which are characteristic of the more complex hydrogen bonding motifs that develop in these larger complex sizes. The following nomenclature describes these different hydrogen bonding patterns. A second shell water molecule that hydrogen bonds to two different inner shell water molecules is a double acceptor (AA), whereas a second shell water molecule that forms only one hydrogen bond to the inner shell is a single acceptor (A). An inner shell water molecule that donates either one or two hydrogen bonds is designated as a single or double donor (D or DD, respectively). Water molecules in the second shell that hydrogen bond to water molecules in the third shell are

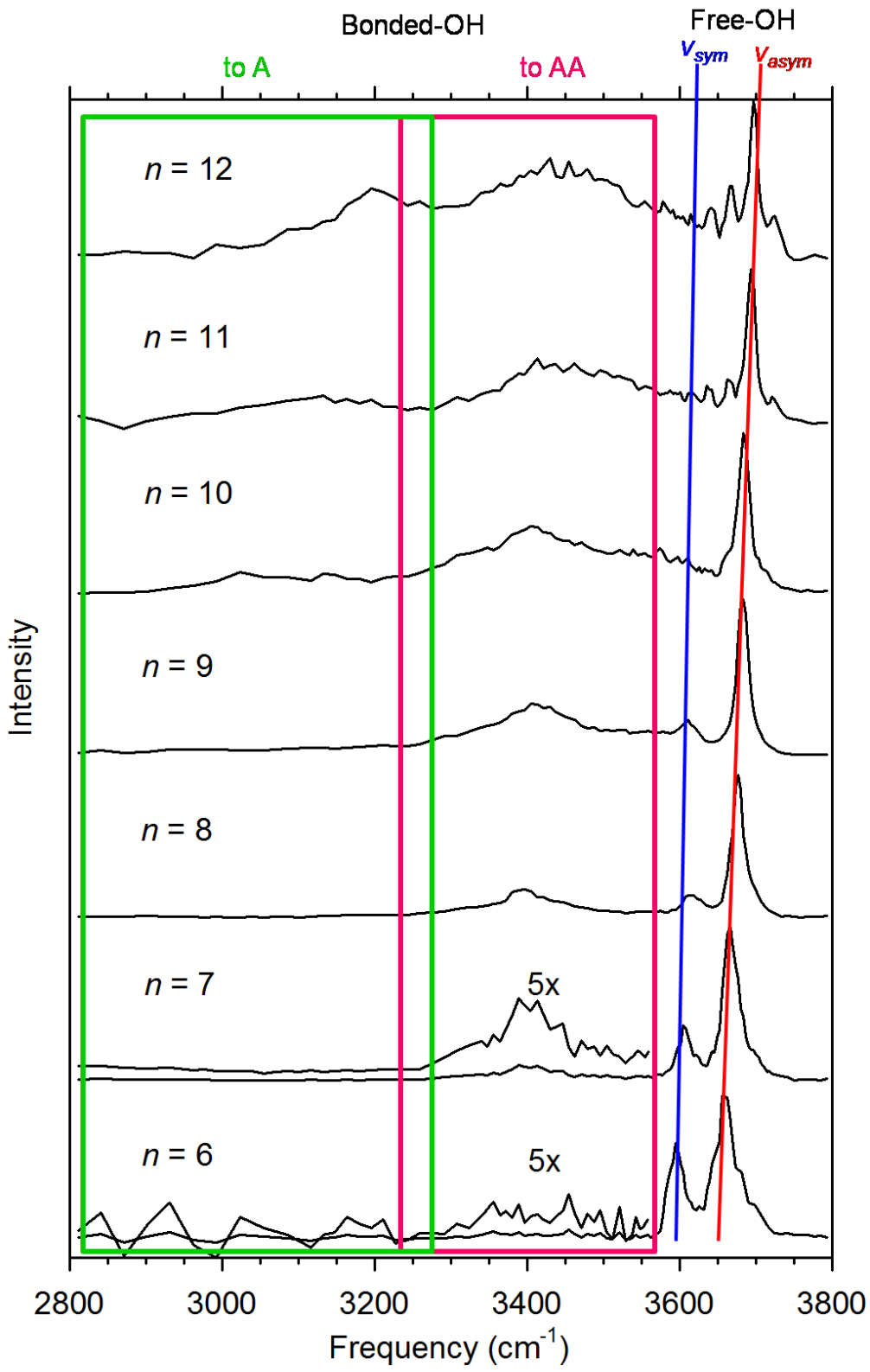

Figure 5.2. IR action spectra of $Zn^{2+}(H_2O)_n$, where $n = 6 – 12$, at 215 K. The common peak positions are marked for both the free-OH and bonded-OH regions.

a combination of both an acceptor and donor water molecule and are named accordingly. These high frequency bands may be assigned on the basis of previously reported IR spectra of similar systems[18,20,24,29,54] and the calculated absorption spectra of low-energy conformations of $Zn^{2+}(H_2O)_x(H_2O)_y(H_2O)_z$, briefly ($x$,$y$,$z$), where x, y, and z are the number of water molecules in the first, second, and third shells, respectively. The most intense bands at ~3690 cm^{-1} correspond to the ν_{asym} stretch of AA water molecules, with a possible contribution of the ν_{asym} stretch of a donor water molecule. The ν_{sym} stretch of the AA water molecule is not easily observed for all complex sizes because it overlaps with the broad intensity of the bonded-OH region. As shown previously,[21] the free-OH ν_{sym} band of acceptor only water molecules (those bound directly to the metal as indicated by the line in Figure 5.2) is preferentially depleted as the complex size increases by water molecules binding to them in the second solvent shell. In contrast, the ν_{asym} band (also indicated by a line in Figure 5.2) remains intense for all complex sizes because the ν_{asym} stretch of the second shell AA water molecules is superimposed on the ν_{asym} of the acceptor only inner shell water molecules. In the spectra for n = 11 and 12, the peaks at ~3635 cm^{-1} and ~3720 cm^{-1} agree well with ν_{sym} and ν_{asym} stretches, respectively, of A water molecules. The bands at ~3665 cm^{-1} are consistent with the ν_{asym} stretch of AAD water molecules.

Photodissociation is also observed at frequencies below 3600 cm^{-1} for n = 7 – 12, as well as n = 6, a case examined in detail below. There is a weak band in the spectra of the n = 7 and 8 complexes between 3300 and 3500 cm^{-1}, a broad band from 3300 – 3600 cm^{-1} for n = 9, and two broad bands in the n = 10 – 12 spectra (3000 – 3300 cm^{-1} and 3300 – 3600 cm^{-1}). The bands from 3300 – 3600 cm^{-1} correspond to hydrogen bonded

OH stretches of D and DD water molecules donating a hydrogen bond to an AA water molecule and indicate the formation of a second solvation shell. Bands below 3300 cm^{-1} are also attributed to stretches of donor water molecules (D, DD, or AAD), but correlate with donation of a hydrogen bond to a single acceptor water molecule. These are commonly found in larger complexes with a heavily populated second shell or in the formation of a third shell.

Theoretical geometries of $Zn^{2+}(H_2O)_n$. The geometries of $Zn^{2+}(H_2O)_{6\text{-}10}$ have been described in detail in Chapter 3. Additional structures for $n = 11 – 12$ are calculated here. The relative 0 K enthalpies and free energies calculated at 215 K are given in Table 5.1 for the low-energy conformers of $n = 6 – 12$. We also note that the relative order of all low-energy complexes at all three levels of theory remains the same at 215 K as was previously found in Chpater 3 for 298 K. For the rest of this discussion, if there is only one low-energy conformer having a particular inner solvent shell size, this nomenclature is abbreviated to the (x,y,z) designation. Depending on complex size, structures with an inner shell of four or five water molecules were found to be most stable at the B3LYP and B3P86 levels of theory, whereas the MP2(full) level predicts GS structures with five or six water molecules in the inner shell. (Relative energies similar to the MP2(full) calculations were obtained in Chapter 3 using the M06 density functional specifically designed for hydrogen bonding.[56,57] M06 calculations for the $n = 11$ and 12 complexes were not pursued here because the absolute hydration energies do not agree with experiment as well as the MP2(full) values.)

Comparison to theory: n = 8. A large number of conformations have been investigated by theory, but here we compare only the spectrum of the lowest-energy

Table 5.1. Relative calculated enthalpy (ΔH_0) and 215 K free energies (ΔG_{215})[a] (kJ/mol) of $Zn^{2+}(H_2O)_x(H_2O)_y(H_2O)_z$, where *x*, *y*, and *z* are the numbers of water molecules in the first, second, and third shells, respectively.[b]

Complex (*x*,*y*,*z*)		B3LYP	B3P86	MP2(full)
$Zn^{2+}(H_2O)_6$	(4,2)_2AA	0.0 (0.0)	0.0 (0.0)	3.8 (4.6)
	(4,2)_AA,A	4.5 (1.6)	4.4 (1.5)	11.7 (9.6)
	(5,1)_A_aA_b	8.2 (3.2)	8.6 (3.6)	4.2 (0.0)
	(6,0)	13.7 (15.0)	14.6 (15.9)	0.0 (2.0)
$Zn^{2+}(H_2O)_7$	(4,3)_3D,DD_2AA,A	0.0 (2.9)	0.0 (2.9)	10.8 (7.0)
	(4,3)_2D,DD_AA,2A	4.1 (0.0)	4.1 (0.0)	18.0 (7.1)
	(5,2)_2A_bA_b	0.2 (7.0)	0.1 (6.9)	0.0 (0.0)
	(6,1)_AA	18.4 (26.2)	18.7 (26.5)	8.6 (9.6)
$Zn^{2+}(H_2O)_8$	(4,4)_2AA,2A	1.8 (0.0)	2.4 (0.0)	14.9 (9.2)
	(4,4)_AA,3A	4.2 (0.5)	4.8 (0.5)	20.7 (13.1)
	(5,3)_3AA	0.0 (3.9)	0.0 (3.3)	0.0 (0.0)
	(6,2)_2AA	16.8 (21.3)	17.7 (21.6)	6.7 (7.3)
$Zn^{2+}(H_2O)_9$	(4,5)_2AA,3A	5.8 (0.0)	6.3 (0.0)	22.1 (11.6)
	(5,4)_4A_bA_b	0.0 (4.8)	0.0 (4.2)	0.0 (0.0)
	(5,4)_2A_bA_b,2A_aA_b	1.3 (6.7)	0.8 (5.8)	1.9 (2.6)
	(6,3)_4D,DD_3AA	16.9 (21.2)	16.7 (20.5)	7.2 (6.8)
$Zn^{2+}(H_2O)_{10}$	(4,6)_2AA,4A	3.5 (0.0)	4.4 (0.0)	18.6 (12.1)
	(5,5)_4A_bA_b,A_a	0.0 (3.0)	0.0 (2.2)	0.0 (0.0)
	(6,4)_4D,2DD_4AA	18.1 (28.3)	16.9 (26.3)	5.5 (12.7)
	(6,4)_5D,DD_3AA,A	19.8 (24.9)	19.7 (24.0)	8.7 (10.8)
$Zn^{2+}(H_2O)_{11}$	(4,6,1)_AA,4A,AAD_A	5.1 (0.0)	6.4 (0.0)	20.2 (12.1)
	(5,5,1)_3A_bA_b,A_a,A_bA_bD_A	0.0 (3.0)	0.0 (1.7)	0.0 (0.0)
	(5,6)_4A_bA_b,2A_a	4.4 (8.5)	6.5 (9.4)	1.3 (2.5)

Table 5.1. continued

	Complex (*x,y,z*)	B3LYP	B3P86	MP2(full)
	(6,5)_4AA,A	20.7 (25.6)	22.2 (25.8)	5.6 (7.5)
$Zn^{2+}(H_2O)_{12}$	(4,6,2)_4A,2AAD_2A	4.7 (0.0)	6.2 (0.0)	20.4 (10.4)
	(5,5,2)_2A_bA_b,A_a,2A_bA_bD _2A	0.0 (4.6)	0.0 (3.2)	0.6 (0.0)
	(5,6,1)_3A_bA_b,A_a,2A_a,A_bA_bD_A	4.3 (8.0)	6.5 (8.7)	2.0 (0.4)
	(6,5,1)_2AA,2AAD,AA_p_A	16.8 (32.5)	16.3 (30.5)	0.2 (10.7)

[a] ΔG_{215} values given in parentheses. [b] Values are single point energies calculated at the level shown using a 6-311+G(2d,2p) basis set with geometries calculated at the B3LYP/6-311+G(d,p) level. Zero point energy correction scaled by 0.989 are included.

structure for each inner shell size to experiment. The most conclusive comparison between experiment and theory for a single complex size is found at $n = 8$, Figure 5.3. Looking first in the free-OH region, there is no evidence of single hydrogen bond acceptors in the experimental spectrum, near 3715 cm^{-1}, largely eliminating the 4-coordinate complexes, calculated to be low in energy by DFT. Additionally, the most intense free-OH peak predicted for the 4-coordinate species are red shifted by ~10 cm^{-1} from experiment, although this conclusion depends on the vibrational scaling factor applied to the theoretical spectra. The narrow shape of the experimental band centered at ~3675 cm^{-1} matches best with the (5,3) structures, calculated to be the GS at the MP2(full) level. The predicted band ranges from 3665 – 3680 cm^{-1}, and the relative intensities of the v_{sym} and v_{asym} bands are also predicted well. It should be remembered that the IRMPD intensities are not always reproduced by a calculated absorption spectrum, a one photon spectrum. In the (6,2) spectrum, the v_{asym} peak is broadened by stretches at ~3700 cm^{-1} resulting from inner shell water molecules that do not donate any hydrogen bonds to the second shell. This predicted broad band is inconsistent with the experimental spectrum as are the relative intensities of the v_{sym} and v_{asym} bands in the (6,2) spectrum. Thus, the good agreement of the experimental spectrum with the band position predicted for the (5,3) structure suggests that the vibrational scaling factor applied here is accurate, in agreement with previous work.[20,41]

A bonded-OH stretch is observed near 3400 cm^{-1} in the IRMPD spectrum with an intensity about 20% that of the free-OH v_{asym}, Figure 5.3. The measured intensity is ~10 times lower than what is predicted by theory for either the (5,3) or (6,2) isomer relative to the free-OH stretches. A similar low intensity has been observed for other hydrated

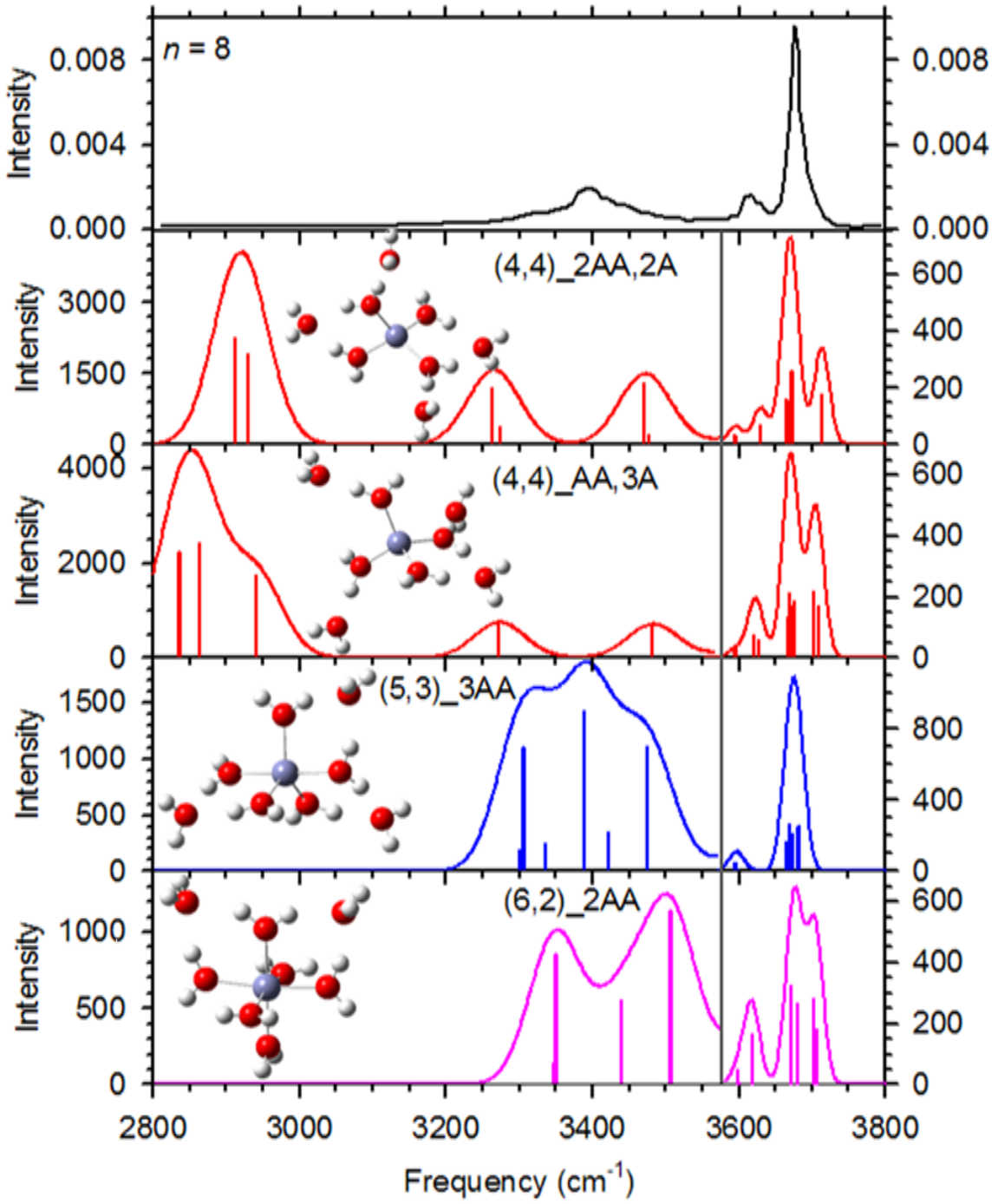

Figure 5.3. Comparison of the experimental IRMPD spectrum for $Zn^{2+}(H_2O)_8$ at 215 K with IR spectra for four low-energy conformers predicted at the B3LYP/6-311+G(d,p) level of theory. In the theoretical spectra the bonded-OH region is broadened by 50 cm^{-1} and the free-OH region is broadened by 15 cm^{-1}. The intensities of these regions are on the left and right y-axis, respectively, in km/mol.

divalent metal ions at small cluster size,[18-21] which may be attributed to several factors,[18,20,26,29] including the broadness of hydrogen-bonded bands relative to free-OH bands, as well as lower photon energy, calculation uncertainties, and anharmonicity. Similar broadening is seen in the bonded-OH region in a multitude of previous studies involving a variety of systems.[18,20,21,26,27,29,30,54,58,59] More intense laser-induced photodissociation in this region has been observed for divalent metal ion crown complexes with methanol,[58] which may be a result of lower binding energies or the different solvent molecule. To take these effects into account, the calculated spectra (for all systems) are plotted using different intensity scales and Gaussian line shapes in the bonded-OH and free-OH regions. The most intense bonded-OH band near 3400 cm^{-1} in the (5,3) complex corresponds to the stretch of a D water molecule bonded to an AA water molecule and agrees best with the experiment, whereas the most intense band for the (6,2) complex is predicted at ~3500 cm^{-1} and corresponds to the stretch of a DD bonded to an AA. Neither (4,4) complex is predicted to show a band at 3400 cm^{-1}. Additionally, both 4-coordinate structures predict an intense band at < 3000 cm^{-1}, corresponding to the donation of a hydrogen bond to an A water molecule, which is not found in the experiment.

Overall, the IRMPD spectrum observed for $n = 8$ agrees well with the calculated (5,3) structures. Small contributions from a (6,2) structure are indicated by the 3675 cm^{-1} band which is slightly broadened at higher frequency, but there is no evidence for contributions from (4,4) complexes. These results are consistent with our MP2(full) results, Table 5.1, and are inconsistent with DFT calculations at 215 K.

n = 6. The two lowest-energy structures of $Zn^{2+}(H_2O)_6$ at the DFT levels of theory are the (4,2)_2AA and (4,2)_AA,A, whereas MP2(full) predicts the 215 K GS to be the (5,1) complex and the 0 K GS to be the (6,0) isomer. The theoretically predicted free-OH ν_{sym} and ν_{asym} stretches of the (4,2)_2AA complex, Figure 5.4, are red shifted compared to experiment and relative intensities of the ν_{sym} and ν_{asym} bands do not match experiment well. The free-OH ν_{sym} band in the (5,1) complex is calculated to be at the same frequency as that observed in the IRMPD spectrum, whereas the ν_{asym} band is calculated to be ~10 cm^{-1} higher, with relative intensities of the two peaks in reasonable agreement with experiment. The calculated ν_{sym} and ν_{asym} bands in the (6,0) spectrum are ~8 and 28 cm^{-1} higher, respectively, again with relative intensities comparable to experiment. The good agreement in band positions suggests that there is a significant population of the 5-coordinate ions in the experiment, although this assignment is not definitive because it depends on the specific scaling factor used. The broadening of the experimental ν_{asym} band at higher frequency may be a result of contributions from the ν_{asym} band of the (6,0) complex. This is consistent with the similar relative free energies of the (5,1) and (6,0) complexes at the MP2(full) level of theory, Table 5.1. This broadening could also be the result of small contributions from the single acceptor water molecule found in (4,2)_AA,A, the DFT GS at 215 K.

The 4- and 5-coordinate complexes for *n* = 6 are predicted to have bands in the bonded-OH region (D or DD) of the experimental spectrum near 3300 cm^{-1}, Figure 5.4. The IRMPD spectrum exhibits very small amounts of photodissociation broadly centered at ~3400 cm^{-1}. If the intensity of the experimental photodissociation in this region is 10 times lower than theory, as found for $Zn^{2+}(H_2O)_8$, then the predicted absorbance intensity

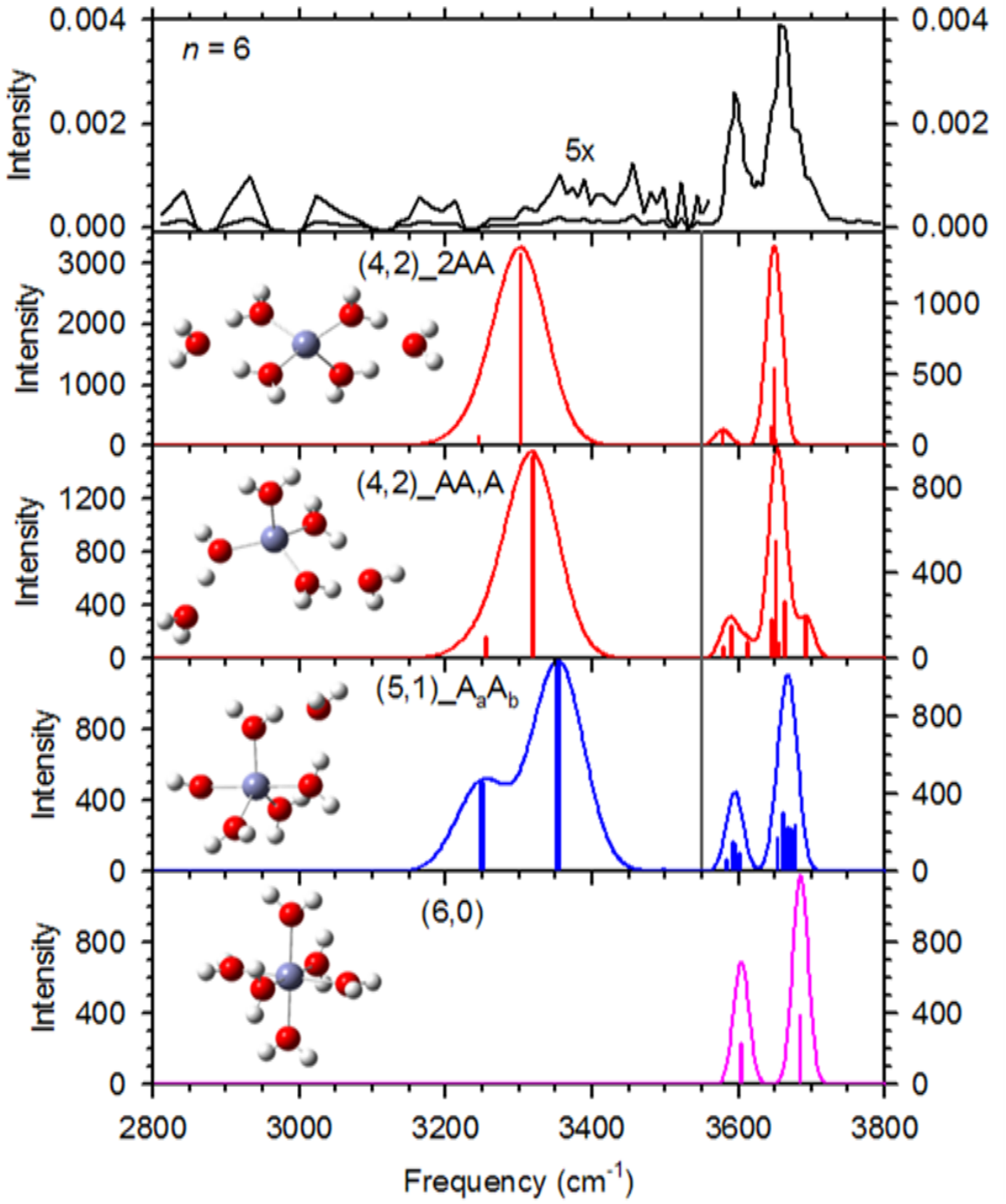

Figure 5.4. Comparison of the experimental IRMPD spectrum for $Zn^{2+}(H_2O)_6$ at 215 K with IR spectra for four low-energy conformers predicted at the B3LYP/6-311+G(d,p) level of theory. In the theoretical spectra the bonded-OH region is broadened by 50 cm^{-1} and the free-OH region is broadened by 15 cm^{-1}. The intensities of these regions are on the left and right y-axis, respectively, in km/mol.

in this region for either the 4- or 5-coordinate complexes would be close to the noise level. On this basis, the very low intensity in the bonded-OH region of the $n = 6$ IRMPD spectrum is reasonable even for CN < 6. To investigate the dissociation in this region more closely, the BIRD and laser photodissociation kinetics are compared, Figure 5.5. These data clearly show laser induced photodissociation at 3390 cm^{-1}, the approximate frequency where maximum photodissociation would occur in the bonded-OH region. This is consistent with the presence of the (5,1) complex, as determined from analysis of the free-OH stretching region.

$n = 7$. The frequencies of the free-OH ν_{sym} and ν_{asym} bands in the IRMPD spectrum of $Zn^{2+}(H_2O)_7$ at 3605 cm^{-1} and 3666 cm^{-1}, respectively, Figure 5.6, match those calculated for the (5,2) structure at 3590 – 3611 cm^{-1} and 3659 – 3667 cm^{-1}. The (6,1) complex has higher frequency peaks centered at 3613 and 3690 cm^{-1}. The relative intensities calculated for both the (5,2) and (6,1) structures are consistent with the IRMPD spectrum with the experimental ν_{asym} peak shape being matched better by the (5,2) spectrum. The predicted peak is broadened slightly on the blue side as a result of stretches from acceptor-only waters, i.e., those which are bound directly to the metal and do not participate in any hydrogen bonding. The maxima in the ν_{sym} and ν_{asym} stretches of both (4,3) complexes are at lower frequencies than observed in the IRMPD spectrum, with additional high frequency bands that do not match the experimental spectrum well. The broadening on the blue side of the ν_{asym} band in the IRMPD spectrum at ~3700 cm^{-1} could a) be from a single acceptor water molecule in either of the 4-coordinate structures, b) correspond to the broadening seen in the (5,2) ν_{asym} band at 3695 cm^{-1}, which is the free-OH stretch of an inner shell acceptor only water as discussed above, or c) be a

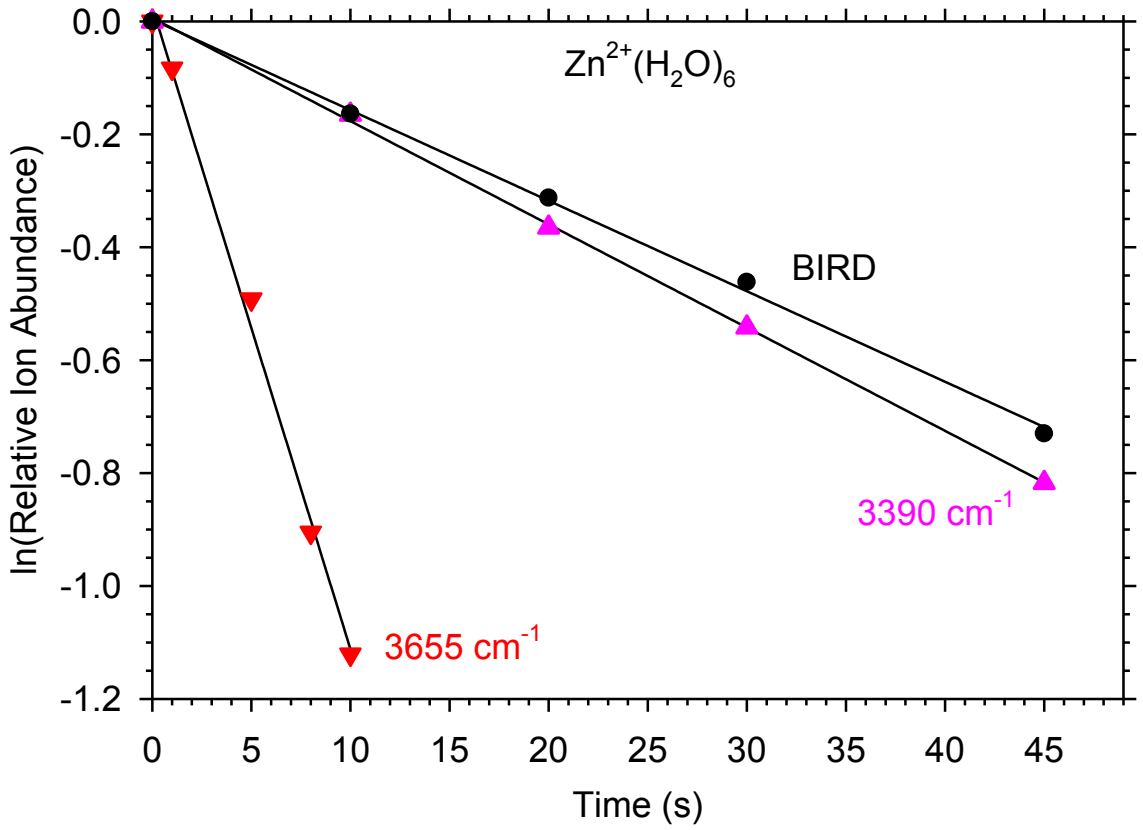

Figure 5.5. BIRD and laser photodissociation data for $Zn^{2+}(H_2O)_6$ at 215 K at the frequencies indicated. The rate constants determined from these data are 0.0160 ± 0.0004 s^{-1} for BIRD, 0.0183 ± 0.0002 and 0.114 ± 0.004 s^{-1} for photodissociation at 3390 and 3655 cm^{-1}, respectively.

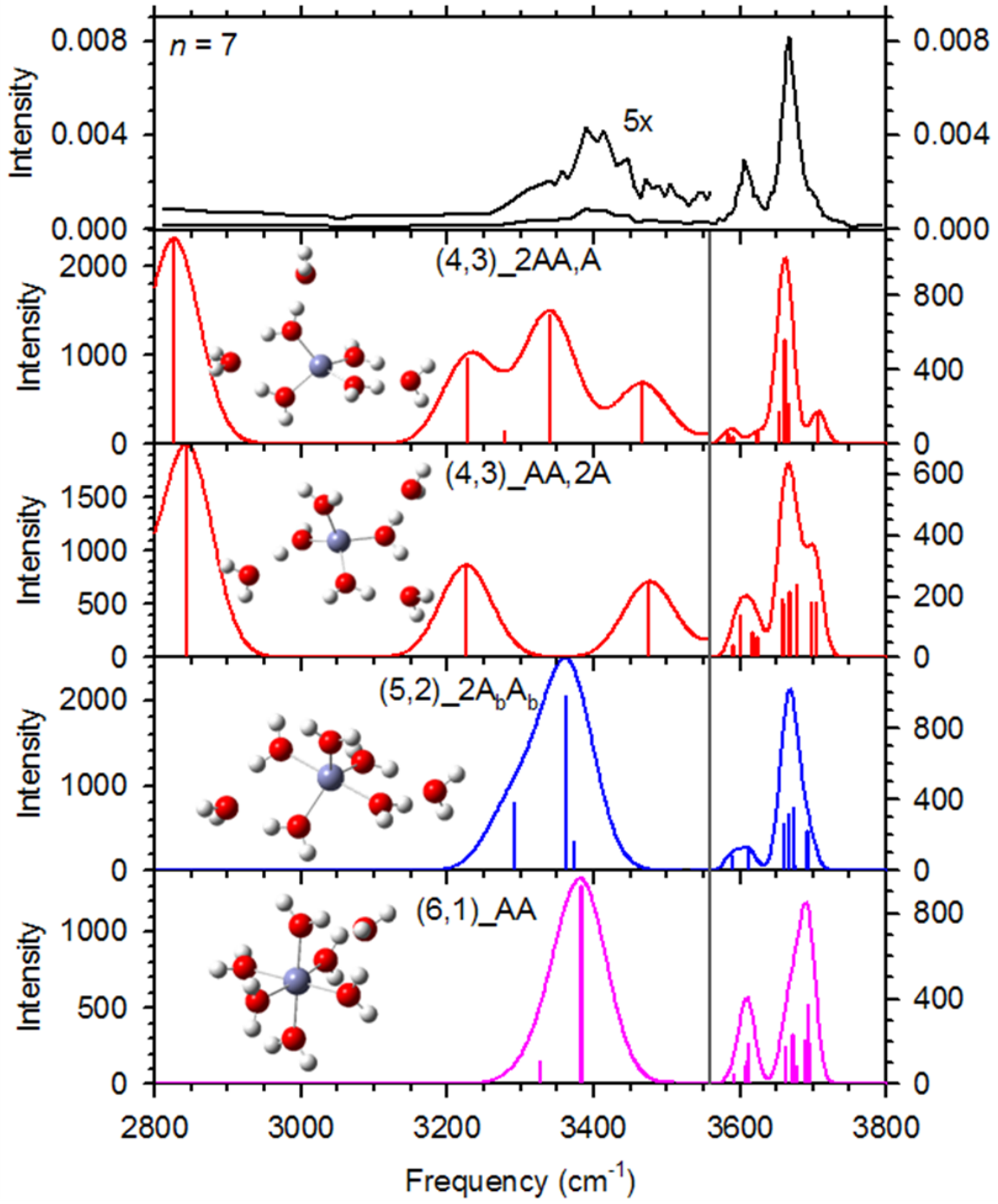

Figure 5.6. Comparison of the experimental IRMPD spectrum for $Zn^{2+}(H_2O)_7$ at 215 K with IR spectra for four low-energy conformers predicted at the B3LYP/6-311+G(d,p) level of theory. In the theoretical spectra the bonded-OH region is broadened by 50 cm^{-1} and the free-OH region is broadened by 15 cm^{-1}. The intensities of these regions are on the left and right y-axis, respectively, in km/mol.

consequence of small contributions from the blue-shifted (6,1)_AA complex. Overall, the predicted (5,2) GS complex agrees best with the experimental spectrum in the free-OH region, although contributions from the 6- and 4-coordinate structures cannot be ruled out, even though these complexes are calculated to be 10 and 7 kJ/mol higher in 215 K free energy at the MP2(full) level, respectively.

There is a small amount of photodissociation in the bonded-OH region of the IRMPD spectrum centered at ~3400 cm^{-1}, Figure 5.6. There is no evidence of the intense peak predicted at ~2850 cm^{-1} in both 4-coordinate complexes; however, this band may not be observed because of the low measured intensity in this region or it may be red shifted out of the spectral range examined. The (4,3)_AA,2A complex is the 215 K free energy GS predicted by DFT and does not have a band centered at ~3400 cm^{-1}. The (4,3), (5,2), and (6,1) complexes have bands just below 3400 cm^{-1}. The experimental band shape in this region matches predicted spectra of the 5- and 6-coordinate complexes best. The lack of intensity in this region could suggest some contribution from a 7-coordinate species; however, the (7,0) complex rearranges to the more stable (6,1) species during geometry optimization, as discussed in Chapter 3 in agreement with an earlier zinc hydration report[14] by Hartmann et al.

n = 9. The (5,4)_$2A_bA_b$,$2A_aA_b$ structure for $Zn^{2+}(H_2O)_9$ is only 2.6 kJ/mol higher in 215 K free energy than (5,4)_$4A_bA_b$ at the MP2(full) level of theory, Table 5.1. Both the free-OH ν_{sym} and ν_{asym} stretches (Figure 5.7) in the calculated spectrum of the former have similar frequencies and relative intensities to those in the IRMPD spectrum. The (5,4)_$2A_bA_b$,$2A_aA_b$ structure binds two of the outer shell water molecules to the apex water and a water in the base of the square pyramid inner solvent shell, as indicated by

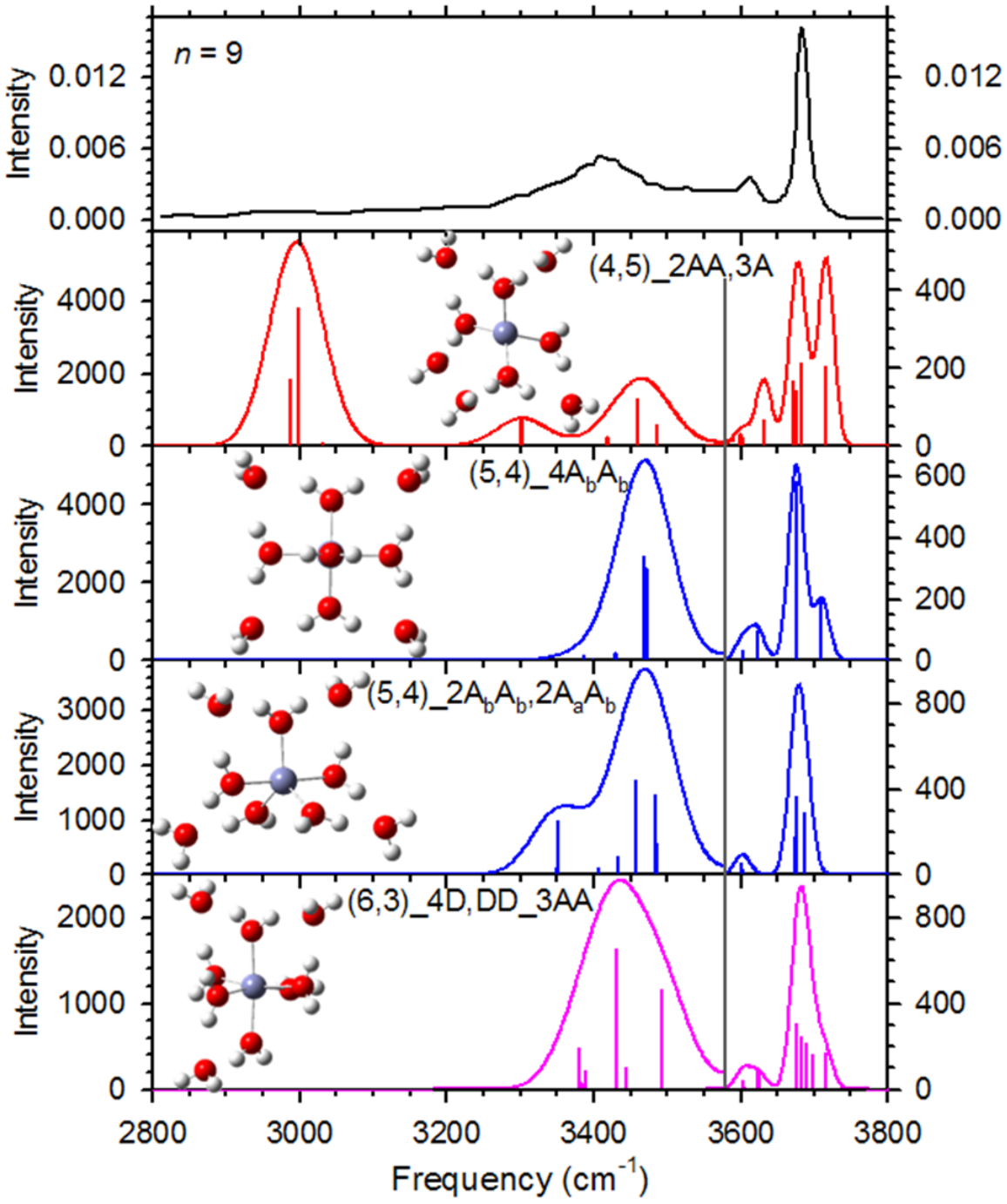

Figure 5.7. Comparison of the experimental IRMPD spectrum for $Zn^{2+}(H_2O)_9$ at 215 K with IR spectra for four low-energy conformers predicted at the B3LYP/6-311+G(d,p) level of theory. In the theoretical spectra the bonded-OH region is broadened by 50 cm^{-1} and the free-OH region is broadened by 15 cm^{-1}. The intensities of these regions are on the left and right y-axis, respectively, in km/mol.

the "a" and "b" subscripts, respectively. The remaining two water molecules are bound to two water molecules in the base (A_bA_b). The free-OH v_{asym} stretch of the (5,4)_$4A_bA_b$ complex is broadened by the OH stretch at 3709 cm^{-1} of an inner shell acceptor-only water molecule, and therefore appears inconsistent with the experimental spectrum. Likewise, the (6,3) complex has band positions that agree with experiment, but is broadened on the blue side for similar reasons as (5,4)_$4A_bA_b$. The (6,3) complex is 7 kJ/mol higher in free energy at 215 K than the (5,4) GS at the MP2(full) level of theory, Table 5.1. Spectra of all 4-coordinate complexes are inconsistent with experiment for n = 9 in the relative intensities, positions, and shapes of the free-OH v_{sym} and v_{asym} bands as well as the intense band at 3000 cm^{-1} in the bonded-OH stretch region. In the bonded-OH region of the experimental spectrum, there is a broad band centered near 3400 cm^{-1} and a band at this frequency is in the calculated spectra of each isomer.

Overall, it seems likely that the spectrum for n = 9 is similar to the n = 8 complex discussed above and is dominated by a CN of five although it may have contributions from 6-coordinate species. The calculated spectra of the 4-coordinate species are inconsistent with experiment. Additionally, the broadening on the blue side of the free-OH v_{asym} stretch discussed above for the n = 6 and 7 complexes is not apparent in the IRMPD spectra for n = 8 and 9 because the majority of inner shell water molecules are now contributing hydrogen bonds to the second solvent shell. This observation suggests that the broadening observed in the smaller complexes is a consequence of inner shell acceptor-only water molecules (i.e., CN = 5 and 6 structures) rather than contributions from single acceptor water molecules from CN = 4 structures. Although it is possible that the CN changes with complex size, this seems unlikely because both the DFT and

MP2(full) levels of theory are fairly consistent with regard to their predictions for the low-energy CN for all values of *n* investigated, i.e., DFT consistently predicts free energy GS structures with CN = 4 and MP2(full) consistently predicts free energy GSs with a CN = 5.

n = 10. Like the smaller complexes, good agreement between the IRMPD and theoretical spectra of $Zn^{2+}(H_2O)_{10}$ in the free-OH region is found for the MP2(full) GS, (5,5)_4A_bA_b,A_a, Figure 5.8. Here, contributions of the ν_{sym} and ν_{asym} of the A_a water molecule appear at 3634 and 3719 cm^{-1}, respectively, consistent with the broadening at ~3635 and 3715 cm^{-1} in the IRMPD spectrum. The position and relative intensities of the free-OH stretches of the AA water molecules at 3634 and 3681 cm^{-1} are in excellent agreement with the experimental spectra. The (6,4)_3AA,A complex is 10.8 kJ/mol higher in 215 K free energy than the (5,5) complex at the MP2(full) level and is also consistent with the IRMPD spectrum in this region, with small contributions from the single acceptor water molecule appearing at 3630 cm^{-1} and 3714 cm^{-1}. The (6,4)_4AA complex is 2 kJ/mol higher than the (6,4)_3AA,A in free energy at 215 K. This complex does not have any contributions of a single acceptor water molecule and does not match the shape of the broad experimental ν_{asym} band. Although contributions from 6-coordinate complexes cannot be ruled out on the basis of spectral comparisons alone, significant contributions from these complexes do not seem likely on the basis of the relative MP2(full) free energies.

In the bonded-OH region, the band centered ~3400 cm^{-1} increases in intensity from the smaller complexes to ~40% of the free-OH ν_{asym} stretch for *n* = 10, Figure 5.8. This band corresponds to the donation to double acceptor water molecules and all

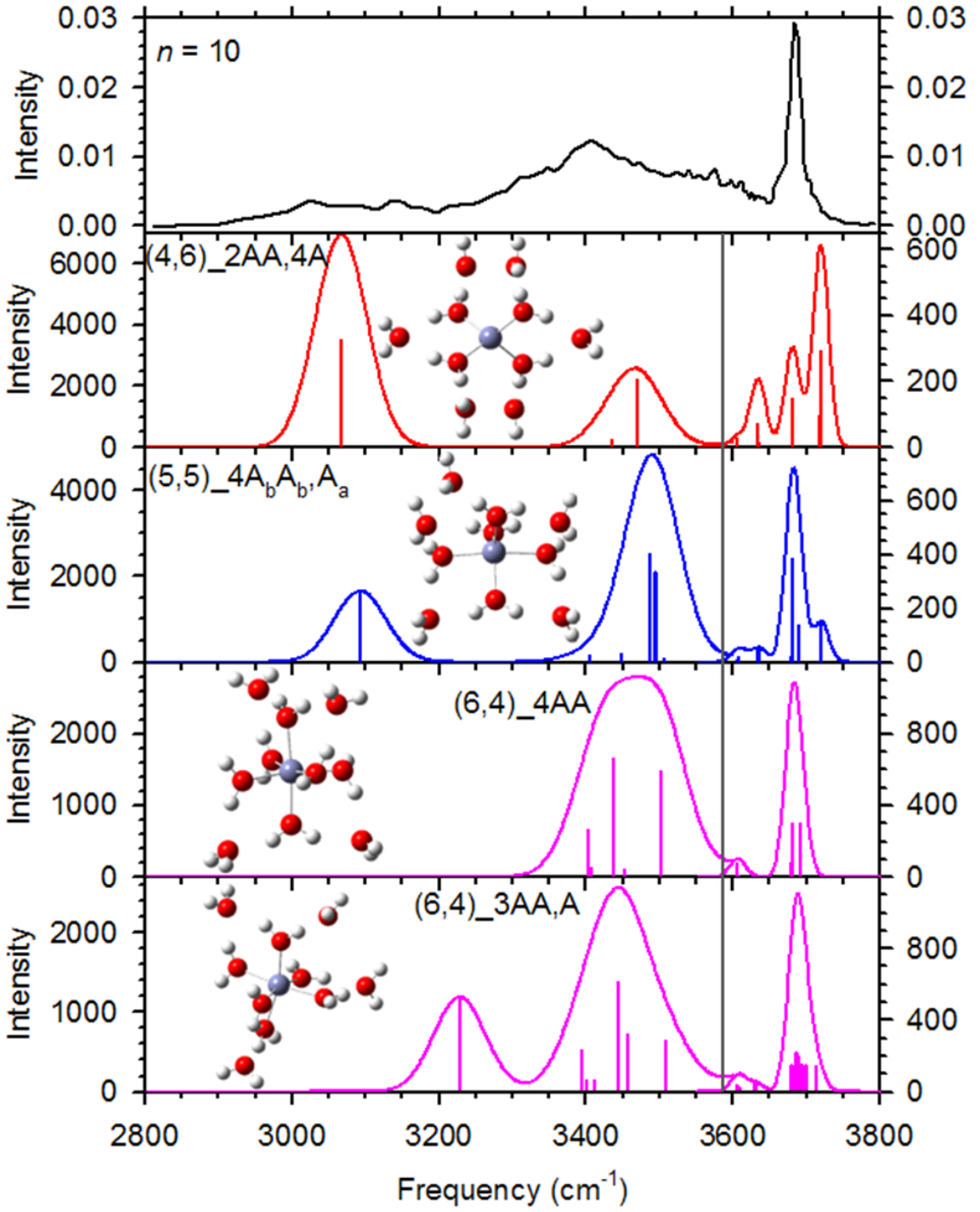

Figure 5.8. Comparison of the experimental IRMPD spectrum for $Zn^{2+}(H_2O)_{10}$ at 215 K with IR spectra for four low-energy conformers predicted at the B3LYP/6-311+G(d,p) level of theory. In the theoretical spectra the bonded-OH region is broadened by 50 cm^{-1} and the free-OH region is broadened by 15 cm^{-1}. The intensities of these regions are on the left and right y-axis, respectively, in km/mol.

theoretically predicted low-energy complexes have a band within 50 – 100 cm^{-1} of the IRMPD band. There is a small amount of additional photodissociation between 3000 – 3200 cm^{-1}, which corresponds to the stretch of a D or DD water molecule attached to an A water molecule in either the second or third shell. The best agreement in relative intensity for both bonded-OH bands is found with the (5,5) complex, although the higher frequency band is blue shifted by about 60 cm^{-1} from experiment, which seems inconsequential given the broadening observed in this region. The peak position of DA water molecules appears at 3227 cm^{-1} for the (6,4)_3AA,A complex and 3092 cm^{-1} for the (5,5)_$4A_bA_b$,A_a structure, where the latter agrees better with the position and relative intensity of the experimental peak. This observation cannot rule out contributions from the (6,4)_3AA,A complex, because the peak at 3227 cm^{-1} may be obscured by the broad photodissociation between 3200 – 3600 cm^{-1}. Both bands are also present in the predicted low-energy 4-coordinate complex, but the relative intensities of the two bands are reversed from the IRMPD spectrum.

n = 11 and 12. The free-OH peaks of the single acceptor water molecules near 3635 and 3720 cm^{-1} for n = 11 and 12 continue to grow in intensity with n, but are still less intense than the ν_{asym} of the double acceptor water molecules at 3695 cm^{-1} in both spectra. Similar to the results for n = 10, the structures having low free energies at the MP2(full) level, all 5-coordinate, match the experimental spectra best, Figures 5.9 and 5.10. For n = 12, there are six isomers that are each within 0.6 kJ/mol of the ΔH_0 GS complex. Only the lowest free energy complexes are shown in Figure 5.10. There is an obvious peak in the IRMPD spectra of both n = 11 and 12 at ~3665 cm^{-1}, which is consistent with the ν_{asym} stretch of an AAD water molecule. This observation indicates

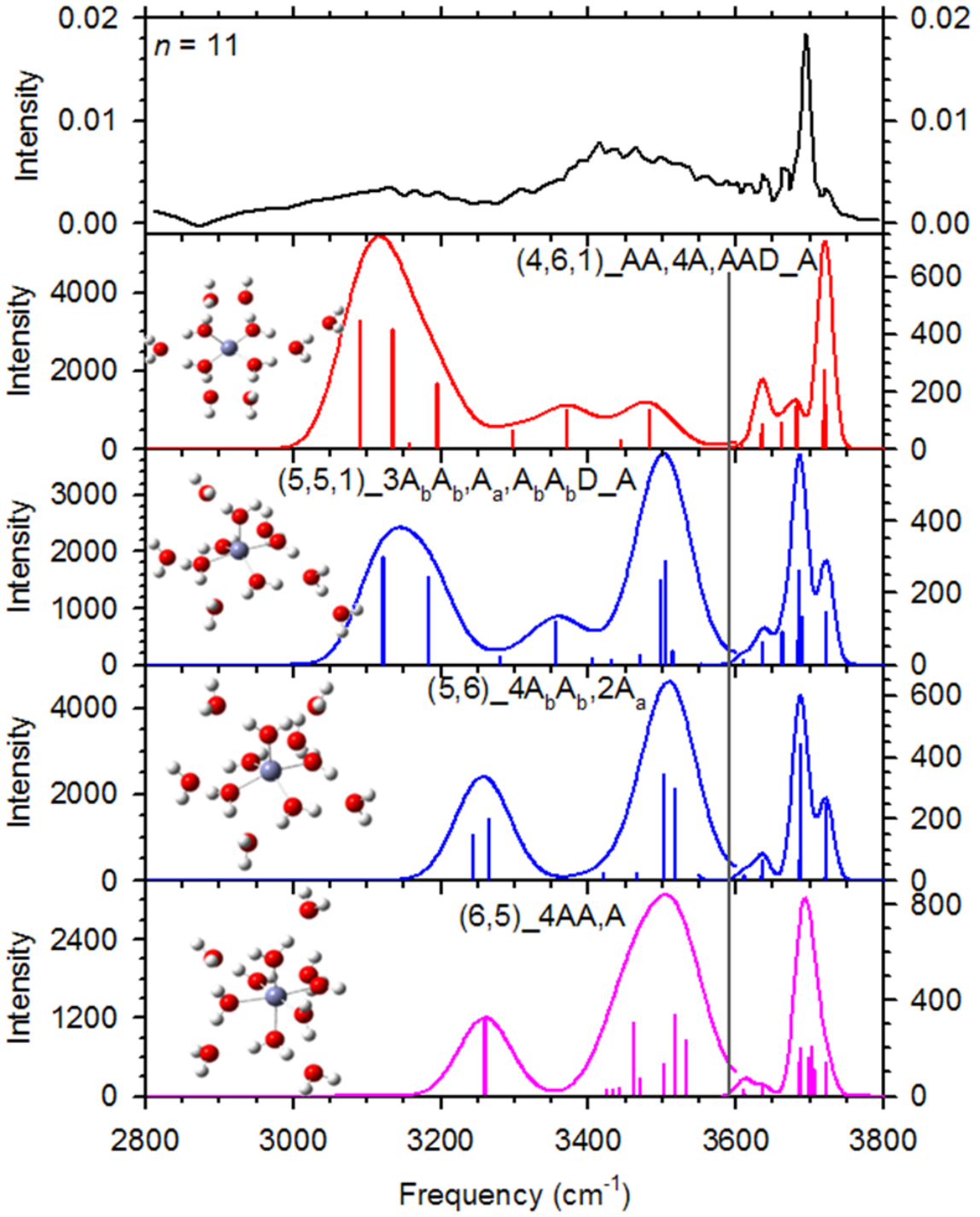

Figure 5.9. Comparison of the experimental IRMPD spectrum for $Zn^{2+}(H_2O)_{11}$ at 215 K with IR spectra for four low-energy conformers predicted at the B3LYP/6-311+G(d,p) level of theory. In the theoretical spectra the bonded-OH region is broadened by 50 cm^{-1} and the free-OH region is broadened by 15 cm^{-1}. The intensities of these regions are on the left and right y-axis, respectively, in km/mol.

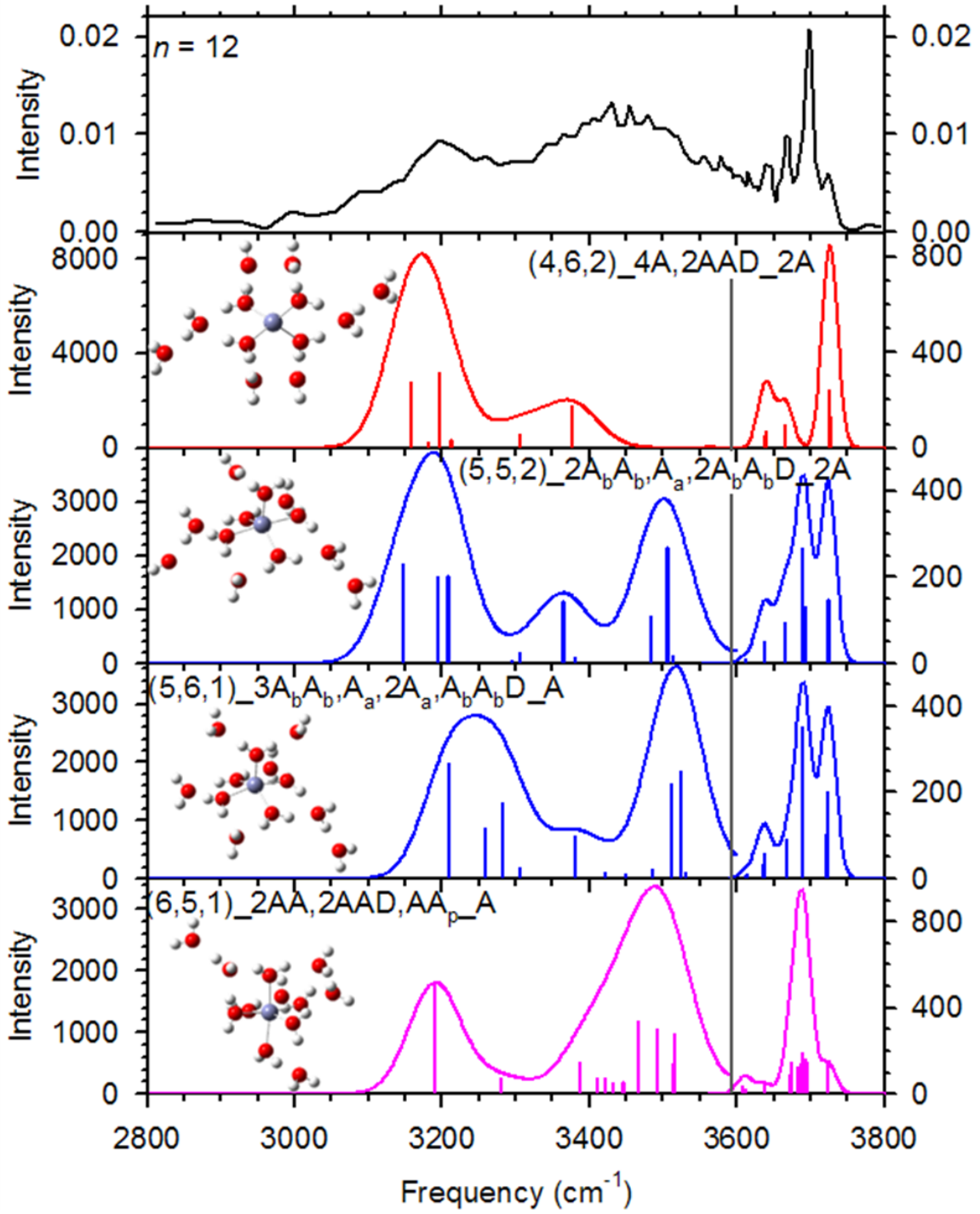

Figure 5.10. Comparison of the experimental IRMPD spectrum for $Zn^{2+}(H_2O)_{12}$ at 215 K with IR spectra for four low-energy conformers predicted at the B3LYP/6-311+G(d,p) level of theory. In the theoretical spectra the bonded-OH region is broadened by 50 cm^{-1} and the free-OH region is broadened by 15 cm^{-1}. The intensities of these regions are on the left and right y-axis, respectively, in km/mol.

the formation of a third solvent shell at these complex sizes and agrees well with the MP2(full) free energy GSs, the (5,5,1) isomer for n = 11 and the (5,5,2) and (5,6,1) isomers for n = 12. It seems likely that both spectra are primarily composed of CN = 5 ions, although some population of CN = 6 cannot be ruled out in either case because of the similarity of the theoretical spectra in this region. Again, the B3LYP GS structures have CN = 4 with predicted contributions from the single acceptor water molecules at ~3730 cm^{-1} that are more intense than the ν_{asym} band of a double acceptor water, in contrast to the IRMPD spectra.

In the bonded-OH region for n = 11 and 12, the band centered ~3400 cm^{-1} continues to increase in intensity as n increases up to 65% of the free-OH ν_{asym} stretch for n = 12, Figures 5.9 and 5.10. The low frequency peak position of the MP2(full) 215 K GS, the (5,5,1) complex, is most consistent with the IRMPD spectrum (~3150 cm^{-1}), whereas these calculated bands for the (5,6) and (6,5) complexes are shifted to the blue by ~100 cm^{-1}. Contributions from these complexes cannot be ruled out because the predicted low frequency band may be obscured by the larger contributions from the (5,5,1) complex or similar structure (although none were found in our explorations). For n = 12, the (5,5,2), (5,6,1), and (6,5,1) complexes match the experiment in bonded-OH peak positions, but the relative intensities between the two peaks agree best with experiment for the (5,6,1) and (6,5,1) complexes. Similar to the n = 10 spectra, the 4-coordinate complexes for both n = 11 and 12 do not match as well as either the 5- or 6-coordinate species because the relative intensities of the low frequency bands are reversed from those observed experimentally.

Overall, it seems that the IRMPD spectra for these larger complexes is dominated by the 5-coordinate species with contributions from the 6-coordinate structures, which cause the red shift of the higher frequency band in the experiment from the predicted spectra of the 5-coordinate complexes. Contributions from multiple structures could also explain the significant broadening in the bonded-OH stretch region.

Comparison to hydrated Cu^{2+} and Ca^{2+}. The ratio of the intensity of the ν_{sym} to ν_{asym} bands of $Zn^{2+}(H_2O)_6$ is 0.67, which is larger compared to that of $Cu^{2+}(H_2O)_6$ (CN = 4, intensity ratio = 0.38), but much smaller than that of $Ca^{2+}(H_2O)_6$ (CN = 6, intensity ratio = 3.94).[18-20] This ratio has been linked to the CN of the ion, with a smaller ratio suggesting the contribution of some second solvent shell formation.[18,20,21,23] This indicates that $Zn^{2+}(H_2O)_6$ has some population with a CN < 6. In addition, the n = 6 spectrum for Zn^{2+} is blue shifted from that of Cu^{2+}, a shift that is not consistent with CN = 4.

Similar to n = 6, the ν_{sym} and ν_{asym} bands of the n = 7 spectrum are blue shifted from that of Cu^{2+} and the intensity ratio between these two peaks is again larger for Zn^{2+}. Both of these observations suggest that Zn^{2+} has a larger CN than Cu^{2+} and are also consistent with the larger ionic radius of Zn^{2+} (0.78 versus 0.72 Å for Zn^{2+} and Cu^{2+}, respectively).[60] The n = 8 and 9 bands also blue shift by 10 – 20 cm^{-1} relative to the ν_{sym} and ν_{asym} stretches of n = 6 and 7, a trend previously correlated with the change in parent ion fragmentation from charge separation to water loss in Cu^{2+}.[20] The free-OH ν_{asym} bands of the n = 8 and 9 complexes of Zn^{2+} match those of Cu^{2+}, whereas the ν_{sym} bands are still slightly blue shifted (~5 – 10 cm^{-1}). This may be indicative of similar hydration

energies at these complex sizes because many water molecules are now in the second solvent shell.

Unlike the $n = 6 – 9$ complexes, there is clear evidence of single acceptor hydrogen bonding near ~3635 and ~3720 cm^{-1} for $n = 11 – 12$, and suggestions of such ligands for $n = 10$. At each of these three complex sizes, the single acceptor peaks are much less intense than those of Cu^{2+}, but more intense than those of Ca^{2+}.[18-20] This observation is in line with the discussion above, i.e., Zn^{2+} appears to have a CN greater than Cu^{2+} but less than Ca^{2+}. This discussion is in agreement with the comparisons above of experimental and theoretical spectra, which demonstrate that the coordination of Zn^{2+} appears to be dominated by CN = 5 for complexes where $n \geq 8$. Spectral comparisons to theory are less conclusive for $n = 6$ and 7, but once these complexes are compared to Cu^{2+} and Ca^{2+}, it seems that the CN of Zn^{2+} is most likely five, agreeing with the trends predicted at the MP2(full) level of theory as well as spectral comparisons of the larger $Zn^{2+}(H_2O)_n$ complexes.

Conclusion

IRMPD action spectroscopy in the region of 2800 – 3800 cm^{-1} and quantum chemical calculations are used to probe the structures of $Zn^{2+}(H_2O)_n$, where $n = 6 – 12$. Additionally, BIRD studies show a decrease in complex stability for $n > 8$ and $n < 8$, where the latter trend is a consequence of the charge separation pathway becoming the energetically favored product compared to loss of a water molecule at $n \leq 7$, similar to results from a previous Cu^{2+} hydration study.[20] These results paired with the quantitative energies determined for reactions 5.1 and 5.2 in Chapters 3 and 4 suggest that the barrier

for reaction 5.2 remains relatively constant while the barrier for reaction 5.1 increases greatly as *n* decreases thereby favoring reaction 5.2 at a given critical size.

Geometry optimizations and vibrational frequency calculations for $Zn^{2+}(H_2O)_n$, where $n = 6 – 12$, were performed at the B3LYP/6-311+G(d,p) level, which has previously been shown to yield results comparable to several other approaches, including those at higher levels of theory (Chapter 3). Single point energies for the comparison of relative energies were performed at B3LYP, B3P86, and MP2(full) levels of theory with a 6-311+G(2d,2p) basis set. On average, the free energy GS structures calculated at 215 K at the DFT levels have a CN = 4, whereas MP2(full) predicts GSs with a CN = 5. Complexes having one more water molecule in the inner shell at each respective level of theory are higher in energy by less than 10 kJ/mol. Theoretical spectra of 4-coordinate complexes, where $n \geq 6$, predict stretches of single acceptor water molecules that are either not present or much less intense than the experiment in both the bonded and free-OH regions. These observations combined with comparisons to Cu^{2+} hydration (CN = 4) largely eliminate the presence of 4-coordinate complexes in the experimental spectra.

The most definitive comparison between the theoretical and experimental spectra for an individual hydrated complex is at $n = 8$ and suggests that the dominant species at this complex size has a CN of five, consistent with the MP2(full) relative energies. Larger complexes also appear to be mostly 5-coordinate, although contributions from 6-coordinate species cannot be ruled out because of the similarity of the theoretical spectra in both regions. No obvious single acceptor spectral features in both spectral regions are found in the experimental spectra of $n = 6 – 9$ but are clearly observed for $n = 11 – 12$. Additionally, features attributed to forming a third solvent shell are found for $n = 11$ and

12. At the MP2(full) level, six coordinate species are about 6 – 10 kJ/mol higher in free energy than the five coordinate complexes for n = 7 – 12, and thereby are predicted to comprise less than 5% of the complexes in a Maxwell Boltzmann distribution at 215 K.

On an individual basis, comparisons of the theoretically predicted spectra to experiment for the n = 6 and 7 complexes are not as conclusive as for the larger hydrated clusters. Comparisons of the relative intensity and position of the free-OH ν_{sym} and ν_{asym} bands with those of Cu^{2+} and Ca^{2+} hydrated complexes suggest that the CN of Zn^{2+} is less than Ca^{2+} (CN = 6) but greater than Cu^{2+} (CN = 4). In the experimental spectrum of n = 6, there is a slight broadening on the blue side of the free-OH ν_{asym}, which could be a consequence of the higher frequency ν_{asym} stretch of the (6,0) species. This is the strongest evidence for a contribution from a 6-coordinate species, where the (6,0) complex is only 2 kJ/mol higher in free energy at 215 K than the (5,1) MP2(full) GS and therefore is predicted to have a population of 25% at 215 K. As for the larger complexes, it appears that the favored n = 6 and 7 complexes are 5-coordinate species, agreeing with comparisons between experiment and theory and also validating the MP2(full) relative energies. Overall, all these comparisons provide evidence that Zn has a CN = 5 with possible contributions from CN = 6.

A key conclusion of this study is that B3LYP and B3P86 relative energies do not appear to be reliable for these hydrated complexes. A hint of this conclusion was found in previous findings from Chapter 3 where the experimental bond dissociation energies for water loss from the n = 6 – 10 complexes were reproduced slightly better (by an average of 2 kJ/mol) by the MP2(full) level of theory than by the B3LYP and B3P86 levels. The M06 functional, which is designed to handle hydrogen bonding better, gave

similar relative energies as MP2, although the absolute hydration energies predicted by M06 are not in as good agreement with experiment as the MP2 results. In this previous chapter, multiple BDEs for $n = 6 – 10$ were reported depending on the level of theory used in the interpretation of the data because this small energetic preference could not definitively determine which level of theory gave the most accurate relative energies. The current study demonstrates that the BDEs obtained in Chapter 3 as interpreted using the predicted lowest-energy structures from the MP2(full)/6-311+G(2d,2p) level are the most reliable.

References

(1) Spiro, T. G. *Zinc enzymes*; J. Wiley: New York, 1983.

(2) Kimura, E. *Pure & Appl. Chem.* **1993**, *65*, 355.

(3) Richens, D. T. *The Chemistry of Aqua Ions*; John Wiley and Sons, Inc: New York, 1997.

(4) Nriagu, J. O. *Zinc in the Environment*; Wiley: New York, 1980.

(5) Peschke, M.; Blades, A. T.; Kebarle, P. *Int. J. Mass Spectrom.* **1999**, *187*, 685.

(6) Peschke, M.; Blades, A. T.; Kebarle, P. *J. Am. Chem. Soc.* **2000**, *122*, 1492.

(7) Peschke, M.; Blades, A. T.; Kebarle, P. *J. Am. Chem. Soc.* **2000**, *122*, 10440.

(8) Shvartsburg, A. A.; Siu, K. W. M. *J. Am. Chem. Soc.* **2001**, *123*, 10071.

(9) Blades, A. T.; Jayaweera, P.; Ikonomou, M. G.; Kebarle, P. *Int. J. Mass Spectrom. Ion Processes* **1990**, *102*, 251.

(10) Rudolph, W. W.; Pye, C. C. *Phys. Chem. Chem. Phys.* **1999**, *1*, 4583.

(11) Chillemi, G.; D'Angelo, P.; Pavel, N. V.; Sanna, N.; Barone, V. *J. Am. Chem. Soc.* **2002**, *124*, 1968.

(12) Wakita, H.; Johansson, G.; Sandstrom, M.; Goggin, P. L.; Hitotshi, O. J. *J. Solution Chem.* **1991**, *20*, 642.

(13) Bock, C. W.; Katz, A. K.; Glusker, J. P. *J. Am. Chem. Soc.* **1994**, *117*, 3754.

(14) Hartmann, M.; Clark, T.; vanEldik, R. *J. Mol. Model.* **1996**, *2*, 354.

(15) Pavlov, M.; Siegbahn, P. E. M.; Sandstrom, M. *J. Phys. Chem. A* **1998**, *102*, 219.

(16) Lee, S.; Kim, J.; Park, J. K.; Kim, K. S. *J. Phys. Chem.* **1996**, *100*, 14329.

(17) Miller, D. J.; Lisy, J. M. *J. Chem. Phys.* **2006**, *124*, 024319.

(18) Bush, M. F.; Saykally, R. J.; Williams, E. R. *ChemPhysChem* **2007**, *8*, 2245.

(19) Bush, M. F.; Saykally, R. J.; Williams, E. R. *J. Am. Chem. Soc.* **2008**, *130*, 15482.

(20) O'Brien, J. T.; Williams, E. R. *J. Phys. Chem. A* **2008**, *112*, 5893.

(21) Bush, M. F.; O'Brien, J. T.; Prell, J. S.; Wu, C. C.; Saylkally, R. J.; Williams, E. R. *J. Am. Chem. Soc.* **2009**, *131*, 13270.

(22) Inokuchi, Y.; Ohshimo, K.; Misaizu, F.; Nishi, N. *J. Phys. Chem. A* **2004**, *108*, 5034.

(23) Walters, R. S.; Pillai, E. D.; Duncan, M. A. *J. Am. Chem. Soc.* **2005**, *127*, 16599.

(24) Yeh, L. I.; Okumura, M.; Myers, J. D.; Prices, J. M.; Lee, Y. T. J. *J. Chem. Phys.* **1989**, *91*, 7319.

(25) Iino, T.; Ohashi, K.; Inoue, K.; Judai, K.; Nishi, N.; Sekiya, H. *Eur. Phys. J. D.* **2007**, *43*, 37.

(26) Shin, J. W.; Hammer, N. I.; Diken, E. G.; Johnson, M. A.; Walters, R. S.; Jaeger, T. D.; Duncan, M. A.; Christie, R. A.; Jordan, K. D. *Science* **2004**, *304*, 1137.

(27) Miyazaki, M.; Fujii, A.; Ebata, T.; Mikami, N. *Science* **2004**, *304*, 1134.

(28) Chang, H. C.; Wu, C. C.; Kuo, J. L. *Int. Rev. Phys. Chem.* **2005**, *24*, 553.

(29) Jiang, J. C.; Wang, Y. S.; Chang, H. C.; Lin, S. H.; Lee, Y. T.; Niedner-Schatteburg, G.; Chang, H. C. *J. Am. Chem. Soc.* **2000**, *122*, 1398.

(30) Wu, C. C.; Lin, C. K.; Chang, H. C.; Jiang, J. C.; Kuo, J. L.; Klein, M. L. *J.Chem. Phys.* **2005**, *122*, 074315.

(31) Bush, M. F.; O'Brien, J. T.; Prell, J. S.; Saykally, R. J.; Williams, E. R. *J. Am. Chem. Soc.* **2007**, *129*, 1612.

(32) Bush, M. F.; Saykally, R. J.; Williams, E. R. *Int. J. Mass Spectrom.* **2006**, *253*, 256.

(33) Wong, R. L.; Paech, K.; Williams, E. R. *Int. J. Mass Spectrom.* **2004**, *232*, 59.

(34) Rodriguez-Cruz, S. E.; Jockusch, R. A.; Williams, E. R. *J. Am. Chem. Soc.* **1998**, *120*, 5842.

(35) Rodriguez-Cruz, S. E.; Jockusch, R. A.; Williams, E. R. *J. Am. Chem. Soc.* **1999**, *121*, 8898.

(36) Rodriguez-Cruz, S. E.; Jockusch, R. A.; Williams, E. R. *J. Am. Chem. Soc.* **1999**, *121*, 1986.

(37) Senko, M. W.; Canterbury, J. D.; Guan, S.; Marshall, A. G. *Rapid Commun. Mass Spectrom.* **1996**, *10*, 1839.

(38) Becke, A. D. *J. Chem. Phys.* **1993**, *98*, 5648.

(39) Lee, C.; Yang, W.; Parr, R. G. *Phys. Rev. B* **1988**, *37*, 785.

(40) Frisch, M. J.; Trucks, G. W.; Schlegel, H. B.; Scuseria, G. E.; Robb, M. A.; Cheeseman, J. R.; Montgomery, J., J. A. ; Vreven, T.; Kudin, K. N.; Burant, J. C.; Millam, J. M.; Iyengar, S. S.; Tomasi, J.; Barone, V.; Mennucci, B.; Cossi, M.; Scalmani, G.; Rega, N.; Petersson, G. A.; Nakatsuji, H.; Hada, M.; Ehara, M.; Toyota, K.; Fukuda, R.; Hasegawa, J.; Ishida, M.; Nakajima, T.; Honda, Y.; Kitao, O.; Nakai, H.; Klene, M.; Li, X.; Knox, J. E.; Hratchian, H. P.; Cross, J. B.; Bakken, V.; Adamo, C.; Jaramillo, J.; Gomperts, R.; Stratmann, R. E.; Yazyev, O.; Austin, A. J.; Cammi, R.; Pomelli, C.; Ochterski, J. W.; Ayala, P. Y.; Morokuma, K.; Voth, G. A.; Salvador, P.; Dannenberg, J. J.; Zakrzewski, V. G.; Dapprich, S.; Daniels, A. D.; Strain, M. C.; Farkas, O.; Malick, D. K.; Rabuck, A. D.; Raghavachari, K.; Foresman, J. B.; Ortiz, J. V.; Cui, Q.; Baboul, A. G.; Clifford, S.; Cioslowski, J.; Stefanov, B. B.; Liu, G.; Liashenko, A.; Piskorz, P.; Komaromi, I.; Martin, R. L.; Fox, D. J.; Keith, T.; Al-Laham, M. A.; Peng, C. Y.; Nanayakkara, A.; Challacombe, M.; Gill, P. M. W.; Johnson, B.; Chen, W.; Wong, M. W.; Gonzalez, C.; Pople, J. A. Gaussian 03, Revision D.01; Gaussian, Inc.: Pittsburgh, PA, 2005.

(41) Kamariotis, A.; Boyarkin, O. V.; Mercier, S. R.; Beck, R. D.; Bush, M. F.; Williams, E. R.; Rizzo, T. R. *J. Am. Chem. Soc.* **2006**, *128*, 905.

(42) NIST Computational Chemistry Comparison and Benchmark Database, NIST Standard Reference Database Number 101 Release 15a, April 2010, Editor: Russell D. Johnson III. http://cccbdb.nist.gov/.

(43) Perdew, J. P. *Phys. Rev. B* **1986**, *33*, 8822.

(44) Moller, C.; Plesset, M. S. *Phys. Rev.* **1934**, *46*, 618.

(45) Bauschlicher Jr., C. W.; Partridge, H. *J. Chem. Phys.* **1995**, *103*, 1788.

(46) Foresman, J. B.; Frisch, A. E. *Exploring Chemistry with Electronic Structure Methods*, 2nd ed.; Gaussian, Inc.: Pittsburgh, PA, 1996.

(47) Price, W. D.; Schnier, P. D.; Jockusch, R. A.; Strittmatter, E. F.; Williams, E. R. *J. Am. Chem. Soc.* **1996**, *118*, 10640.

(48) Price, W. D.; Williams, E. R. *J. Phys. Chem. A* **1997**, *101*, 8844.

(49) Dunbar, R. C.; McMahon, T. B. *Science* **1998**, *279*, 194.

(50) James, A. M.; Lord, M. P. *Macmillan's Chemical and Physical Data*; Macmillan: London, UK, 1992.

(51) Huheey, J. E.; Keiter, E. A.; Keiter, R. L. *Inorganic Chemistry: Principles of Structure and Reactivity* 4th ed.; HarperCollins: New York, USA, 1993.

(52) Shimanouchi, T. *Molecular Vibrational Frequencies*, 69 ed.; NIST Chemistry Webbook, National Institute of Standards and Technology: Gaithersburg, MD, http://webbook.nist.gov, (retrieved July 5, 2010)

(53) O'Brien, J. T.; Prell, J. S.; Berden, G.; Oomens, J.; Williams, E. R. *Int. J. Mass Spectrom.* **2010**, *297*, 116.

(54) Headrick, J. M.; Diken, E. G.; Walters, R. S.; Hammer, N. I.; Christie, R. A.; Cui, J.; Myshakin, E. M.; Duncan, M. A.; Johnson, M. A.; Jordan, K. D. *Science* **2005**, *308*, 1765.

(55) Weinheimer, C. J.; Lisy, J. M. *J. Chem. Phys.* **1996**, *105*, 2938.

(56) Zhao, Y.; Truhlar, D. G. *Theor. Chem. Acc.* **2008**, *120*, 215.

(57) Zhao, Y.; Truhlar, D. G. *Acc. Chem. Res.* **2008**, *41*, 157.

(58) Rodriguez, J. D.; Lisy, J. M. *J. Phys. Chem. A* **2009**, *113*, 6462.

(59) Mizuse, K.; Hamashima, T.; Fujii, A. *J. Phys. Chem. A* **2009**, *113*, 12134.

(60) Wilson, R. G.; Brewer, G. R. *Ion Beams with Applications to Ion Implantation*; Wiley: New York, 1973.

CHAPTER 6

SEQUENTIAL BOND ENERGIES AND BARRIER HEIGHTS FOR THE WATER LOSS AND CHARGE SEPARATION DISSOCIATION PATHWAYS OF $CD^{2+}(H_2O)_N$, $N = 3 - 11$

Abstract

The bond dissociation energies for losing one water from $Cd^{2+}(H_2O)_n$ complexes, $n = 3 - 11$, are measured using threshold collision-induced dissociation (TCID) in a guided ion beam tandem mass spectrometer coupled with a thermal electrospray ionization source. Kinetic energy dependent cross sections are obtained for $n = 4 - 11$ complexes and analyzed to yield 0 K threshold measurements for loss of one, two, and three water ligands after accounting for multiple collisions, kinetic shifts, and energy distributions. The threshold measurements are converted from 0 K to 298 K values to give the hydration enthalpies and free energies for sequentially losing one water from each complex. Theoretical geometry optimizations and single point energy calculations are performed on reactant and product complexes using several levels of theory and basis sets to obtain thermochemistry for comparison to experiment. The charge separation process, $Cd^{2+}(H_2O)_n \rightarrow CdOH^+(H_2O)_m + H^+(H_2O)_{n-m-1}$, is also observed for $n = 4$ and 5

Adapted with permission from Cooper, T. E.; Armentrout, P.B., *Chem. Phys. Lett.* **2010**, *486*, 1. Copyright 2010 Elsevier BV.
Adapted with permission from Cooper, T. E.; Armentrout P. B., *J. Chem. Phys.* **2011**, *134*, 114308. Copyright 2011 American Institute of Physics.

and the competition between this process and water loss is analyzed. Rate-limiting transition states for the charge separation process at $n = 3 – 6$ are calculated and compared to experimental threshold measurements resulting in the conclusion that the critical size for this dissociation pathway of hydrated cadmium is $n_{crit} = 4$.

Introduction

Cadmium is an especially toxic and environmentally hazardous substance, whose anthropogenic emissions have been categorized to be 18 times higher than naturally occurring rates.[1,2] Because cadmium can deactivate important proteins and enzymes, bio-accumulate, and has a biological half-life of 10 – 30 years, the United States environmental protection agency (EPA) has classified cadmium as a priority pollutant. With such a large anthropogenic discharge into the environment, cadmium is quickly breaching valuable aqueous resources around the world, particularly in industrialized countries. An accurate and complete understanding of the thermochemical properties and reaction pathways of $Cd^{2+}(H_2O)_n$ complexes is necessary for the efficient removal of this metal pollutant from these aqueous systems.

The hydration of metal cations, both singly and multiply charged, has been studied extensively in the gas phase over the past two decades.[3-16] Such studies had never included the thermochemistry for hydration of cadmium until our first preliminary letter[17] in which we experimentally examined $Cd^{2+}(H_2O)_n$, $n = 4 – 11$, and discussed previous experimental and theoretical work[18-25] on cadmium coordination behavior. This study focused on the dominant reaction pathway, primary water loss in reaction 6.1.

$$Cd^{2+}(H_2O)_n \rightarrow Cd^{2+}(H_2O)_{n-1} + H_2O \quad (6.1)$$

This is followed by sequential loss of additional water molecules at higher energies. As will be seen below, particular sized complexes also undergo a charge separation process, reaction 6.2.

$$Cd^{2+}(H_2O)_n \rightarrow CdOH^{+}(H_2O)_m + H^{+}(H_2O)_{n-m-1} \quad (6.2)$$

The latter reaction is observed as a primary dissociation channel only for complexes of n = 4 and 5. In the present chapter, we examine the competition between reactions 6.1 and 6.2 in detail, thereby providing further thermodynamic information for both channels.

Similar to the hydration of $Zn^{2+}(H_2O)_n$ examined in Chapter 3 and elsewhere,[7,26-31] the ground state (GS) structures and coordination number (CN) for hydrated Cd^{2+} are highly dependent on the level of theory used. Our preliminary results on $Cd^{2+}(H_2O)_n$ explored the experimental dissociation pathways as predicted by MP2(full)/SD/6-311+G(2d,2p)//B3LYP/SD/6-311+G(d,p) (with the Stuttgart-Dresden (SD) effective core potential and basis set for Cd)[32] calculations of the low-energy structures and found excellent agreement between experimental and theoretical bond energies for water loss. These results indicate CN = 6, whereas B3LYP/SD/6-311+G(2d,2p)//B3LYP/SD/6-311+G(d,p) low-energy structures of $Cd^{2+}(H_2O)_n$ have a smaller primary hydration shell (CN = 4 or 5, depending on complex size). As shown previously in Chapters 3 and 4, our experimental thermochemistry can rely on the specific isomer considered, specifically how many inner shell versus outer shell water ligands are present in the reactants and products. In order to obtain a complete understanding of the Zn^{2+} hydration energies, we

reported multiple bond dissociation energies (BDEs) for $Zn^{2+}(H_2O)_n$, where $n = 6 – 10$, based on differing low-energy structures predicted at MP2(full) and B3LYP levels. Results from this previous study combined with results from Chapter 5, which investigated the infrared multiple photon dissociation (IRMPD) spectroscopy investigation on $Zn^{2+}(H_2O)_n$, where $n = 6 – 12$, support the GS structures predicted at the MP2(full) level over those predicted at the B3LYP and B3P86 levels. Consequently, in the present Chapter, the thermochemical properties of $Cd^{2+}(H_2O)_n$, $n = 3 – 11$, are based on the GS structures predicted at the MP2(full) level using two different basis sets.

Compared to our previous report,[17] we have recalculated the $Cd^{2+}(H_2O)_n$ structures at the B3LYP/SD/6-311+G(d,p) level to ensure that they are fully converged after the frequency calculation. We also perform additional optimization and single point energy calculations using a size-consistent basis set for all atoms (Def2TZVP and Def2TZVPP).[33] Ultimately, the analysis performed in the present study finds the threshold energies reported earlier for reaction 6.1 remain essentially the same, but now includes additional themochemical results and discussions of the cross sections and competition between reactions 6.1 and 6.2. Additionally, the new theoretical results are compared with the corresponding primary thresholds for reaction 6.1.

Experimental and Theoretical Section

Experimental procedures. The experimental methods used to form the $Cd^{2+}(H_2O)_n$ complexes and obtain the kinetic energy dependent cross sections for the collision-induced dissociation are described in detail in Chapter 2. Briefly, the complexes are formed at room temperature in an electrospray ionization (ESI) source coupled with an ion funnel and radio frequency (rf) hexapole ion guide. An in-source

fragmentation technique, utilizing electrodes in the hexapole region of our source,[34] was used to increase the amount of the $n = 4 – 6$ complexes produced by our ESI source. Increasing the voltage on the electrodes enhances the intensity of smaller metal hydrate complexes as described previously for $Ca^{2+}(H_2O)_n$ complexes;[34] however, for $Cd^{2+}(H_2O)_n$ complexes, increasing the electrode voltage past the intensity peak for the $n = 4$ complex generates only charge separation products with no hydrated complexes smaller than $n = 4$ being observed. After mass selection, complexes are collided at varying pressures of Xe (typically about 0.05, 0.10, and 0.20 mTorr) and intensities of the reactant and product ions are measured. Product and reactant ion intensities as a function of the ion kinetic energy in the lab frame are converted to absolute cross sections as a function of relative energy and are extrapolated to zero pressure to ensure single collision conditions, as outlined elsewhere.[35-37]

Quantum chemical calculations. Calculations were performed using the *Gaussian03* package,[38] using structures found in Chapter 3 for $Zn^{2+}(H_2O)_n$ complexes as starting geometries for the $Cd^{2+}(H_2O)_n$ complexes. Geometry optimizations were performed at the B3LYP[39,40] level of theory with a 6-311+G(d,p) basis set on the waters and the Stuttgart-Dresden (SD) ECP and basis set on Cd^{2+}. Geometry optimizations were also performed at the B3LYP/Def2TZVP level, where the Def2TZVP basis set includes triple zeta + polarization functions and the SD ECP. Both basis sets and ECPs were obtained from the EMSL basis set exchange[41] and have a small effective core of 28 electrons for Cd.[32] Vibrational frequencies and rotational constants were also calculated at both levels of theory. The calculations have been performed to ensure that each structure is fully converged after the frequency calculation.

As described in Chapter 2, the transition state (TS) for reaction 6.2 is tight such that there must be an associated Coulomb barrier along the reactant coordinate for this dissociation channel. These tight TSs of the charge separation processes were obtained using TS optimization calculations at the B3LYP/Def2TZVP level and were found to have one imaginary frequency. Calculations of the TS for reaction 6.2 using the SD/6-311+G(d,p) basis set failed, yielding more than one negative frequency or unreasonable structures. The benefit of the Def2TZVP (as well as Def2TZVPP) basis sets is that they are balanced basis sets for all atoms, which could be the reason the SD/6-311+G(d,p) basis set failed for these tight TS calculations. The rate limiting TSs of reaction 6.2 are labeled according to the products formed, i.e., TS[m + (n-m-1)]. All other structures were found to be vibrationally stable using either basis set. Frequencies were scaled by 0.989[42] before being used in the RRKM threshold analysis described in Chapter 2 and in the calculation of the zero point energy (ZPE) and thermal corrections. The optimized parameters of the water loss pathways modeled were not dependent on whether the frequencies used in the modeling were calculated with the Def2TZVP or SD/6-311+G(d,p) basis set. Single point energies (SPEs) were calculated at the B3LYP, B3P86,[43] and MP2(full)[44] levels of theory using the SD/6-311+G(2d,2p) and Def2TZVPP basis sets. Basis set superposition error (BSSE) corrections were calculated for reaction 6.1 in the full counterpoise (cp) limit.[45,46]

Results and Discussion

CID cross sections. Experimental cross sections for collision-induced dissociation with Xe were acquired for $Cd^{2+}(H_2O)_n$, n = 4 – 11, Figure 6.1. In all cases the loss of a single water molecule, reaction 6.1, is the dominant process, followed by

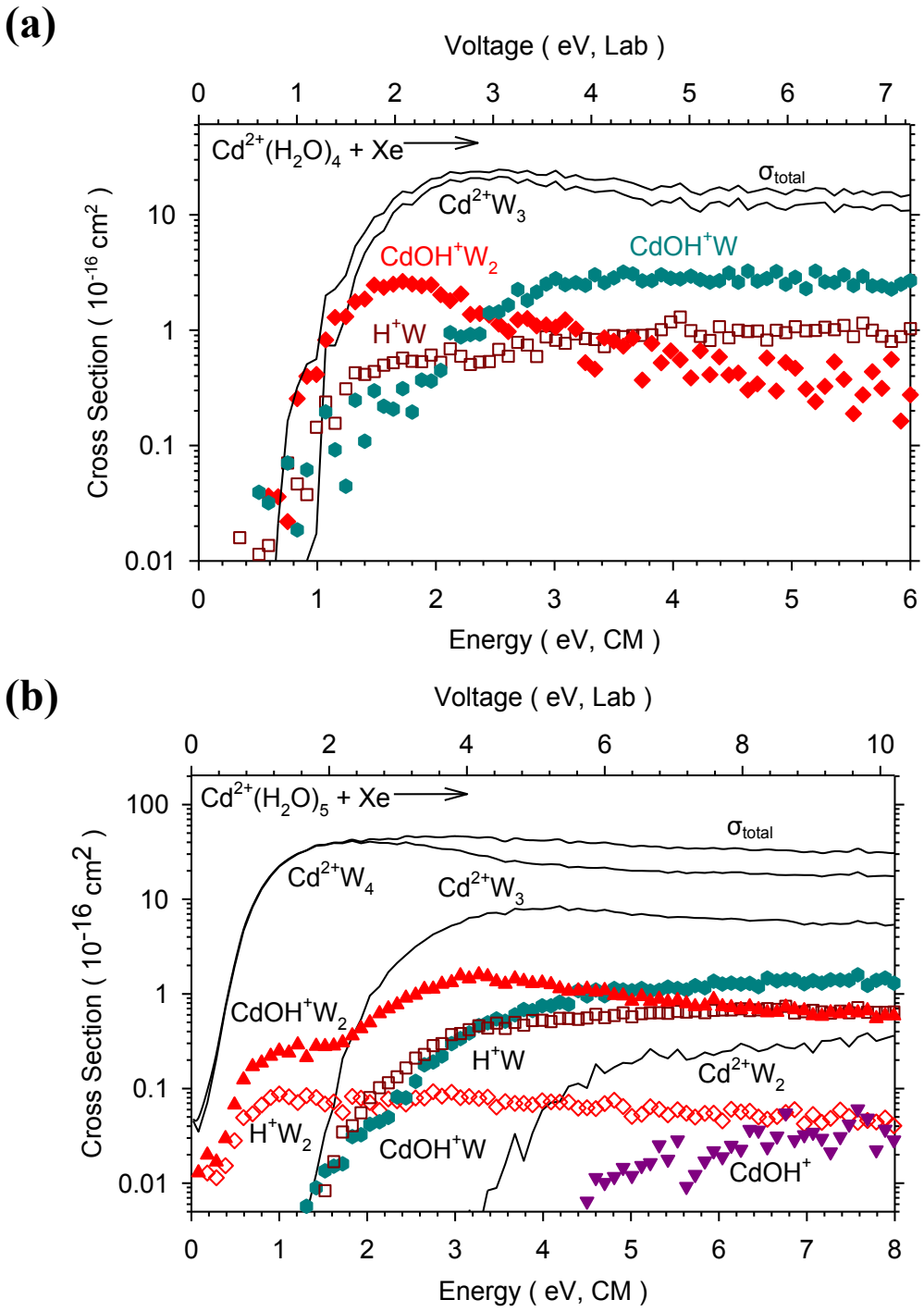

Figure 6.1. CID cross sections for the sequential water loss (lines in parts a – c and open symbols in parts d – h) and charge separation processes (symbols in parts a – c and solid symbols in parts d – h) for $Cd^{2+}W_n$, where n = 4 – 11 and W = H_2O colliding with Xe at 0.2 mTorr as a function of energy in the laboratory (upper x-axis) and center-of-mass (lower x-axis) frames.

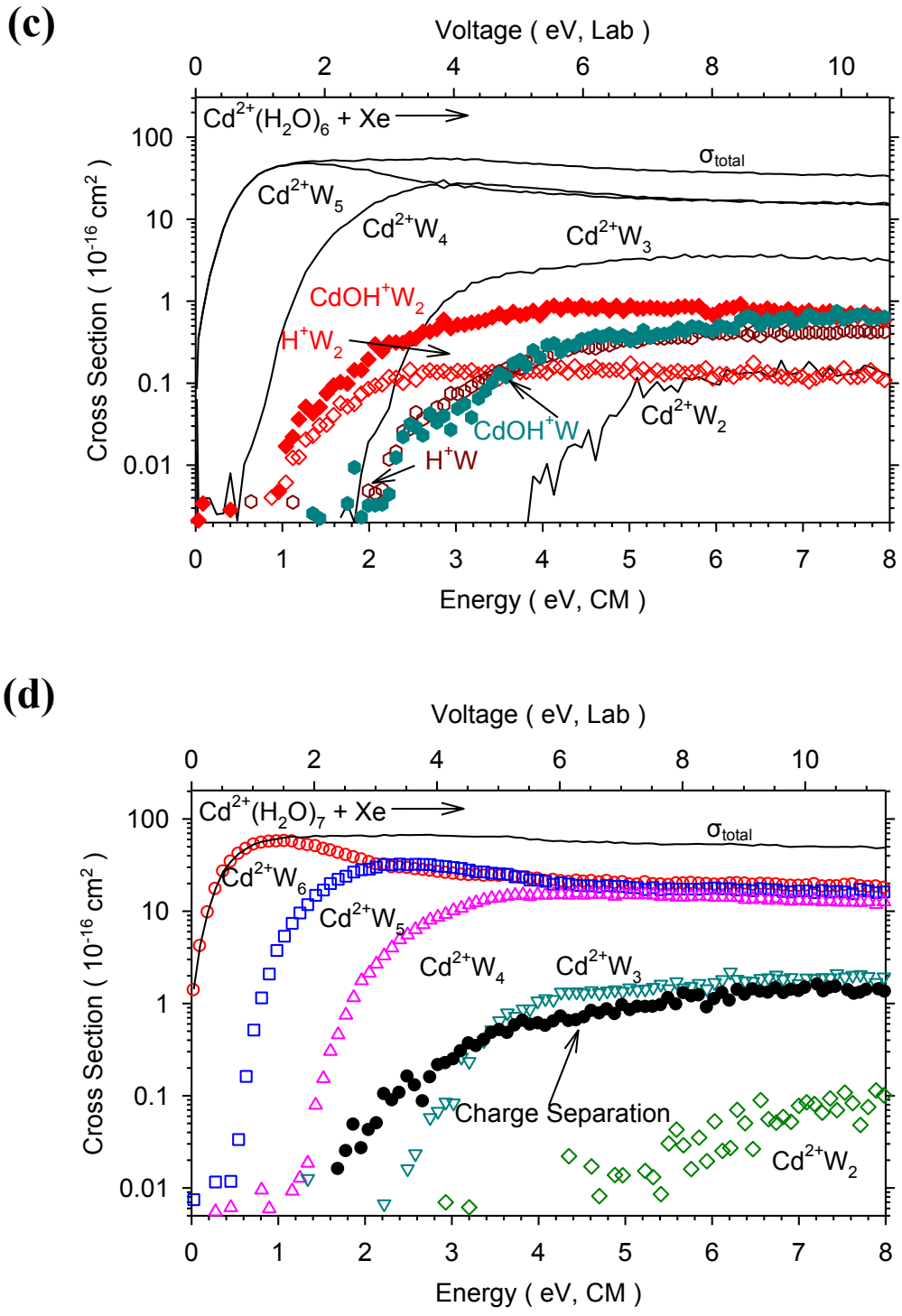

Figure 6.1. continued

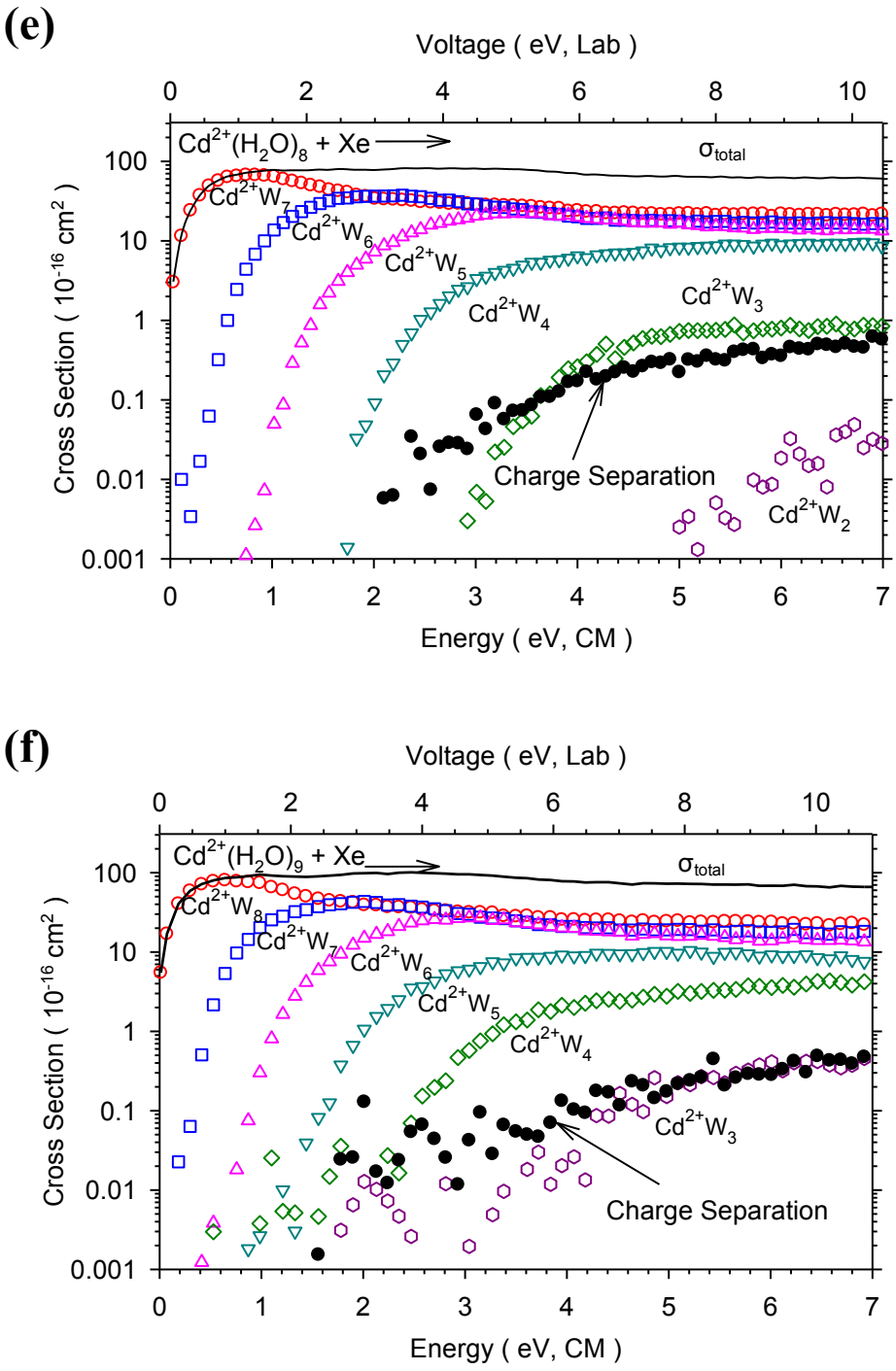

Figure 6.1. continued

(g)

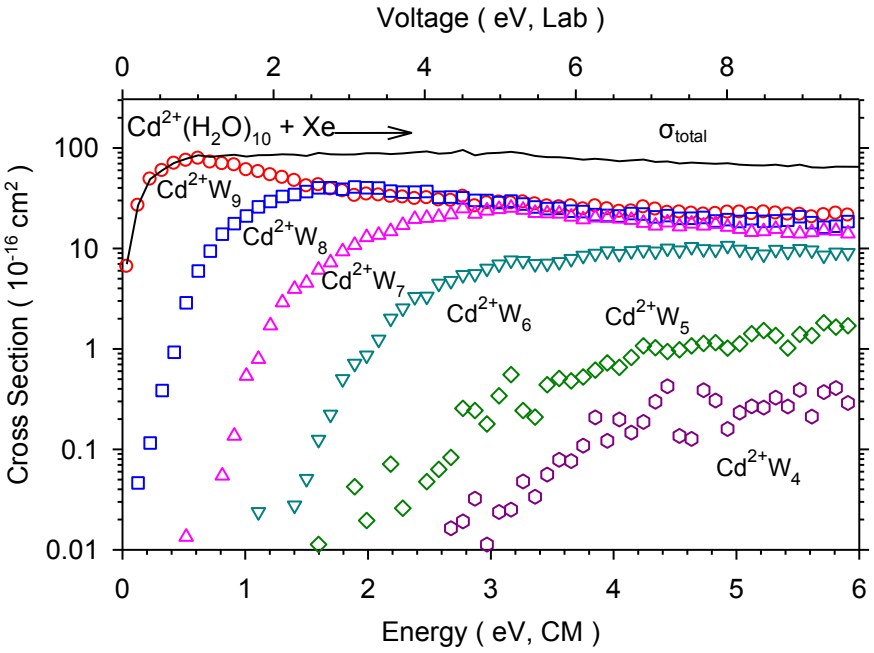

(h)

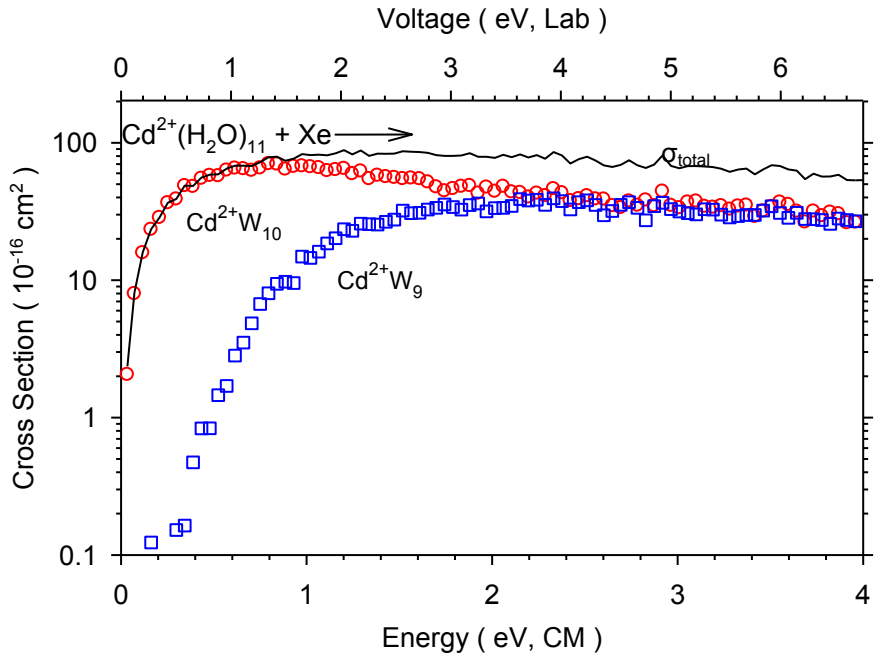

Figure 6.1. continued

loss of additional water molecules as the translational energy increases. The individual products for reactions 6.1 and 6.2 are shown in Figures 6.1a – c, the cases where reaction 6.2 complicates the dissociation of $Cd^{2+}(H_2O)_5$, $Cd^{2+}(H_2O)_4$, and possibly $Cd^{2+}(H_2O)_3$. The total cross section of all charge separation products is shown in Figures 6.1d – f, because in these three systems, these products do not compete with the two lowest energy water loss channels. Only the sequential water loss products from the dissociation of $Cd^{2+}(H_2O)_{10}$ and $Cd^{2+}(H_2O)_{11}$ are shown in Figures 6.1g and h, respectively. At these larger complex sizes, the charge separation products were not observed because the reactant ion intensity is small as is the extent of fragmentation to yield charge separation products.

n = 4. The $Cd^{2+}(H_2O)_4$ reactant dissociates via both reactions 6.1 and 6.2, Figure 6.1a. The lowest energy charge separation process observed corresponds to reaction 6.3,

$$Cd^{2+}(H_2O)_4 + Xe \rightarrow CdOH^{+}(H_2O)_2 + H^{+}(H_2O) + Xe \qquad (6.3)$$

which has a lower apparent threshold than that for formation of $Cd^{2+}(H_2O)_3$ in reaction 6.1. This observation along with the quantitative thresholds presented below show that reaction 6.3 is thermodynamically favored over reaction 6.1. Because of this, our thermal ESI source is limited to producing reactant ions of $n \geq 4$, as discussed in detail previously for the hydrated Zn^{2+} system in Chapters 3 and 4. Despite being energetically favored, the magnitude of the cross section for charge separation is smaller compared to that for water loss above about 1.3 eV, clearly indicating that charge separation is an entropically disfavored reaction. Although the loss of H_2O is energetically more costly than reaction 6.3, the relative threshold difference between the two dissociation pathways is small and

reaction 6.1 is entropically favored thereby allowing the observation of $Cd^{2+}(H_2O)_3$ and $Cd^{2+}(H_2O)_2$ complexes at high collision energies in our CID experiments (Figures 6.1b – f).

The magnitudes of the cross sections for $CdOH^+(H_2O)_2$ and $H^+(H_2O)$ formed in reaction 6.3 should be identical, but that for the protonated water cluster is smaller than that of its hydrated cadmium hydroxide cation partner. Similar observations are made in all systems examined here, Figures 6.1a – c, and in Chapter 4 for zinc dication hydrates. This difference is a result of the lower collection efficiency of the lighter product ion. Because the products of the charge separation process pass over a large Coulomb barrier, there is considerable kinetic energy release in the product channel. In particular, the lighter product ion can have large kinetic energies that can exceed the center of mass velocity, meaning that a portion of these ions can travel backwards in the laboratory frame and are lost at the entrance to the octopole ion guide under the focusing conditions usually used. Focusing conditions in which such backward scattered products are reflected at the entrance and therefore collected at the detector can be used and demonstrate that the protonated water cross sections increase to match those of the hydrated metal hydroxide cation. Under such conditions, the cross sections of all heavy ion products (i.e., the singly charged hydrated metal hydroxide and the doubly charged hydrated metal) are unaffected. However, these focusing conditions greatly lower the overall reactant ion intensity leading to an increase in the total experimental collection time and reduced signal to noise. Therefore, the data shown are collected under standard focusing conditions with the understanding that the hydrated metal hydroxide cation

cross section is the more accurate determination of the absolute cross section for the charge separation processes.

The $CdOH^+(H_2O)_2$ product cross section decreases above 1.8 eV, indicating that it must be dissociating, as also indicated by the observance of $CdOH^+(H_2O)$. The onset in the $CdOH^+(H_2O)$ product cross section exhibits a pressure effect, such that the low energy feature below 1.8 eV disappears upon extrapolation to zero pressure, Figure 6.1a. Above about 2.4 eV in Figure 6.1a, there is a 40% increase in the $H^+(H_2O)$ product cross section, observed more easily on a linear y-axis scale, that is mirrored in the sum of the cadmium hydroxide product cross sections. This increase is believed to correspond to reaction 6.4.

$$Cd^{2+}(H_2O)_3 + Xe \rightarrow CdOH^+(H_2O) + H^+(H_2O) + Xe \qquad (6.4)$$

This reaction is plausible because the charge separation process should be energetically favored over the loss of a water ligand for all complexes smaller than $n = 4$, a trend discussed in Chapter 4 for the related zinc system. Therefore, the $CdOH^+(H_2O)$ product cross section can have contributions from both reaction 6.4 and water ligand loss from the $CdOH^+(H_2O)_2$ product, while $H^+(H_2O)$ is formed in both reactions 6.3 and 6.4. These trends and pathways are discussed further below in the context of the available thermochemistry.

Although the relative magnitudes of the product cross sections shown in Figure 6.1a provide good qualitative information, the absolute magnitudes of these products may be inaccurate because the $^{114}Cd^{2+}(H_2O)_4$ reactant has the same mass as $K^+(H_2O)_3$, a common contaminant in these solutions. This is also the reason why no $Cd^{2+}(H_2O)_2$

product is shown in Figure 6.1a, as this product has the same mass as a $K^+(H_2O)_2$ product. Utilization of other isotopes of Cd^{2+} were equally problematic because the other main isotopes of Cd have mass overlaps with other common contaminant ions found in our instrument: $Ca^{2+}(H_2O)_8$ and $H^+(H_2O)_5$. Studies using different metals hydrated with D_2O have been attempted, but the intensities of pure $M^{2+}(D_2O)_n$ complexes formed in our source are not sufficient to conduct TCID experiments. It should be noted that this contamination problem does not affect the thermochemical and threshold information derived from the primary water loss or charge separation products of the dissociation of $n = 4$. It only affects the absolute values of the cross sections and therefore the $\sigma_{0,j}$ values (described in Chapter 2) used in the modeling. No other $Cd^{2+}(H_2O)_n$ complexes had similar difficulties.

n = 5. In the dissociation of $Cd^{2+}(H_2O)_5$, products are observed for reactions 6.1 and 6.5, Figure 6.1b.

$$Cd^{2+}(H_2O)_5 + Xe \rightarrow CdOH^+(H_2O)_2 + H^+(H_2O)_2 + Xe \qquad (6.5)$$

Both products formed in reaction 6.5 have a higher apparent threshold than the water loss product from reaction 6.1 indicating that reaction 6.1 is energetically favored over reaction 6.5. Products of reaction 6.5 have a much smaller cross section than the $Cd^{2+}(H_2O)_4$ product (by over two orders of magnitude) because reaction 6.5 is both thermodynamically and entropically disfavored over reaction 6.1. Reaction 6.3 is also observed in the sequential dissociation of $Cd^{2+}(H_2O)_5$, as evidenced by the increase in magnitude of the $CdOH^+(H_2O)_2$ cross section above ~1.4 eV. Further, this second feature is not observed in the $H^+(H_2O)_2$ product cross section, but does match the appearance of

the $H^+(H_2O)$ product associated with reaction 6.3. As in Figure 6.1a, the threshold for reaction 6.3 (as exhibited by both the second feature of $CdOH^+(H_2O)_2$ and the onset of $H^+(H_2O)$) appears close to but slightly below that for formation of $Cd^{2+}(H_2O)_3$. Examination of the $CdOH^+(H_2O)$ cross section also shows two features, both of which start at ~1 eV above the more obvious onsets in the $CdOH^+(H_2O)_2$ cross section. In both cases, the $CdOH^+(H_2O)$ product is probably formed by water loss from the $CdOH^+(H_2O)_2$ product formed in reactions 6.3 and 6.5, but could also have contributions from reaction 6.4 at higher energies, as discussed in further detail below.

n = 6. The dominant reaction observed in the dissociation of $Cd^{2+}(H_2O)_6$ is loss of a single water molecule, followed by the sequential loss of additional water molecules as the collision energy increases down to $n_{min} = 2$. For $n = 6$, no additional charge separation products were observed other than those already discussed for the smaller complexes, Figure 6.1c. Thus reaction 6.2 is higher in energy than both reaction 6.1 and the sequential loss of another water ligand to form $Cd^{2+}(H_2O)_4$, consistent with the discussions above and Figure 6.1b. Above about 2 eV, the $CdOH^+(H_2O)_2$ product continues to increase in magnitude while the $H^+(H_2O)_2$ product cross section levels and then begins to gradually decrease above 3 eV, most likely corresponding to a water loss dissociation. As in Figure 6.1b, the additional increase in the $CdOH^+(H_2O)_2$ product cross section matches the appearance of the $H^+(H_2O)$ product indicating the onset of reaction 6.3. Unlike Figures 6.1a and 6.1b, the products of reaction 6.3 appear to have a higher apparent threshold than that for the formation of $Cd^{2+}(H_2O)_3$, but because these ion intensities are now all much smaller, this is simply an issue of sensitivity. As in Figure 6.1b, the $CdOH^+(H_2O)$ cross section exhibits two features that probably

correspond to water loss dissociation from the $CdOH^+(H_2O)_2$ products formed in reactions 6.3 and 6.5 with possible contributions from reaction 6.4.

n = 7 – 11. In all cases, the dominant reactions are the loss of a single water molecule, reaction 6.1, followed by loss of additional water molecules as the collision energy increases, Figures 6.1d – h. For these five systems, the charge separation reactions observed do not complicate the dissociation of the first two water ligands. The $Cd^{2+}(H_2O)_{11}$ reactant was observed with very small intensity such that data for loss of only the first two water ligands was collected, Figure 6.1h, although loss of three waters was observed experimentally.

As mentioned above, the smallest cadmium water complex observed is $Cd^{2+}(H_2O)_2$, Figures 6.1b – 6.1e. $Cd^{2+}(H_2O)_3$ and $Cd^{2+}(H_2O)_2$ product cross sections are considerably smaller than that of the $Cd^{2+}(H_2O)_4$ product by factors of about 2 and 60 at elevated collision energies in Figure 6.1b (and even larger factors for larger parent complexes). In addition, the energy gaps between the onsets of $Cd^{2+}(H_2O)_4$, $Cd^{2+}(H_2O)_3$, and $Cd^{2+}(H_2O)_2$ are considerably larger than between any other pair of sequential products. These observations parallel those found in our hydration studies of Zn^{2+} (n_{min} = 3) but are distinct from those found for Ca^{2+} and Sr^{2+} (n_{min} = 0).[47,48] For all four metal dications, the general trends are explained by gradually increasing hydration energies as *n* decreases, and this explanation is sufficient for Ca^{2+} and Sr^{2+}. For both Zn^{2+} and Cd^{2+}, another possible contribution comes from the enhanced stability given by the $18e^-$ rule, as fulfilled for their *n* = 4 complexes, and discussed further below. Another contributing factor to the substantial decrease in the magnitude of the $Cd^{2+}(H_2O)_2$ cross section comes from the energetic preference for the charge separation reaction 6.4 versus reaction 6.1

for the dissociation of $n = 3$. At high energies, the $CdOH^+(H_2O) + H_3O^+$ product channel has a larger magnitude than the entropically favored $Cd^{2+}(H_2O)_2 + H_2O$ product channel, in contrast to observations for reactions 6.3 and 6.5 versus reaction 6.1 for $n = 4$ and 5, respectively. The relative energetics are discussed more quantitatively below. Of course, such minimum sizes have been reported previously for $Cd^{2+}(H_2O)_n$ as $n_{min} = 1$[9] and ≤ 7;[10] however, such comparisons are not very useful as the minimum size observed is very dependent on instrumental sensitivity, source conditions, and collision conditions.

Theoretical geometries: $Cd^{2+}(H_2O)_n$. In the 0 K GS geometries for $n = 1 – 6$, all water ligands bind directly to the cadmium ion, in agreement with previous works,[24,25] and are comparable to structures reported for $Zn^{2+}(H_2O)_n$ in Chapter 3 and $Ca^{2+}(H_2O)_n$.[48] Not surprisingly, the cadmium complexes have longer metal oxide bond distances than their zinc analogues by 0.20 – 0.23 Å because the cadmium ion radius is larger by 0.21 Å (0.99 Å for Cd^{2+} versus 0.78 Å for Zn^{2+}), but have shorter metal oxide bonds than the analogous calcium complexes by 0.08 – 0.18 Å because of the larger ion radius of Ca^{2+} (1.05 Å).[49] The $Cd^{2+}(H_2O)_n$, where $n = 1 – 6$, complexes have C_{2v}, D_{2d}, D_3, S_4, C_{2v}, and T_h symmetries, respectively. As also found previously,[25] the $Cd^{2+}(H_2O)_3$ complex is slightly more symmetric than $Zn^{2+}(H_2O)_3$, which only has C_2 symmetry.

As water molecules bind in the second or third solvent shells, our (x,y,z) nomenclature describes the different conformations of $Cd^{2+}(H_2O)_x(H_2O)_y(H_2O)_z$, where x, y, and z are the number of water molecules in the first, second, and third shells, respectively. When needed, this designation is augmented by the hydrogen bonding motif of the isomer, where a second shell water molecule that hydrogen bonds to two different inner shell water molecules is a double acceptor (AA), whereas a second shell

water molecule that forms only one hydrogen bond to the inner shell is a single acceptor (A). An inner shell water molecule that donates either one or two hydrogen bonds is designated as a single or double donor (D or DD, respectively). Water molecules in the second shell that hydrogen bond to water molecules in the third shell are a combination of both an acceptor and donor water molecule and are named accordingly.

A number of additional higher energy isomers were also calculated for all inner shell sizes of the $n = 5 - 11$ complexes. Because of the large number of high and low-energy isomers investigated using the two different basis sets, only the low-energy complexes for each level of theory are discussed here. Relative 0 K enthalpies and 298 K free energies for the low-energy isomers of different inner shell sizes are presented in Table 6.1 for results calculated using both the SD/6-311+G(2d,2p) and Def2TZVPP basis sets at the B3LYP and MP2(full) levels. Similar calculations using the B3P86 level of theory were also performed, yielding results close to those of the B3LYP level and therefore are not presented here. In general, trends in the relative energetics for both basis sets are in agreement with each other, although specific complexes where results disagree are discussed below.

For $n = 6$, the 0 K GS is the (6,0) structure at each level of theory and at 298 K for MP2(full) and B3LYP/Def2TZVPP calculations; whereas, B3LYP/SD/6-311+G(2d,2p) calculations find that the (6,0) complex is within 1 kJ/mol of a (5,1)_A_a GS complex (where the A_a designation indicates that the sixth water is singly hydrogen bound to the apex water in a square pyramid inner shell). The (5,1)_A_bA_b complex is also low in energy at the DFT levels, where the second shell water forms two hydrogen bonds with the base of the square pyramidal inner shell, as designated by the A_b nomenclature.

Table 6.1. Relative calculated enthalpies (ΔH_0) and Free Energies (ΔG_{298})[a] in kJ/mol of $Cd^{2+}(H_2O)_n$.

		SD/6-311+G(2d,2p)		Def2TZVPP	
n	Complex name	B3LYP[b]	MP2(full)[b]	B3LYP[c]	MP2(full)[c]
5	(5,0)	0.0 (0.0)	0.0 (0.0)	0.0 (0.0)	0.0 (0.0)
	(4,1)_A	11.1 (4.8)	26.2 (20.0)	9.9 (4.9)	18.6 (13.6)
6	(6,0)	0.0 (1.4)	0.0 (0.0)	0.0 (0.0)	0.0 (0.0)
	(5,1)_A_bA_b	3.7 (1.0)	17.1 (13.1)	3.0 (0.6)	11.0 (8.6)
	(5,1)_A_a	10.7 (0.0)	26.8 (14.7)	10.0 (0.6)	19.5 (10.1)
	(4,2)_2AA	9.8 (15.8)	35.0 (39.6)	8.1 (13.7)	22.8 (28.4)
7	(6,1)_AA	4.8 (1.0)	0.0 (0.0)	7.1 (2.8)	0.0 (0.0)
	(5,2)_2A_bA_b	0.0 (1.6)	8.4 (13.8)	0.0 (0.9)	0.7 (5.9)
	(5,2)_A_bA_b,A_a	7.1 (0.0)	18.4 (15.1)	7.5 (0.0)	9.9 (6.8)
	(4,3)_4D_AA,2A	15.5 (3.6)	41.7 (33.6)	14.8 (3.1)	26.5 (19.2)
	(7,0)	39.8 (31.8)	22.4 (18.2)	42.9 (35.5)	26.3 (23.3)
8	(6,2)_4D_2AA	2.9 (1.2)	0.0 (0.0)	5.6 (5.0)	0.0 (3.1)
	(6,2)_2D,DD_2AA	3.8 (4.0)	0.9 (2.7)	10.1 (1.5)	4.9 (0.0)
	(5,3)_2A_bA_b,A_aA_b	0.0 (2.2)	11.8 (15.6)	0.0 (0.4)	3.3 (7.5)
	(5,3)_3A_bA_b	2.3 (2.2)	13.7 (15.3)	2.4 (0.0)	5.3 (6.7)
	(5,3)_2A_bA_b,A_b	5.7 (0.0)	19.8 (15.7)	6.3 (0.2)	11.6 (9.3)
	(4,4)_2AA,2A	15.4 (9.4)	43.6 (39.3)	14.2 (6.1)	27.6 (23.2)
9	(6,3)_6D_3AA	0.0 (4.5)	0.0 (4.0)	0.0 (8.9)	0.0 (4.8)
	(6,3)_4D,DD_3AA	2.8 (1.0)	2.4 (0.0)	2.9 (4.4)	2.6 (0.0)
	(5,4)_3A_bA_b,A_a	7.3 (0.2)	23.5 (15.8)	6.1 (3.3)	16.5 (9.6)
	(4,5)_AA,4A	25.0 (0.0)	61.1 (35.6)	22.0 (0.0)	44.7 (18.7)
10	(6,4)_4AA	0.0 (5.6)	0.0 (0.3)	0.0 (4.8)	0.0 (0.0)
	(6,4)_3AA,A	3.0 (4.2)	4.1 (0.0)	3.7 (7.1)	3.9 (2.5)

Table 6.1. continued

		SD/6-311+G(2d,2p)		Def2TZVPP	
n	Complex name	B3LYP[b]	MP2(full)[b]	B3LYP[c]	MP2(full)[c]
	(6,4)_2AA,AAD,A_1A_2	4.5 (12.5)	2.8 (5.5)	5.5 (15.4)	3.9 (8.9)
	(5,5)_4A_bA_b,A_a	0.8 (0.0)	17.3 (11.2)	0.0 (0.0)	9.5 (4.6)
	(4,6)_2AA,4A	17.1 (7.6)	51.2 (36.4)	14.0 (1.8)	35.3 (18.3)
11	(6,5)_3AA,AAD,A_1A_2	0.0 (13.3)	0.0 (6.5)	0.5 (16.8)	0.0 (6.4)
	(6,5)_4AA,A	3.5 (5.5)	4.8 (0.0)	3.5 (9.1)	4.4 (0.0)
	(5,5,1)_3A_bA_b,A_a,A_bA_bD_A	2.2 (0.0)	23.0 (16.7)	0.0 (0.0)[d]	12.9 (3.1)[d]
	(7,4)_4AA	28.9 (40.3)	19.9 (24.4)	30.9 (44.9)	23.1 (27.2)

[a] ΔG_{298} values given in parenthesis. [b] Single point energies calculated at each respective level shown using a SD/6-311+G(2d,2p) basis set with geometries calculated at B3LYP/SD/6-311+G(d,p). ZPE correction included. [c] Single point energies calculated at each respective level shown using a Def2TZVPP basis set with geometries calculated at B3LYP/Def2TZVP. ZPE correction included. [d] Structure never converged in the geometry optimization calcall step.

(5,2)_2A_bA_b (the DFT GS at 0 K), and (5,2)_A_bA_b,A_a (the DFT GS at 298 K). This latter structure has one A water molecule forming a single hydrogen bond to the inner shell thereby making a weaker bond compared to an AA water, but such an arrangement is entropically favored over the (5,2)_2A_bA_b because of the near free rotation allowed for the A water.

In the work of Pye et al.[25] a slightly different (6,1)_AA complex was reported as the GS, having C_2 symmetry (such that there are fewer hydrogen bonds between water molecules in the inner shell), which we find to be higher in energy by 3 kJ/mol at 0 K, after including ZPE correction, (3 kJ/mol for $\Delta\Delta G_{298}$, after thermal correction to 298 K) at the MP2(full)/SD/6-311+G(2d,2p) level. Chillemi et al.[24] reported a (7,0) GS with C_2 symmetry using a Hartree Fock (HF) level of theory with the LANL2DZ ECP on Cd^{2+} and a cc-pVTZ basis set on the waters. However, we find that (7,0) is higher than the (6,1)_AA complex by 23 kJ/mol at 0 K (19 kJ/mol for $\Delta\Delta G_{298}$) using the SD ECP on Cd. This is in accord with the theoretical and experimental results from Pye and co-workers,[25] who found that (7,0) is about 20 kJ/mol higher in energy than their (6,1)_AA complex at both the HF and MP2 levels using a number of different basis sets and ECPs. They also found no evidence of a heptacoordinate structure using Raman spectroscopy.

For n = 8, the MP2(full)/SD/6-311+G(2d,2p) GS is the (6,2)_4D_2AA complex at both 0 and 298 K, whereas, the (6,2)_2D,DD_2AA complex is 1 – 3 kJ/mol higher in energy, Figure 6.2. Interestingly, at the MP2(full)/Def2TZVPP level, the (6,2)_2D,DD_2AA complex is the free energy GS by 3 kJ/mol but higher in 0 K enthalpy ($\Delta\Delta H_0$ = 5 kJ/mol). Clearly these two complexes are isoenergetic with each other at the

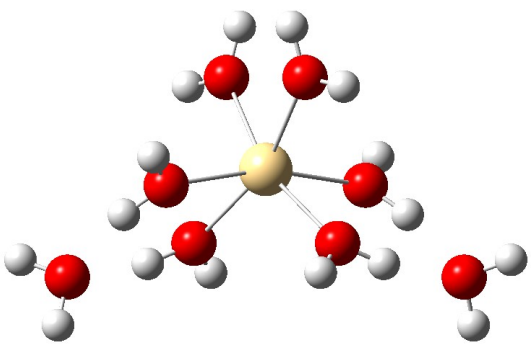

(6,2)_4D_2AA

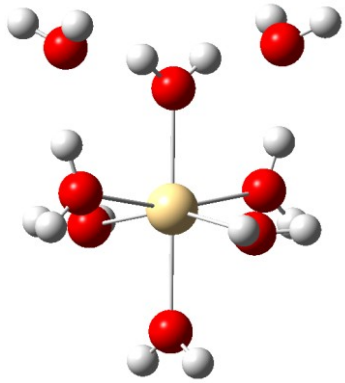

(6,2)_2D,DD_2AA

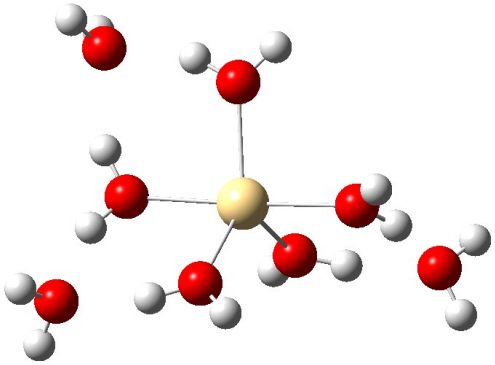

(5,3)_2A_bA_b,A_aA_b

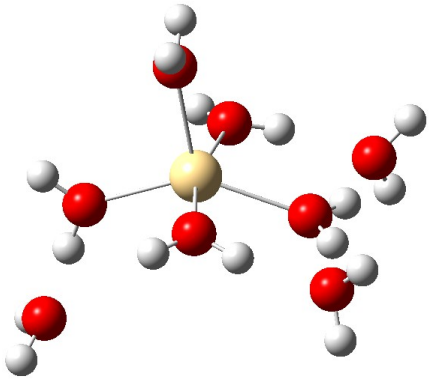

(5,3)_2A_bA_b,A_b

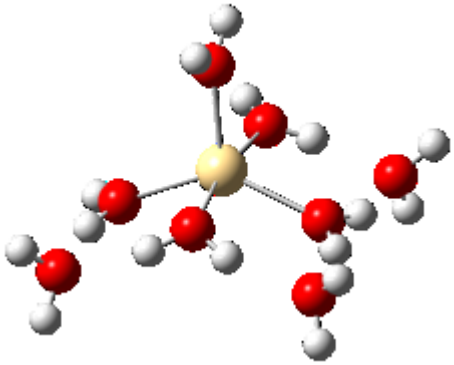

(5,3)_3A_bA_b

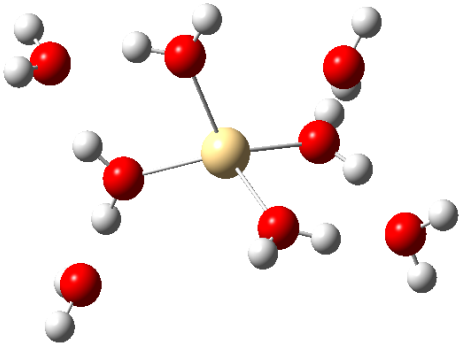

(4,4)_2AA,2A

Figure 6.2. Low-energy isomers of $Cd^{2+}(H_2O)_8$ calculated at the B3LYP/SD/6-311+G(d,p) level of theory.

MP2(full) level. The DFT relative energies for these (6,2) complexes are higher in energy by 1 – 5 kJ/mol in 298 K free energy ($\Delta\Delta H_0$ = 3 – 10 kJ/mol) over 5-coordinate complexes using either basis set. These DFT levels predict the 0 K GS to be (5,3)_2A_bA_b,A_aA_b, however, this complex has essentially the same (within 2 kJ/mol) 298 K free energy as the (5,3)_2A_bA_b,A_b and (5,3)_3A_bA_b complexes. All 5-coordinate complexes are higher in 298 K free energy than the 6-coordinate GS by 7 – 16 kJ/mol at the MP2(full) level. The (4,4)_2AA,2A complex is higher in 298 K free energy by 6 – 9 kJ/mol at the DFT levels and 23 – 39 kJ/mol at the MP2(full) level.

For *n* = 9 and 10, the 0 K GSs are the (6,3)_6D_3AA and (6,4)_4AA complexes at all levels of theory. At 298 K, MP2(full) calculations find that the (6,3)_4D,DD_3AA complex is favored by 4 kJ/mol using either basis set and for *n* = 10, find two low-energy complexes at 298 K, (6,4)_4AA and (6,4)_3AA,A, which lie within 4 kJ/mol of one another at 0 and 298 K. In contrast, DFT calculations find that the 6-coodinate species are higher in free energy for both *n* = 9 and 10. For *n* = 9, the (4,5)_AA,4A complex is the 298 K GS using either basis set, but is higher in 0 K enthalpy ($\Delta\Delta H_0$ = 22 – 25 kJ/mol). Close in free energy to the (4,5) complex is the (5,4)_3A_bA_b,A_a, similar to (5,5)_4A_bA_b,A_a, the DFT free energy GS structure for *n* = 10 found with both basis sets.

For *n* = 11, the 0 K GS complex at the B3LYP/SD/6-311+G(2d,2p) and both MP2(full) levels is the (6,5)_3AA,AAD,A_1A_2 complex, where one double acceptor water hydrogen bonds to both the first and second solvent shell (A_1A_2) thereby forming a ring-like series of hydrogen bonds (which we have previously called AA_p because a pseudo third solvent shell is formed). Thus, there is also a second shell water that is both a double acceptor and donor water molecule (AAD). At 298 K, the (6,5)_4AA,A free

energy GS complex is lower by 6 – 7 kJ/mol at the MP2(full) level using either basis set; however, this complex is 6 – 9 kJ/mol higher in free energy than the (5,5,1)_3AA,A,AAD_A structure at the DFT levels (although this structure could not be fully converged using the Def2TZVP basis set because of large motions and displacements of the single acceptor waters). No 4-coordinate structures were calculated at this complex size. The (7,4)_4AA complex is higher in energy at all levels by 20 – 45 kJ/mol.

Comparison to $Zn^{2+}(H_2O)_n$. The conflicting theoretical results on the predicted low-energy structures between the DFT and MP2(full) levels are similar to our recent investigation of zinc hydration, Chapters 3 and 4. In the case of hydrated zinc, the DFT levels favored 4-coordinate complexes as the GSs, with 5- and 6-coordinate complexes higher in 298 K free energy by 1 – 12 kJ/mol and 7 – 36 kJ/mol, respectively, for n = 6 – 10. In contrast, the MP2(full) level of theory favored 5-coordinate complexes over both 4- and 6-coordinate structures by 2 – 8 kJ/mol and 4 – 16 kJ/mol, respectively. The M06 functional,[50,51] which is specifically designed to handle hydrogen bonding, gave similar relative energies as those predicted by the MP2(full) level. The experimental bond dissociation energies (BDEs) for water loss from the n = 6 – 10 complexes were reproduced by an average of 2 kJ/mol better using the structures and energies predicted by the MP2(full) level of theory over the B3LYP and B3P86 levels. (Calculations using the M06 functional were in poor agreement with experiment, Chapter 3.) Although a 2 kJ/mol difference is hardly conclusive, this observation suggests that the GS structure of gas phase hydrated Zn^{2+} is 5-coordinate and that the MP2(full) level is more accurate than B3LYP and B3P86 for these systems. This conclusion was recently confirmed by

infrared photodissociation spectroscopic studies, Chapter 5, which show a preference for a coordination number of five with possible contributions from six. No evidence consistent with 4-coordinate species was observed. A key conclusion of this spectroscopy study was that B3LYP and B3P86 relative energies do not appear to be reliable for these hydrated complexes, therefore, the MP2(full) predicted low-energy complexes of $Cd^{2+}(H_2O)_n$ will be used in the analysis of our experimental data.

The results of the MP2(full) calculations predict that the low-energy structures of hydrated Cd^{2+} have an inner shell of six, one water molecule larger than those predicted for hydrated Zn^{2+}. This difference is a consequence of the larger ionic radius of Cd^{2+} versus that of Zn^{2+}, 0.99 and 0.78 Å,[49] respectively, and the higher nuclear charge of the Cd^{2+} ion.

Theoretical geometries: charge separation transition states. The rate-limiting step of reaction 6.2 is needed for the thermochemical analysis of this dissociation and involves the $H^+(H_2O)_{n-m-1}$ pulling away from the complex leaving $CdOH^+(H_2O)_m$, where $m = 3$ for $n = 6$, $m = 2$ for $n = 5$ and 4, and $m = 1$ for $n = 3$. The optimized tight TSs of the charge separation processes occurring for $n = 3 – 6$ are shown in Figure 6.3. In all cases, both the $CdOH^+(H_2O)_m$ and $H^+(H_2O)_{n-m-1}$ portions of each TS have geometries similar to their respective GS products. Although complete reaction coordinate diagrams were not calculated for these charge separation reactions, the TSs shown correspond to the Coulomb barrier associated with the approach of the two singly charged product ions, which must be the rate-limiting TS along the reaction coordinate. This was explicitly shown to be the case in Chapter 4 for the charge separation of $Zn^{2+}(H_2O)_7$ where the

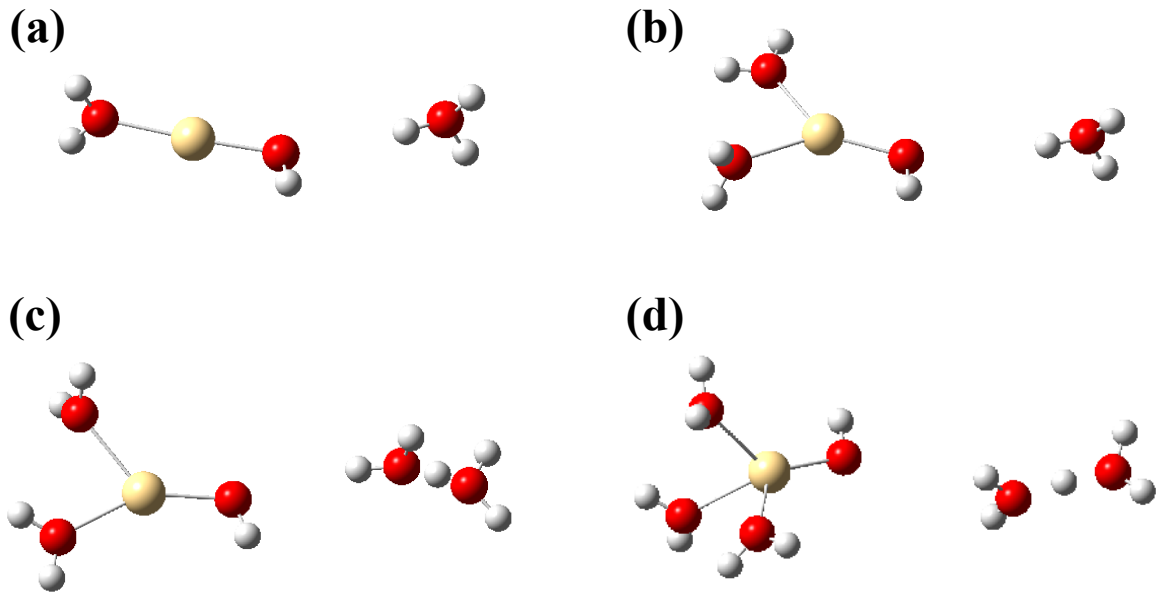

Figure 6.3. Optimized rate-limiting transition states of the n = 3, 4, 5, and 6 charge separation products $CdOH^+(H_2O)_m + H^+(H_2O)_{n-m-1}$, where m = 1, 2, 2 and 3 and n-m-1 = 1, 1, 2, and 2 for parts a – d, respectively, calculated at the B3LYP/Def2TZVP level of theory.

complete reaction coordinate was calculated. The barrier heights of these processes will be discussed in quantitative detail below.

Thermochemical results. Cross sections for the primary and secondary dissociation products were analyzed in several ways, with Table 6.2 summarizing the average optimum modeling parameters. Threshold E_0 values are given for the primary dissociation of each complex from modeling a single dissociation channel and including lifetime effects. If lifetime effects are not included, the threshold obtained from analysis is higher because of a kinetic shift, which is appreciable for most complexes, and increases from 0.18 eV at n = 4 to 0.68 eV at n = 11. The vibrational frequencies calculated at the B3LYP/SD/6-311+G(d,p) level were used in the RRKM analysis presented here, although it was verified that the optimum modeling parameters do not change outside of the listed uncertainties when frequencies calculated at the B3LYP/Def2TZVP level are used instead. Because theory predicts close relative energetics for these systems, the experimental data for the n = 8 and 10 complexes were also interpreted assuming two additional structures. For n = 10, MP2(full)/SD/6-311+G(2d,2p) calculations indicate that the (6,4)_3AA,A isomer is in thermal equilibrium with the (6,4)_4AA reactant and may dissociate to the (6,3)_6D_3AA complex. Assuming that the n = 10 reactant complex is (6,4)_3AA,A instead of (6,4)_4AA lowers the threshold by 0.05 eV to 0.44 ± 0.05 eV because of a change in the kinetic shift. Similar changes in kinetic shifts are discussed in detail in our previous zinc hydration study in Chapter 3. Briefly, if the assumed reactant complex has more outer shell waters with lower torsional frequencies (i.e., more single acceptor water molecules), it has a higher density of states, which lowers the rates of dissociation. This in turn

Table 6.2. Optimized Parameters from Analysis of CID Cross Sections[a]

n	Reactant	Product	σ_0	*N*	E_0 (eV)	$\Delta S^{\dagger}_{1000}$ (J/mol K)
4	(4,0)	(3,0)[b]	52 (3)	0.6 (0.1)	1.61 (0.05)	25 (5)
	(4,0)	TS[2+1][b]	5 (1)	0.4 (0.1)	1.34 (0.04)	29 (5)
	(4,0)	(3,0)[c]	48 (3)	0.8 (0.1)	1.52 (0.04)	20 (5)
		TS[2+1][c]	0.03 (0.03)	0.8 (0.1)	1.31 (0.03)	29 (5)
5	(5,0)	(4,0)[b]	70 (4)	0.8 (0.1)	1.11 (0.05)	60 (5)
	(5,0)	(4,0)[d]	72 (4)	0.8 (0.1)	1.11(0.05)	60 (5)
		(3,0)[d]	29 (4)	0.8 (0.1)	2.73 (0.05)	
	(5,0)	TS[2+2][b]	2 (2)	0.1 (0.2)	1.21 (0.07)	39 (5)
	(5,0)	(4,0)[c]	68 (7)	0.8 (0.2)	1.10 (0.03)	60 (8)
		TS[2+2][c]	0.1 (0.2)	0.8 (0.2)	1.14 (0.03)	39 (5)
	(5,0)	(3,0)[e]	39 (11)	0.2 (0.1)	2.72 (0.11)	22 (5)
		(2,0)[e]	1 (0.5)	0.2 (0.1)	4.85 (0.18)	
6	(6,0)	(5,0)[b]	64 (4)	0.9 (0.1)	0.90 (0.05)	56 (5)
	(6,0)	(5,0)[d]	65 (3)	0.9 (0.1)	0.90 (0.04)	56 (5)
		(4,0)[d]	60 (20)	0.9 (0.1)	2.10 (0.05)	
	(6,0)	(4,0)[e]	60 (12)	0.7 (0.2)	1.97 (0.08)	57 (5)
		(3,0)[e]	11 (3)	0.7 (0.2)	3.75 (0.20)	
7	(6,1)	(6,0)[b]	80 (4)	0.8 (0.1)	0.70 (0.05)	39 (4)
	(6,1)	(6,0)[d]	77 (5)	0.9 (0.1)	0.67 (0.05)	41 (4)
		(5,0)[d]	78 (12)	0.9 (0.1)	1.67 (0.07)	
8	(6,2)	(6,1)[b]	96 (5)	0.8 (0.1)	0.66 (0.06)	63 (5)
	(6,2)	(6,1)[d]	88 (5)	0.9 (0.1)	0.62 (0.08)	63 (4)
		(6,0)[d]	75 (7)	0.9 (0.1)	1.37 (0.09)	
	(6,2)_2D,DD_2AA	(6,1)[b]	95 (5)	0.8 (0.1)	0.67 (0.06)	69 (5)

Table 6.2. continued

n	Reactant	Product	σ_0	*N*	E_0 (eV)	$\Delta S^{\dagger}_{1000}$ (J/mol K)
9	(6,3)_4D,DD_3AA	(6,2)[b]	109 (2)	0.8 (0.1)	0.61 (0.05)	59 (5)
	(6,3)_4D,DD_3AA	(6,2)[d]	103 (3)	0.7 (0.1)	0.62 (0.06)	59 (4)
		(6,1)[d]	70 (11)	0.7 (0.1)	1.34 (0.08)	
10	(6,4)	(6,3)[b]	95 (6)	0.9 (0.1)	0.49 (0.05)	18 (5)
	(6,4)	(6,3)[d]	91 (2)	0.9 (0.1)	0.45 (0.06)	19 (4)
		(6,2)[d]	75 (5)	0.9 (0.1)	1.16 (0.07)	
	(6,4)_3AA,A	(6,3)[b]	91 (2)	0.9 (0.1)	0.44 (0.05)	9 (5)
11	(6,5)_4AA,A	(6,4)[b]	59 (4)	1.1 (0.1)	0.43 (0.05)	23 (4)
	(6,5)_4AA,A	(6,4)[d]	59 (4)	1.1 (0.1)	0.41 (0.06)	23 (5)
		(6,3)[d]	37 (5)	1.1 (0.1)	1.06 (0.09)	

[a] Uncertainties in parentheses. [b] Single channel dissociation model. [c] Competitive dissociation model. [d] Sequential dissociation model. [e] Tertiary fit using the sequential dissociation model.

increases the kinetic shift thereby lowering the 0 K threshold, as seen for the (6,4)_3AA,A reactant. For n = 8, the (6,2)_2D,DD_2AA primary dissociation to (6,1)_AA is now included because the MP2(full)/Def2TZVPP level predicts this reactant complex to be the 298 K free energy GS as opposed to the (6,2)_4D_2AA complex predicted by the MP2(full)/SD/6-311+G(2d,2p) level. Here, there is a negligible change to the threshold (a difference of 0.01 eV) because of the similarities in the hydrogen bonding network of these two complexes.

Competitive analysis: water loss vs. charge separation. The dissociation pathways of $Cd^{2+}(H_2O)_4$ and $Cd^{2+}(H_2O)_5$ are both influenced by the competition between the water loss and charge separation processes. For competing channels, the thermodynamically favored reaction pathway will remain largely unaffected, but the threshold of the disfavored pathway will shift to lower energies once competition is accounted for, known as a competitive shift. (Note that the uncertainty in the relative thresholds for competing channels is typically lower than the combined absolute uncertainties for each individual channel because several contributions to the uncertainty cancel in the relative value.) For reasons discussed previously in our study of charge separation in the zinc system, Chapter 4, the lowest five vibration frequencies of the tight TSs were changed to rotational degrees of freedom in our threshold analysis for n = 4 and 5 to better reproduce the energy dependence of the experimental cross sections of the charge separation products. For each of these TSs, one vibrational frequency corresponds to a torsion of the complex about the reaction coordinate and the other four vibrations are rotations of each incipient product, $CdOH^+(H_2O)_m$ and $H^+(H_2O)_{n-m-1}$.

Figure 6.4 shows a representative model for the competitive dissociation of $Cd^{2+}(H_2O)_4$. The rate limiting TSs for reaction 6.2 are abbreviated according to the products formed, i.e., TS[m + (n-m-1)]. For n = 4, the thermodynamically favored TS[2+1] has a threshold of 1.31 – 1.34 eV whether the cross section is fit independently or with competition; whereas the water loss channel shifts down from 1.61 ± 0.05 eV to 1.52 ± 0.04 eV, a competitive shift of 0.09 ± 0.03 eV, Table 6.2. The charge separation dissociation pathway is favored by 0.18 – 0.21 ± 0.03 eV over the water loss channel. A similar competitive shift of 0.08 eV for the analogous water loss dissociation channel was seen in the zinc hydration study, which favored the charge separation channel by 0.13 eV for the dissociation of $Zn^{2+}(H_2O)_7$, Chapter 4.

The water loss threshold for n = 5 remains between 1.10 – 1.11 eV regardless of how this cross section is analyzed, Table 6.2. However, the threshold for charge separation at n = 5, TS[2+2], is 1.14 ± 0.03 eV and shifts up by 0.07 ± 0.04 eV if competition is not included. This competitive shift is smaller than that for the analogous charge separation dissociation of $Zn^{2+}(H_2O)_8$ (also the thermodynamically disfavored pathway) of 0.16 eV. The competitive shift seen for the $Cd^{2+}(H_2O)_5$ system is probably smaller because of the proximity in the thresholds for the water loss and charge separation pathways, which only differ by 0.03 – 0.04 ± 0.03 eV in favor of the water loss channel, compared to the $Zn^{2+}(H_2O)_8$ system, where the water loss pathway is favored by 0.07 – 0.09 eV.

Water loss secondary threshold energies. There is no primary charge separation process to complicate the dissociation of $Cd^{2+}(H_2O)_n$, where n = 6 – 11, therefore, the secondary water loss using a sequential model with equations described in Chapter 2 and

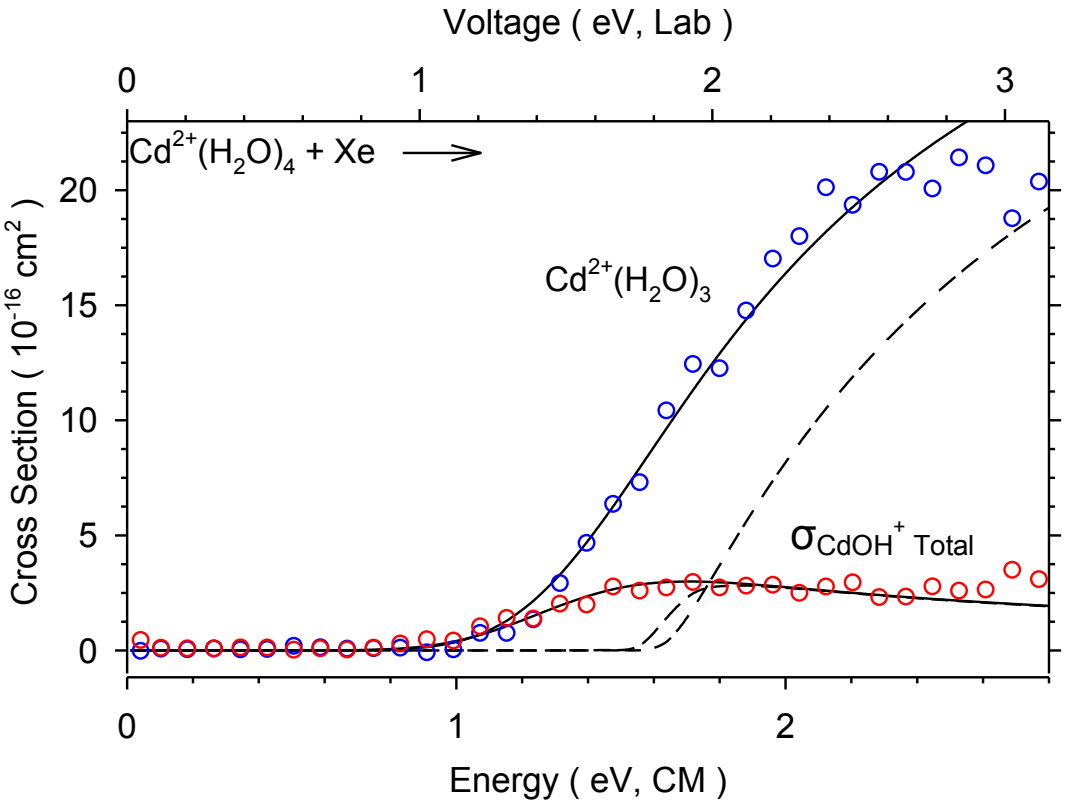

Figure 6.4. Cross sections for the CID of $Cd^{2+}(H_2O)_4$ with 0.15 mTorr of Xe. Solid lines show the best fit to the primary water loss and the competing charge separation product ion using the primary model convoluted over the kinetic and internal energy distributions of the neutral and ionic reactants. Dashed lines show the models in the absence of experimental kinetic energy broadening for reactants with an internal energy of 0 K. Optimized parameters for this model are found in Table 6.2.

elsewhere[52,53], and the results are reported in Table 6.2. In modeling the secondary (and primary) dissociation, the reactant isomer is assumed to be the 298 K GS (as this species should have the dominant population in a thermally equilibrated source) and the product isomer is the 0 K GS (as our threshold analysis is dominated by the lowest 0 K enthalpy species), which goes on to dissociate to the 0 K GS secondary product isomer, as described in Chapter 3. As for competing channels, the uncertainty in the "sequential BDE", which is derived from the difference between the primary and secondary thresholds, is typically lower than the calculated absolute uncertainty for primary and secondary thresholds because several contributions to the uncertainty in the energy cancel in the relative value. A representative model is shown in Figure 6.5 for the sequential dissociation of $Cd^{2+}(H_2O)_8$ assumed to be a (6,2)_4D_2AA reactant dissociating to (6,1) + H_2O and (6,0) + $2H_2O$. From this point forward, we abbreviate our naming scheme to (x,y) for the lowest energy isomer of each inner solvent shell, except for instances where the ΔG_{298} and ΔH_0 complexes differ at the MP2(full)/SD/6-311+G(2d,2p) level, where the full name of the ΔG_{298} GS is given. In cases where the GS differs between the two basis sets, the full name of the GS predicted by the Def2TZVPP basis set is given.

For the sequential dissociation of $Cd^{2+}(H_2O)_{11}$, modeled as (6,5)_4AA,A → (6,4) + H_2O → (6,3) + $2H_2O$, the sequential BDE for the dissociation energy of $Cd^{2+}(H_2O)_9$-H_2O is 0.65 ± 0.07 eV. This result is 0.16 ± 0.09 eV higher in energy than the primary water loss threshold of 0.49 ± 0.05 eV for n = 10 when modeled as a (6,4) → (6,3) + H_2O process. This difference will be discussed further below.

The secondary threshold for n = 10 is 1.16 ± 0.07 eV, modeled as (6,4) → (6,3) + H_2O → (6,2) + $2H_2O$, yielding a primary-secondary threshold difference of 0.71 ± 0.05

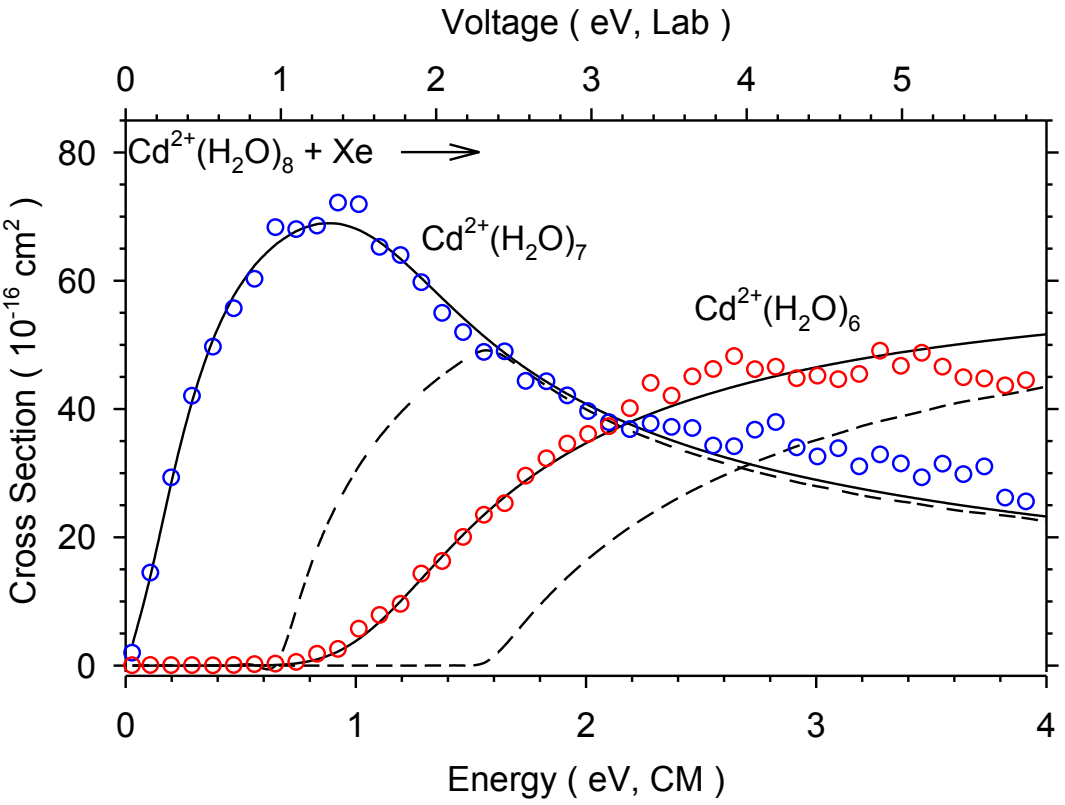

Figure 6.5. Zero pressure extrapolated cross sections for the CID of $Cd^{2+}(H_2O)_8$ with Xe. Solid lines show the best fit to both the primary and secondary water loss products using the sequential model convoluted over the kinetic and internal energy distributions of the neutral and ionic reactants. Dashed lines show the models in the absence of experimental kinetic energy broadening for reactants with an internal energy of 0 K. Optimized parameters for this model are found in Table 6.2.

eV for $Cd^{2+}(H_2O)_8$-H_2O. This sequential BDE is 0.10 ± 0.08 eV higher than the primary dissociation threshold for n = 9. For n = 9, the sequential model gives a relative threshold value of 0.72 ± 0.03 eV for $Cd^{2+}(H_2O)_7$-H_2O, as modeled assuming a (6,3)_4D,DD_3AA → (6,2) + H_2O → (6,1) + 2H_2O process, only 0.06 ± 0.07 eV higher than the primary dissociation threshold for n = 8, within experimental uncertainty. For n = 6 – 8, the primary-secondary threshold differences are 0.05 – 0.10 eV higher than their primary dissociation counterparts. Specifically, for n = 8 the sequential BDE for $Cd^{2+}(H_2O)_6$-H_2O is 0.75 ± 0.03 eV, which is in good agreement with the primary threshold for n = 7 at 0.70 ± 0.05 eV. The relative primary-secondary thresholds for $Cd^{2+}(H_2O)_5$-H_2O and $Cd^{2+}(H_2O)_4$-H_2O are 1.00 ± 0.03 eV and 1.20 ± 0.04 eV, respectively. These are 0.10 ± 0.06 and 0.09 ± 0.06 eV higher in energy than their primary counterparts of 0.90 ± 0.05 eV and 1.11 ± 0.05 eV for n = 6 and 5, respectively.

The sequential dissociation at n = 5 is modeled as a (5,0) → (4,0) + H_2O → (3,0) + 2H_2O process; however, the secondary dissociation to form the (3,0) product is complicated by competition with the charge separation process, reaction 6.3. Unfortunately this sequential competition cannot be modeled using our computational program for data analysis, CRUNCH. Ignoring this complication, we find that the sequential BDE for $Cd^{2+}(H_2O)_3$-H_2O is 1.62 ± 0.03 eV, which is in excellent agreement with the primary dissociation threshold determined without including competition with the charge separation reaction 6.3, 1.61 ± 0.05 eV for n = 4. We anticipate that the competitive shift found for n = 4, 0.09 ± 0.03 eV should apply to both of these processes. Additionally, we analyzed the tertiary threshold of the n = 6 reactant to provide another sequential BDE for the n = 4 complex, Table 6.2. We find the difference between the

tertiary and secondary thresholds for $Cd^{2+}(H_2O)_3$-H_2O is 1.78 ± 0.14 eV, 0.16 – 0.17 ± 0.15 eV higher than the primary and sequential thresholds, just outside the experimental uncertainty. This process should also be influenced by competition with charge separation and therefore should also have the 0.09 ± 0.03 eV competitive shift applied.

Because of the contamination discussed above, no secondary threshold was available for sequential analysis of the (4,0) → (3,0) + H_2O → (2,0) + $2H_2O$ dissociation. In an attempt to provide a bond energy for the n = 3 complex, the tertiary dissociation of the n = 5 reactant was analyzed using the sequential model, Table 6.2. In a previous analysis of higher order dissociations of the $K^+(NH_3)_n$ system, where n = 2 – 5, the absolute tertiary and quaternary thresholds were high (as is commonly found) and the relative energies were also somewhat high (and increasing with the order of the process), but within experimental uncertainty of values determined from lower order processes.[53] In the sequential dissociation of the $Cd^{2+}(H_2O)_5$ reactant, the tertiary threshold for the formation of $Cd^{2+}(H_2O)_2$ was analyzed, where the relative tertiary-secondary sequential BDE for $Cd^{2+}(H_2O)_2$-H_2O is 2.13 ± 0.14 eV. This sequential dissociation is complicated by reaction 6.3 and possibly 6.4 in a similar fashion to the sequential BDE of $Zn^{2+}(H_2O)_5$-H_2O, which was found to have an experimental competitive shift of 0.20 ± 0.03 eV in Chapter 4. Using this analogous competitive shift of the Zn^{2+} system, we estimate that the BDE of n = 3 is closer to 1.93 ± 0.14 eV. The sizable experimental uncertainty found for this dissociation as well as the tertiary-secondary energy for $Cd^{2+}(H_2O)_3$-H_2O is a result of the scatter in the cross sections resulting from the needed zero pressure extrapolation, which is appreciable for a tertiary water loss process. Both tertiary processes were also modeled using raw data at the lowest Xenon pressure, ~0.05

mTorr, although here the thresholds for both the secondary and tertiary processes were not fit with high fidelity because of the low energy features in the threshold regions resulting from multiple collisions.

Comparison of bond dissociation energies: primary vs. sequential. The sequential model has been proven to give accurate experimental BDEs for singly charged systems metal systems[53] and was used in our previous study on Zn^{2+} hydration, Chapter 3. For Cd^{2+} hydration, the sequential BDEs are 1 – 15 kJ/mol higher in energy than the corresponding primary values, Table 6.3, with a mean absolute deviation (MAD) of 7.9 kJ/mol for n = 4 – 10, just outside of experimental uncertainty. The largest energy differences between the two values are seen for the n = 10 and 9 complexes, 15.4 ± 8.7 and 9.6 ± 7.7 kJ/mol, respectively.

In the zinc system, a large difference between the primary and sequential BDEs was also observed for the n = 9 complex, 17.3 ± 8.2 kJ/mol. In Chapter 3, it was hypothesized that the presence of higher energy isomers in our reactant ion beams could lead to primary dissociation thresholds that are low by the excitation energies of the higher energy complexes. In contrast, the sequential BDE is not influenced by alternate isomers in the reactant beam because the primary and secondary thresholds are lowered by the same amount of energy, such that the relative measurement of the two thresholds is unaffected. Additionally, these alternate isomers are more common for large values of n, where more hydrogen bonding is possible such that there are more complexes with smaller relative energy differences.

For $Cd^{2+}(H_2O)_9$ and $Cd^{2+}(H_2O)_{10}$, the free energy GSs are higher in 0 K enthalpy by 2 – 4 kJ/mol and may cause the primary dissociation to be lowered by this amount

Table 6.3. Comparison of 0 K experimental bond energies (kJ/mol) to theoretical values.

n	Reactant	Product	Exp, Primary[a]	Exp, Sequential[a]	Exp, Weighted Average[b]	MP2(full)/SD/ 6-311+G(2d,2p)[c]	MP2(full)/ Def2TZVPP[d]
3	(5,0)	(2,0)		186 ± 14[e]		175.4 (189.6)	185.7 (193.6)
4	(4,0)	(3,0)	146.7 ± 3.9	147.7 ± 4.1[f]	147.2 ± 5.7	144.4 (158.6)	154.5 (162.9)
			146.7 ± 5.6[e]				
5	(5,0)	(4,0)	107.1 ± 4.8	115.8 ± 3.9	112.3 ± 6.1	106.3 (120.9)	110.3 (119.1)
6	(6,0)	(5,0)	86.8 ± 4.8	96.5 ± 2.9	93.9 ± 5.0	97.7 (114.0)	99.1 (108.5)
7	(6,1)_AA	(6,0)	67.5 ± 4.8	72.4 ± 2.9	71.1 ± 5.0	71.1 (80.2)	75.6 (82.7)
8	(6,2)_4D_2AA	(6,1)	63.7 ± 5.8	69.5 ± 2.9	68.3 ± 5.2	73.7 (82.5)	76.4 (83.4)
	(6,2)_2D,DD_2AA	(6,1)	64.6 ± 5.8			72.7 (81.6)	71.6 (78.5)
9	(6,3) _4D,DD_3AA	(6,2)	58.9 ± 4.8	68.5 ± 4.8	63.7 ± 6.8	67.7 (76.4)	71.8 (78.6)
10	(6,4)_4AA	(6,3)	47.3 ± 4.8	62.7 ± 6.8	52.4 ± 7.8	54.9 (63.6)	58.0 (64.8)
	(6,4)_3AA,A	(6,3)	42.5 ± 4.8			52.8 (59.5)	54.1 (60.9)
11	(6,5)_4AA,A	(6,4)	41.5 ± 4.8			49.2 (55.9)	51.2 (56.2)
MADs	Primary			7.9[g]		7.0 (16.7)[h]	9.6 (16.9)[g]
MADs	Sequential					4.8 (8.3)[h]	4.2 (9.3)[h]
MADs	Weighted Average					3.5 (12.5)[h]	5.8 (13.0)[h]

[a] Values from Table 6.2. [b] Weighted average of the primary and sequential BDEs. [c] MP2(full)/SD/6-311+G(2d,2p)//B3LYP/SD/6-311+G(d,p) level. ZPE corrected. Values listed with (without) cp correction. [d] MP2(full)/Def2TZVPP//B3LYP/Def2TZVP level. ZPE corrected. Values listed with (without) cp correction. [e] Tertiary sequential energy including an estimated competitive shift of 19.3 ± 2.9 kJ/mol. [f] Values including an 8.6 ± 2.9 kJ/mol correction for competition. [g] Mean absolute deviation between primary and sequential BDEs. [h] Mean absolute deviation between experiment and theory with (without) cp correction.

compared to the sequential model threshold. Thus, this hypothesis does not explain the full magnitude of the difference. Additionally, the sequential BDEs for n = 5 and 6 are also 9 – 10 kJ/mol higher than the primary values and no higher-energy isomers are predicted to be in thermal equilibrium with the reactant GSs at the MP2(full) level. Good agreement between the sequential and primary values is found for n = 4, 7, and 8. For n = 4, the primary and sequential values are 146.7 ± 5.6 and 147.7 ± 4.1 kJ/mol, respectively, after accounting for the 8.6 ± 2.9 kJ/mol competitive shift noted above. The relative secondary-tertiary BDE for $Cd^{2+}(H_2O)_3$-H_2O is higher at 163 ± 14 kJ/mol, but agrees with the other values within the large experimental uncertainty. The judicious application of the sequential model as an upper limit for higher order processes has been discussed previously.[53]

The sequential BDEs seem to provide accurate upper limits either within or just outside the experimental uncertainty of the primary BDEs, exceeding these by anywhere from 1 – 16 kJ/mol for all values of n examined here. This model seems to be an excellent alternative to obtain thresholds not readily obtained from a primary water loss because of limitations of the ion source, the charge separation process, or signal intensity of the smaller complexes. Additionally, observations and results from this study and those found in Chapters 3 and 4 on hydrated Zn^{2+} suggest that this model may in fact be slightly more accurate for complexes where theory predicts multiple high and low-energy isomers to be in thermal equilibrium with each other, as discussed above. It seems low primary BDEs are more common at larger complexes as seen for Cd^{2+} at n = 9 – 11 and Zn^{2+} for n = 9 and 10, where more structures with a variety of hydrogen bonding are in thermal equilibrium. In addition, because of the many low frequency motions of the

second shell waters, these larger complexes may be harder to thermalize in our source because of the larger numbers of internal degrees of freedom or may be collisionally excited during extraction from the source much more easily in such a way that their population is no longer in thermal equilibrium before reaching the collision cell. For the above reasons, the sequential BDEs may be more accurate than the primary BDEs at larger complex sizes because the sequential energies should be unaffected by the presence of higher energy complexes.

Ultimately, there is no experimental means of distinguishing the accuracy of the primary versus sequential BDEs for the dissociation of $Cd^{2+}(H_2O)_n$, and hence, we have calculated their weighted average, Table 6.3. The weighted average of these BDEs give MADs between experiment and cp corrected theory of about 5 kJ/mol using either basis set (~12 kJ/mol without cp correction). The weighted average also reflects an increase in the experimental uncertainty for larger complexes where the assumption of a room temperature population distribution may not be accurate, as noted above.

Experimental vs. theory: water loss. Figure 6.6 is a direct comparison of experimental and MP2(full) theoretical 0 K hydration energies from Table 6.3. These 0 K bond dissociation energies include ZPE and counterpoise corrections. Single point energies were calculated at the B3LYP, B3P86, and MP2(full) with SD/6-311+G(2d,2p) and Def2TZVPP basis sets from geometry optimizations using B3LYP/SD/6-311+G(d,p) and B3LYP/Def2TZVP levels of theory, respectively. As discussed above, there is evidence that our most accurate interpretation of the data comes from the relative energies and low-energy structures predicted at the MP2(full) level, therefore only the BDEs calculated at the MP2(full) level are given in Table 6.3 and Figure 6.6.

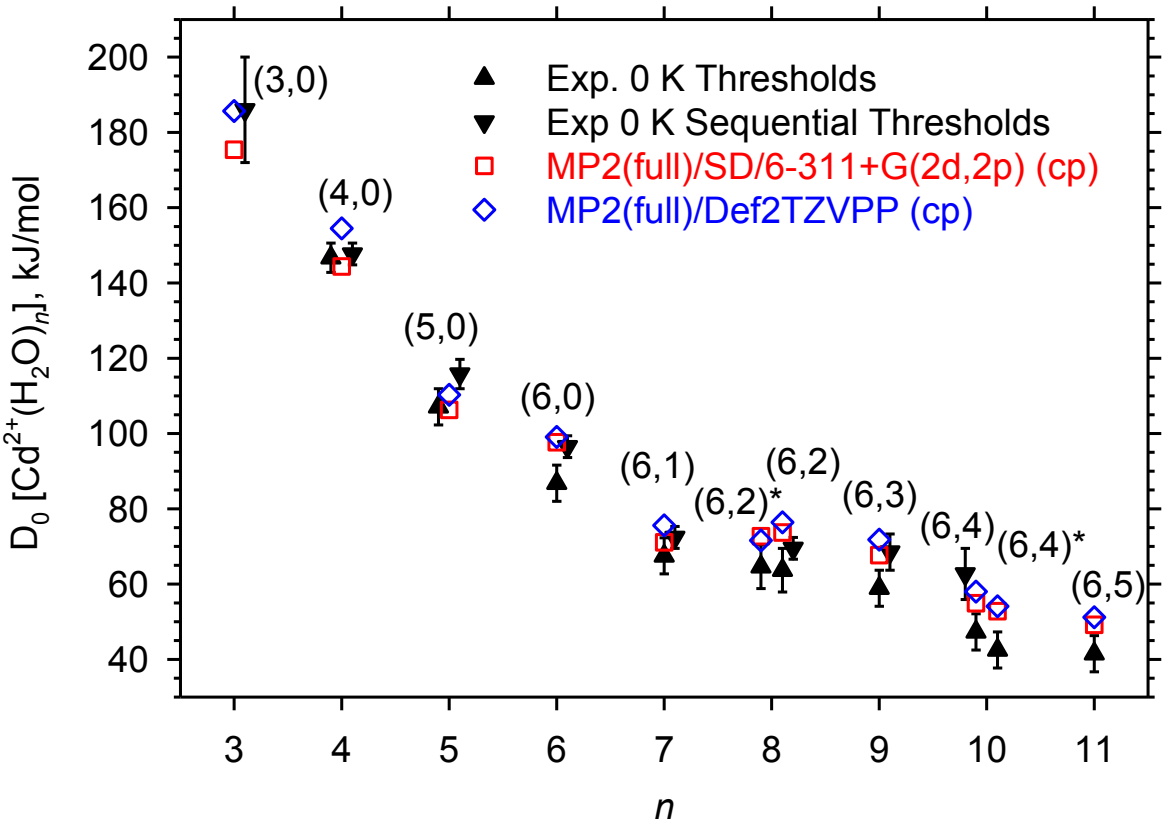

Figure 6.6. Comparison of experimental (solid symbols) and MP2(full) theoretical (open symbols) hydration enthalpies at 0 K for both the SD/6-311+G(2d,2p) and Def2TZVPP basis sets. All theoretical results shown are counterpoise corrected. The (6,2)* corresponds to the MP2/Def2TZVPP predicted (6,2)_2D,DD_2AA reactant isomer while (6,2) is the MP2/SD/6-311+G(2d,2p) predicted (6,2)_4A_2AA. The (6,4)* corresponds to the (6,4)_3AA,A reactant isomer which is in thermal equilibrium with the (6,4) = (6,4)_4AA reactant at the MP2(full)/SD/6-311+G(2d,2p) level.

A comparison of the primary BDEs to the MP2(full)/SD/6-311+G(2d,2p) values with and without counterpoise corrections have already been discussed in detail along with a comparison to theoretical values obtained from the literature.[17,25] Briefly, electronic binding energies are reported in the literature for $n = 4 – 7$, but use a smaller basis set than used here and were not corrected for zero point energies or BSSE.[25,54] These values were corrected by the zero point energies calculated here and are presented elsewhere.[17] For $n = 4 – 6$, the literature values tend to overestimate the 0 K hydration energies at the MP2 level by up to 10 kJ/mol compared to the present MP2(full) results without cp correction. However, the $n = 7$ literature dissociation value is lower in energy by 11 kJ/mol, where the structural and energetic differences discussed above for the two (6,1)_AA complexes partially account for this difference. Clearly there is good agreement between the experimental and theoretical results and the qualitative trends in the experimental values are reproduced in the theoretical BDEs calculated here.

The sequential BDE for water loss at $n = 3$ of 186 ± 14 kJ/mol is found by modeling the tertiary dissociation of the $Cd^{2+}(H_2O)_5$ reactant and applying a 19.3 ± 2.9 kJ/mol competitive shift found an analogous dissociation in the zinc hydration study, as explained above. This higher order sequential process is anticipated to be an upper limit to the BDE for this complex size as discussed above and agrees within 1 kJ/mol with the MP2(full)/Def2TZVPP result (within 11 kJ/mol of the MP2(full)/SD/6-311+G(2d,2p) result). The experimental BDE for the water loss at $n = 4$ of 146.7 ± 3.9 kJ/mol includes explicit modeling of competition with charge separation. Our previously reported value at $n = 4$ was slightly higher (~1 kJ/mol) because the competitive shift was estimated using that found for the analogous complex size in our zinc hydration study.

Looking at the overall trends in Figure 6.6 there are three distinct patterns in the experimental BDEs that are reproduced by the theoretical numbers. These patterns are most likely a consequence of the three distinct types of waters found in the hydrogen bond networks of the predicted GS structures. Moving from $n = 3 – 6$, each BDE decreases from the previous complex, consistent with each water dissociating from the complex being directly coordinated to the metal ion, as predicted by the MP2(full) level of theory. The primary BDEs of the $n = 7 – 9$ complexes are similar, within 10 kJ/mol of each other (sequential BDEs within 4 kJ/mol), because each of these dissociations involve the loss of a second shell AA water molecule. Lowest in energy are the BDEs found for the $n = 10$ and 11 complexes. If the results for $n = 10$ are interpreted as corresponding to the (6,4)_3AA,A complex (the MP2(full)/SD/6-311+G(2d,2p) 298 K free energy GS), then the experimental BDEs for $n = 10$ and 11 are within 1 kJ/mol of each other. This is consistent with the interpretation that both complexes lose a second shell A water molecule, which binds more weakly than an AA water because it has only a single hydrogen bond to the inner shell. Alternatively, the results for $n = 10$ can be interpreted in terms of the (6,4)_4AA complex, predicted to be in thermal equilibrium using either basis set at the MP2(full) level. Now the experimental and theoretical BDEs for $n = 10$ lie below those of $n = 9$ (by 6 – 11 kJ/mol experimental, 13 – 14 kJ/mol theory) and above those of $n = 11$ (by 6 kJ/mol experimental, 3 – 4 kJ/mol theory), Table 6.3. Here an AA water is lost, explaining why it is more strongly bound than the A water of the $n = 11$ complex, but is bound more weakly than those for $n = 7 – 9$ because this complex is forced to have two inner shell DD water molecules that each share two second shell water ligands. In the case of $n = 10$, there is not sufficient experimental evidence to

definitively conclude which of the two possible complexes is actually being probed in our experiments because experiment and theory are self consistent for both possibilities. It is certainly possible that the experimental results are a superposition of both configurations.

Our experimental primary BDEs agree best with the SD/6-311+G(2d,2p) basis set with a mean absolute deviation (MAD) of 6.9 kJ/mol and a MAD between the sequential BDEs and theory of 4.8 kJ/mol. Comparisons between experiment and theoretical results from the Def2TZVPP basis set give MADs of 9.0 and 4.2 kJ/mol for the primary and sequential BDEs, respectively. In general, the MP2(full)/Def2TZVPP level gives theoretical BDEs 1 – 10 kJ/mol higher in energy than those of the MP2(full)SD/6-311+G(2d,2p) level. A similar trend was seen in a recent report on the inner shell hydration energies of Sr^{2+},[47] where BDEs calculated with the MP2(full)/Def2TZVPP basis set were higher by 1 – 6 kJ/mol over those calculated at MP2(full)/SD/6-311+(2d,2p) for n = 1 – 5 and lower by 1 kJ/mol at n = 6. One difference between these two levels of theory is that the counterpoise correction for the SD/6-311+G(2d,2p) basis set is larger, ranging from 7 – 14 kJ/mol, whereas, the correction using the Def2TZVPP basis set is only 4 – 10 kJ/mol. The larger correction for the SD/6-311+G(2d,2p) basis set is most likely because the basis set is not size-consistent for all atoms (unlike Def2TZVPP), and because the basis set on Cd is smaller than the Def2TZVPP basis set.

Charge separation barrier heights. Theoretical results for the charge separation processes are compared with experimental results in Table 6.4. The predicted energetic barriers for n = 3, 5, and 6 are relatively constant at 79 – 91 kJ/mol at the DFT levels and at 94 – 117 kJ/mol at MP2(full). Similar barrier heights were also calculated for $Zn^{2+}(H_2O)_n$ charge separation when n = 5 – 7, where the predicted barrier heights ranged

Table 6.4. Comparison of 0 K transition state energies to theory and water loss bond energies (kJ/mol).

n	Reactant	Product	Experiment	B3LYP[a]	B3P86[a]	MP2(full)[a]
3	(3,0)	TS[1 + 1]		83.0	83.9	93.6
		$CdOH^+(H_2O) + H^+(H_2O)$		-88.2	-88.1	-74.0
		(2,0)	186 (14)[b]	185.9	188.4	185.7
4	(4,0)	TS[2 + 1]	126.4 (2.9)[c]	128.8	128.5	139.5
		$CdOH^+(H_2O)_2 + H^+(H_2O)$		-23.7	-24.1	-10.1
		(3,0)	146.7 (3.9)[c]	151.7	154.2	154.5
5	(5,0)	TS[2 + 2]	110.0 (2.9)[c]	81.3	78.9	105.0
		$CdOH^+(H_2O)_2 + H^+(H_2O)_2$		-62.9	-66.1	-37.0
		(4,0)	107.1 (4.8)[d]	104.8	106.9	110.3
6	(6,0)	TS[3 + 2]		90.7	86.9	117.2
		$CdOH^+(H_2O)_3 + H^+(H_2O)_2$		-41.5	-46.9	-14.5
		(5,0)	86.8 (4.8)[d]	92.1	93.6	99.1

[a] Single point energies calculated at the level shown using a Def2TZVPP basis set using geometries optimized at a B3LYP/Def2TZVP level. All values are ZPE corrected. [b]Value taken from Table 6.3 using the sequential dissociation model to analyze a tertiary threshold. [c] Values taken from Table 6.2 using competitive dissociation model. [d] Values taken from Table 6.2 using the primary dissociation channel model.

from 66 – 75 (83 – 94) kJ/mol at DFT (MP2(full)) levels, Chapter 4. In contrast with these similar barriers, the predicted barrier for $n = 4$ is higher in energy by 38 – 50 kJ/mol and 22 – 46 kJ/mol, respectively, compared to the $n = 3$, 5 and 6 TSs, Table 6.4. Examination of the reverse Coulomb barrier shows a more systematic result in which the barrier decreases as n increases, i.e., 171, 153, 144, 132 kJ/mol for $n = 3 – 6$, respectively, at the B3LYP level (168, 150, 142, and 132 kJ/mol at the MP2(full) level), agreeing with trends discussed in Chapter 4 for Zn^{2+} hydration. In part, this decrease in the reverse Coulomb barrier as n increases can explained by increasing charge delocalization for larger values of n because of the increasing number of waters on each part of the TS and the charge separation products.

The increase in the predicted forward barrier height for the $n = 4$ complex may be understood in part by the 18 e^- rule, which is fulfilled at the $Cd^{2+}(H_2O)_4$ complex leading to an enhanced stability of the $n = 4$ complex. Thus, the larger barrier height leads to a lower absolute exothermicity for $n = 4$ compared to the values found for $n = 3$, 5, and 6. The stability of the $n = 4$ complex is also evidenced by the relatively large increase (38 - 47 kJ/mol) in the predicted water loss BDEs from $n = 5$ to 4. Indeed, this increase exceeds that predicted for $n = 4$ to 3, 31 – 34 kJ/mol, even though water loss BDEs are expected to increase as n decreases.

The experimental measurement of the charge separation TS energy increases by almost 16 kJ/mol from $n = 5$ to 4, changing from 110.0 ± 2.9 kJ/mol for TS[2+2] to 126.4 ± 2.8 kJ/mol for TS[2+1], Table 6.4, agreeing with the predicted trends discussed above. There is good agreement in this TS energy between experiment and theory at $n = 4$, with the MP2(full) value being somewhat high (by 13 kJ/mol). For $n = 5$, MP2(full)

calculations predict a barrier height that is in best agreement (within 5 kJ/mol) with the experimental TS[2 + 2] barrier, whereas values predicted by both DFT levels are too low by ~30 kJ/mol.

Water loss vs. charge separation. The 0 K thresholds and theoretically predicted energies for both the charge separation and water loss dissociation pathways are compared in Table 6.4. For the $n = 3$ complex, there is no experimental barrier height measured for TS[1 + 1] although theory predicts this barrier ranges from 83 – 94 kJ/mol. Some evidence for this process is observed in the dissociations of the $n = 4$ complex, Figure 6.1a, as discussed above. Here, $Cd^{2+}(H_2O)_4$ can dissociate by reaction 6.1 followed by reaction 6.4 to form to form $CdOH^+(H_2O) + H^+(H_2O) + H_2O$, which is calculated to require 235 (248) kJ/mol at the B3LYP (MP2(full)) levels, i.e., the sum of the energy for loss of the water molecule and the TS[1 + 1] barrier height. This prediction is consistent with the increase observed in the $H^+(H_2O)$ cross section near ~2.4 eV, as well as a 30% increase in the total cadmium hydroxide cross section occurring at the same energy. The evidence for this reaction is not definitive, however, because the $CdOH^+(H_2O)$ and $H^+(H_2O)$ products can also be formed via an alternative route, namely reaction 6.6 (forming $CdOH^+(H_2O)_2$ and $H^+(H_2O)$) followed by reaction 6.6.

$$CdOH^+(H_2O)_2 + Xe \rightarrow CdOH^+(H_2O) + H_2O + Xe \qquad (6.6)$$

Reaction 6.6 is predicted to require 91 (99) kJ/mol. When combined with the barrier for TS[2+1] from Table 6.4, the energy for the reaction 6.3 + 6.6 pathway is predicted to cost 220 (239) kJ/mol. Thus, the reaction 6.3 + 6.6 pathway, predicted to be 9 – 15 kJ/mol lower in energy than reaction 6.1 + 6.4 pathway, is believed to correspond to the

observed onset in the $CdOH^+(H_2O)$ cross section above ~1.8 eV in Figure 6.1a, as mentioned above. The experimental data for both the $H^+(H_2O)$ and $CdOH^+(H_2O)$ cross sections are in qualitative agreement with the predicted relative energies between these two sequential processes. Further evidence of reaction 6.6 is observed in the $CdOH^+(H_2O)$ product cross sections in Figures 6.1b and 6.1c. In both of these cross sections, there are two features that each start ~1 eV (96 kJ/mol) above the more obvious onsets in the $CdOH^+(H_2O)_2$ cross sections, as discussed above, which is in qualitative agreement with the predicted BDE of reaction 6.6 (91 – 99 kJ/mol). Further indirect indications of reaction 6.4 center on the dissociation behavior of the $Cd^{2+}(H_2O)_3$ complex. The experimental water loss BDE for $n = 3$ is 186 ± 14 kJ/mol, in excellent agreement with the bond energies predicted by all levels calculated using the Def2TZVPP basis set, Table 6.4. Compared to this energy, the predicted barrier of reaction 6.4 is much lower in energy, by 92 – 105 kJ/mol. In agreement with our qualitative discussions above, this large energetic preference of reaction 6.4 probably explains the very low observed magnitude of the $Cd^{2+}(H_2O)_2$ product.

At the $n = 4$ complex, experimental and theoretical results both suggest that reaction 6.2 is energetically favored over reaction 6.1 by 20 ± 3 and 15 - 26 kJ/mol, respectively. For $n = 5$, the relative experimental thresholds for reactions 6.1 and 6.5 favor the water loss dissociation pathway by ~3 ± 3 kJ/mol. In contrast, theory suggests that the charge separation reaction is energetically favored over the water loss dissociation by 5 – 28 kJ/mol, depending on the level. As discussed above, the relative apparent thresholds in Figures 6.1b and 6.1c for these competing dissociations also suggest that water loss is the energetically favored dissociation pathway. No

experimental charge separation products were observed in the primary dissociation of n = 6 and it does not seem likely that the charge separation reaction is energetically favored over water loss in agreement with the predicted MP2(full) energies (water loss favored by 18 kJ/mol), but contrary to the DFT results (charge separation favored by 1 – 7 kJ/mol). In agreement with our conclusions above, the MP2(full) theoretical results appear to provide a better quantitative reproduction of experimental results for charge separation than DFT approaches.

The thermal ESI source used in this study is limited to producing complexes of sizes $n \geq n_{crit}$, as demonstrated previously for hydrated Zn^{2+} (Chapter 3) and in our in-source fragmentation studies.[34] For hydrated Cd^{2+}, we are able to generate the n = 4 complex, albeit at low signal intensities, suggesting that $n_{crit} \leq 4$. A large discrepancy between the levels of theory in the predicted barrier heights was found previously in Chapter 4 for hydrated Zn^{2+}, which suggests that theory is not adequately describing the barrier heights for charge separation, although for hydrated Cd^{2+}, MP2(full) gives better agreement to the experimental barrier heights and relative energies between the competing channels. Consequently, we use these experimental observations combined with the experimental relative BDE results to conclude that the critical size for charge separation in the $Cd^{2+}(H_2O)_n$ system is n_{crit} = 4, where n_{crit} is defined as the maximum-sized cluster for which charge separation is energetically favored over the loss of one water ligand (first defined in Chapter 4).

This value agrees with previous work by Shvartsburg and Siu, although they assign this value as a lower limit because the determination depends on instrumental sensitivity and their definition of critical size does not depend on the energetics of the

reaction.[9] Shvartsburg and Siu also suggest that the critical size depends directly on the second ionization energy of the metal, a hypothesis pioneered by the Kebarle group[3,4,6] and charge separation mechanism suggest by the Williams group[8] for a series of different metal ions. In agreement with this, hydration studies in our laboratory find the energy dependent critical size changes as $Sr^{2+} < Ca^{2+} < Cd^{2+} < Zn^{2+}$,[47,48] an order that also mirrors their second ionization energies.

Conversion to 298 K. Using the calculated frequencies and rotational constants of the transition states, a rigid rotor/harmonic oscillator approximation was applied to convert the 0 K primary water loss threshold energies of the $n = 4 – 11$ complexes, the sequential BDE of the $n = 3$ complex, and the 0 K charge separation barrier heights of the $n = 4$ and 5 reactants to 298 K values in Table 6.5. The uncertainties in these conversion factors are found by scaling the vibrational frequencies up and down by 10%. Like the hydration energies, the free energies of hydration decrease as the size of the $Cd^{2+}(H_2O)_n$ increases. The $\Delta\Delta G_{298}$ values also decease as the complexes increase in size. The entropies of dissociation, $T\Delta S_{298}$, remain relatively constant as there are no major solvent shell rearrangements between these structures.

There are two possible conversion values for the charge separation TSs depending on whether the five low frequency torsions are treated as vibrations or rotors. The 298 K energies for the charge separation TSs at $n = 4$ and 5 are 123.5 and 104.8 kJ/mol, respectively, when the five lowest frequency vibrations are treated as rotors. When these vibrations are treated as low frequency torsions, the 298 K energies rise to 128.2 and 110.1 kJ/mol yielding a difference between the conversion values of ~5 kJ/mol. This difference between the two conversion methods along with trends in the entropies of

Table 6.5. Conversion of 0 K thresholds to 298 K enthalpies and free energies for the charge separation transition states for $Cd^{2+}(H_2O)_{4,5}$ and water loss dissociations from $Cd^{2+}(H_2O)_n$, where $n = 3 – 11$. All values in kJ/mol with uncertainties in parentheses.

Reactant	Product	ΔH_0[a]	$\Delta H_{298} - \Delta H_0$[b]	ΔH_{298}	$T\Delta S_{298}$[b]	ΔG_{298}
(3,0)	(2,0)	186 (14)	1.2 (0.4)	187 (14)	28.2 (1.3)	159 (14)
(4,0)	(3,0)	146.7 (3.9)	1.1 (0.4)	147.8 (3.9)	34.2 (1.3)	113.6 (4.1)
	TS[2+1]	126.4 (2.9)	-2.9 (0.3)[c]	123.5 (2.9)	20.5 (1.5)	103.0 (3.3)
			1.8 (0.2)[d]	128.2 (2.9)	4.7 (0.3)	123.5 (2.9)
(5,0)	(4,0)	107.1 (4.8)	2.5 (0.6)	109.6 (4.8)	42.6 (1.4)	67.0 (5.0)
	TS[2+2]	110.0 (2.9)	-5.2 (0.4)[c]	104.8 (2.9)	24.3 (1.8)	80.5 (3.4)
			0.1 (0.3)[d]	110.1 (2.9)	8.9 (0.6)	101.2 (3.0)
(6,0)	(5,0)	86.8 (4.8)	1.4 (0.5)	88.2 (4.8)	41.4 (1.4)	46.8 (5.0)
(6,1)_AA	(6,0)	67.5 (4.8)	3.5 (0.4)	71.0 (4.8)	36.2 (1.0)	34.8 (4.9)
(6,2)_4D_2AA	(6,1)	63.7 (5.8)	3.9 (0.4)	67.6 (5.8)	43.1 (1.0)	24.5 (5.9)
(6,3)_4D,DD_3AA	(6,2)	58.9 (4.8)	4.1 (0.4)	63.0 (4.8)	42.5 (1.0)	20.5 (4.9)
(6,4)_4AA	(6,3)	47.3 (4.8)	1.7 (0.3)	49.0 (4.8)	32.3 (1.2)	16.7 (4.9)
(6,5)_4AA,A	(6,4)	41.5 (4.8)	1.2 (0.4)	42.7 (4.8)	31.6 (1.3)	11.1 (5.0)

[a]Experimental values from Table 6.3. [b]Values calculated from the vibrations and rotations calculated at the B3LYP/SD/6-311+G(d,p) level (for water loss energies) and at the B3LYP/Def2TZVP level (for charge separation barrier heights). Uncertainties found by scaling the frequencies up and down by 10%. [c] Values calculated with the lowest 5 vibrations of the TS being treated as rotations. [d]Values calculated using all vibrations.

dissociation, $T\Delta S_{298}$, and the ΔG_{298} values are similar to those reported for the charge separation TSs of hydrated Zn^{2+} in Chapter 4. Namely, the $T\Delta S_{298}$ values are larger when the first five vibrations are treated as rotors thereby decreasing the ΔG_{298} values compared to results when all vibrations are used in the TS.

Conclusion

Complementing our previous article on Cd^{2+} hydration,[17] the present study examines collision-induced dissociation cross sections for $Cd^{2+}(H_2O)_n$, where n = 4 - 11, in more detail with regard to the primary charge separation products for n = 4 and 5, $CdOH^+(H_2O)_m + H^+(H_2O)_{n-m-1}$, and the sequential loss of two or three waters from the reactant complex, where n = 5 - 11. Compared to our previous study,[17] computations in the present work ensure that all low and high-energy complexes are fully converged after the frequency calculation. These additional calculations change the relative energies by less than 2 kJ/mol for all complexes investigated and did not affect our experimental thresholds and modeling parameters for water loss channels. However, the structures reported in this paper along with the conversion to 298 K energies are our most accurate.

Ordinarily, our best experimental results are believed to correspond to the measurement of primary dissociation thresholds as they have fewer uncertainties regarding the distribution of energy available to the dissociating species. However, BDEs obtained from our sequential dissociation model of higher order thresholds provide relatively good agreement with results determined from the primary dissociation channel. The sequential values are slightly higher than the primary thresholds by 1 – 16 kJ/mol, where these differences are highest for the larger values of n (as also found for $Zn^{2+}(H_2O)_n$, $n \geq 9$) and for the tertiary-secondary relative energies. The higher sequential

bond energies at larger complex sizes may indicate that there are distributions of low and high-energy complexes in these reactant beams, which would lower the primary thresholds by those excitation energies. Because such excitations affect both primary and secondary thresholds equally, it is plausible that the sequential model may be more accurate for BDEs of such complexes.

The trends in the relative BDEs for the $Cd^{2+}(H_2O)_n$ systems exhibit three distinct regions in both the experimental and theoretical values. For $n = 3 – 6$, the BDEs decrease rapidly with increasing n because the waters are directly bound to the metal, whereas for $n = 7 – 9$, the waters lost are in the second shell and form two hydrogen bonds to the first shell (AA). For $n = 10$ and 11, the simplest interpretation is that the most weakly bound water ligands are in the second shell forming a single hydrogen bond with the inner shell (A), although there is the possibility that for $n = 10$, the water lost is also AA but must share an inner shell donor with another second shell ligand.

The experimental cross sections show that charge separation occurs at $n = 4$ and 5 and possibly at $n = 3$, although definitive observation of the latter is obscured because the same products are also formed by alternative lower-energy routes. The molecular parameters for the tight TSs associated with charge separation are calculated and used to analyze the product cross sections for the CID of $Cd^{2+}(H_2O)_4$ and $Cd^{2+}(H_2O)_5$ by including the competition between water loss and charge separation reactions. Accounting for this competition is necessary for obtaining accurate bond energies of these complexes. On the basis of these experimental thresholds, the $Cd^{2+}(H_2O)_n$ system is determined to have a critical size of $n_{crit} = 4$ for the charge separation reaction. The predicted reverse Coulomb barrier for the charge separation processes at $n = 3 – 6$

systematically decreases as n increases, whereas theoretical predictions show that the barriers for the charge separation reactions at n = 3, 5, and 6 are similar in energy, while the barrier for n = 4 is much higher in energy. It appears that the forward barrier height at n = 4 is higher because of the increased stability of this reactant complex as a consequence of the 18 e^- rule. This conclusion is further validated by an increase to the experimental barrier heights for charge separation from n = 5 to 4 and by the observation that all levels of theory find a difference between the n = 3 and 4 hydration energies that is smaller than the difference between the n = 4 and 5 hydration energies, Table 6.4.

References

(1) Salomons, W.; Förstner, U.; Mader, P. *Heavy metals : problems and solutions*; Springer-Verlag: Berlin ; New York, 1995.

(2) Fergusson, J. E. *The heavy elements : Chemistry, environmental impact, and health effects*, 1st ed.; Pergamon Press: Oxford ; New York, 1990.

(3) Blades, A. T.; Jayaweera, P.; Ikonomou, M. G.; Kebarle, P. *Int. J. Mass Spectrom. Ion Processes* **1990**, *102*, 251.

(4) Blades, A. T.; Palitha, J.; Ikonomou, M. G.; Kebarle, P. *J. Chem. Phys.* **1990**, *92*, 5900.

(5) Peschke, M.; Blades, A. T.; Kebarle, P. *J. Phys. Chem. A* **1998**, *102*, 9978.

(6) Peschke, M.; Blades, A. T.; Kebarle, P. *Int. J. Mass Spectrom.* **1999**, *187*, 685.

(7) Peschke, M.; Blades, A. T.; Kebarle, P. *J. Am. Chem. Soc.* **2000**, *122*, 10440.

(8) Beyer, M.; Williams, E. R.; Bondybey, V. E. *J. Am. Chem. Soc.* **1999**, *121*, 1565.

(9) Shvartsburg, A. A.; Siu, K. W. M. *J. Am. Chem. Soc.* **2001**, *123*, 10071.

(10) Cheng, Z. L.; Siu, K. W. M.; Guevremont, R.; Berman, S. S. *J. Am. Soc. Mass Spectrom.* **1992**, *3*, 281.

(11) Barran, P. E.; Walker, N. R.; Stace, A. J. *J. Chem. Phys.* **2000**, *112*, 6173.

(12) Stace, A. J. *J. Phys. Chem. A* **2002**, *106*, 7993.

(13) Dalleska, N. F.; Tjelta, B. L.; Armentrout, P. B. *J. Phys. Chem.* **1994**, *98*, 4191.

(14) Dalleska, N. F.; Honma, K.; Sunderlin, L. S.; Armentrout, P. B. *J. Am. Chem. Soc.* **1994**, *116*, 3519.

(15) Faherty, K. P.; Thompson, C. J.; Aguirre, F.; Michne, J.; Metz, R. B. *J. Phys. Chem. A* **2001**, *105*, 10054.

(16) Thompson, C. J.; Husband, J.; Aguirre, F.; Metz, R. B. *J. Phys. Chem. A* **2000**, *104*, 8155.

(17) Cooper, T. E.; Armentrout, P. B. *Chem. Phys. Lett.* **2010**, *486*, 1.

(18) Richens, D. T. *The Chemistry of Aqua Ions*; John Wiley and Sons, Inc: New York, 1997.

(19) D'Angelo, P.; Chillemi, G.; Barone, V.; Mancini, G.; Sanna, N.; Persson, I. *J. Phys. Chem. B* **2005**, *109*, 9178.

(20) Rudolph, W. W.; Pye, C. C. *J. Phys. Chem. B* **1998**, *102*, 3564.

(21) Lee, E. P. F.; Soldan, P.; Wright, T. G. *J. Phys. Chem. A* **2001**, *105*, 8510.

(22) Hofer, T. S.; Tran, H. T.; Schwenk, C. F.; Rode, B. M. *J. Comput. Chem.* **2004**, *25*, 211.

(23) Kritayakornupong, C.; Plankensteiner, K.; Rode, B. M. *J. Phys. Chem. A* **2003**, *107*, 10330.

(24) Chillemi, G.; Barone, V.; D'Angelo, P.; Mancini, G.; Persson, I.; Sanna, N. *J.Phys. Chem. B* **2005**, *109*, 9186.

(25) Pye, C. C.; Tomney, M. R.; Rudolph, W. W. *Can. J. Anal. Sci. Spect.* **2006**, *51*, 140.

(26) Bock, C. W.; Katz, A. K.; Glusker, J. P. *J. Am. Chem. Soc.* **1994**, *117*, 3754.

(27) Katz, A. K.; Glusker, J. P.; Beebe, S. A.; Bock, C. W. *J. Am. Chem. Soc.* **1996**, *118*, 5752.

(28) Pavlov, M.; Siegbahn, P. E. M.; Sandstrom, M. *J. Phys. Chem. A* **1998**, *102*, 219.

(29) Lee, S.; Kim, J.; Park, J. K.; Kim, K. S. *J. Phys. Chem.* **1996**, *100*, 14329.

(30) Hartmann, M.; Clark, T.; vanEldik, R. *J. Mol. Model.* **1996**, *2*, 354.

(31) Hartmann, M.; Clark, T.; vanEldik, R. *J. Amer. Chem. Soc.* **1997**, *119*, 7843.

(32) Andrae, D.; Haeussermann, U.; Dolg, M.; Stoll, H.; Preuss, H. *Theo. Chem. Acc* **1990**, *77*, 123.

(33) Weigend, F.; Ahlrichs, R. *Phys. Chem. Chem. Phys.* **2005**, *7*, 3297.

(34) Carl, D. R.; Moision, R. M.; Armentrout, P. B. *J. Am. Soc. Mass Spectrom.* **2009**, *20*, 2312.

(35) Ervin, K. M.; Armentrout, P. B. *J. Chem. Phys.* **1985**, *83*, 166.

(36) Hales, D. A.; Lian, L.; Armentrout, P. B. *Int. J. Mass Spectrom. Ion Process.* **1990**, *102*, 269.

(37) Schultz, R. H.; Crellin, K. C.; Armentrout, P. B. *J. Am. Chem. Soc.* **1991**, *113*, 8590.

(38) Frisch, M. J.; Trucks, G. W.; Schlegel, H. B.; Scuseria, G. E.; Robb, M. A.; Cheeseman, J. R.; Montgomery, J., J. A. ; Vreven, T.; Kudin, K. N.; Burant, J. C.; Millam, J. M.; Iyengar, S. S.; Tomasi, J.; Barone, V.; Mennucci, B.; Cossi, M.; Scalmani,

G.; Rega, N.; Petersson, G. A.; Nakatsuji, H.; Hada, M.; Ehara, M.; Toyota, K.; Fukuda, R.; Hasegawa, J.; Ishida, M.; Nakajima, T.; Honda, Y.; Kitao, O.; Nakai, H.; Klene, M.; Li, X.; Knox, J. E.; Hratchian, H. P.; Cross, J. B.; Bakken, V.; Adamo, C.; Jaramillo, J.; Gomperts, R.; Stratmann, R. E.; Yazyev, O.; Austin, A. J.; Cammi, R.; Pomelli, C.; Ochterski, J. W.; Ayala, P. Y.; Morokuma, K.; Voth, G. A.; Salvador, P.; Dannenberg, J. J.; Zakrzewski, V. G.; Dapprich, S.; Daniels, A. D.; Strain, M. C.; Farkas, O.; Malick, D. K.; Rabuck, A. D.; Raghavachari, K.; Foresman, J. B.; Ortiz, J. V.; Cui, Q.; Baboul, A. G.; Clifford, S.; Cioslowski, J.; Stefanov, B. B.; Liu, G.; Liashenko, A.; Piskorz, P.; Komaromi, I.; Martin, R. L.; Fox, D. J.; Keith, T.; Al-Laham, M. A.; Peng, C. Y.; Nanayakkara, A.; Challacombe, M.; Gill, P. M. W.; Johnson, B.; Chen, W.; Wong, M. W.; Gonzalez, C.; Pople, J. A. Gaussian 03, Revision D.01; Gaussian, Inc.: Pittsburgh, PA, 2005.

(39) Becke, A. D. *J. Chem. Phys.* **1993**, *98*, 5648.

(40) Lee, C.; Yang, W.; Parr, R. G. *Phys. Rev. B* **1988**, *37*, 785.

(41) Schuchardt, K. L.; Didier, B. T.; Elsethagen, T.; Sun, L. S.; Gurumoorthi, V.; Chase, J.; Li, J.; Windus, T. L. *J. Chem. Inf. Model.* **2007**, *47*, 1045.

(42) Bauschlicher Jr., C. W.; Partridge, H. *J. Chem. Phys.* **1995**, *103*, 1788.

(43) Perdew, J. P. *Phys. Rev. B* **1986**, *33*, 8822.

(44) Möller, C.; Plesset, M. S. *Phys. Rev.* **1934**, *46*, 618.

(45) Boys, S. F.; Bernardi, R. *Mol. Phys.* **1970**, *19*, 553.

(46) van Duijneveldt, F. B.; van Duijneveldt, J. G. C. M.; van Lenthe, J. H. *Chem. Rev.* **1994**, *94*, 1873.

(47) Carl, D.; Chatterjee, B. K.; Armentrout, P. B. *J. Chem. Phys.* **2010**, *132*, 044303.

(48) Carl, D. R.; Moision, R. M.; Armentrout, P. B. *Int. J. Mass Spectrom.* **2007**, *265*, 308.

(49) Wilson, R. G.; Brewer, G. R. *Ion Beams with Applications to Ion Implantation*; Wiley: New York, 1973.

(50) Zhao, Y.; Truhlar, D. G. *Theor. Chem. Acc.* **2008**, *120*, 215.

(51) Zhao, Y.; Truhlar, D. G. *Accounts Chem. Res.* **2008**, *41*, 157.

(52) Rodgers, M. T.; Armentrout, P. B. *J. Chem. Phys.* **1998**, *109*, 1787.

(53) Armentrout, P. B. *J. Chem. Phys.* **2007**, *126*, 234302.

(54) Pye, C. C., personal communication, October 13, 2009.

CHAPTER 7

INFRARED SPECTROSCOPY OF DIVALENT ZINC AND CADMIUM CROWN ETHER SYSTEMS: CONFORMATIONAL INSIGHT INTO ENVIRONMENTAL REMEDIATION

Abstract

The gas-phase structures of transition metal dication (Zn^{2+} and Cd^{2+}) complexes with varying sized crown ethers, 12-crown-4 (12c4), 15-crown-5 (15c5), and 18-crown-6 (18c6), are investigated using infrared multiple photon dissociation (IRMPD) spectroscopy and quantum mechanical calculations. The measured spectra span the 750 – 1600 cm^{-1} infrared range utilizing light generated by a free electron laser and are compared to predicted spectra calculated at the B3LYP/6-311+G(d,p) or B3LYP/Def2TZVP levels of theory. Spectra with the largest and most flexible crown ether, 18c6, indicate that the crown is highly distorted, wrapping in a tight cage-like structure around both dications studied. The 15c5 adopts a folded orientation for the Zn^{2+} complex, yet is almost planar when complexed with the larger Cd^{2+} ion. The Zn^{2+}(12c4) spectrum has bands appearing at lower frequencies than the other systems, consistent with an open conformation such that the metal is exposed, lying above the center of mass

Adapted with permission from Cooper, T. E.; Carl D. R.; Oomens, J.; Steill, J. D.; Armentrout, P. B. *J. Phys. Chem. A*, **2011**, *115*, 5408.

of the crown ether ring. The open structures of the Zn^{2+}(12c4) and Cd^{2+}(15c5) complexes have implications for solvent interactions in the condensed phase. The conformation of each metal-crown complex is highly dependent on metal size, charge, and crown ether flexibility, such that a delicate balance of minimizing the metal-oxygen bond lengths, but maximizing the oxygen-oxygen distances arises. These competing influences are reflected in both the spectra and lowest-energy conformations.

Introduction

Heavy metals are used extensively in industrialized countries and their contamination of water resources has caused widespread concern over the pollution of food resources, drinking water, and eventually the atmosphere. These metals are one of the most hazardous classes of pollutants and pose a serious health concern because of their nonbiodegradablity, toxicity, and carcinogenic properties.[1] Although zinc is an essential nutrient, found in several important proteins and enzymes, its high anthropogenic usage has led to the infiltration of aqueous systems and caused levels of this metal to reach the point of contamination.[1-4] Cadmium can replace zinc in physiological binding sites, thereby deactivating their function. Because it can bio-accumulate and its discharge is 18 times higher than naturally occurring rates, the United States environmental protection agency (EPA) has classified cadmium as a priority pollutant.[5,6] For all these reasons and more, numerous remediation efforts are underway, including development of macrocycles, e.g., polyethers such as crowns, that could be used as recyclable, multidentate ligands for the selective sequestration of heavy metal ions from contaminated water. Many studies have been performed to probe the selective binding of doubly charged metal pollutants to novel crown ethers.[7-14]

According to the "best fit model",[11] crown ether selectivity is based on binding ions with radii that match well with the crown ether cavity diameter. These studies demonstrate that crown ether selectivity for metals depends on the relative metal-crown binding versus metal solvation.[15] In that regard, metal-crown complexes can be differentially stabilized in solution when the cation is partially exposed thereby making solvation of the metal sterically feasible. However, a size-matching trend is not reproduced in the gas phase,[16-19] as elucidated in several early qualitative experimental and theoretical studies.[20-23] Quantitatively, gas-phase studies using threshold collision-induced dissociation (TCID) clearly demonstrate stronger binding energies for smaller alkali metals and for larger crowns.[19,24-28] These trends can be attributed to the higher charge density of the smaller metal and the greater number of oxygen sites of larger crowns.

In addition to the thermochemistry of metal-macrocycle interactions, it is important to identify their gas-phase conformations for a complete understanding of metal selectivity and possible metal sequestration. One approach to obtain insight into such conformational data is to study complexes of singly and doubly charged metals with simple macrocyclic ligands like 12-crown-4 (12c4), 15-crown-5 (15c5), and 18-crown-6 (18c6) ethers and concomitantly determine the level of theory required to predict accurate structural and energetic values of these complexes. Numerous theoretical works have calculated such conformations and solvent effects on both singly and doubly charged metal-crown complexes.[16-19,24,29-42] Only recently has infrared (IR) action spectroscopy, specifically infrared multiple photon dissociation (IRMPD), been used as an experimental

method to address these conformational questions on isolated and solvated alkali metal crown complexes.[33,34,36-38,41]

Here, we have undertaken a systematic conformational investigation of heavy metal-crown ether complexes, namely Zn^{2+}(crown) and Cd^{2+}(crown), by means of measuring the IRMPD action spectra for the dissociation of these complexes, where crown = 12c4 (Zn^{2+} only), 15c5, and 18c6. The conformations are identified by comparing the experimental spectra to linear absorption spectra predicted by quantum chemical calculations of the low-energy structures calculated at the B3LYP/6-311+G(d,p) level for Zn^{2+}(crown) and B3LYP/Def2TZVP level for Cd^{2+}(crown). Relative energies for these complexes are calculated using B3LYP, B3P86, and MP2(full) levels with the 6-311+G(2d,2p) basis set for Zn^{2+}(crown) complexes and Def2TZVPP for Cd^{2+}(crown) complexes.

Experimental and Theoretical Methods

Mass spectrometry and IRMPD spectroscopy. A 4.7 T Fourier transform ion cyclotron resonance (FT-ICR) mass spectrometer[43-45] coupled to a beamline of the free electron laser for infrared experiments (FELIX)[46] was used to record the IRMPD spectra. Reactant ion complexes were formed by electrospray ionization (ESI) using a Micromass Z-spray source and a solution of 1mM zinc nitrate (or cadmium chloride) and 1mM crown in 50:50 MeOH:H_2O solution with a solution flow rate of ~10 μL/min. All chemicals were obtained from Aldrich. Ions were accumulated in a hexapole trap for ~4 s prior to being pulse injected into the ICR cell via an rf octopole ion guide. Before entering the ICR cell, ions are decelerated out of the octopole in such a way that they can be captured without a gas pulse and collisional heating of the ions is avoided.[45] Once

trapped in the cell, the ion of interest is mass isolated using a stored waveform inverse Fourier transform (SWIFT) excitation pulse and is expected to be in thermal equilibrium at ~300 K. Spectra were recorded over the wavelength range of 13.0 μm (770 cm^{-1}) to 6.3 μm (1580 cm^{-1}). FELIX pulse energies were around 50 mJ/macropulse of 5 μs duration. The ion of interest was irradiated for 2.5 – 3 s, which corresponds to interaction with approximately 12 – 15 macropulses. The full width at half maximum (FWHM) bandwidth of the laser was typically 0.5% of the central wavelength.

IRMPD spectra were constructed by plotting the total ionic fragmentation yield as a function of the wavenumber of the radiation. In the case of the Zn^{2+}(12c4) spectrum, the reactant ion depletion versus the wavenumber is also plotted because of the low signal-to-noise ratio in the fragmentation yield of this complex. The Zn^{2+}(12c4) reactant was formed by collisionally activating the $Zn^{2+}(12c4)_2$ dimer complex through sustained off-resonance irradiation collision-induced dissociation (SORI-CID),[47] using typical experimental parameters detailed elsewhere.[44] For the larger complexes, the C–O stretch band (1000 – 1100 cm^{-1}), which is the most intense band in these spectra, was also probed with a 5 dB attenuated laser energy to avoid saturation.

Quantum chemical calculations. Likely conformers for the Zn^{2+}(crown) complexes, where crown = 12c4, 15c5, and 18c6, were examined with a simulated annealing procedure using the AMBER (version 9) program.[48] Briefly, this procedure searches for possible stable isomers in each system's conformational space using a molecular mechanics based force field. Each isomer is subsequently optimized in NWCHEM[49] using a low level of theory, HF/3-21G.[50,51] Using the Gaussian 03 suite of programs,[52] low-lying structures for each system (~30 complexes) were further optimized

at the B3LYP/6-31G(d) level[53,54] using the "loose" keyword, which utilizes a large step size (0.01 au) and rms force constant (0.0017) to ensure a rapid geometry convergence. Unique structures remaining after this procedure were chosen for further geometry optimization and calculation of vibrational frequencies at the B3LYP/6-311+G(d,p) level ensuring structural convergence during the frequency calculation. The Zn^{2+}(crown) structures were used as starting geometries for the Cd^{2+}(crown) complexes. Here the same geometry optimization procedures were followed using the B3LYP/Def2TZVP level, where Def2TZVP is a size consistent basis set for all atoms and includes triple zeta + polarization functions with an effective core potential (ECP) on Cd having 28 electrons.[55,56] The Def2TZVP basis set and ECP were obtained from the EMSL basis set exchange.[57]

For comparison to experiment, the vibrational frequencies and intensities were calculated using the harmonic oscillator approximation at the B3LYP level and were broadened using a 20 cm^{-1} FWHM Gaussian line shape. Frequencies were scaled by 0.980, which is a slightly smaller adjustment than previous scaling factors ranging from 0.960 – 0.972 for alkali metal 18c6 and K^{+}(15c5) complexes calculated using the B3LYP level of theory and smaller basis sets, either the 6-31G(d) or 6-31++G(d,p).[34,38] Using the Gaussian 09 suite of programs,[58] single point energy calculations were carried out for the 5 – 10 most stable structures at the B3LYP, B3P86,[59] and MP2(full)[60] levels using the 6-311+G(2d,2p) basis set for Zn complexes and Def2TZVPP for Cd complexes. The relative energies between each isomer include zero point energy (ZPE) corrections to yield 0 K values and thermal corrections to 298.15 K. These corrections use the calculated frequencies scaled by 0.989, a scaling factor determined by Bauschlicher and

Partridge to give accurate ZPE corrections at the B3LYP level using a 6-311+G(3df,2p) basis set.[61]

Results and Discussion

Theoretical results. The lowest-energy structure for Zn^{2+}(12c4) is shown in Figure 7.1 as a representative for typical conformations of all M^{2+}(crown) complexes investigated. In all M^{2+}(crown) complexes, the lowest energy structures have oxygens (either 4, 5, or 6 depending on the size of the crown) directly coordinated to the metal dication. The structures differ in the dihedral angles of the crown around the charge. Rather than identify such structures by arbitrary names, we have attempted to devise a more systematic nomenclature to identify the conformations of M^{2+}(crown). This nomenclature begins with the symmetry point group in brackets, followed by a description of the crown orientation as defined by several dihedral angles. For a consistent naming of these cyclic species, the dihedrals begin at the shortest M–O bond and continue around the crown toward the next shortest M–O bond (to the right or counter-clockwise in the views shown here). If the second shortest M–O bond is an equal number of O's away, then the crown nomenclature proceeds in the same direction to the third shortest M–O bond. Bond lengths and dihedrals are presented in Table 7.1 for the low-energy conformers. Two dihedrals are used to describe if each oxygen is "up" (u) or "down" (d) from the two adjacent carbons in the ring. For O_1 in Figure 7.1, the two dihedrals measured are O_8–Zn–O_1–C_{26} and O_{22}–Zn–O_1–C_2. If the dihedrals are both ≤165° and negative and positive in sign, respectively, then the oxygen is above the two adjacent carbons and is labeled "u". If the dihedrals are both ≤165° and positive and

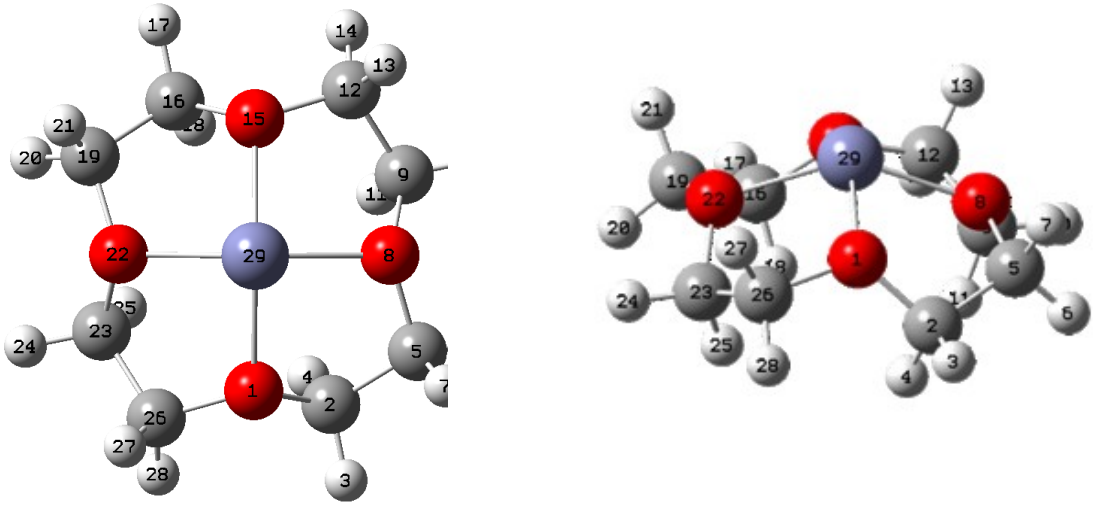

Figure 7.1. Top and side view of a low-energy structure for Zn^{2+}(12c4) calculated at B3LYP/6-311+G(d,p) with all atoms numbered.

Table 7.1. Selected geometry parameters of the most stable M^{2+}(crown) conformers optimized at the B3LYP/6-311+G(d,p) and B3LYP/Def2TZVP levels for Zn and Cd containing complexes.[a]

Complex	Structure	r(M–O) (Å)	∠MOC_RC_R (°)[b]	∠$OC_RC_RO_R$ (°)[b]	∠O_RMOC_L/ ∠O_LMOC_R (°)[b]	O•••O (Å)[c]
Zn^{2+}(12c4)	$[C_4]u_+u_+u_+u_+$	2.021 (4)	+39.5 (4)	-47.6 (4)	-151.8/+125.2 (4)	2.694 (4), 3.810 (2)
	$[C_4]u_-u_-u_-u_-$	2.021 (4)	-32.9 (4)	+47.5 (4)	-125.0/+151.8 (4)	2.695 (4), 3.811 (2)
	$[C_S]u_-u_+p_+u_-$	1.998	-47.5	+48.5	-144.7/+144.7	2.751(2), 3.450
		2.003	+28.3	-48.5	-118.4/+132.3	2.636, 3.933
		1.999	+36.3	-48.7	+169.2/-169.2	2.636
		2.003	-35.9	+48.7	-132.3/+118.4	
	$[C_1]u_-u_-u_-u_+$	1.992	-25.3	+45.1	-141.7/+131.0	2.673, 3.878, 2.677
		2.018	-30.4	+47.0	-128.1/+159.3	2.710, 3.657
		2.017	-40.5	+45.4	-110.2/+149.1	2.702
		2.039	+30.9	-43.5	-147.6/+140.1	
Zn^{2+}(15c5)	$[C_1]d_-u_+d_+u_+d_+$	2.077	-45.2	+46.7	+170.2/-163.1	2.572, 3.995, 3.823, 2.614
		2.115	+41.4	-50.3	-153.0/+142.3	2.640, 3.753, 4.111
		2.097	+38.0	-49.2	+171.6/-144.4	2.706, 3.739
		2.102	+37.3	-52.7	-142.3/+118.4	2.660

Table 7.1. continued

Complex	Structure	r(M–O) (Å)	∠MOC_RC_R (°)[b]	∠$OC_RC_RO_R$ (°)[b]	∠O_RMOC_L/ ∠O_LMOC_R (°)[b]	O•••O (Å)[c]
		2.121	+36.8	-46.8	+119.7/-151.9	
	$[C_1]d_+u_+d.d.u_-$	2.066	+36.1	-43.2	+125.3/-133.4	2.681, 3.857, 3.645, 2.706
		2.095	+40.2	-50.1	-152.8/+127.9	2.619, 4.077, 3.541
		2.074	-40.4	+45.6	+157.8/-152.9	2.632, 3.923
		2.078	-43.5	+52.3	+155.9/-129.7	2.649
		2.085	-38.1	+44.1	-114.5/+144.0	
	$[C_2]p.d.u.d.u_-$	2.047	-28.5	+38.2	-170.8/-170.8	2.590, 3.862, 3.861, 2.590
		2.010	-48.0	+52.0	+160.9/-122.3	2.647, 3.651, 4.097
		2.076	-37.1	+49.2	-119.2/+138.5	2.726, 3.650
		2.076	-33.0	+52.0	+138.5/-119.2	2.647
		2.010	-33.9	+38.2	-122.3/160.9	
Zn^{2+}(18c6)	$[D_2]p_+u_+d_+p_+u_+d_+$	2.151 (2)[d]	+12.4 (2)	-39.4 (2)	-169.9/-169.9 (2)	2.581 (3), 3.448 (3), 4.302
		2.156 (2)	+42.0 (2)	-55.1 (2)	-143.3/+96.0 (2)	2.709 (2), 3.448, 3.568, 4.137
		2.156 (2)	+50.1 (2)	-39.4 (2)	+96.0/-143.3 (2)	2.581, 4.137, 3.568

Table 7.1. continued

Complex	Structure	r(M–O) (Å)	$\angle MOC_RC_R$ (°)[b]	$\angle OC_RC_RO_R$ (°)[b]	$\angle O_RMOC_L$/ $\angle O_LMOC_R$ (°)[b]	O•••O (Å)[c]
	$[C_1]u_+d_+u\_p\_d\_u\_$	2.140[d]	+51.8	-47.8	-169.6/+145.1	2.613, 3.330, 4.284, 3.550, 2.656
		2.159	+44.2	-48.8	+107.5/-127.8	2.761, 3.232, 3.530, 4.172
		2.149	-48.0	+39.5	-104.2/+129.8	2.595, 4.141, 3.539
		2.157[d]	-12.9	+39.6	+167.4/+175.7	2.585, 3.564
		2.169	-46.7	+53.8	+149.3/-96.4	2.688
		2.149	-46.5	+49.5	-106.9/+138.1	
	$[C_2]p_+u_+d_+p_+u\_d_+$	2.122[d]	+15.9	-39.8	-176.4/-178.6	2.598, 3.530, 4.234, 3.234, 2.611
		2.145	+42.0	-54.7	-145.3/+101.3	2.690, 3.530, 3.505, 4.149
		2.145	+47.1	-39.8	+101.3/--145.3	2.598, 4.149, 3.505
		2.122[d]	+22.3	-40.1	-178.6/-176.4	2.611, 3.234
		2.151	-33.7	+44.9	-123.8/+113.9	2.755
		2.151	+41.8	-40.1	+113.9/-123.8	
Cd^{2+}(15c5)	$[C_1]d_+d\_u_+d\_u_+$	2.242	+24.6	-46.3	+162.5/-172.8	2.662, 4.301, 4.292, 2.670
		2.310	-42.0	+55.6	+147.9/-159.6	2.723, 4.372, 4.377

Table 7.1. continued

Complex	Structure	r(M–O) (Å)	∠MOC_RC_R (°)[b]	∠$OC_RC_RO_R$ (°)[b]	∠O_RMOC_L/ ∠O_LMOC_R (°)[b]	O•••O (Å)[c]
		2.282	+44.1	-55.2	-152.4/+151.2	2.724, 4.344
		2.286	-42.3	+55.8	+149.3/-147.5	2.736
		2.309	+43.2	-50.0	-151.7/+148.8	
	$[C_1]d_-u_+u_+d_-u_-$	2.249	-39.7	+51.3	+172.3/-155.5	2.688, 4.301, 4.001, 2.718
		2.306	+43.9	-52.0	-152.8/+147.7	2.767, 4.241, 4.370
		2.262	+46.1	-56.7	-154.9/+128.0	2.744, 4.278
		2.285	-39.1	+57.6	+144.3/-145.4	2.753
		2.281	-40.8	+41.8	-112.8/+154.1	
	$[C_1]u_-d_-u_-d_-d_-$	2.251	-20.8	+42.3	-159.4/+168.0	2.726, 3.820, 4.267, 2.675
		2.282	-42.3	+56.4	+146.7/-108.5	2.737, 4.301, 4.349
		2.274	-25.3	+43.3	-140.7/+161.1	2.759, 4.158
		2.275	-52.3	+52.1	+162.4/-113.0	2.748
		2.284	-45.0	+51.0	+158.8/-139.8	

Table 7.1. continued

Complex	Structure	r(M–O) (Å)	∠MOC_RC_R (°)[b]	∠$OC_RC_RO_R$ (°)[b]	∠O_RMOC_L/ ∠O_LMOC_R (°)[b]	O•••O (Å)[c]
		2.363 (2)	+43.6 (2)	-59.5 (2)	-146.4/+104.8 (2)	2.758 (2), 3.883, 4.124, 4.433
		2.366 (2)	+48.1 (2)	-44.8 (2)	+105.0/-148.8 (2)	2.683, 4.433, 4.231
	$[C_2]u_+d_+u_+d.d.u_-$	2.363[d]	+54.0	-52.8	-168.6/+147.1	2.691, 3.835, 4.723, 3.957, 2.729
		2.379	+42.9	-58.5	+116.8/-132.6	2.837, 3.835, 4.204, 4.466
		2.379	+28.2	-52.8	-132.6/+116.8	2.691, 4.466, 4.204
		2.363[d]	-35.5	+53.0	+147.1/-168.6	2.729, 3.957
		2.388	-44.5	+58.7	+146.0/-108.6	2.751
		2.388	-47.8	+53.0	-108.6/+146.0	
	$[C_1]d.d.u.p.d_+u_+$	2.344[d]	-38.9	+54.5	+150.1/-160.6	2.750, 3.970, 4.680, 3.776, 2.711
		2.351	-38.6	+58.2	+142.1/-115.6	2.746, 3.987, 4.170, 4.444
		2.371	-47.2	+45.2	-106.8/+153.6	2.682, 4.424, 4.106
		2.347[d]	-20.8	+43.9	-174.1/+172.8	2.685, 3.642
		2.359	+27.1	-49.8	+135.9/-112.1	2.802
		2.353	+35.0	-55.0	-139.3/+108.3	

[a] Values in parentheses indicate degeneracies. [b] Dihedral angle moving right (R) or left (L) from the starting atom, where right moves in the direction to the next shortest M–O bond. [c] Distance between each oxygen in the crown moving to the right from starting atom toward the next shortest M–O bond. [d] Oxygen located in the axial position of the M^{2+}(18c6) configuration.

negative, respectively, then the oxygen is below and labeled "d". If the absolute values of each dihedral are greater than 165°, then the oxygen is nearly in plane with the surrounding carbons and labeled "p". For example, these two angles are –151.8°/+125.2° for O_1 in Figure 7.1 such that O_1 is u. The u, d, and p designations are then augmented by a description of the M–O–C–C dihedral angles, which range from –50° to +50° for all complexes. The sign describes the orientation of the last carbon as either above (+) or below (–) the metal, e.g., in Figure 7.1, ∠Zn–O_1–C_2–C_5 is +39.5°. Using this method, the entire crown is circumnavigated, sequentially describing each O's orientation relative to its surrounding carbons as well as the ring torsions. The structure in Figure 7.1 has C_4 symmetry, each oxygen is up, and all ∠ZnOCC are + leading to the name: $[C_4]u_+u_+u_+u_+$. Note that we have also recorded the ∠OCCO dihedrals, typically 30 – 60° either positive or negative, in Table 7.1, but the orientation of this dihedral is almost always the opposite sign of the ∠ZnOCC dihedral and therefore is generally omitted from our naming scheme. In the Zn^{2+}(18c6) system, one high-energy isomer has a $[C_1]u_+d_{++}u_+u_+d_+p_+$ orientation, where the crown contorts so heavily around the metal that these two angles have the same direction for the second oxygen, as noted by the d_{++}.

Relative 0 K enthalpies and 298 K free energies for the low-energy isomers are calculated at three different levels of theory and given in Table 7.2 for the M^{2+}(crown) systems, where the relative 298 K Gibbs free energies may be more useful for describing the experimental distribution of conformers. There is good agreement in the trends between the DFT and MP2(full) levels for all complexes calculated.

Table 7.2. Relative calculated enthalpy (ΔH_0) and 298 K free energies (ΔG_{298})[a] (kJ/mol) of M^{2+}(crown).[b]

Complex	Structure	B3LYP	B3P86	MP2(full)
Zn^{2+}(12c4)	$[C_4]u_+u_+u_+u_+$	0.0 (0.5)	0.0 (0.5)	0.0 (0.7)
	$[C_4]u\_u\_u\_u\_$	0.1 (0.4)	0.1 (0.4)	0.0 (0.5)
	$[C_S]u\_u_+p_+u\_$	2.8 (0.0)	2.9 (0.0)	2.7 (0.0)
	$[C_1]u\_u\_u\_u_+$	6.4 (3.5)	6.6 (3.6)	7.5 (4.7)
Zn^{2+}(15c5)	$[C_1]d\_u_+d_+u_+d_+$	0.0 (0.0)	0.0 (0.0)	0.0 (0.0)
	$[C_1]d_+u_+d\_d\_u\_$	5.2 (4.6)	5.4 (4.8)	7.5 (6.9)
	$[C_2]p\_d\_u\_d\_u\_$	10.3 (9.2)	10.6 (9.5)	13.4 (12.3)
Zn^{2+}(18c6)	$[D_2]p_+u_+d_+p_+u_+d_+$	0.0 (2.7)	0.0 (2.6)	0.1 (3.2)
	$[C_1]u_+d_+u\_p\_d\_u\_$	0.4 (0.0)	0.6 (0.0)	0.0 (0.0)
	$[C_2]p_+u_+d_+p_+u\_d_+$	2.8 (1.5)	4.3 (2.9)	7.1 (6.3)
Cd^{2+}(15c5)	$[C_1]d_+d\_u_+d\_u_+$	0.0 (0.0)	0.0 (0.0)	0.0 (0.0)
	$[C_1]d\_u_+u_+d\_u\_$	15.4 (14.6)	14.8 (14.0)	14.1 (13.3)
	$[C_1]u\_d\_u\_d\_d\_$	33.9 (34.3)	33.4 (33.7)	33.3 (33.7)
Cd^{2+}(18c6)	$[C_2]p_+u_+d_+p_+u_+d_+$	0.0 (0.0)	0.4 (0.0)	1.3 (0.6)
	$[C_2]u_+d_+u_+d\_d\_u\_$	0.1 (0.8)	0.0 (0.3)	0.0 (0.0)
	$[C_1]d\_d\_u\_p\_d_+u_+$	1.8 (1.0)	2.1 (0.8)	3.5 (2.0)

[a] ΔG_{298} values given in parentheses. [b] Values are single point energies calculated at the level shown using a 6-311+G(2d,2p) basis set on Zn containing complexes and Def2TZVPP on Cd containing complexes. Geometries calculated at the B3LYP/6-311+G(d,p) level on Zn containing complexes and B3LYP/Def2TZVP on Cd containing complexes. Zero point energy corrections scaled by 0.989 are included.

12c4. As mentioned above, the Zn^{2+}(12c4) complex was not produced directly by the ESI source, but instead formed by collisionally activating $Zn^{2+}(12c4)_2$. The efficient formation of the latter dimer complex can be explained by the low energy structures calculated for Zn^{2+}(12c4) because the metal ion sits on top of the cavity of the crown, Figure 7.2. The ionic diameter of Zn^{2+} (1.56 Å)[62] is slightly larger than the cavity diameter of 12c4 (1.20 – 1.50 Å)[63] forcing the metal to sit out of the plane of the oxygens. This exposure of the metal dication should allow the zinc dication of Zn^{2+}(12c4) to undergo partial solvation in solution, which has been found to be a determining role in the selectivity of these macrocyclic ligands.[16,17,19,28,33,36,41] Such solvation was observed experimentally in the present study by the formation of Zn^{2+}(12c4)(DMF), DMF = dimethyformamide, a solvent contaminant remaining in the instrument from previous experiments, although no spectrum of this complex was taken.

The 0 K ground state (GS) structures of Zn^{2+}(12c4) have C_4 symmetry, where the crown is oriented in such a way that the local dipoles on all four oxygen point up toward the dication in either a $[C_4]u_+u_+u_+u_+$ or $[C_4]u_-u_-u_-u_-$ orientation, Figures 7.2a and 7.2b. Note that these two C_4 structures are enantiomers and therefore have the same energies and structural details. Other enantiomeric species exist for the other metal-crown complexes, but as their parameters are the same, they are not explicitly provided in any other case. The free energy GS, $[C_S]u_-u_+p_+u_-$, Figure 7.2c, has no rotational symmetry because one oxygen is oriented such that it is planar with the neighboring carbons in a p_+ orientation. In the C_S complex, the average M–O bond decreases (by ~ 0.02 Å) at the cost of smaller O–O distances. The balance of these attractive (M–O) and repulsive (O–O) interactions is evident by computing a charge distribution using a full natural bond

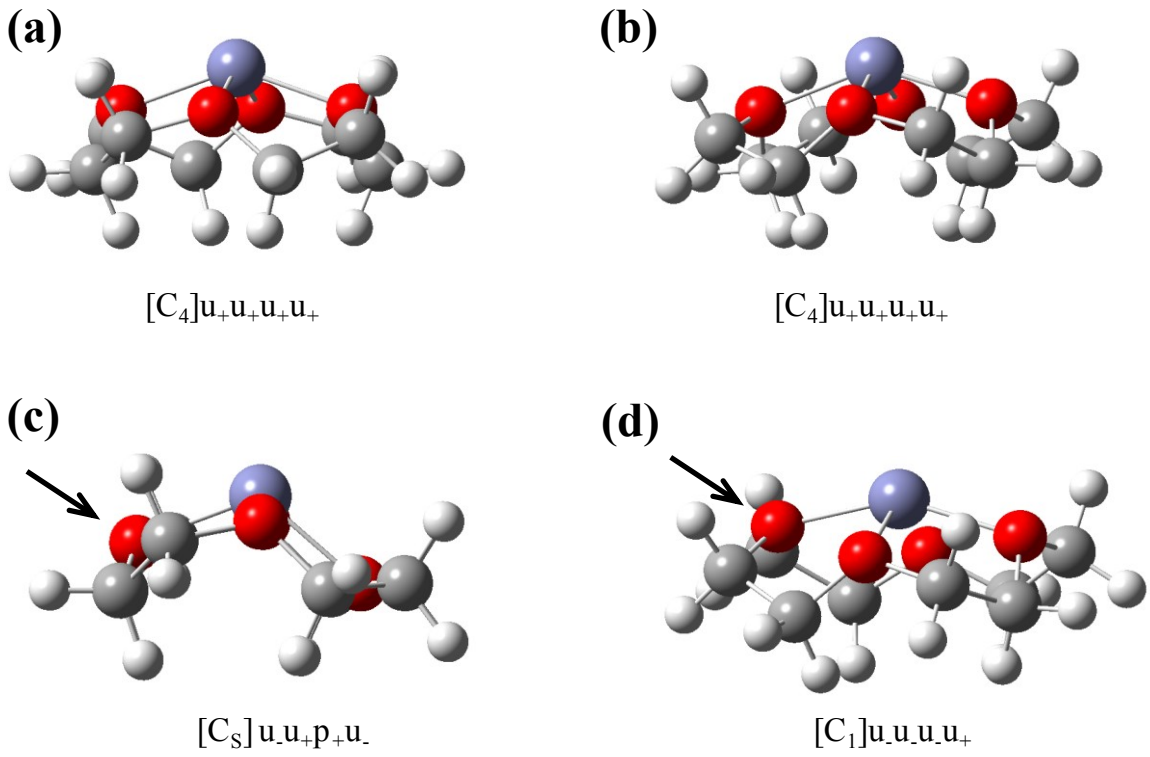

Figure 7.2. Side views of the low-energy isomers of Zn^{2+}(12c4) calculated at the B3LYP/6-311+G(d,p) level of theory. The arrow indicates the shortest M–O bond and the first oxygen in the naming scheme, r_1.

orbital (NBO) analysis[64] at the B3LYP/6-311+G(2d,2p) level, Table 7.3. In the C_S complex, the p_+ oxygen has a relatively short M–O bond length, but because of its orientation, it is much closer to the oxygen on the opposite side of the crown, Table 7.1, thereby increasing the repulsive interaction of their lone-pair electrons. As such, the remaining two O's can maximize their O–O length and have the most metal interaction from an increased electron donation of the O to the metal as evident by their higher charge in the NBO analysis. The C_4 complex allows the O's to maximize the distance from one another at the cost of longer M–O bond lengths, allowing for an even charge distribution to the binding sites of the crown, Tables 7.1 and 7.3.

The C_S and C_4 structures are within 1 kJ/mol of each other in 298 K free energy, Table 7.2. A similar C_S orientation for Li^+(12c4) was recently reported as the GS structure.[31,37] The C_4 symmetric structures are also in fairly good agreement with those calculated previously for Li^+,[30,31,35,39] which has a slightly smaller ionic radius (0.70 versus 0.78 Å for Zn^{2+}).[63] The average Zn–O bond length is larger by 0.01 – 0.12 Å compared to that for Li^+ because of the larger ionic radius of Zn^{2+}.[30,35,39] Similarly close relative energetics between the C_4 and C_S/C_1 structures of Li^+(12c4) have also been reported.[30,31,39] The $[C_1]u\_u\_u\_u_+$ structure, Figure 7.2d, is higher than the GS in 298 K free energy by 3 – 5 kJ/mol, but is similar to the $[C_4]$ structure in the crown orientation, with all O's pointing up from their surrounding carbons; however, here the M–O distances vary by up to 0.047 Å, Table 7.1.

No data was acquired for Cd^{2+}(12c4) because SORI-CID of the experimentally formed $Cd^{2+}(12c4)_2$ complexes resulted in the fragmentation and charge separation of the

Table 7.3. Natural charge from NBO analysis on the most stable M^{2+}(crown) conformers calculated at the B3LYP/6-311+G(2d,2p) level (B3LYP/Def2TZVPP for Cd containing complexes).

Complex	Structure	Natural Charge: O[a]	Natural Charge: M[b]
Zn^{2+}(12c4)	$[C_4]u_+u_+u_+u_+$	-0.681 (4)	1.513
	$[C_4]u_-u_-u_-u_-$	-0.681 (4)	1.513
	$[C_S]u_-u_+p_+u_-$	-0.682, -0.676, -0.694, -0.676	1.490
	$[C_1]u_-u_-u_-u_+$	-0.688, -0.681, -0.672, -0.678	1.505
Zn^{2+}(15c5)	$[C_1]d_-u_+d_+u_+d_+$	-0.679, -0.667, -0.675, -0.676, -0.670	1.435
	$[C_1]d_+u_+d_-d_-u_-$	-0.683, -0.676, -0.669, -0.676, -0.673	1.422
	$[C_2]p_-d_-u_-d_-u_-$	-0.686, -0.671, -0.674, -0.674, -0.671	1.424
Zn^{2+}(18c6)	$[D_2]p_+u_+d_+p_+u_+d_+$	-0.675 (2), -0.664 (4)	1.375
	$[C_1]u_+d_+u_-p_-d_-u_-$	-0.674, -0.671, -0.671, -0.677, -0.662, -0.667	1.377
	$[C_2]p_+u_+d_+p_+u_-d_+$	-0.678, -0.662, -0.662, -0.678, -0.669, -0.669	1.374
Cd^{2+}(15c5)	$[C_1]d_+d_-u_+d_-u_+$	-0.605, -0.578, -0.583, -0.584, -0.578	1.531
	$[C_1]d_-u_+u_+d_-u_-$	-0.605, -0.578, -0.589, -0.585, -0.582	1.532
	$[C_1]u_-d_-u_-d_-d_-$	-0.603, -0.579, -0.597, -0.581, -0.587	1.537
Cd^{2+}(18c6)	$[C_2]p_+u_+d_+p_+u_+d_+$	-0.590 (2), -0.569 (2), -0.571 (2)	1.500
	$[C_2]u_+d_+u_+d_-d_-u_-$	-0.580, -0.576, -0.576, -0.580, -0.569, -0.569	1.493
	$[C_1]d_-d_-u_-p_-d_+u_+$	-0.577, -0.575, -0.569, -0.589, -0.577, -0.575	1.496

[a] Natural charge of each oxygen in the crown moving to the right from the shortest M–O bond toward the next shortest M–O bond. [b] Natural charge of the metal ion.

crown forming singly charged cadmium products. As such, no calculations were performed on this complex.

15c5. The lowest-energy structures for Zn^{2+}(15c5) and Cd^{2+}(15c5) are shown in Figure 7.3. The larger cavity of 15c5 (1.70 – 2.20 Å)[63] allows Zn^{2+} to easily fit inside the crown. The attraction of the metal dication to the oxygen lone pair electrons causes the crown to distort, thereby shortening the M–O bond lengths. The lowest energy structure of Zn^{2+}(15c5) is cage-like, with the crown surrounding the ion. Thus, two oxygens lie above of the metal and the other three lie on the other side, Figure 7.3 (side view). Because two adjacent oxygens are forced to lie on the same side of the metal, there are repulsive oxygen-oxygen and local dipole-dipole interactions. Thus, one of these O's has transferred the least amount of charge to the metal ion and thus has the most negative natural charge (-0.679), as found in the NBO analysis, Table 7.3. Interestingly, this oxygen has the shortest M–O bond length, but because of the distortions of the crown, it also has the shortest O–O distances to its neighbors, Table 7.1. Higher energy conformers are fairly similar, changing in M–O bond length and the crown dihedrals as well as other less significant variations in the intermolecular distances and angles of the crown. The highest energy conformer calculated is 9 – 12 kJ/mol higher in 298 K free energy and has a symmetric C_2 axis through one of the oxygens and opposing C–C bond, [C_2]p.d.u.d.u..

The GS complex of Cd^{2+}(15c5) differs from that of Zn^{2+}(15c5) in that the crown is relatively flat. This corresponds to a good fit between the cavity size of the crown and the ion size (diameter: 1.98 Å)[62] such that the neighboring O's are allowed to maximize their distance, at the cost of longer M–O bond lengths, Table 7.1. The higher-energy

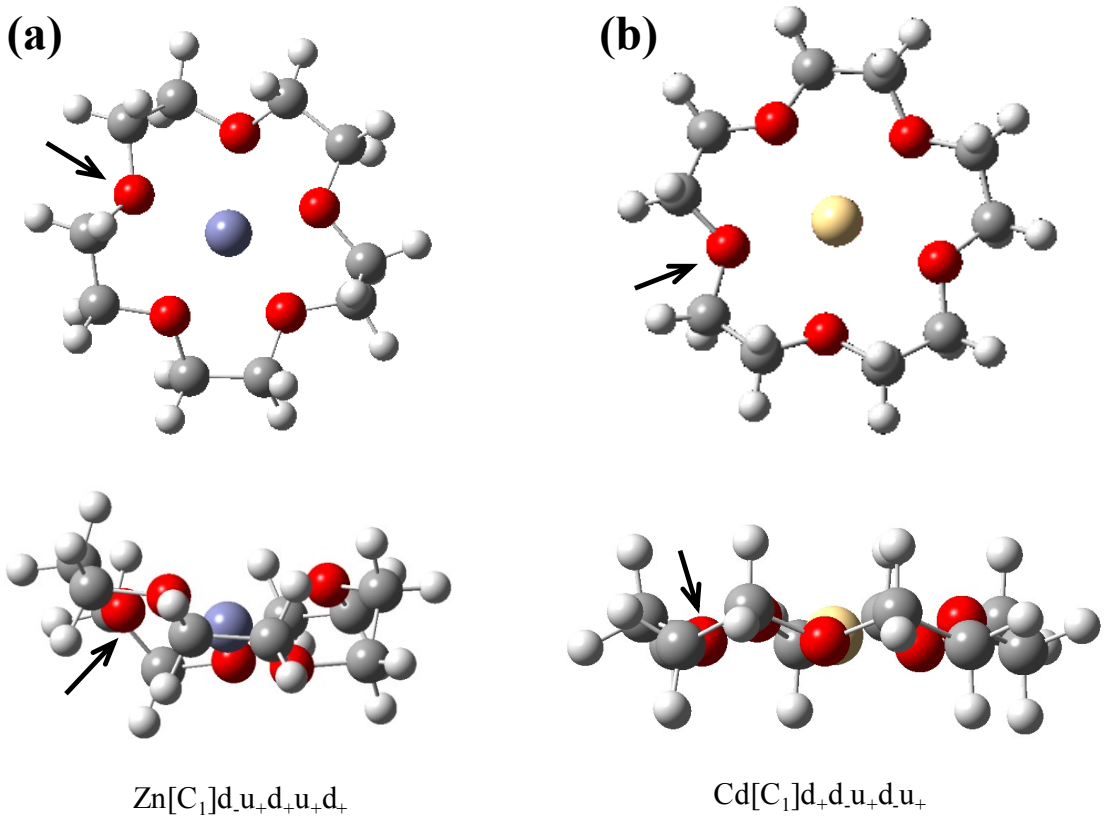

Figure 7.3. Top and side views of the low-energy isomers of Zn^{2+}(15c5) and Cd^{2+}(15c5) calculated at the B3LYP/6-311+G(d,p) and B3LYP/Def2TZVPP levels of theory. The arrow indicates the shortest M–O bond and the first oxygen in the naming scheme, r_1.

conformer, $[C_1]$d_u$_+$u$_+$d_u_, has a slightly more distorted crown that wraps around the metal ion with shorter M–O bonds in a similar fashion to the zinc GS. This forces O–O interactions both from the neighboring O's and those across the crown that now point toward each other, as evident in the more negative natural charges on the O's in the distorted crown compared to the almost planar GS structure, Table 7.3. Obviously there is a balance between the dication-oxygen attraction and the repulsive forces between the lone-pair electrons in the oxygen-oxygen interactions. The $[C_1]$u_d_u_d_d_ structure of Cd^{2+}(15c5) is close to having C_2 symmetry (similar to the $Zn^{2+}[C_2]$p_d_u_d_u_ complex discussed above) and is 33 – 34 kJ/mol higher in 298 K free energy than the near planar GS complex.

Comparing the Zn^{2+}(15c5) GS to previously reported structures for Li^+(15c5), there is a similar cage-like complex, although the Li^+ structure is slightly more flat than that of Zn.[18,35,40] Interestingly, the Zn–O bond lengths are 0.07 – 0.08 Å smaller than the average Li–O bond length using similar levels of theory.[18] Although Zn^{2+} has a larger ionic radius than Li^+, the higher charge density of Zn^{2+} causes the 15c5 to distort more than upon complexation with Li^+. Similar structural comparisons can be made between Cd^{2+} and Na^+ because the two metal ions have similar ionic radii (0.99 and 0.98 Å, respectively).[62] A recent report[35] finds that Na^+ does not fit well in the cavity of 15c5 and lies slightly above the crown with minimum and maximum Na–O bond lengths that are 0.07 and 0.09 Å, respectively, longer than corresponding minimum and maximum Cd–O distances. This is in agreement with earlier calculations from Hill and Feller on Na^+(15c5),[18] who also found that the metal sits slightly above the crown and the average Na–O distance to be 0.03 – 0.04 Å longer than the average Cd–O bond length calculated

here. These comparisons demonstrate that the match between a metal and the cavity of a crown depends on more than just the ionic radius and cavity size because the charge of the metal affects the orientation of the crown and possibly its selectivity.

18c6. Similar to the structures above, the lowest-energy conformations of Zn^{2+}(18c6) adopt configurations where the metal dication is fully enclosed by the ether O's and is located in a central binding site within the crown cavity, Figure 7.4a – c. Two structures are isoenergetic with each other at 0 K, $[D_2]p_+u_+d_+p_+u_+d_+$ and $[C_1]u_+d_+u_-p_-d_-u_-$, Table 7.2; however the highly symmetric D_2 structure is ~3 kJ/mol higher in 298 K free energy at all levels of theory. Similar to the D_2 structure is $[C_2]p_+u_+d_+p_+u_-d_+$, Figure 7.4c, which is 1 – 3 kJ/mol higher in free energy at the DFT levels (6 kJ/mol at MP2(full)), Table 7.2. Several other C_1 and C_2 structures were found to lie 3 – 22 kJ/mol higher in energy. One common factor between all structures is the similar pseudo-octahedral position of the crown oxygens around the metal ion, similar to the S_6 structure reported by Glendening et al. for Li^+(18c6).[16] For example, in the $[D_2]p_+u_+d_+p_+u_+d_+$ complex, the two p_+ oxygens form the shortest bonds to Zn and are located in the axial positions of the pseudo-octahedron with ∠OZnO of 180°. The remaining O's are in the equatorial positions with slightly longer ZnO bonds (by 0.005 Å) and ∠OZnO of 74° and 106° to the axial O's. Because of the constraints of the cyclic crown, the equatorial O's do not form a perfect octahedral orientation, but instead a sequence where oxygens alternate positions above and below the dication with ∠OZnO of 78°, 112°, and 147° to each other. For the C_2 structure, the shortest Zn–O bond lengths are again to the axial O's, while the equatorial O's are longer by ~0.02 Å, Table 7.1. In the low-energy C_1 structure, the axial positions are filled with the shortest and third longest Zn–O bonds

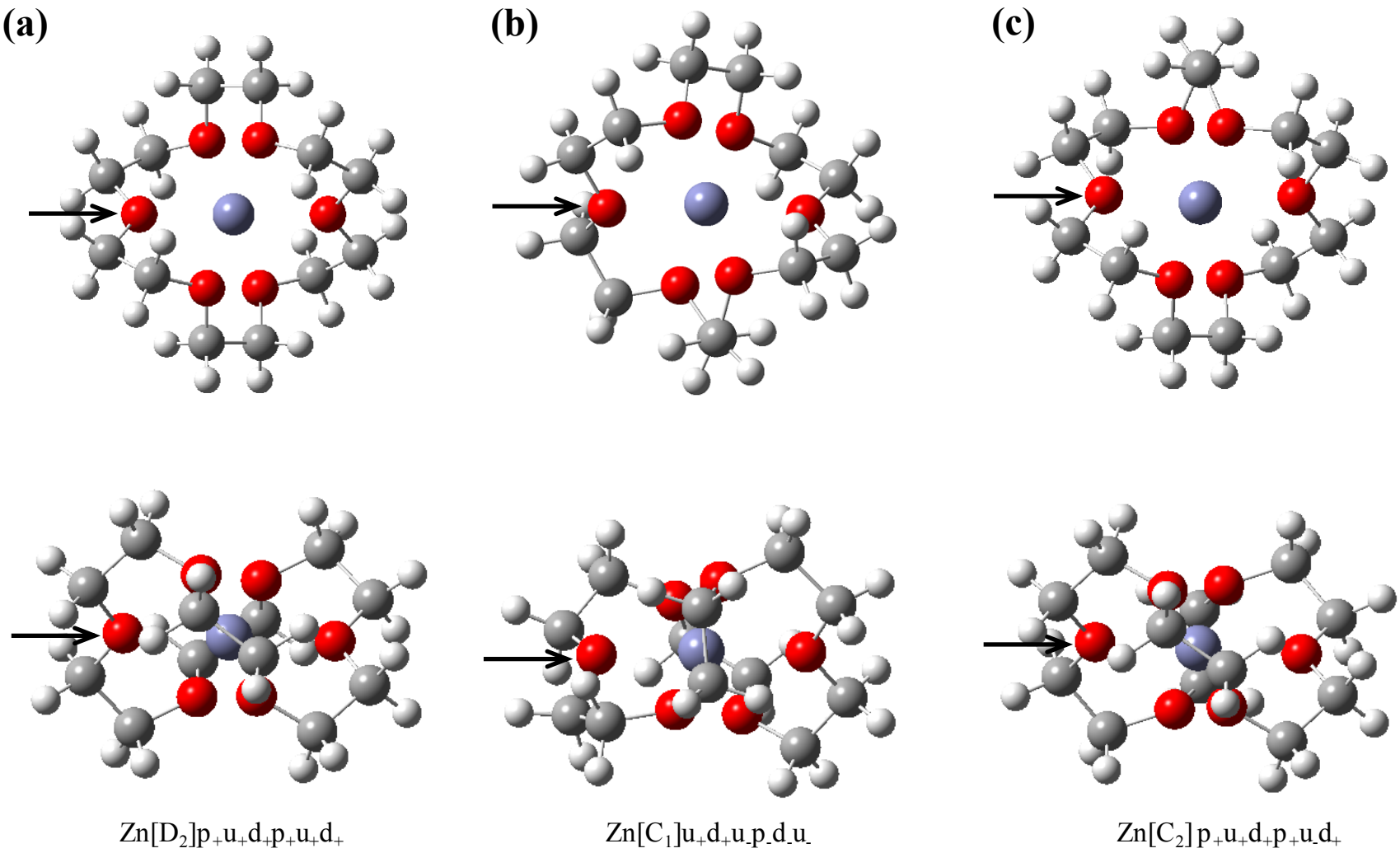

Figure 7.4. Top and side views of the low-energy isomers of Zn^{2+}(18c6) (parts a – c) and Cd^{2+}(18c6) (parts d – f) calculated at the B3LYP/6-311+G(d,p) and B3LYP/Def2TZVPP levels of theory. The arrow indicates the shortest (and also axial) M–O bond and the first oxygen in the naming scheme, r_1.

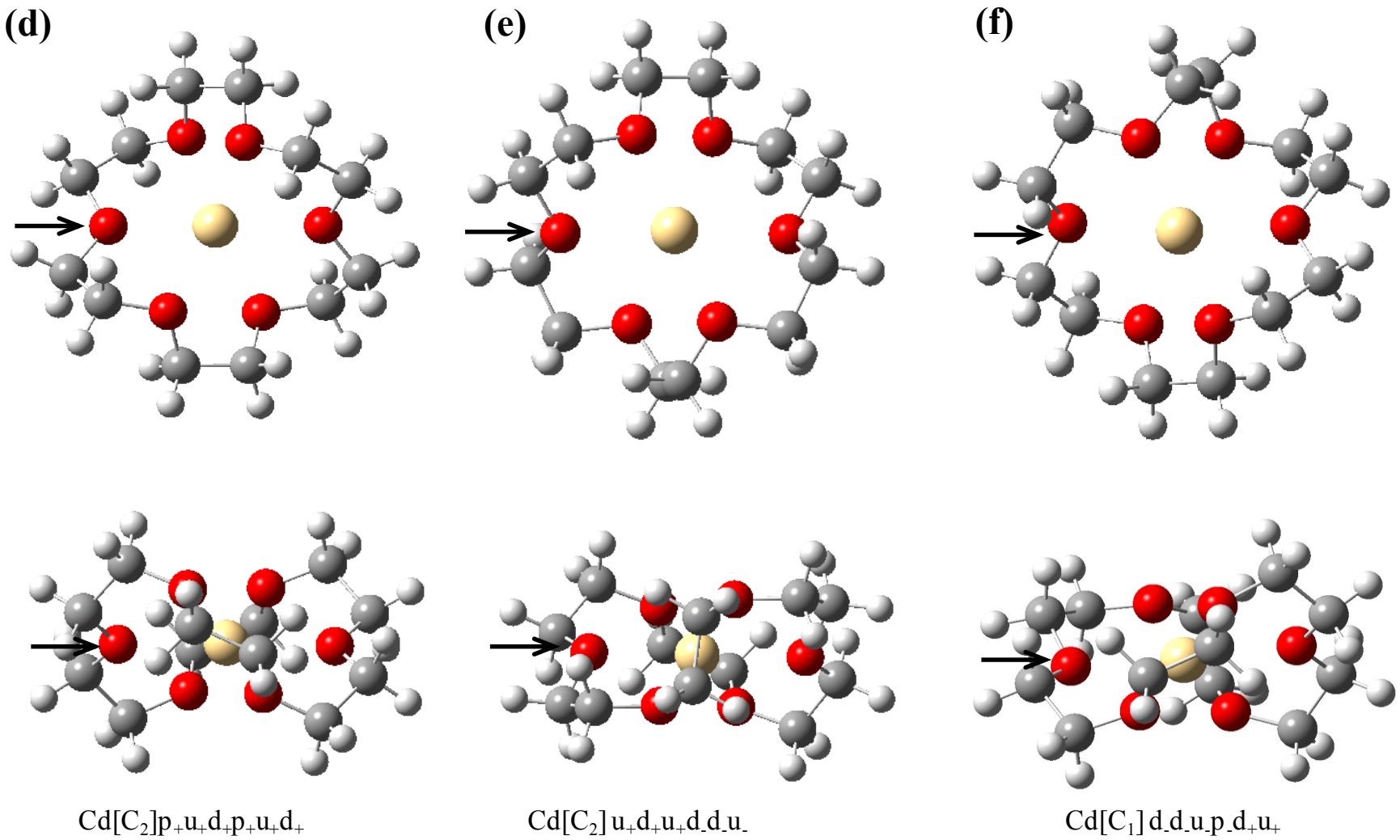

Figure 7.4. continued

(longer by 0.017 Å, Table 7.1). In all three structures, NBO analysis reveals that the axial O's generally have more negative charge than the equatorial O's because of their closer proximity to the neighboring O's, Tables 7.1 and 7.3. Instead the natural charge on the equatorial O's is less negative because they are able to maximize their distance from at least one adjoining oxygen thereby allowing an increase in the amount of electron donation to the metal.

The low-energy structures for Cd^{2+}(18c6), Figure 7.4d – f, are similar to those discussed above for Zn^{2+}. Again, the metal ion is central to the cavity of the crown coordinating to all six oxygens in a cage-like, pseudo-octahedron. The $[C_2]p_+u_+d_+p_+u_+d_+$ complex is lowest in energy at the DFT levels and is very close to having the D_2 symmetry seen for the Zn^{2+} complex. Again the p_+ oxygens have the shortest bond length to the cadmium and are 177° from each other in the axial positions. The crown is slightly less folded than the Zn^{2+} complexes because of the larger size of the cadmium ion. The ∠OCdO angles between the equatorial O's are 71°, 127°, and 139°, while the average ∠OCdO angles between the axial and equatorial oxygens are ~70° and 110°. Similar to the Zn^{2+} complexes, $Cd^{2+}[C_2]u_+d_+u_+d\_d\_u\_$ is isoenergetic with the $[C_2]p_+u_+d_+p_+u_+d_+$ complex at DFT levels and is the GS at the MP2(full) level by ~1 kJ/mol, Table 7.2. The $[C_1]d\_d\_u\_p\_d_+u_+$ is 1 – 2 kJ/mol higher in 298 K free energy and 2 – 4 kJ/mol higher at 0 K.

Several differences are noted when comparing both Zn^{2+}(18c6) and Cd^{2+}(18c6) GSs to their respective Li^+ and Na^+ counterparts previously reported in literature. Early ab-initio calculations and ion mobility experiments show that Li^+(18c6) is compact with the metal cation centrally located in the crown cavity.[16,42] A more recent report calculates

the Li^+(18c6) complex to be more severely distorted, where the cation coordinates to five of the six oxygens in the crown in an almost planar orientation and the remaining O is forced out of the plane.[35] More recently, the Lisy group found a preference for Li^+ to bind closely to three of the six oxygens in the cavity using quantum chemical theory and IR predissociation (IRPD) spectroscopy on argon-tagged Li^+(18c6) probed in the CH stretching region.[37] In contrast, Martinez-Haya et al. used IRMPD spectroscopy concentrating on the C–O stretching band to assign a symmetric D_2, cage-like folded conformer as the GS. Their quantum chemical calculations found the asymmetric open structure to be 12 kJ/mol higher in energy.[38] The Li–O bond lengths of their D_2 GS are 0.04 – 0.08 Å larger than those found for $Zn[D_2]p_+u_+d_+p_+u_+d_+$, as a consequence of the higher charge density of the Zn^{2+}. Several attempts were made to theoretically locate such asymmetric, open structures for the Zn^{2+}(18c6) complex, as reported for Li^+(18c6) and Mn^{2+}(18c6),[35-37] however, each attempt resulted in either ring cleavage or the structure would collapse to a lower energy, cage-like conformer.

In comparison to Cd^{2+}(18c6), the Na^+(18c6) GS is a relatively flat D_{3d} structure (although two C_1 structures with much shorter M–O bond lengths and slight curvature of the crown were close in energy).[38] Martinez-Haya et al. assign a significant experimental population to the folded C_1 structure with a possible contribution from the flatter, symmetric conformer.[38] In agreement with the comparisons above, upon complexation with Cd^{2+}, 18c6 prefers a more folded orientation with shorter M–O bonds (by ~0.15 Å) than those found for Na^+(18c6).

The Zn^{2+} and Cd^{2+} ions are both slightly larger than their closest alkali metal counterparts, yet have smaller M–O bonds in the 15c5 and 18c6 systems. This is a direct

reflection of the higher nuclear charge and subsequent increase in the charge density of the dications compared to the monocations. In the 12c4 system, shorter bonds were not formed because the Zn^{2+} metal ion is too large for the cavity of the crown, leading to steric hindrance. Comparing the M–O bond lengths between the Zn and Cd structures, there is about a 0.2 Å increase in the average bond length, Table 7.1, which is a reflection of the increase in the ionic radius from 0.78 to 0.99 Å. Both of these trends show that the conformation of the metal crown ether complex depends on the charge of the metal ion as well as its size, leading to possible implications on selectivity.

IRMPD spectra. Photodissociation spectra from ~750 to almost 1600 cm^{-1} are measured for 15c5 and 18c6 complexed with Zn^{2+} and Cd^{2+} along with a depletion spectrum of Zn^{2+}(12c4), Figure 7.5. For the Zn^{2+}(15c5) and Zn^{2+}(18c6) complexes, photodissociation resulted in the fragmentation and charge separation of the ring forming $ZnOH^+(C_2H_4O)_n$, where n = 1 – 3 for 15c5 and n = 1 – 4 for 18c6. The partner product of this charge separation was observed and is the $(C_2H_3)(C_2H_4O)^+$ ion, which also undergoes secondary losses of C_2H_2 and C_2H_4 groups. In both Cd^{2+} spectra, the metal containing product observed was a singly charged $[Cd(C_2H_3O)]^+$ (m/z 157 for ^{114}Cd) fragment. The direct partner product, $H^+(C_2H_4O)_n$ where n = 4 for 15c5 and n = 5 for 18c6, was not observed, but secondary crown fragments of $(C_2H_3O)^+(C_2H_4O)_2$ (m/z 131), $H^+(C_2H_4O)_2$ (m/z 89), $(C_2H_3O)^+(C_2H_4O)$ (m/z 87) were recorded. Photodissociation of 18c6 complexed with either metal also resulted in the loss of an intact ether segment, neutral C_2H_4O, to form M^{2+}(15c5). For complexes with 15c5 and 18c6, the spectra in Figure 7.5 correspond to the total relative ionic fragmentation yield as a function of laser wavelength. Spectra of individual product masses and parent ion depletion spectra were

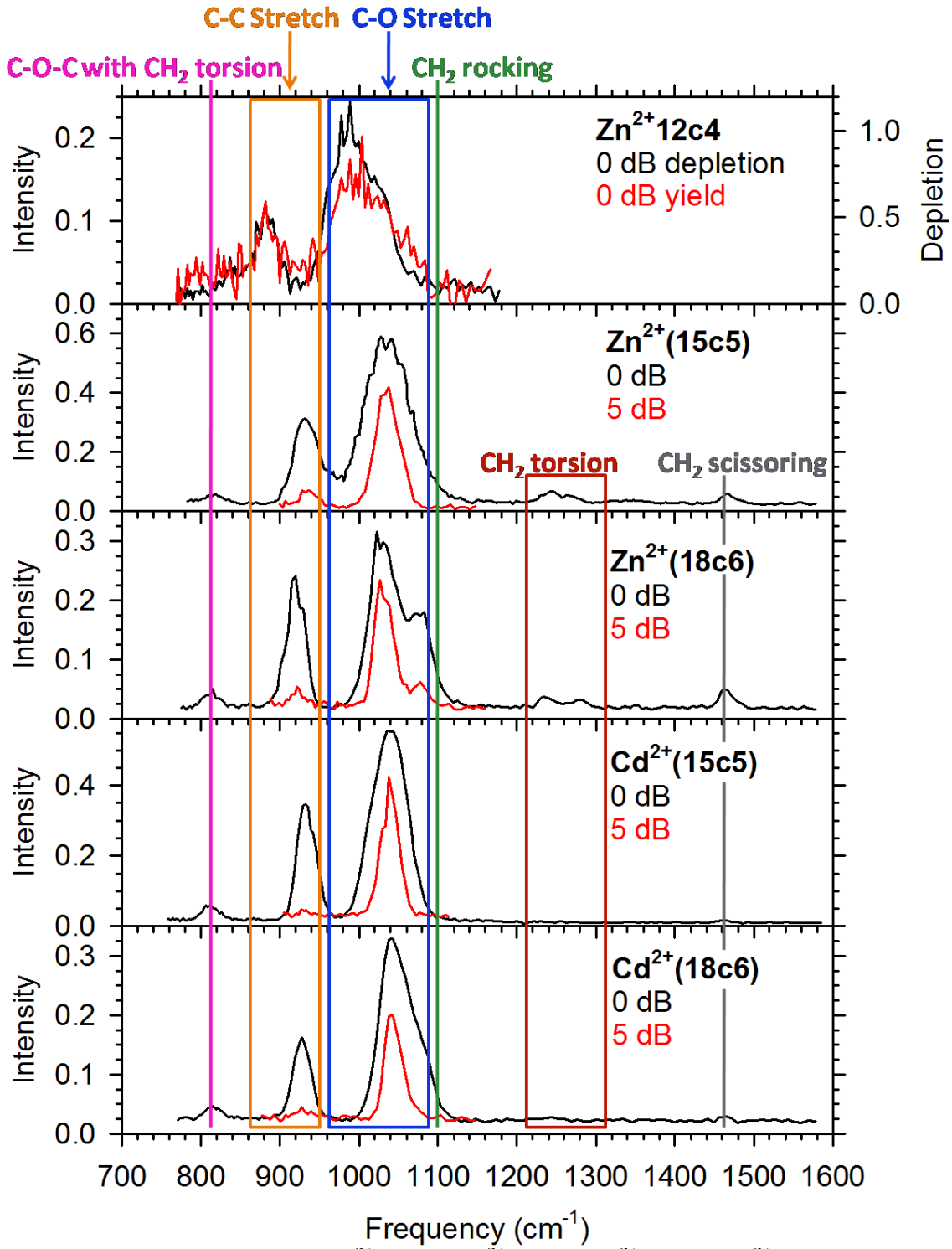

Figure 7.5. IRMPD spectra of Zn^{2+}(12c4), Zn^{2+}(15c5), Zn^{2+}(18c6), Cd^{2+}(15c5), and Cd^{2+}(18c6). The approximate motions of the various observed peaks are annotated.

also generated for comparison and are similar to those in Figure 7.5, although the relative intensities of peaks do vary among the spectra. Very few products were observed in the photodissociation of Zn^{2+}(12c4) because the reactant intensity was low and the complex is tightly bound resulting in little fragmentation, hence the depletion spectrum is also examined here. Because of these difficulties with the Zn^{2+}(12c4) system, the spectrum only spans 770 – 1180 cm^{-1}.

Assignments of the vibrational modes and of the corresponding GS structures rely on the overall agreement between the IRMPD spectra and the linear IR harmonic spectra predicted by theory, as well as previous assignments in this region for alkali crown complexes.[34,38] In each of the 15c5 and 18c6 spectra, the most intense band lies near 1040 cm^{-1}, Figure 7.5, and corresponds to the C – O stretching modes of these complexes. As such, this band provides the best probe for the coordination of the crown to the metal dication and will be the most diagnostic band used in the comparison of experimental and theoretical spectra. The peak of this band is red shifted by ~100 cm^{-1} from the neutral crown species[65] because of the partial electron transfer from the O's in the crown to the metal dication, as described by Walters et al.[66] for hydrated metal cation systems. Notably, this band is broader for Zn^{2+} complexed with 15c5 (FWHM ~ 40 cm^{-1}) than the corresponding Cd^{2+} spectrum (FWHM ~30 cm^{-1}). In the Zn^{2+}(18c6) spectrum, the C-O stretching band clearly exhibits two distinct peaks at 1025 and 1078 cm^{-1}. In the Cd^{2+}(18c6) spectrum, the main peak is centered at ~1043 cm^{-1}, but there is additional broadening on the blue side, suggestive of an incompletely resolved band.

The largest shift in the C-O stretching band is seen in the Zn^{2+}(12c4) spectrum, where the broad (FWHM ~ 80 cm^{-1}) peak is centered at ~1000 cm^{-1}, corresponding to a

red shift of ~140 cm^{-1} from neutral 12c4[65] and a shift of 25 – 43 cm^{-1} from the larger crown dication complexes. This red shift from both the neutral and the larger M^{2+}(crown) complexes is because of the increased electrostatic potential of the Zn^{2+}(12c4) complex, i.e., having fewer oxygens means each one donates more electron density to the zinc ion. Thus this complex has the shortest M–O bond lengths of all complexes calculated here, Table 7.1. Such an observation may also correspond to enhanced stability of the 12c4 complex with the Zn^{2+} ion. This stability may be understood by the $18e^-$ rule, which is fulfilled with the lone-pairs of the 4 O's in 12c4, and is also consistent with 12c4's selectivity for Li^+, as suggested by a best-fit model.[11]

The second most intense band in these spectra is attributed to the C–C stretching modes, centered near 930 cm^{-1} in the 15c5 and 18c6 spectra and 880 cm^{-1} in the Zn^{2+}(12c4) spectrum. In all spectra, the difference between the C–C and C–O stretching bands is 110 – 120 cm^{-1} (largest in the Cd^{2+}(18c6) spectrum). All remaining peaks in the spectra are quite small and do not vary appreciably as the metal or crown is changed. The peak centered near 810 cm^{-1} is a C–O–C bend coupled with CH_2 torsions; those from 1230 – 1280 cm^{-1} are CH_2 torsions; and at ~1465 cm^{-1} are CH_2 scissoring motions (referred to as bends in a previous report[38]), Figure 7.5. There may be a tail on the blue side of each C–O stretching band at ~1100 cm^{-1}, which would be attributable to a CH_2 rocking motion. Finally, there is also a possible band from 1340 – 1360 cm^{-1} corresponding to the CH_2 wagging motions of the crown, seen most clearly after magnification of the high frequency bands in the Zn^{2+}(15c5) spectrum presented below. These assignments are in agreement with those reported previously for alkali metal cation crown complexes,[34,38] although the C–O stretching bands observed here are red shifted by

20 – 40 cm^{-1} from the alkali crown complexes. This is expected because of the increased perturbation of the crown from the higher charge density of the metal dications and resulting shorter M–O bond lengths.

Comparison to theory: Zn^{2+}(12c4). For the most part, the calculated linear IR spectra of the various conformers for a given complex are very similar, such that comparisons with the experimental IRMPD spectra are shown only for the low-energy conformers of each complex. It should be remembered that the experimental IRMPD intensities need not be reproduced by the calculated one-photon absorption spectrum, but the relative intensities between bands often offer a good qualitative comparison to experiment. Perhaps the most conclusive comparison between experiment and theory is found for Zn^{2+}(12c4), Figure 7.6. Here the calculated C–O and C–C stretches of the C_4 0 K GS are at 1010 and 904 cm^{-1}, respectively, and thus is blue-shifted compared with the experimental bands at ~1000 and ~880 cm^{-1}, although this conclusion is dependent on the vibrational scaling factor applied to the theoretical spectra. Additionally, these symmetric structures have a narrow C–O stretching band, which certainly does not agree with experiment. Instead the experimental peak positions and broad asymmetric shape of the C–O band are reproduced nicely by the theoretical spectrum predicted for the free energy GS, $[C_S]u_-u_+p_+u_-$. The predicted C–O stretching bands include three relatively intense peaks at 988, 1018, and 1045 cm^{-1}, which result from combined symmetric (ν_{sym}) and asymmetric (ν_{asym}) C–O stretches of the different oxygens. The lowest frequency mode at 988 cm^{-1} is the C–O–C ν_{sym} of the u_- and opposing p_+ O's combined with motions of the ν_{asym} stretch of the u_+ and opposing u_-. The ν_{sym} of the u_- and p_+ O's pushes and pulls each oxygen toward the metal, while the ν_{asym} stretch of the u_+ and

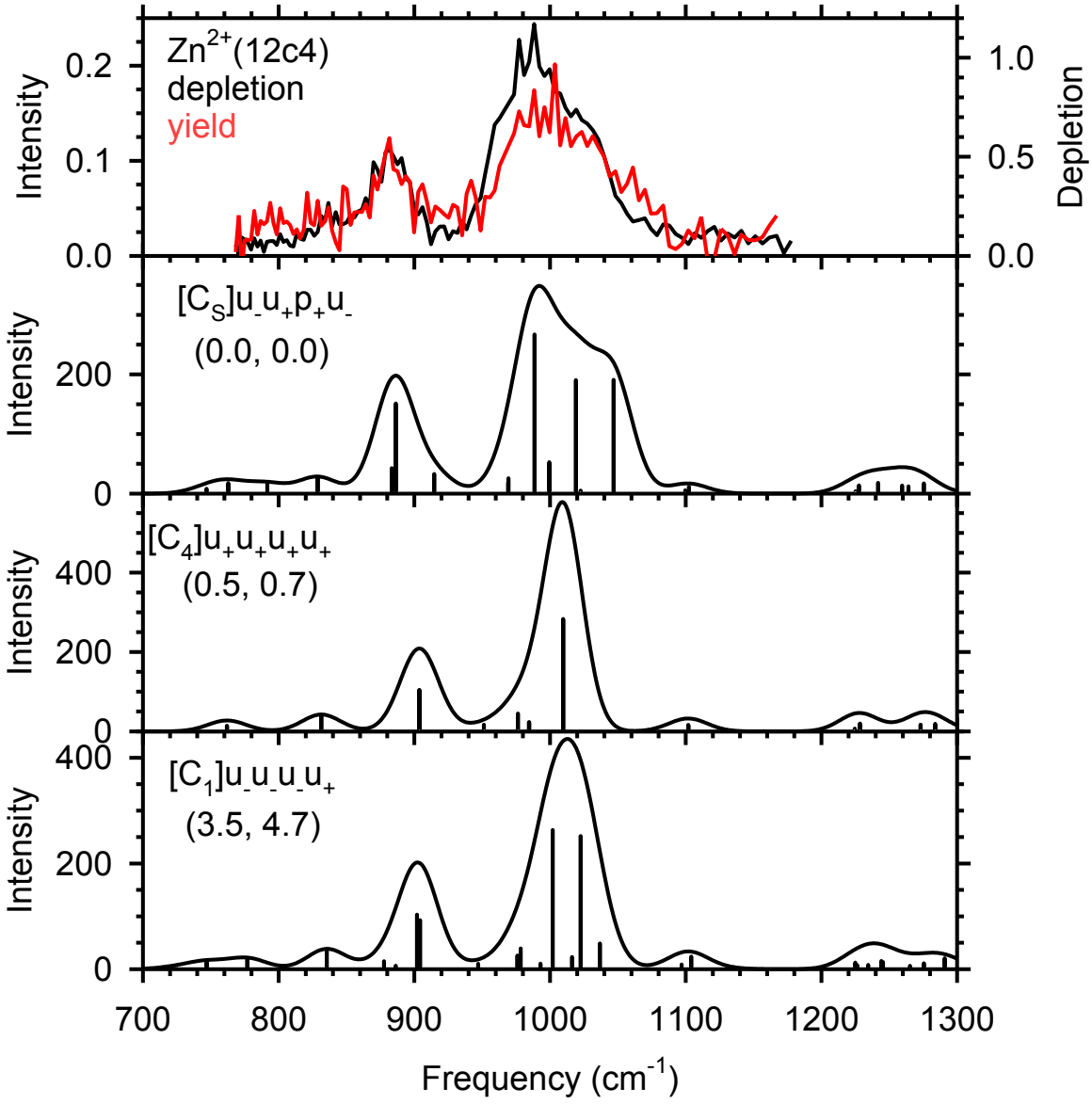

Figure 7.6. Comparison of the experimental IRMPD spectrum of Zn^{2+}(12c4) with IR spectra of three low-energy conformers predicted at the B3LYP/6-311+G(d,p) level. Relative 298 K free energies from Table 7.2 are given in parenthesis calculated at the B3LYP and MP2(full) levels using a 6-311+G(2d,2p) basis set.

opposing u_- O's displaces each oxygen in a side-to-side movement away from its neighbors. These motions combine to maximize the distances from each neighboring oxygen thereby maximizing the attractive interactions with the metal, leading to greater electron transfer from the oxygens to the metal, Table 7.3, thereby explaining the lower frequency. This explains the 20 cm^{-1} red shift from the C–O stretching band in the symmetric C_4 complexes. The two higher frequency modes in the C_S spectrum at 1018 and 1047 cm^{-1} are the ν_{asym} motions of the opposing u_- and p_+ O's, which are forced to interact more with each other and with their neighbors, as described above. The 1047 cm^{-1} band is a large side-to-side ν_{asym} motion of the p_+ oxygen and smaller side-to-side motions of the two neighboring O's. These motions combine to alternately bring the p_+ oxygen closer to one of its O neighbors. The NBO analysis reveals that this p_+ oxygen donates the least amount of charge to the metal (most negative natural charge, Table 7.3) because it has the closest O–O distances to its neighbors (2.636 Å, Table 7.1). This maximizes the O–O repulsive force, leading to the highest frequency C–O stretch observed. The 1018 cm^{-1} band corresponds to a similar movement of the u_- oxygen with the shortest bond, which has the second most negative natural charge and lies on the opposite side of the p_+ oxygen, again leading to a blue shift in the C–O stretch compared to the C_4 complex. This u_- oxygen has longer O–O distances to its neighbors than the p_+ oxygen by 0.115 Å, Table 7.1, explaining the red shift from the similar motions of the p_+ oxygen.

The predicted C–C stretch of the C_S complex at 885 cm^{-1} is also in excellent agreement with experiment, and the relative intensities of the two bands are predicted well by the C_S complex, Figure 7.6. The $[C_1]u_-u_-u_-u_+$ structure is 4 – 5 kJ/mol above the

298 K free energy GS. The C–O and C–C stretches are higher in frequency than experiment by ~20 cm^{-1} and the predicted C–O band shape does not match well.

The good agreement between the positions, relative intensities, and shapes of the bands in the experimental spectrum compared to those predicted for the C_S structure suggests that the vibrational scaling factor applied here is accurate. The C_4 complexes are predicted to be < 1 kJ/mol higher in 298 K free energy such that they could each comprise ~30% of the reactants at 300 K if an equilibrium distribution were present. Some contribution of the C_4 complexes cannot be ruled out because of spectral overlap. Contributions from the higher energy C_1 structure also cannot be ruled out for similar reasons, although this complex is 3 – 5 kJ/mol in 298 K free energy above the GS, such that an equilibrium distribution predicts it should comprise only 6 – 8% of the reactants at 300 K.

Comparison to theory: 15c5. The experimental spectra for Zn^{2+}(15c5) and Cd^{2+}(15c5) are quite similar to one another with C–O and C–C stretching bands that peak at ~1040 and 930 cm^{-1}, respectively, Figures 7.7a and 7.7b. As noted above, the Zn^{2+}(15c5) spectrum has a broader C–O stretching band than that in the Cd^{2+} spectrum. This difference is nicely predicted by the theoretical GS spectra. For Zn^{2+}(15c5), the GS is $[C_1]d_-u_+d_+u_+d_+$, which has a C–O stretching band that is in good agreement with experiment in both its position and shape, Figure 7.7a. There are two intense vibrations at 1024 and 1037 cm^{-1} and several higher frequency vibrations reproducing the broader shape of this experimental band. Similar to the vibrations described in the Zn^{2+}(12c4) complex, the lowest frequency stretch maximizes the attractive M-O and minimizes repulsive O-O intermolecular forces through a combination of ν_{sym} and ν_{asym} movements

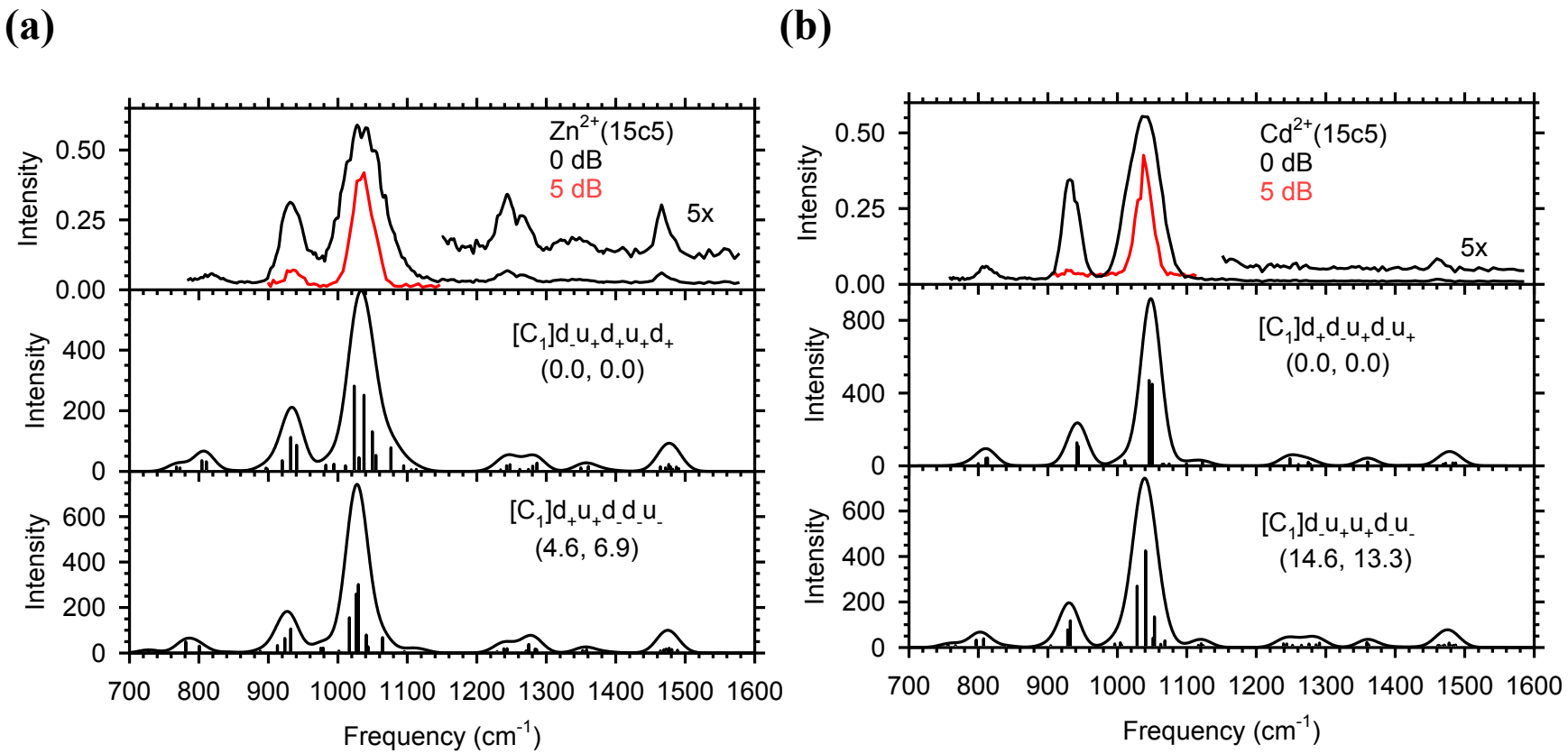

Figure 7.7. Comparison of the experimental IRMPD spectra of Zn^{2+}(15c5) and Cd^{2+}(15c5) with IR spectra of two low-energy conformers predicted at the B3LYP/6-311+G(d,p) and B3LYP/Def2TZVP levels. Relative 298 K free energies from Table 7.2 are given in parenthesis calculated at the B3LYP and MP2(full) levels.

of the different oxygens. The highest frequency bands are a series of v_{asym} movements where the oxygens with the most negative natural charge move toward each other. Exact assignment of these stretches is complicated because the crowns are cyclic and there is a CH_2 rocking motion overlaid in the higher frequency C–O stretches. The predicted GS spectrum agrees well with experiment in all other regions as well, including the C–C stretch at ~930 cm^{-1} and weak bands at ~ 810, 1250, and 1470 cm^{-1}.

As mentioned above, the peak of the CH_2 wagging mode at ~1340 cm^{-1} is visible in the Zn^{2+}(15c5) spectrum after magnification of the high frequency bands. The position of this band agrees within 10 cm^{-1} of the predicted band of either low-energy isomer. The $[C_1]d_+u_+d.d.u_-$ conformer is 5 – 7 kJ/mol higher in 298 K free energy, with a similar predicted spectrum as the GS because of the similar metal-crown binding motif. The C–O stretching band peaks at 1027 cm^{-1}, a red shift of ~10 cm^{-1} from both experiment and the predicted GS spectra, probably because the M–O bond lengths of this complex are slightly shorter compared to the GS. This band is also slightly narrower (FWHM ~ 20 cm^{-1}) than either the C_1 GS (FWHM ~ 30 cm^{-1}) or experiment (FWHM ~ 40 cm^{-1}). Also, the peak for the C–O–C bending with CH_2 torsions is shifted to the red by 20 cm^{-1} from the GS (~25 cm^{-1} from experiment). Overall, the experimental spectrum is in excellent agreement with that of the predicted GS, but because the deviations from the higher energy spectrum are minor, contributions to the experimental spectrum from the $[C_1]d_+u_+d.d.u_-$ cannot be ruled out by spectral comparison, although its population in an equilibrium distribution is only 6 – 13%.

Comparing the Zn^{2+} and Cd^{2+} experimental spectra, the shape of the C–O stretching band is narrower in the Cd^{2+} system, as mentioned above. This is explained by

the low-energy structure for Cd^{2+}(15c5), which adopts a less folded binding motif than the Zn^{2+} complexes. The GS complex at all levels of theory has all O's in almost the same plane as the centrally located cadmium. Because of this, the crown can maximize the average distance between each neighboring oxygen, at the cost of a longer average M–O distance. The two main vibrations in the predicted spectra are side-to-side ν_{asym} movements of the different O's such that no oxygen is displaced closer to the metal ion, in contrast to the combination of ν_{sym} and ν_{asym} stretches described above. Consequently, the C–O stretching band of the GS is narrow, in agreement with the shape of the experimental band, Figure 7.7b. The C–O stretching peak is at 1045 cm^{-1}, agreeing within 5 cm^{-1} of experiment. The other obvious peaks in the experimental spectrum are the C–C stretch at 930 cm^{-1} and C–O–C bend with CH_2 torsions at 810 cm^{-1}. Both agree nicely with the predicted band positions and shapes of the GS, as does the minor band near 1460 cm^{-1}, the CH_2 scissoring motion.

The higher energy conformer of Cd^{2+}(15c5) has a slightly more distorted crown that wraps around the metal more with closer M–O bond lengths causing a red shift of the C–O stretching frequencies from the GS spectrum, and broadening from higher frequencies because of the unfavorable O–O interactions, as discussed above for Zn^{2+}(15c5). The predicted spectra of both conformers are sufficiently similar that no definitive conclusion can be drawn by spectral comparisons alone. The $[C_1]d_-u_+u_+d_-u_-$ is the lowest excited conformer in free energy, but still higher than the GS by 13 – 15 kJ/mol, Table 7.2, suggesting that excited conformers are not appreciably populated for this system (< 0.5%).

Comparison to theory: 18c6. The three lowest free energy conformers of Zn^{2+}(18c6) reproduce the experimental spectra well with minor deviances in both the D_2 and C_2 predicted spectra, Figure 7.8a. Good overall agreement with experiment is found when comparing the spectrum for $[C_1]u_+d_+u\_p\_d\_u_-$, which is favored by 2 – 6 kJ/mol in 298 K free energy over the D_2 and C_2 complexes, Table 7.2. The C–O stretching band has two obvious peaks in the experimental spectrum centered at 1025 and 1080 cm^{-1}. This splitting of the C–O band is reproduced in the predicted spectrum of the $[C_1]u_+d_+u\_p\_d\_u_-$ with similar band positions after convolution (1023 and 1080 cm^{-1}), shapes, and relative intensities, Figure 7.8a. The most intense C–O stretch after convolution is at 1023 cm^{-1} and consists of two motions, each being fairly intense. The lowest frequency vibration at 1019 cm^{-1} consists of a ν_{sym} stretch of the axial O's, where each oxygen is pulled closer to the metal ion, and a side-to-side ν_{asym} of the equatorial O's. Remarkably, these motions combine to maximize the Zn–O attraction while minimizing the O–O distances. The second motion of this peak is located at 1032 cm^{-1} and is the ν_{asym} stretch of one axial oxygen (which has the shortest M–O bond length) as well as two equatorial O's in a combined motion that maximizes the distance between the axial and equatorial O's but minimizes the distance between the two equatorial O's. The highest frequency peak at ~1080 cm^{-1} consists of the side-to-side ν_{asym} of the axial and equatorial O's thereby creating an overall motion that brings the axial O's closer to neighboring lone pairs and increasing intermolecular repulsive forces. Similar splitting is seen in the C-O bands of the D_2 and C_2 complex spectra, where the main lower frequency C–O stretches agree with experiment, but the higher frequency peaks are shifted slightly, in both cases because of differences in the M–O bond lengths. The D_2 complex has the longest axial

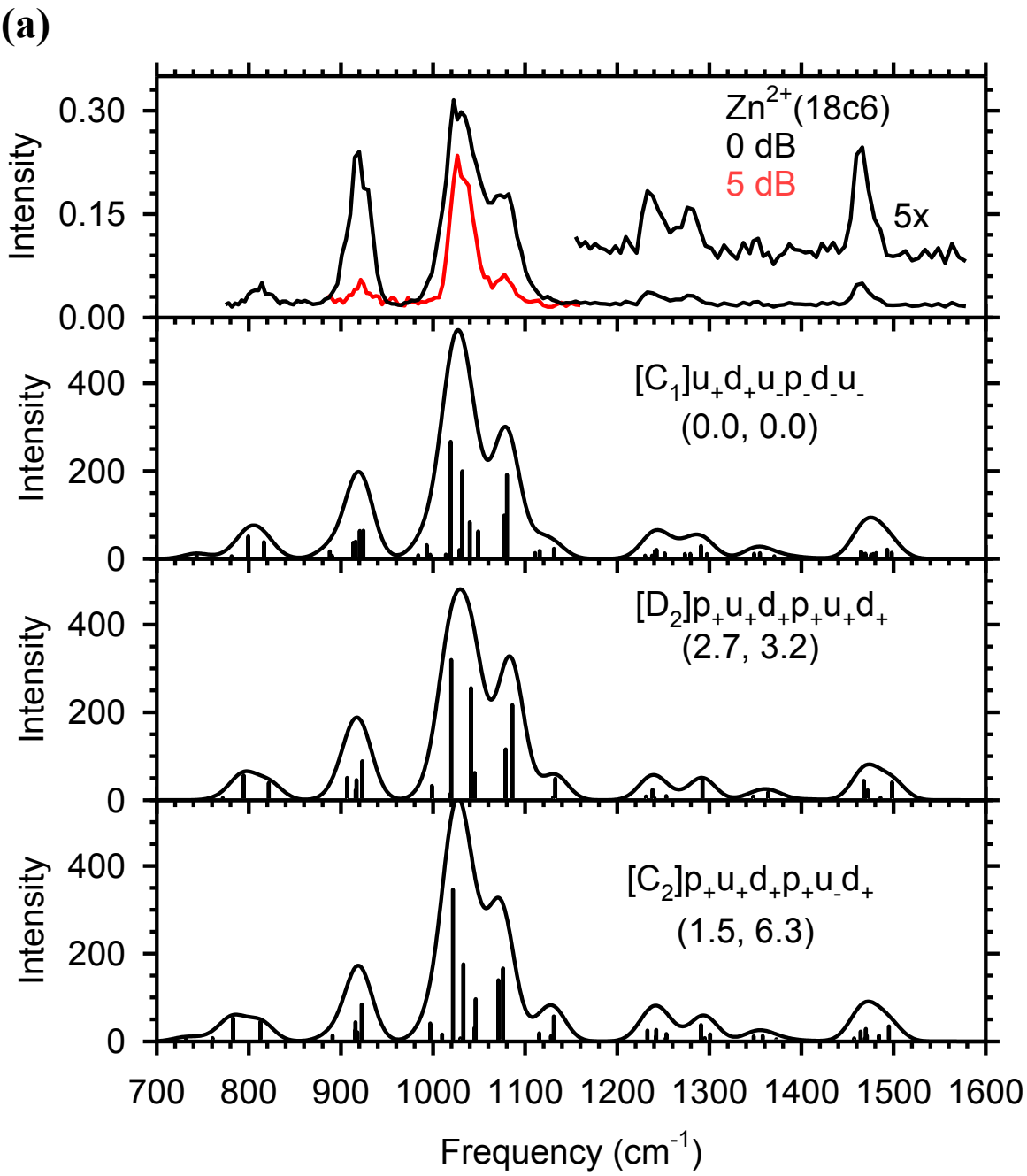

Figure 7.8. Comparison of the experimental IRMPD spectra of Zn^{2+}(18c6) and Cd^{2+}(18c6) with IR spectra of three low-energy conformers predicted at the B3LYP/6-311+G(d,p) and B3LYP/Def2TZVP levels. Relative 298 K free energies from Table 7.2 are given in parenthesis calculated at the B3LYP and MP2(full) levels.

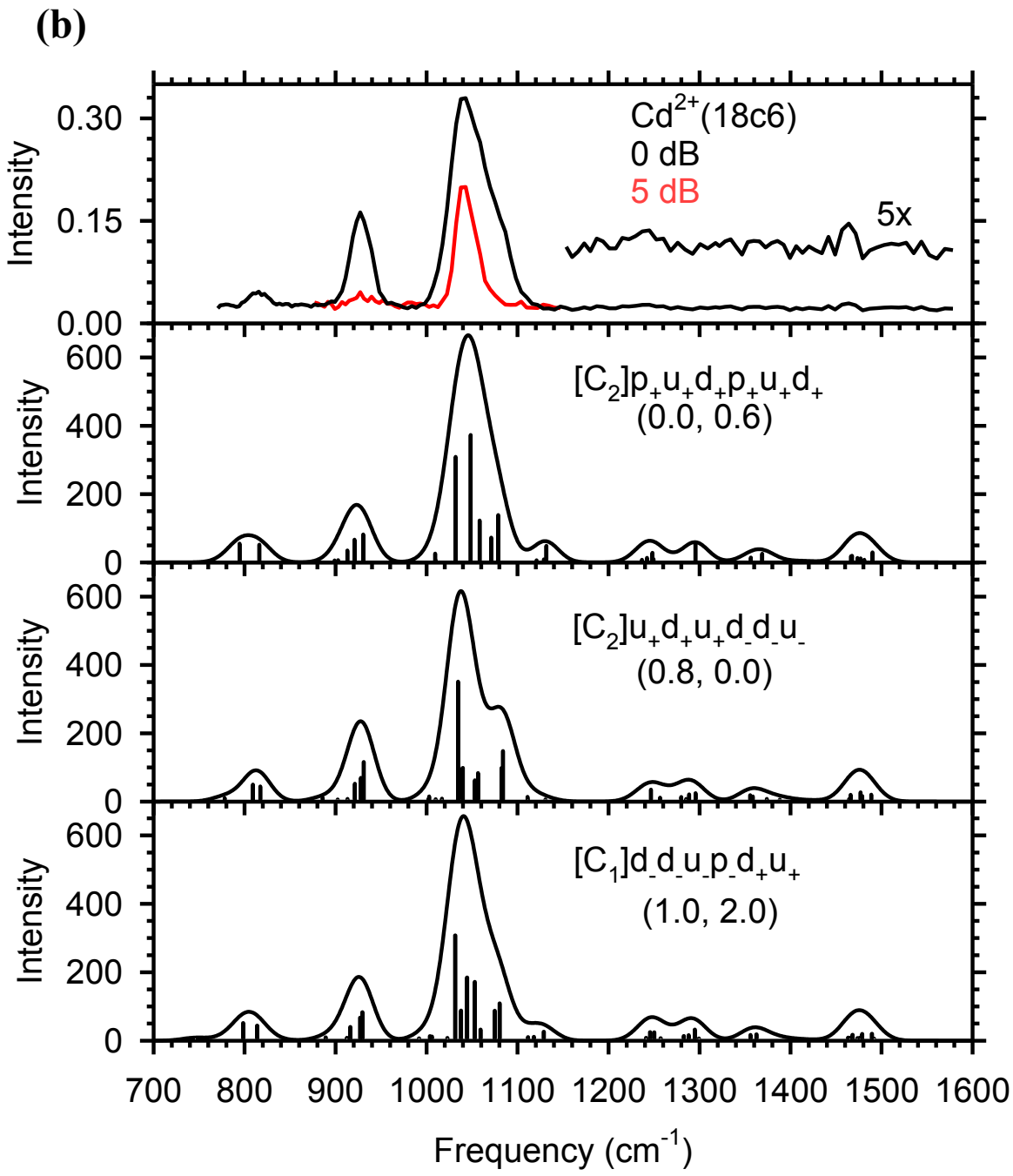

Figure 7.8. continued

Zn–O bond lengths, Table 7.1, and its band is centered at 1085 cm^{-1}, while the C_2 complex has the shortest axial Zn–O bond length and the band shifts down near 1075 cm^{-1}. Overall, these shifts in band position are not significant enough to make a definitive assignment.

The minor bands in the predicted $[C_1]u_+d_+u\_p\_d\_u_-$ spectrum also reproduce the experiment nicely, Figure 7.8a. In the experimental spectrum, there is a tail on the blue side of the C–O stretching band at ~1120 cm^{-1} in the 0 dB spectrum, which may be assigned to a CH_2 rocking motion, although exact assignment is difficult because this motion is fairly weak and not resolved experimentally. In the $[C_1]u_+d_+u\_p\_d\_u_-$ spectrum, this band is reproduced in position, shape, and intensity relative to the main C–O stretching band. In both symmetric structures, this CH_2 rocking motion is overestimated in intensity and occurs at slightly higher frequencies thereby splitting from the C–O stretching band more than found in the experiment. The C–O–C bend with CH_2 torsions band at 810 cm^{-1} has a narrow band shape more similar to the C_1 structure than the broader bands of either the D_2 or C_2 complexes. The CH_2 torsions bands centered at 1225 and 1280 cm^{-1} are reproduced nicely in the C_1 spectrum, whereas the D_2 and C_2 spectra have peaks that are more split and are centered at 1235 and 1295 cm^{-1}, although these differences are minor. In all three theoretical spectra, the C–C stretching and CH_2 scissoring modes agree with experiment in band positions (within 5 cm^{-1}) and shapes. Clearly the $[C_1]u_+d_+u\_p\_d\_u_-$ spectrum alone reproduces the experiment over the entire wavelength region, however, because of similarities in the structures and predicted spectra, contributions from the more symmetric conformers cannot be ruled out on the basis of spectral comparisons alone. All three structures have similar energies, and it is

likely that all three are formed experimentally. In an equilibrium distribution, the [C_1] complex is expected to comprise ~60% of the reactant beam while the symmetric structures each contribute ~20% using DFT energies; however at the MP2(full) level, the [C_2] complex rises in 298 K free energy and should not be appreciably populated (< 6%). Only the conformers much higher in energy can be intrinsically ruled out from spectral comparisons, although these are not explicitly compared here because of the large number of high-energy isomers.

In the Cd^{2+}(18c6) system, the main C–O stretching band shifts (~20 cm^{-1}) to slightly higher frequencies than the Zn^{2+}(18c6) species, but the higher frequency band remains at similar frequencies, such that the C–O band is no longer obviously split, Figure 7.8b. The lack of splitting in this system is not surprising considering that Cd^{2+}(18c6), although forming the pseudo-octahedron structure, is not as tightly folded as the Zn^{2+}(18c6) conformers and maximizes the O–O distances, as discussed above. Although the motions of the C–O stretching band are similar to those described above for Zn^{2+}(18c6), the intermolecular M–O distances are much longer, causing less splitting of the C–O stretching band from the different combined motions. In addition, compared to the three low-energy Zn complexes, NBO analysis reveals less electron transfer to the Cd metal (evident by its more positive charge) and a more equal charge distribution between the axial and equatorial O's. In [C_2]$u_+d_+u_+d_-d_-u_-$, two equatorial O's are closer together than the other two structures, which causes the slightly larger splitting in this spectrum for reasons outlined above in the Zn^{2+} system.

Similar to the Zn^{2+}(18c6) system, the lowest three conformers of Cd^{2+}(18c6) are within 2 kJ/mol in 298 K free energy. For all these complexes, the spectra are similar

varying only slightly in the C–O stretching region because of minor differences in the M–O bond lengths and O–O interactions as well as in the CH_2 rocking motion. The $[C_2]u_+d_+u_+d\_d\_u\_$ structure has the smallest predicted CH_2 rocking contribution near 1120 cm^{-1}, similar to experiment; however, because the experimental spectrum has very little contribution from any minor bands, drawing conclusions on the basis of these bands may not be accurate. Because the binding motifs and energetics of these structures are so similar, no definitive conclusions can be drawn regarding any structural or symmetric preferences for this system, although it is apparent that the most stable binding configuration of the 18c6 complexed with a metal dication has been located within a broad class. Namely, the crown is highly distorted forming a tight cage around the dication with O's in an axial position ~180° from each other and the remaining four O's along the equator in alternating positions below and above the metal, Figure 7.4d – f.

Comparison to alkali–crown counterparts. It appears that the main contribution to the Zn^{2+}(12c4) spectrum is from the C_S structure, which is predicted as the 298 K free energy GS by all levels of theory used here. The assignment of a C_S GS is in agreement with previous experimental and theoretical work on the analogous Li^+(12c4) complex.[31,37] As mentioned above, Zn^{2+}(12c4) has the lowest frequency C–O stretching band of all systems studied here, which can be understood by the fulfillment of the 18e-rule, and possible size selectivity for the Zn^{2+} metal similar to 12c4's selectivity for Li^+.[11] Armentrout and coworkers also observed an usually high binding energy of Li^+ to 12c4, much greater than that for Na^+(18c6), but were unable to experimentally form the 15c5 and 18c6 complexes of Li^+ for comparison in the binding energies.[19]

Except for the Zn^{2+}(12c4) system, the Zn^{2+}(18c6) spectrum has the most red shifted C–O stretching band, almost 20 cm^{-1} larger than that of the Cd^{2+}(18c6) spectrum. Likewise, a similar red shift was seen in the C–O stretching band of Li^{+}(18c6) compared to Na^{+}(18c6).[38] The relative positions of these two bands in the Zn and Cd spectra may be explained by the qualitative trend described by Armentrout and coworkers in their quantitative thermodynamic studies of alkali (Na^{+}, K^{+}, Rb^{+}, Cs^{+}) crown (12c4, 15c5, 18c6) complexes, where a consistent energetic preference for the smallest metal in the largest crown was found.[19] Armentrout and coworkers also reported only a slight increase (0.02 eV) in the binding energy of Na^{+}(18c6) compared to Na^{+}(15c5). This agrees qualitatively with the similar peak positions of the C–O stretching bands in the Cd^{2+}(15c5) and Cd^{2+}(18c6) spectra.

As discussed above, the broadening and splitting of the C–O stretch band seen in the Zn^{2+}(18c6) and Cd^{2+}(18c6) spectra is a consequence of a more tightly folded complex. The crown distorts heavily around the metal such that the combined motions of the different oxygens causes a broadening of the band from maximizing M–O attractive forces and minimizing O–O repulsive forces. Similar to these observations, the C–O stretch in the Li^{+}(18c6) and Na^{+}(18c6) spectra are both broad and the structures assigned are folded, whereas the larger K^{+} ion has a narrow C–O stretching band indicating a flatter structure.[38] In both cases, this band in the Zn^{2+} and Cd^{2+} systems is broader than those of their respective similar-sized, alkali counterparts. This agrees with our discussions above that the higher charge density of the metal causes the crown to distort more around the metal.

Conclusion

Infrared multiple photon dissociation spectroscopy is used in conjunction with quantum chemical calculations to provide insights into the fundamental interactions between varying sized crown ethers and group 12 metal dications. Comparison of these experimental spectra with IR spectra calculated at the B3LYP/6-311+G(d,p) and B3LYP/Def2TZVP levels allow for the elucidation of likely conformers present in the gas phase. Examination of the C–O and C-C stretching bands yields the most structural information while the other bands in the spectra are minor and generally do not deviate significantly from conformer to conformer. Folded structures are found for Zn^{2+}(15c5), Zn^{2+}(18c6), and Cd^{2+}(18c6), whereas more open structures are observed for the Zn^{2+}(12c4) and Cd^{2+}(15c5) systems. Conformational assignments based on spectral comparisons agree with the GSs predicted by the relative energetics computed at the B3LYP, B3P86, and MP2(full) levels, such that either DFT or MP2(full) methods seem adequate for describing these host/guest interactions. The spectra and GS conformations observed here are also compared to those of similar sized alkali metal cation crown complexes. These comparisons demonstrate that the increased charge density of the metal dication shifts the C–O stretch of the crown ethers to lower frequencies. In addition, because of the increased electrostatic interactions, the crown distorts more around the metal, thereby forming shorter M–O bonds and increasing the electron donation from each oxygen to the metal causing splitting and broadening of the C–O stretching band for the folded structures. This broadening is also seen in the Zn^{2+}(12c4) complex, which forms an almost square pyramidal shape, with the Zn ion exposed at the apex of the pyramid. Compared to the larger crown complexes, lower frequency motions

of the Zn^{2+}(12c4) complex are observed and may be explained by the fulfillment of the 18e- rule and possibly the metal cation selectivity of the 12c4 complex. In the 15c5 and 18c6 systems, the crown is able to overcome the geometric constraints introduced by its backbone and wraps itself more tightly around the metal compared to its orientation in comparably sized alkali systems. In all systems studied, the combined motions of C–O stretches were described by theory and found to depict the delicate balance of the intermolecular attractive M-O and repulsive O-O forces, as evident by broadening and splitting of the C-O stretching band.

The fundamental interactions and structural parameters elucidated here give insight into the selectivity of the crowns for metal ions. Selectivity is not simply a best fit model. Metal charge plays a significant role in the orientation and alignment of the oxygen dipoles such that a balance is struck between the attractive and repulsive intermolecular forces of the crown. For the most part, condensed phase selectivity depends critically on solvation amount and type. Folded structures are expected to remain stable in nonpolar or low-polarity solvents. However, in polar solvents, open structures like Zn^{2+}(12c4) and Cd^{2+}(15c5) may gain in importance because the complex can be strongly stabilized by direct, partial solvation of the metal dication. Obviously, the effect of microsolvation is highly dependent on the size of the ion, type of solvent, amount of solvation, and crown ether cavity size. As such, microhydration of the metal crown is probably necessary to understand the aqueous selectivity of these crown ether systems.[19,36]

References

(1) Richens, D. T. *The Chemistry of Aqua Ions*; John Wiley and Sons, Inc: New York, 1997.

(2) Spiro, T. G. *Zinc enzymes*; J. Wiley: New York, 1983.

(3) Kimura, E. *Pure & Appl. Chem.* **1993**, *65*, 355.

(4) Nriagu, J. O. *Zinc in the Environment*; Wiley: New York, 1980.

(5) Salomons, W.; Förstner, U.; Mader, P. *Heavy metals : problems and solutions*; Springer-Verlag: Berlin ; New York, 1995.

(6) Fergusson, J. E. *The heavy elements : Chemistry, environmental impact, and health effects*, 1st ed.; Pergamon Press: Oxford ; New York, 1990.

(7) Horwitz, E. P.; Dietz, M. L.; Fisher, D. E. *Solvent Extr. Ion Exch.* **1991**, *9*, 1.

(8) Vaidya, B.; Porter, M. D.; Utterback, M. D.; Bartsch, R. A. *Anal. Chem.* **1997**, *69*, 2688.

(9) Laney, E. E.; Lee, J. H.; Kim, J. S.; Huang, X. W.; Jang, Y. C.; Hwang, H. S.; Hayashita, T.; Bartsch, R. A. *React. Funct. Polym.* **1998**, *36*, 125.

(10) Baumann, T. F.; Reynolds, J. G.; Fox, G. A. *React. Funct. Polym.* **2000**, *44*, 111.

(11) Pedersen, C. J.; Frensdorff, H. K. *Angew. Chem., Int. Ed.* **1972**, *11*, 16.

(12) Izatt, R. M.; Terry, R. E.; Nelson, D. P.; Chan, Y.; Eatough, D. J.; Bradshaw, J. S.; Hansen, L. D.; Christensen, J. J. *J. Am. Chem. Soc.* **1976**, *98*, 7626.

(13) Izatt, R. M.; Rytting, J. H.; Nelson, D. P.; Haymore, B. L.; Christensen, J. J. *Science* **1969**, *164*, 443.

(14) Izatt, R. M.; Pawlak, K.; Bradshaw, J. S.; Bruening, R. L. *Chem. Rev.* **1995**, *95*, 2529.

(15) Michaux, G.; Reisse, J. *J. Am. Chem. Soc.* **1982**, *104*, 6895.

(16) Glendening, E. D.; Feller, D.; Thompson, M. A. *J. Am. Chem. Soc.* **1994**, *116*, 10657.

(17) Feller, D. *J. Phys. Chem. A* **1997**, *101*, 2723.

(18) Hill, S. E.; Feller, D. *Int. J. Mass Spectrom.* **2000**, *201*, 41.

(19) Armentrout, P. B. *Int. J. Mass Spectrom.* **1999**, *193*, 227.

(20) Peiris, D. M.; Yang, Y. J.; Ramanathan, R.; Williams, K. R.; Watson, C. H.; Eyler, J. R. *Int. J. Mass Spectrom.* **1996**, *158*, 365.

(21) Anderson, J. D.; Paulsen, E. S.; Dearden, D. V. *Int. J. Mass Spectrom.* **2003**, *227*, 63.

(22) Chu, I.-H.; Zhang, H.; Dearden, D. V. *Pure Appl. Chem.* **1993**, *65*, 423.

(23) Maleknia, S.; Brodbelt, J. S. *J. Am. Chem. Soc.* **1992**, *65*, 4295.

(24) Ray, D.; Feller, D.; More, M. B.; Glendening, E. D.; Armentrout, P. B. *J. Phys. Chem. A* **1996**, *100*, 16116.

(25) More, M. B.; Ray, D.; Armentrout, P. B. *J. Phys. Chem. A* **1997**, *101*, 831.

(26) More, M. B.; Ray, D.; Armentrout, P. B. *J. Phys. Chem. A* **1997**, *101*, 4254.

(27) More, M. B.; Ray, D.; Armentrout, P. B. *J. Phys. Chem. A* **1997**, *101*, 7007.

(28) More, M. B.; Ray, D.; Armentrout, P. B. *J. Am. Chem. Soc.* **1999**, *121*, 417.

(29) Kim, H.-S. *J. Phys. Chem. B* **2004**, *108*, 11753.

(30) El-Azhary, A. A.; Al-Kahtani, A. A. *J. Phys. Chem. A* **2005**, *109*, 8041.

(31) Al-Rusaese, S.; Al-Kahtani, A. A.; El-Azhary, A. A. *J. Phys. Chem. A* **2006**, *110*, 8676.

(32) Gajewski, M.; Tuszynski, J.; Hirotoshi, M.; Miyoshi, E.; Klobukowski, M. *Inorg. Chim. Acta* **2008**, *361*, 2166.

(33) Rodriguez, J. D.; Lisy, J. M. *Int. J. Mass Spectrom.* **2009**, *283*, 135.

(34) Martinez-Haya, B.; Hurtado, P.; Hortal, A. R.; Steill, J. D.; Oomens, J.; Merkling, P. J. *J. Phys. Chem. A* **2009**, *113*, 7748.

(35) De, S.; Boda, A.; Ali, S. M. *THEOCHEM* **2010**, *941*, 90.

(36) Rodriguez, J. D.; Lisy, J. M. *J. Phys.Chem. A* **2009**, *113*, 6462.

(37) Rodriguez, J. D.; Kim, D.; Tarakeshwar, P.; Lisy, J. M. *J. Phys. Chem. A* **2010**, *114*, 1514.

(38) Martinez-Haya, B.; Hurtado, P.; Hortal, A. R.; Hamad, S.; Steill, J. D.; Oomens, J. *J. Phys. Chem. A* **2010**, *114*, 7048.

(39) Hill, S. E.; Feller, D.; Glendening, E. D. *J. Phys. Chem. A* **1998**, *102*, 3813.

(40) Ali, S. M.; Maity, D. K.; De, S.; Shenoi, M. R. K. *Desalination* **2008**, *2008*, 181.

(41) Rodriguez, J. D.; Vaden, T. D.; Lisy, J. M. *J. Am. Chem. Soc.* **2009**, *131*, 17277.

(42) Lee, S.; Wyttenbach, T.; Helden, G. v.; Bowers, M. T. *J. Am. Chem. Soc.* **1995**, *117*, 10159.

(43) Valle, J. J.; Eyler, J. R.; Oomens, J.; Moore, D. T.; van der Meer, A. F. G.; von Heldon, G.; Meijer, G.; Hendrickson, C. L.; Marshall, A. G.; Blakney, G. T. *Rev. Sci. Instrum.* **2005**, *76*, 023103.

(44) Polfer, N. C.; Oomens, J. *Phys. Chem. Chem. Phys.* **2007**, *9*, 3804.

(45) Polfer, N. C.; Oomens, J.; Moore, D. T.; von Helden, G.; Meijer, G.; Dunbar, R. C. *J. Am. Chem. Soc.* **2006**, *128*, 517.

(46) Oepts, D.; van der Meer, A. F. G.; van Amersfoort, P. W. *Infrared Phys. Technol.* **1995**, *36*, 297.

(47) Senko, M. W.; Speir, J. P.; McLafferty, F. W. *Anal. Chem.* **1994**, *66*, 2801.

(48) Pearlman, D. A.; Case, D. A.; Caldwell, J. W.; Ross, W. R.; Cheatham, T. E.; DeBolt, S.; Ferguson, D.; Seibel, G.; Kollman, P. *Comp. Phys. Commun.* **1995**, *91*, 1.

(49) Bylaska, E. J.; de Jong, W. A.; Kowalski, K.; Straatsma, T. P.; Valiev, M.; Wang, D.; Aprà, E.; Windus, T. L.; Hirata, S.; Hackler, M. T.; Zhao, Y.; Fan, P.-D.; Harrison, R. J.; Dupuis, M.; Smith, D. M. A.; Nieplocha, J.; Tipparaju, V.; Krishnan, M.; Auer, A. A.; Nooijen, M.; Brown, E.; Cisneros, G.; Fann, G. I.; Früchtl, H.; Garza, J.; Hirao, K.; Kendall, R.; Nichols, J. A.; Tsemekhman, K.; Wolinski, K.; Anchell, J.; Bernholdt, D.; Borowski, P.; Clark, T.; Clerc, D.; Dachsel, H.; Deegan, M.; Dyall, K.; Elwood, D.; Glendening, E.; Gutowski, M.; Hess, A.; Jaffe, J.; Johnson, B.; Ju, J.; Kobayashi, R.; Kutteh, R.; Lin, Z.; Littlefield, R.; Long, X.; Meng, B.; Nakajima, T.; Niu, S.; Pollack, L.; Rosing, M.; Sandrone, G.; Stave, M.; Taylor, H.; Thomas, G.; Lenthe, J. v.; Wong, A.; Zhang, Z. NWChem, A Computational Chemistry Package for Parallel Computers; Version 4.5 ed.; Pacific Northwest National Laboratory: Richland, Washington 99352, 2003.

(50) Roothaan, C. C. *Rev. Mod. Phys.* **1951**, *23*, 69.

(51) Binkley, J. S.; Pople, J. A.; Hehre, W. J. *J. Am. Chem. Soc.* **1980**, *102*, 939.

(52) Frisch, M. J.; Trucks, G. W.; Schlegel, H. B.; Scuseria, G. E.; Robb, M. A.; Cheeseman, J. R.; Montgomery, J., J. A. ; Vreven, T.; Kudin, K. N.; Burant, J. C.; Millam, J. M.; Iyengar, S. S.; Tomasi, J.; Barone, V.; Mennucci, B.; Cossi, M.; Scalmani, G.; Rega, N.; Petersson, G. A.; Nakatsuji, H.; Hada, M.; Ehara, M.; Toyota, K.; Fukuda, R.; Hasegawa, J.; Ishida, M.; Nakajima, T.; Honda, Y.; Kitao, O.; Nakai, H.; Klene, M.; Li, X.; Knox, J. E.; Hratchian, H. P.; Cross, J. B.; Bakken, V.; Adamo, C.; Jaramillo, J.; Gomperts, R.; Stratmann, R. E.; Yazyev, O.; Austin, A. J.; Cammi, R.; Pomelli, C.; Ochterski, J. W.; Ayala, P. Y.; Morokuma, K.; Voth, G. A.; Salvador, P.; Dannenberg, J. J.; Zakrzewski, V. G.; Dapprich, S.; Daniels, A. D.; Strain, M. C.; Farkas, O.; Malick, D. K.; Rabuck, A. D.; Raghavachari, K.; Foresman, J. B.; Ortiz, J. V.; Cui, Q.; Baboul, A. G.; Clifford, S.; Cioslowski, J.; Stefanov, B. B.; Liu, G.; Liashenko, A.; Piskorz, P.; Komaromi, I.; Martin, R. L.; Fox, D. J.; Keith, T.; Al-Laham, M. A.; Peng, C. Y.; Nanayakkara, A.; Challacombe, M.; Gill, P. M. W.; Johnson, B.; Chen, W.; Wong, M.

W.; Gonzalez, C.; Pople, J. A. Gaussian 03, Revision D.01; Gaussian, Inc.: Pittsburgh, PA, 2005.

(53) Becke, A. D. *J. Chem. Phys.* **1993**, *98*, 5648.

(54) Ditchfield, R.; Hehre, W. J.; Pople, J. A. *J. Chem. Phys.* **1971**, *54*, 724.

(55) Weigend, F.; Ahlrichs, R. *Phys. Chem. Chem. Phys.* **2005**, *7*, 3297.

(56) Andrae, D.; Haeussermann, U.; Dolg, M.; Stoll, H.; Preuss, H. *Theo. Chem. Acc* **1990**, *77*, 123.

(57) Schuchardt, K. L.; Didier, B. T.; Elsethagen, T.; Sun, L. S.; Gurumoorthi, V.; Chase, J.; Li, J.; Windus, T. L. *J. Chem. Inf. Model.* **2007**, *47*, 1045.

(58) Frisch, M. J.; Trucks, G. W.; Schlegel, H. B.; Scuseria, G. E.; Robb, M. A.; Cheeseman, J. R.; Scalmani, G.; Barone, V.; Mennucci, B.; Petersson, G. A.; Nakatsuji, H.; Caricato, M.; Li, X.; Hratchian, H. P.; Izmaylov, A. F.; Bloino, J.; Zheng, G.; Sonnenberg, J. L.; Hada, M.; Ehara, M.; Toyota, K.; Fukuda, R.; Hasegawa, J.; Ishida, M.; Nakajima, T.; Honda, Y.; Kitao, O.; Nakai, H.; Vreven, T.; Montgomery, J., J. A. ; Peralta, J. E.; Ogliaro, F.; Bearpark, M.; Heyd, J. J.; Brothers, E.; Kudin, K. N.; Staroverov, V. N.; Kobayashi, R.; Normand, J.; Raghavachari, K.; Rendell, A.; Burant, J. C.; Millam, J. M.; Iyengar, S. S.; Tomasi, J.; Cossi, M.; Rega, N.; Millam, J. M.; Klene, M.; Knox, J. E.; Cross, J. B.; Bakken, V.; Adamo, C.; Jaramillo, J.; Gomperts, R.; Stratmann, R. E.; Yazyev, O.; Austin, A. J.; Cammi, R.; Pomelli, C.; Ochterski, J. W.; Martin, R. L.; Morokuma, K.; Zakrzewski, V. G.; Voth, G. A.; Salvador, P.; Dannenberg, J. J.; Dapprich, S.; Daniels, A. D.; Farkas, O.; Foresman, J. B.; Ortiz, J. V.; Cioslowski, J.; Fox, D. J. Gaussian 09, Revision A.02; Gaussian Inc.: Pittsburgh, PA, 2009.

(59) Perdew, J. P. *Phys. Rev. B* **1986**, *33*, 8822.

(60) Möller, C.; Plesset, M. S. *Phys. Rev.* **1934**, *46*, 618.

(61) Bauschlicher, C. W., Jr.; Maitre, P. J. *J. Phys. Chem.* **1995**, *99*, 3444.

(62) Wilson, R. G.; Brewer, G. R. *Ion Beams with Applications to Ion Implantation*; Wiley: New York, 1973.

(63) Steed, J. W. *Coord. Chem. Rev.* **2001**, *215*, 171.

(64) Reed, A. E.; Curtiss, L. A.; Weinhold , F. *Chem. Rev.* **1988**, *88*, 899.

(65) NIST Mass Spec Data Center, S.E. Stein, director, "Infrared Spectra" in NIST Chemistry WebBook, NIST Standard Reference Database Number 69, Eds. P.J. Linstrom and W.G. Mallard, National Institute of Standards and Technology, Gaithersburg MD, 20899, http://webbook.nist.gov.

(66) Walters, R. S.; Pillai, E. D.; Duncan, M. A. *J. Am. Chem. Soc.* **2005**, *127*, 16599.

CHAPTER 8

STURCTURAL ELUCIDATION OF BIOLOGICAL AND TOXICOLOGICAL COMPLEXES: INVESTIGATION OF MONOMERIC AND DIMERIC COMPLEXES OF HISTIDINE WITH MULTIPLY CHARGED TRANSITION METAL (ZN AND CD) CATIONS USING IR ACTION SPECTROSCOPY

Abstract

The gas-phase structures of singly and doubly-charged complexes involving transition metal cations, Zn and Cd, bound to the amino acid histidine (His) as well as de-protonated His (His–H) are investigated using infrared multiple photon dissociation (IRMPD) spectroscopy utilizing light generated by a free electron laser. IRPMD spectra are measured for $CdCl^+$(His), $[Zn(His–H)]^+$, $[Cd(His–H)]^+$, $Zn^{2+}(His)_2$, and $Cd^{2+}(His)_2$ in the 550 – 1800 cm^{-1} range. These studies are complemented by quantum mechanical calculations of the predicted linear absorption spectra at the B3LYP/6-311+G(d,p) and B3LYP/Def2TZVP levels. The monomeric spectra are similar to one another and indicate that histidine coordinates to the metal in a charge solvated (CS) tridentate form in the $CdCl^+$(His) complex and has a similar tridentate configuration with a de-protonated

carboxylic acid terminus in the $[M(His–H)]^+$ complexes. The preference for these particular complexes is also found in the relative energetics calculated at the B3LYP, B3P86, and MP2(full) levels. The spectra of the dimer complexes have obvious CS characteristics suggesting that at least one of the His ligands is charge solvated; however, there are also signatures for a salt-bridge (SB) formation in the second His ligand. The definitive assignment of a SB ligand is complicated by the presence of the CS ligand and conflicting relative energetics from the different levels of theory.

Introduction

Under physiological conditions, zinc exists as the divalent Zn^{2+} cation and plays a significant role as the metal center of carbonic anhydrase, a metalloenzyme with three histidine (His) residues coordinated to a zinc ion, and in the zinc finger protein.[1-6] The zinc finger protein module is abundant in all mammalian genes and is responsible for DNA and RNA-binding, cell cycle signaling, and protein-protein interactions.[4] The classic binding motif of the zinc finger has Zn^{2+} directly coordinated to two His and two cysteine (Cys) residues,[1] but $Zn^{2+}(His)(Cys)_3$ formation has also been identified. Both motifs are associated with proteins that recognize, bind, and repair DNA and RNA.[5,7] The zinc finger is a sensitive target for toxic heavy metals like Cd^{2+} because the zinc ion can be replaced by even low concentrations of certain metals, thereby inhibiting the functionality of the zinc-dependent complex.[8] This inactivation has a profound effect on genomic stability, the reproductive system, brain development, and may increase the risk of tumor development.[7,8] Because cadmium can bio-accumulate and anthropomorphic emissions into the environment are 18 times higher than naturally occurring rates, human and environmental exposure to this metal is a major threat.[8-10] In contrast to the zinc

finger proteins, it has been suggested that the carbonic anhydrase metalloenzyme may not be completely deactivated by replacement of Zn^{2+} with Cd^{2+}.[11]

Using a variety of condensed phase experimental techniques for structural determination (e.g. crystallography, NMR), the mechanism for protein inactivation by removal of the zinc is presumed to be structural changes or chemical modification (oxidation) of the coordinating residues.[1-5,7,8,12] These proposed mechanisms of deactivation are influenced by varying protein structures, protein interactions, and solvent. Studying these complexes in isolation may be beneficial to better understand the modifications of the coordinating residues upon metal substitution.

One strategy for investigating the fundamental interactions between a metal and its metal-site in a protein is to study these metals coordinated to the pertinent chelating residues in the gas-phase, creating a biomimetic complex. This approach has been used for monomeric, dimeric, and trimeric complexes of histidine and similar molecules like aromatic amino acids, tryptophan (Trp) and phenylalanine (Phe), with singly and doubly charged metal cations as well as in protonated dipeptides and complexed with variety of singly charged anions.[13-25] Here, we have undertaken a systematic conformational investigation of zinc and cadmium binding one and two His residues using infrared multiple photon dissociation (IRMPD) action spectroscopy and quantum chemical calculations.

As mentioned above, physiologically relevant complexes have both one and two His coordinated directly to Zn^{2+}. Hence IRMPD spectra were obtained for $M^{2+}(His)_2$, where M = Zn and Cd. The doubly charged monomeric complexes, M^{2+}(His), were not formed experimentally, but the spectra of deprotonated His with both metals, [M(His-

H)]$^+$, were also measured. To see whether deprotonation affects the structure, the spectrum of the $CdCl^+$(His) complex was also measured. Conformations are identified by comparing experimental spectra to single photon spectra predicted by quantum chemical calculations of low-energy structures calculated at the B3LYP/6-311+G(d,p) level for Zn^{2+} complexes and B3LYP/Def2TZVP for Cd^{2+} complexes. Relative energies for these complexes are calculated using B3LYP, B3P86, and MP2(full) levels with the 6-311+G(2d,2p) basis set for Zn^{2+} complexes and Def2TZVPP basis set for Cd^{2+} complexes. Structural elucidation of these complexes will lead to fundamental understanding of the effect of the metal on such a biologically important binding site.

Experimental and Theoretical Methods

Mass spectrometry and IRMPD spectroscopy. A 4.7 T Fourier transform ion cyclotron resonance (FT-ICR) mass spectrometer[14,26,27] coupled to a beamline of the free electron laser for infrared experiments (FELIX)[28] was used to record the IRMPD spectra. Reactant ion complexes were formed by electrospray ionization (ESI) using a Micromass Z-spray source and a solution of 1mM zinc nitrate (or cadmium chloride) and 1mM His in 50:50 MeOH:H_2O solution with a solution flow rate of ~10 μL/min. All chemicals were obtained from Aldrich. Ions were accumulated in a hexapole trap for ~4 s prior to being pulse injected into the ICR cell via an rf octopole ion guide. Before entering the ICR cell, ions are decelerated out of the octopole in such a way that they can be captured without a gas pulse such that collisional heating of the ions is avoided.[14] Once trapped in the cell, the ion of interest is mass isolated using a stored waveform inverse Fourier transform (SWIFT) excitation pulse. Spectra were recorded over the wavelength range of 18.2 μm (550 cm^{-1}) to as far as 5.5 μm (1830 cm^{-1}). FELIX pulse energies were around

50 mJ/macropulse of 5 μs duration. The ion of interest was irradiated for 3 – 3.5 s at 5 or 10 Hz macropulse repetition rate, which corresponds to interaction with approximately 15 – 18 macropulses at 5 Hz or 30 – 35 macropulses at 10 Hz. For all but the $[Cd(His-H)]^+$ spectrum, various intense bands in the spectra were also probed with a 3 dB attenuated laser energy to avoid saturation and better represent relative intensities and peak shapes. The full width at half maximum (FWHM) bandwidth of the laser was typically 0.5% of the central wavelength. IRMPD spectra were constructed by plotting the total ionic fragmentation yield as a function of the wavenumber of the radiation.

The ESI source generated $Zn^{2+}(His)_2$, $Cd^{2+}(His)_2$, and $CdCl^+(His)$ directly. The $[M(His-H)]^+$ species were not directly produced in the ESI source but were generated by irradiating larger ions with a 40-W continuous-wave CO_2 laser for 1s, and then allowing the resulting ions to cool for an additional 1s before irradiation with the FELIX light. $[Zn(His–H)]^+$ was formed from $[Zn(His-H)NH_3]^+$ and $[Cd(His-H)]^+$ was formed from the $Cd^{2+}(His)_2$ species.

Quantum chemical calculations. Starting geometries for $Zn^{2+}(His)$ complexes were taken from geometries of $Li^+(His)$ complexes.[16] Using the Gaussian 09 suite of programs,[29] these structures were further optimized at the B3LYP/6-31G(d) level[30,31] using the "loose" keyword, which utilizes a large step size (0.01 au) and rms force constant (0.0017) to ensure a rapid geometry convergence followed by geometry optimization at the B3LYP/6-311+G(d,p) level. From $Zn^{2+}(His)$, the His residue was deprotonated at likely sites and the loose optimization step repeated. Unique structures remaining after this procedure were chosen for further geometry optimization and vibrational frequency calculations at the B3LYP/6-311+G(d,p) level ensuring structural

convergence during the frequency calculation. The $[Zn(His-H)]^+$ and $Zn^{2+}(His)$ complexes were also used as the starting geometries for the $[Cd(His-H)]^+$ and $CdCl^+(His)$ systems, respectively. Here the same geometry optimization procedures were followed using the B3LYP/Def2TZVP level, where Def2TZVP is a size consistent basis set for all atoms and includes triple zeta + polarization functions with an effective core potential (ECP) on Cd having 28 electrons (small core).[32,33] The Def2TZVP basis set and ECP were obtained from the EMSL basis set exchange.[34] Because of their large size and many degrees of freedom, a comprehensive structure search for the dimeric complexes was not undertaken, but low-energy binding motifs found for $Zn^{2+}(His)$ were combined to give likely complexes of $Zn^{2+}(His)_2$ and $Cd^{2+}(His)_2$. Once constructed, we performed geometry optimization and frequency calculations for these complexes similar to those described for the monomeric complexes.

For comparison to experiment, the vibrational frequencies and IR intensities were calculated using the harmonic oscillator approximation at the B3LYP level and were broadened using a 20 cm^{-1} FWHM Gaussian line shape. Frequencies were scaled by 0.975, consistent with scaling factors found appropriate in other studies of this spectral region on similar complexes of His.[16,19-21,35]

Single point energy calculations were carried for the most stable structures at the B3LYP, B3P86,[36] and MP2(full)[37] levels using the 6-311+G(2d,2p) basis set for Zn complexes and Def2TZVPP basis set for Cd complexes. The relative energies between each isomer include zero point energy (ZPE) corrections to yield 0 K values and thermal corrections to free energies at 298.15 K. These corrections use the calculated frequencies

scaled by 0.989, a scaling factor determined by Bauschlicher and Partridge to give accurate ZPE corrections at the B3LYP level using a 6-311+G(3df,2p) basis set.[38]

Results and Discussion

Theoretical results. The low-lying structures found for $CdCl^+$(His) are shown in Figure 8.1 and illustrate the likely coordination modes of His to to both Zn^{2+} and Cd^{2+}. The Cl^- is a spectator ion and has little effect on the Cd–His coordination, as also seen previously for $CdCl^+$(Trp).[19] The nomenclature used to identify different structural isomers is similar to that described previously for the IRMPD studies of other metal-amino acids.[39-41] Briefly, conformations in this study are identified by their metal binding site in brackets, followed by a description of the His orientation by a series of four dihedral angles. For the charge solvated (CS) structures, these angles start with the carboxylic acid hydrogen to define the H–O–C–C_α angle and proceed along the molecule ending with the "pros" nitrogen (N_1, also commonly designated as N_π of the imidazole side chain, which is the nitrogen closest to the β-carbon of the backbone. These angles define the O–C–C_α–C_β, C–C_α–C_β–C, C_α–C_β–C–N_1 dihedrals and are distinguished as *cis* (c, for angles between 0° – 50°), *gauche* (g, 50° – 135°), and *trans* (t, 135° – 180°). For most salt-bridge (SB) conformations, the proton originally on the carboxylic acid is attached to either the alpha-amino (N_α) or N_1 nitrogens. For these complexes, the first dihedral angle starts at this bridging proton and moves along the molecule toward the deprotonated site and is labeled using a subscript according to where this proton is located (either N_α or N_1). The remaining three dihedrals are the same as above starting at the CO^- involved in the salt-bridge. Salt-bridges are also formed between the N_α and N_1

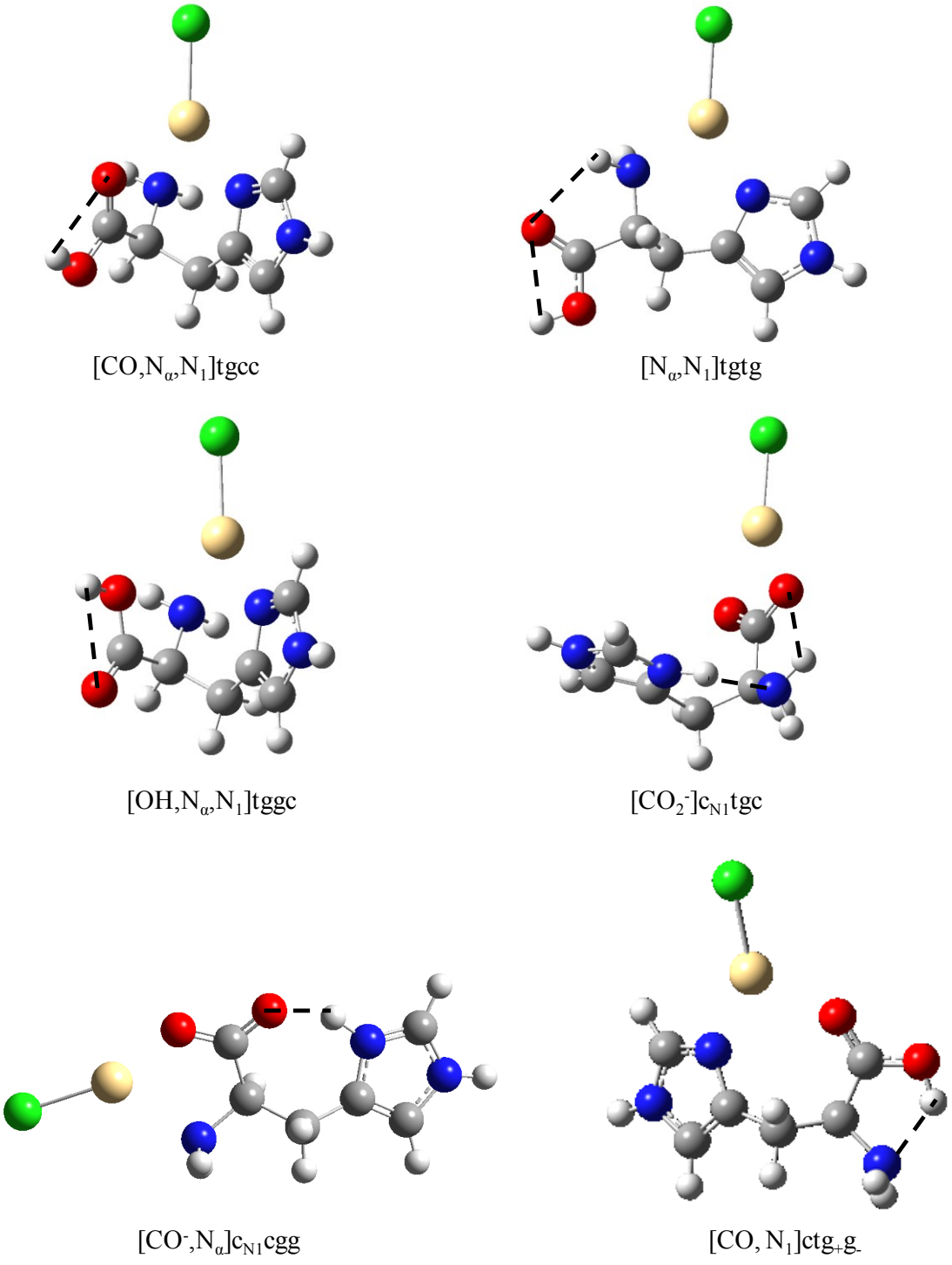

Figure 8.1. Structures of the $CdCl^{+}$(His) complexes calculated at the B3LYP/Def2TZVP level of theory. Hydrogen bonds are indicated by dashed lines.

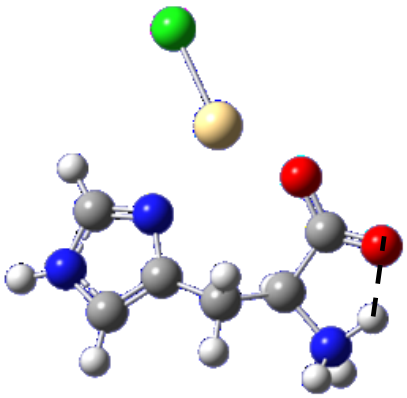

$[CO^{-},N_1]c_{N\alpha}ggg$

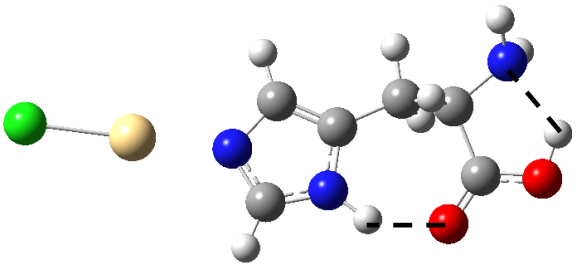

$[N_3]ctgg$

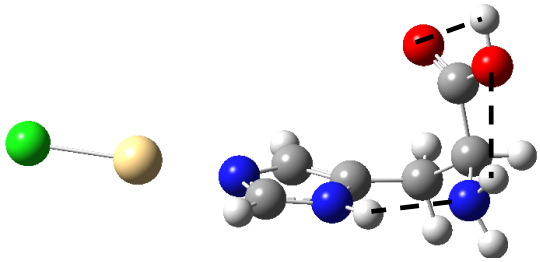

$[N_3]ttgt$

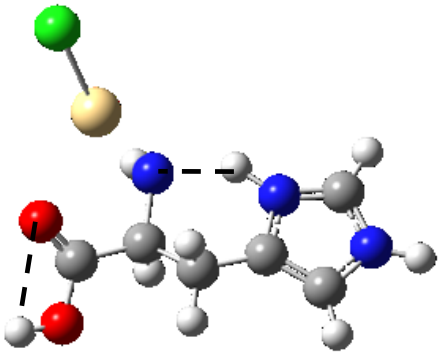

$[CO, N_{\alpha}^{-}]tgtg$

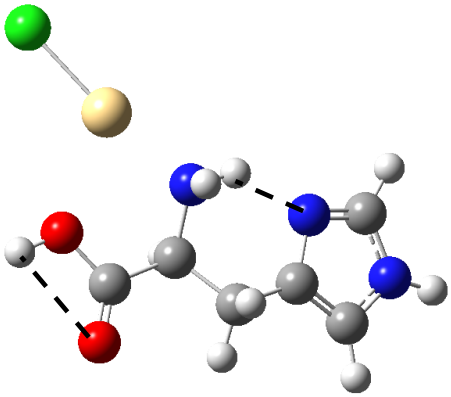

$[OH,N_{\alpha}]tttc$

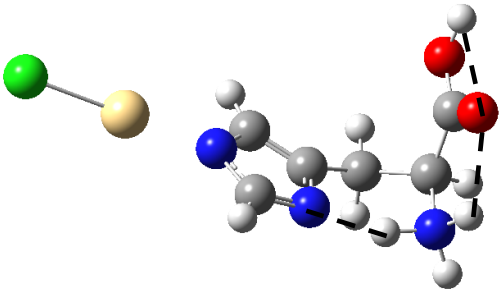

$[N_3^{-}]tggg$

Figure 8.1. continued

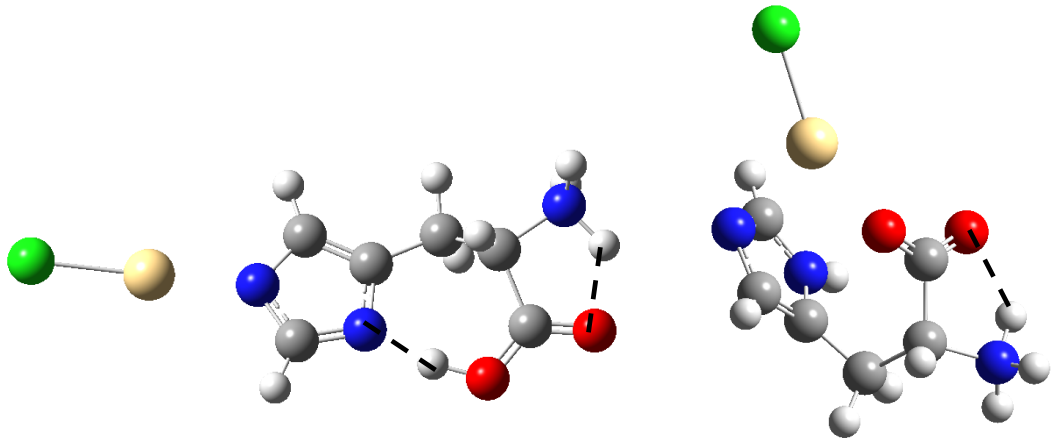

$[N_3^-]cggg$ $[CO^-,N_3]c_{N\alpha}gcg$

Figure 8.1. continued

atoms, leaving the carboxylic acid group intact. These structures are higher in energy and the nomenclature remains the same as the CS complexes, with the particular SB motif explicitly noted. In all conformations, the C_β–C–N_1–C, C–N_1–C–N_3 (where N_3 is the "tele" or far nitrogen in the imidazole, also designated N_τ elsewhere), and N_1–C–N_3–C dihedrals are consistently found to have a "tcc" designation because of the steric constraints of the imidazole ring. Thus, these orientations are omitted from our nomenclature. For the deprotonated complexes studied here, $[M(His\text{-}H)]^+$, the question of CS versus SB does not arise, although there are many possible deprotonation sites from each complex. As such, the nomenclature includes a "–H_n" designation following the coordination sites, where *n* defines the deprotonation site. If the deprotonation site is the NH_2 group on the alpha carbon then the H–N_α–C_α–C_β dihedral is given in parenthesis to define the angle of the proton still remaining. The nomenclature of the dimeric complexes combines names of the monomeric complexes in a straightforward fashion.

Monomeric Species. Relative energies, including zero-point energy (ZPE) corrections with respect to the ground state (GS) calculated at three different levels of theory, are given in Table 8.1 for the $CdCl^+$(His) and $[M(His–H)]^+$ complexes. Because the relative Gibbs free energies at 298 K may be more relevant in describing the experimental distributions, these values are also listed in Table 8.1 and complexes are ordered with respect to increasing 298 K free energy at the B3LYP level. Table 8.1 includes all likely coordination sites for the $CdCl^+$(His) system, although conformers having similar coordination sites but different dihedral angles were calculated but do not greatly affect the predicted spectra. Because of the large number of possible structures and deprotonation sites, only selected isomers are listed in Table 8.1 for the $[M(His–H)]^+$

Table 8.1. Relative enthalpy at 0 K (ΔH_0) and free energies at 298 K (ΔG_{298})[a] (kJ/mol) of low-lying conformers of cationized monomeric His and His–H.[b]

Complex	Structure	B3LYP	B3P86	MP2(full)
$CdCl^+$(His)	$[CO,N_\alpha,N_1]$tgcc	0.0 (0.0)	0.0 (0.0)	0.0 (0.0)
	$[N_\alpha,N_1]$tgtg	19.8 (15.9)	22.6 (18.7)	30.2 (26.3)
	$[OH,N_\alpha,N_1]$tggc	24.6 (22.4)	26.6 (24.5)	22.6 (20.5)
	$[CO_2^-]c_{N1}$tgc	34.8 (29.6)	39.0 (33.8)	63.5 (58.3)
	$[CO^-,N_\alpha]c_{N1}$cgg	32.3 (31.0)	34.4 (33.0)	64.9 (63.5)
	$[CO,N_1]$ctg$_+$g$_-$	41.2 (37.9)	43.9 (40.6)	61.6 (58.4)
	$[CO^-,N_1]c_{N\alpha}$ggg	64.6 (60.9)	64.9 (61.2)	80.4 (76.8)
	$[N_3]$ctgg	70.0 (68.2)	73.3 (71.5)	95.0 (93.2)
	$[N_3]$ttgt	73.1 (68.9)	79.9 (75.6)	89.8 (85.6)
	$[CO,N_\alpha^-]$tgtg[c]	86.1 (84.4)	85.4 (83.7)	105.7 (104.0)
	$[OH,N_\alpha]$tttc[c]	88.0 (84.8)	92.1 (88.9)	103.1 (99.9)
	$[N_3^-]$tggg[c]	88.2 (85.4)	89.1 (86.3)	95.0 (92.2)
	$[N_3^-]$cggg[d]	113.0 (111.6)	109.6 (108.2)	125.8 (124.4)
	$[CO^-,N_3]c_{N\alpha}$gcg	154.1 (150.5)	156.0 (152.4)	155.1 (151.5)
$[Cd(His–H)]^+$	$[CO^-,N_\alpha,N_1]$-H_{CO}ggc	0.0 (0.0)	0.0 (0.0)	0.0 (0.0)
	$[CO,N_\alpha^-,N_1]$-$H_{N\alpha}$(t)tgcc	24.7 (24.2)	26.2 (25.7)	29.6 (29.2)
	$[CO,N_\alpha^-,N_1]$-$H_{N\alpha}$(c)tgcc	38.3 (37.8)	38.9 (38.4)	39.0 (38.5)
	$[CO,N_\alpha,N_1]$-H_{N3}tggg	80.0 (79.6)	80.2 (79.8)	73.3 (72.9)
	$[N_3]$-$H_{N\alpha}$(t)ttgg	272.0 (261.2)	301.0 (290.2)	27.9 (17.2)
	$[N_3]$-$H_{N\alpha}$(c)ctgg	282.4 (273.2)	309.5 (300.3)	25.4 (16.2)
$[Zn(His–H)]^+$	$[CO^-,N_\alpha,N_1]$-H_{CO}ggc	0.0 (0.0)	0.0 (0.0)	0.0 (0.0)
	$[CO, N_\alpha^-,N_1]$-$H_{N\alpha}$(t)tggc	43.8 (43.7)	44.9 (44.7)	48.2 (48.0)
	$[CO,N_\alpha^-,N_1]$-$H_{N\alpha}$(c)tggc	54.0 (53.9)	53.7 (53.6)	53.9 (53.8)
	$[CO,N_\alpha,N_1]$-H_{N3}tgcc	102.0 (102.1)	101.4 (101.5)	98.8 (98.9)

Table 8.1. continued

Complex	Structure	B3LYP	B3P86	MP2(full)
	$[N_3]$-$H_{N\alpha}$(t)ttgc	379.8 (369.7)	410.8 (400.6)	108.6 (98.4)
	$[N_3]$-$H_{N\alpha}$(t)cggg	385.0 (377.0)	416.0 (408.0)	170.7 (162.8)

[a] ΔG_{298} values given in parentheses. [b] Values are single point energies calculated at the level shown using a 6-311+G(2d,2p) basis set on Zn containing complexes and Def2TZVPP on Cd containing complexes. Geometries calculated at the B3LYP/6-311+G(d,p) level on Zn containing complexes and B3LYP/Def2TZVP on Cd containing complexes. Zero point energy corrections scaled by 0.989 are included. [c] Salt-bridge between N_α and N_1. [d] Salt-bridge between the $N_\alpha H_3^+$, COOH, and N_1^- groups.

systems, higher energy structures were calculated but not presented here (and these are found to disagree with the experimental spectra).

The CS tridentate [CO,N_α,N_1]tgcc structure is the lowest energy conformation for $CdCl^+$(His) at all three levels of theory. This structure is similar to the CS1 conformation reported as the GS configuration by Dunbar and coworkers in their study of Ba^{2+}(His) and Ca^{2+}(His).[15] Other CS conformations with [N_α,N_1] and [OH,N_α,N_1] coordination sites are 16 – 26 kJ/mol higher in 298 K free energy than the GS, Table 8.1. The lowest energy SB structures reported previously[15] for Ca^{2+} and Ba^{2+}, have [CO_2^-] and [CO^-,N_α] coordination sites, Figure 8.1. Interestingly these structures are 30 – 34 kJ/mol higher in 298 K free energy at the density functional theory (DFT) levels, but are predicted to be 58 – 64 kJ/mol higher than the GS at the MP2(full) level. On the basis of the trends seen in Table 8.1, the MP2(full) level favors CS complexes and predicts SB structures to be much higher in energy compared to the predicted relative energetics of the same structures at the DFT levels. Previous work has found that the CS structures of M^{2+}(Trp) are highly stable for small, doubly charged metals like Cd and Zn.[22] However, contributions from SB structures cannot be ruled out by relative energetics alone as calculations tend to overestimate the stability of the CS structures versus SB conformers of M^{2+}(His) as determined on the basis of spectral assignments.[15]

The higher energy complexes not shown include several [CO,N_1] conformers, where each one differs slightly in the orientation of the amino acid such that the direction of the gauche dihedral angles must also be specified (either + or -). The lowest of these is included in Figure 8.1 and Table 8.1. Each structure is predicted to be 38 – 60 kJ/mol above the GS and to have fairly similar vibrational frequencies, although the position and

relative intensity of the COH bend is dependent on the orientation of the hydroxyl and alpha amino groups. The $[CO,N_\alpha^-]$tgtg complex is the lowest energy SB structure in which the proton bridges N_α and N_1, Figure 8.1, but is still 46 – 55 kJ/mol higher in 298 K free energy than the $[CO_2^-]$ SB complex. The $[N_3]$ctgg and $[N_3]$ttgt complexes have similar metal coordination and extended configurations, but differ in the orientation of the alpha-amino and carboxylic acid groups and resulting intermolecular H-bonding. In $[N_3]$ctgg, the proton on the hydroxyl H-bonds with the NH_2 group, while the proton on N_1 H-bonds to the carbonyl group. In $[N_3]$ttgt, the NH_2 group accepts a H-bond from the proton on the N_1, while the hydroxyl oxygen H-bonds with the NH_2 group. These changes result in free energy differences of $\Delta\Delta G_{298}$ = -7.6 – 4.1 kJ/mol. Similar differences are seen in the intramolecular binding of the amino acid between the two extended SB structures, $[N_3^-]$tggg and $[N_3^-]$cggg. In the former, the NH_3^+ group H-bonds to both the N_1 of the imidazole ring and the carbonyl oxygen, whereas in the $[N_3^-]$cggg complex, the NH_3^+ H-bonds to the carbonyl and the hydroxyl H-bonds to the N_1 atom, Figure 8.1. As such, in the latter structure two H-bonds are used to form a salt-bridge between three groups: $N_\alpha H_3^+$, COOH, and N_1^-. The highest energy structure located is a SB with the metal coordinated to both "ends" of the amino acid in a $[CO^-,N_3]$ fashion and is 150 – 153 kJ/mol higher than the GS structure.

For the deprotonated $[M(His–H)]^+$ species, the lowest-energy structure for both the Zn and Cd systems corresponds to a tridentate GS, $[CO^-,N_\alpha,N_1]$, with a deprotonated carboxylic acid terminus, Table 8.1. This is in agreement with previous work on $[Zn(Phe)(Phe–H)]^+$, which found a similar deprotonation and coordination of Phe–H.[14] Both Zn and Cd form a $[CO^-,N_\alpha,N_1]$-H_{CO}ggc configuration, which is predicted as the GS

for all three levels of theory. This structure is similar to [CO,N_α,N_1]tgcc of Figure 8.1 without the hydroxyl oxygen. Deprotonation is also possible from the N_α and N_3 sites. Deprotonation of either of the two hydrogens on the alpha amino group form the next higher-energy complexes, [CO,N_α,N_1^-]-$H_{N\alpha}$(t)tgcc and [CO,N_α,N_1^-]-$H_{N\alpha}$(c)tgcc for $[M(His\text{-}H)]^+$, although the latter complex differs slightly in the dihedral angles for Zn. The former structure is 24 – 29 (44 – 48) kJ/mol higher in 298 K free energy than the GS for Cd (Zn) and the latter structure is another 9 – 14 (6 – 10) kJ/mol higher. The two structures are differentiated by the $H_{N\alpha}$ (t) or (c) dihedral, where the t orientation allows this proton to point toward the oxygen of the carbonyl, whereas in the less stable c orientation, it points away. Deprotonation of N_3 in the imidazole ring results in a Cd[CO,N_α,N_1]-H_{N3}tggg (Zn[CO,N_α,N_1]-H_{N3}tgcc) configuration that is 73 – 80 (99 – 102) kJ/mol in 298 K free energy than the GS complex, Table 8.1.

Relative energetics of higher energy structures for the remaining coordination sites were calculated, although these complexes are > 40 kJ/mol for both systems at all levels of theory. Interestingly, there are two extended structures calculated for both metal systems where the predicted relative energetics between the DFT and MP2(full) levels are in especially poor agreement, and therefore included in Table 8.1. For both systems, the [N_3]-$H_{N\alpha}$(t)ttgg and [N_3]-$H_{N\alpha}$(c)ctgg complexes are very high in energy at the DFT levels $\Delta\Delta G_{298K}$ = 261 – 300 (370 – 408) kJ/mol, but are only 16 – 17 (98 – 163) kJ/mol higher than the GS at the MP2(full) level. These structures differ in the orientation of the alpha amino group similar to the [N_3] complexes described above for the $CdCl^+$(His) system. Briefly, in the [N_3]-$H_{N\alpha}$(t)ttgg complex, the HN_α^- group accepts a H-bond from the N_1 group, while donating a H-bond to the hydroxyl oxygen. In the [N_3]-$H_{N\alpha}$(c)ctgg

complex, HN_α^- accepts a H-bond from the hydroxyl group and N_1H H-bonds to the carbonyl. The discrepancy between the predictions of different levels of theory of these complexed amino acids obviously extends further than just the CS versus SB question.

Dimeric Species. Relative energies including ZPE with respect to the GS are given in Table 8.2 for the $Zn^{2+}(His)_2$ and $Cd^{2+}(His)_2$ complexes. Structures of the $Zn^{2+}(His)_2$ complexes are shown in Figure 8.2. Higher energy species were also calculated, but not presented here. The majority of the low-energy structures have one charge-solvated His with a $[CO,N_\alpha,N_1]$ coordination. In the $Zn^{2+}(His)_2$ system, the lowest-energy structure at the DFT levels is a $[CO,N_\alpha,N_1]$tggc/$[CO^-,N_\alpha]c_{N1}$cgg complex, where the second His ligand is in a SB conformation, Figure 8.2. At the MP2(full) level, this complex is fairly high in 298 K free energy ($\Delta\Delta G_{298K}$ = 26.0 kJ/mol) because SB configurations are disfavored by this level of theory, as discussed above.

Disagreements between the levels of theory are also seen for the next two low-energy complexes which involve the binding of CS and SB structures, Table 8.2. The $[CO,N_\alpha,N_1]$ tggc/$[CO_2^-]c_{N1}$tgc is only 2 – 3 kJ/mol above the GS in 298 K free energy at the DFT levels, but this increases to 32 kJ/mol at the MP2(full) level (6 kJ/mol above the lowest CS/SB structure). On the second His, the zinc is coordinated to the carboxylate group with Zn–O distances of 2.099 and 2.139 Å. Similar to this structure is the tetrahedral coordination of the $[CO,N_\alpha,N_1]$ tggc/$[CO^-]c_{N1}$tgc complex. On the SB His, the zinc dication is coordinated mainly to one oxygen of the carboxylate instead of the entire CO_2^- group with Zn–O distances of 1.909 and 2.774 Å. This 4-coordinate structure is higher in energy than the respective GSs by 9 – 12 kJ/mol at the DFT levels and 40 kJ/mol at the MP2(full) level (14 kJ/mol above the lowest CS/SB structure).

Table 8.2. Relative enthalpy at 0 K (ΔH_0) and free energies at 298 K (ΔG_{298})[a] (kJ/mol) of low-lying conformers of cationized dimeric His.[b]

Complex	Structure	B3LYP	B3P86	MP2(full)
$Zn^{2+}(His)_2$	$[CO,N_\alpha,N_1]tggc/[CO^-,N_\alpha]c_{N1}cgg$	0.0 (0.0)	0.0 (0.0)	31.3 (26.0)
	$[CO,N_\alpha,N_1]tggc/[CO_2^-]c_{N1}tgc$	6.6 (1.8)	7.8 (3.0)	41.8 (31.7)
	$[CO,N_\alpha,N_1]tggc/[CO^-]c_{N1}tgc$	10.0 (8.9)	13.1 (12.0)	46.2 (39.9)
	$[CO^-,N_\alpha]c_{N1}cgg/[CO^-,N_\alpha]c_{N1}cgg$	10.2 (10.2)	13.8 (13.8)	73.3 (68.0)
	$[CO,N_\alpha,N_1]tgcc/[CO,N_\alpha,N_1]tgcc$	5.5 (10.8)	6.2 (11.5)	0.0 (0.0)
	$[CO,N_\alpha,N_1]tgcc/[CO,N_1]ctgg$	14.7 (17.7)	14.4 (17.4)	30.2 (27.9)
$Cd^{2+}(His)_2$	$[CO,N_\alpha,N_1]tgcc/[CO_2^-]t_{N1}tgc$	4.1 (0.0)	6.2 (0.0)	42.5 (31.9)
	$[CO,N_\alpha,N_1]tgcc/[CO,N_\alpha,N_1]tgcc$	0.0 (6.5)	0.0 (4.4)	0.0 (0.0)
	$[CO,N_\alpha,N_1]tgcc/[CO^-,N_\alpha]c_{N1}cgg$	8.8 (8.9)	9.3 (7.3)	46.7 (40.2)
	$[CO,N_\alpha,N_1]tgcc/[CO_2^-]c_{N1}cgg$	21.5 (15.5)	26.6 (18.6)	65.1 (52.6)
	$[CO,N_\alpha,N_1]tgcc/[CO,N_1]ctgg$	20.2 (21.7)	20.3 (19.6)	41.3 (36.2)
	$[CO^-,N_\alpha]c_{N1}cgc/[CO^-,N_\alpha]c_{N1}cgc$	22.7 (22.1)	25.9 (23.2)	92.0 (84.8)

[a] ΔG_{298} values given in parentheses. [b] Values are single point energies calculated at the level shown using a 6-311+G(2d,2p) basis set on Zn containing complexes and Def2TZVPP on Cd containing complexes. Geometries calculated at the B3LYP/6-311+G(d,p) level on Zn containing complexes and B3LYP/Def2TZVP on Cd containing complexes. Zero point energy corrections scaled by 0.989 are included.

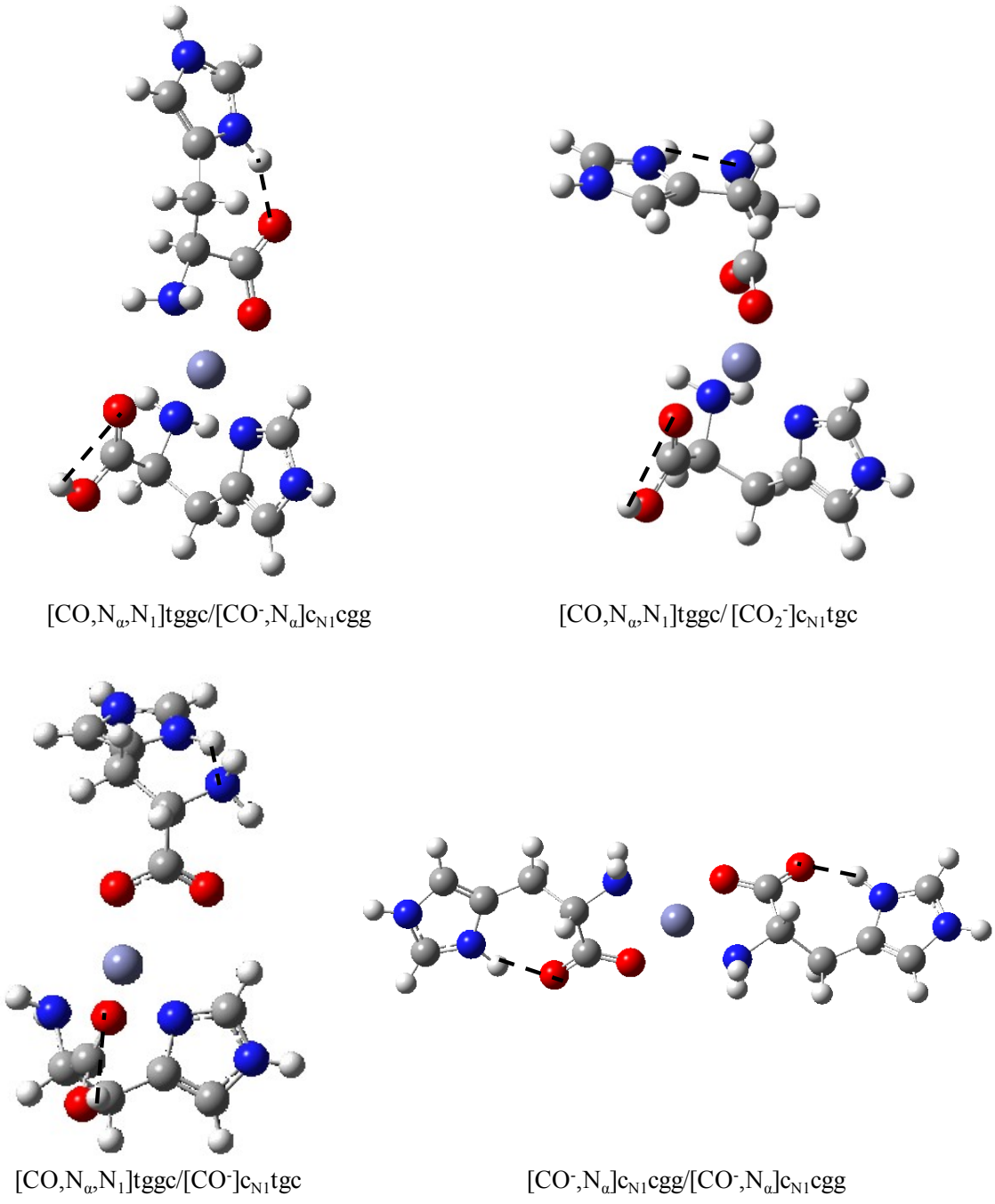

Figure 8.2. Low-energy structures of the $Zn^{2+}(His)_2$ complexes calculated at the B3LYP/6-311+G(d,p) level of theory. Hydrogen bonds are indicated by dashed lines.

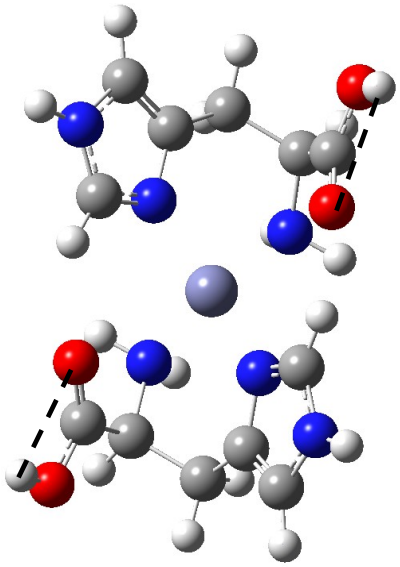

[CO,N_{α},N_1]tgcc/[CO,N_{α},N_1]tgcc

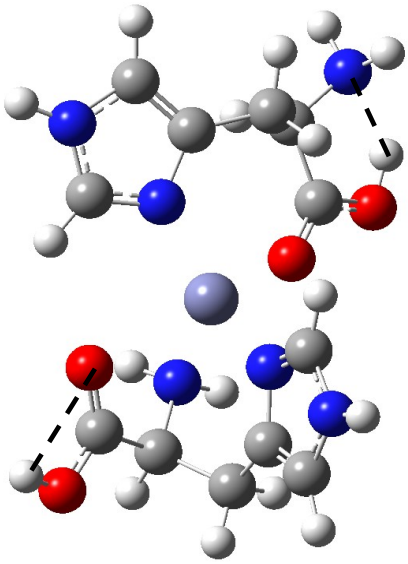

[CO,N_{α},N_1]tgcc/[CO,N_1]ctgg

Figure 8.2. continued

Slightly above this complex in energy at the DFT levels is a SB/SB complex with C_2 symmetry, $[CO^{-},N_{\alpha}]c_{N1}cgg/[CO^{-},N_{\alpha}]c_{N1}cgg$, although because both ligands have a SB formation this particular configuration is 68 kJ/mol higher than the MP2(full) GS, Table 8.2. Instead, the MP2(full) GS is also a C_2 symmetric structure where both ligands are the charge-solvated GS discussed above, $[CO,N_{\alpha},N_1]tggc/[CO,N_{\alpha},N_1]tggc$, Figure 8.2. The CO groups are further from the metal such that the Zn–O distances are 2.964 Å, which is an increase of 0.524 Å compared to the Zn–O distance of the carbonyl in the CS ligand in the $[CO,N_{\alpha},N_1]tggc/[CO^{-},N_{\alpha}]c_{N1}cgg$ complex. This large increase in the zinc–carbonyl coordination is most likely a result of crowding and steric hindrance of the amino acid trying to coordinate six binding sites around the small zinc ion (ionic radius = 0.78 Å[42]) and because the carbonyl is quite close to the imidazole ring of the opposing His ligand, Figure 8.2.

To reduce this crowding around Zn^{2+}, we constructed a 5-coordinate CS/CS complex, $[CO,N_{\alpha},N_1]$ tgcc/$[CO,N_1]$ctgg. In this complex, the Zn–O distance to the carbonyl on the bidentate ligand is 2.066 Å and on the tridentate His is 2.585 Å. The 5-coordinate orientation of the two His residues forms an almost square-pyramidal complex such that the N_1 of $[CO,N_1]$ ligand is the apex of the pyramid, Figure 8.2. This complex is 6 – 28 kJ/mol higher in 298 K free energy than the 6-coordinate $[CO,N_{\alpha},N_1]/[CO,N_{\alpha},N_1]$ CS/CS structure. Several other CS/CS, CS/SB, and SB/SB combinations were attempted such that the zinc would be binding to either four, five, or six sites in the His ligands, but these are sufficiently high in energy ($\Delta\Delta G_{298K} \geq 17$ kJ/mol) at all levels of theory, Table 8.2, that they are not expected to comprise greater than 1% of the reactant ions.

Similar low-energy structures were found for the $Cd^{2+}(His)_2$ system, Table 8.2. Here the 298 K free energy GS at the DFT levels is again a CS/SB configuration, $[CO,N_\alpha,N_1]$ tgcc/$[CO_2^-]c_{N1}$tgc, however, this complex is 4 – 6 kJ/mol higher in 0 K enthalpy at the DFT levels and is disfavored in both 0 K enthalpy and 298 K free energy by 32 – 42 kJ/mol at MP2(full). Instead the 0 K GS at the DFT and MP2(full) levels is a CS/CS complex with C_2 symmetry, namely the $[CO,N_\alpha,N_1]$tgcc/$[CO,N_\alpha,N_1]$tgcc conformer, which agrees with the overall 298 K GS predicted by MP2(full). Although there are similarities between the two $[CO,N_\alpha,N_1]$/ $[CO,N_\alpha,N_1]$ structures of the Zn and Cd systems, the larger Cd ion has a small but noticeable effect on the coordination behavior as well as the resulting relative energetics. The larger size of the Cd^{2+} ion (ionic radius = 0.99 Å[42]) allows for an easier six-fold coordination of the two histidines to the metal such that the two CO groups are coordinated closer to the metal with Cd–O distances of 2.652 Å. This distance is 0.312 Å shorter than the Zn–O bond in the analogous CS/CS structure discussed above for $Zn^{2+}(His)_2$, but is still longer by 0.223 Å compared to the Cd–O distance of the carbonyl in the CS ligand of $[CO,N_\alpha,N_1]$ tgcc/$[CO_2^-]c_{N1}$tgc. The longer Cd–O distances in the CS/CS complex again result from slight crowding around the cadmium ion, although this crowding has substantially decreased compared to the Zn system. Finally, compared to the predicted DFT GS of the $Zn^{2+}(His)_2$ system, the analogous structure for $Cd^{2+}(His)_2$ is $[CO,N_\alpha,N_1]$ tgcc/$[CO^-,N_\alpha]c_{N1}$cgg and is 7 – 9 kJ/mol higher in 298 K free energy (40 kJ/mol at MP2(full)). Similar to $Zn^{2+}(His)_2$, several other higher energy isomers were calculated using CS/CS, CS/SB, and SB/SB configurations, however, because these conformations

are high in 298 K free energy, their spectra will not be compared to experimental spectra below and their structures will not be discussed explicitly here.

IRMPD spectroscopy. Photodissociation spectra of $CdCl^+$(His), $[Zn(His–H)]^+$, $[Cd(His–H)]^+$, $Zn^{2+}(His)_2$, and $Cd^{2+}(His)_2$ were examined from ~550 to slightly past 1800 cm^{-1}, Figure 8.3. For $CdCl^+$(His), the photodissociation pathways correspond to loss of H_2O, NH_3, OH, and OH + CO. The photodissociation of $[M(His-H)]^+$ species mainly resulted in loss of CO_2. For $M^{2+}(His)_2$, photodissociation resulted in fragmentation and charge separation forming $[M(His-H)]^+ + H^+$(His) products, with the H^+(His) product undergoing subsequent loss of H_2O and H_2O + CO. The IRMPD action spectra shown correspond to the relative intensity of all product ions as a function of laser wavelength. Spectra of individual product masses and parent ion depletion spectra were also generated for comparison and are similar to the overall corresponding yield spectrum for the monomeric and dimeric species.

Comparison of the IRMPD spectra in Figure 8.3 shows the similarities between the spectra of the Zn and Cd containing species. The experimental bands are identified on the basis of previous work[14-16,19-21,41,43] as well as comparisons to theoretical spectra. From this, the lines drawn through all the spectra at ~610, ~1155 and ~1725 cm^{-1} mark the three major bands in the $CdCl^+$(His) spectra. The 610 cm^{-1} band is primarily a COH wagging motion, although there are contributions of an NH_2 rocking motion and imidazole wagging as discussed below. The 1155 cm^{-1} band is primarily a COH bending motion of the free OH in a charge solvated structure, although appreciable $HN_\alpha CH$ and HN_3CH bending motions are involved as well. Notably the $[M(His–H)]^+$ spectra do not exhibit the band at ~1155 cm^{-1} because the carboxylic acid terminus is now deprotonated.

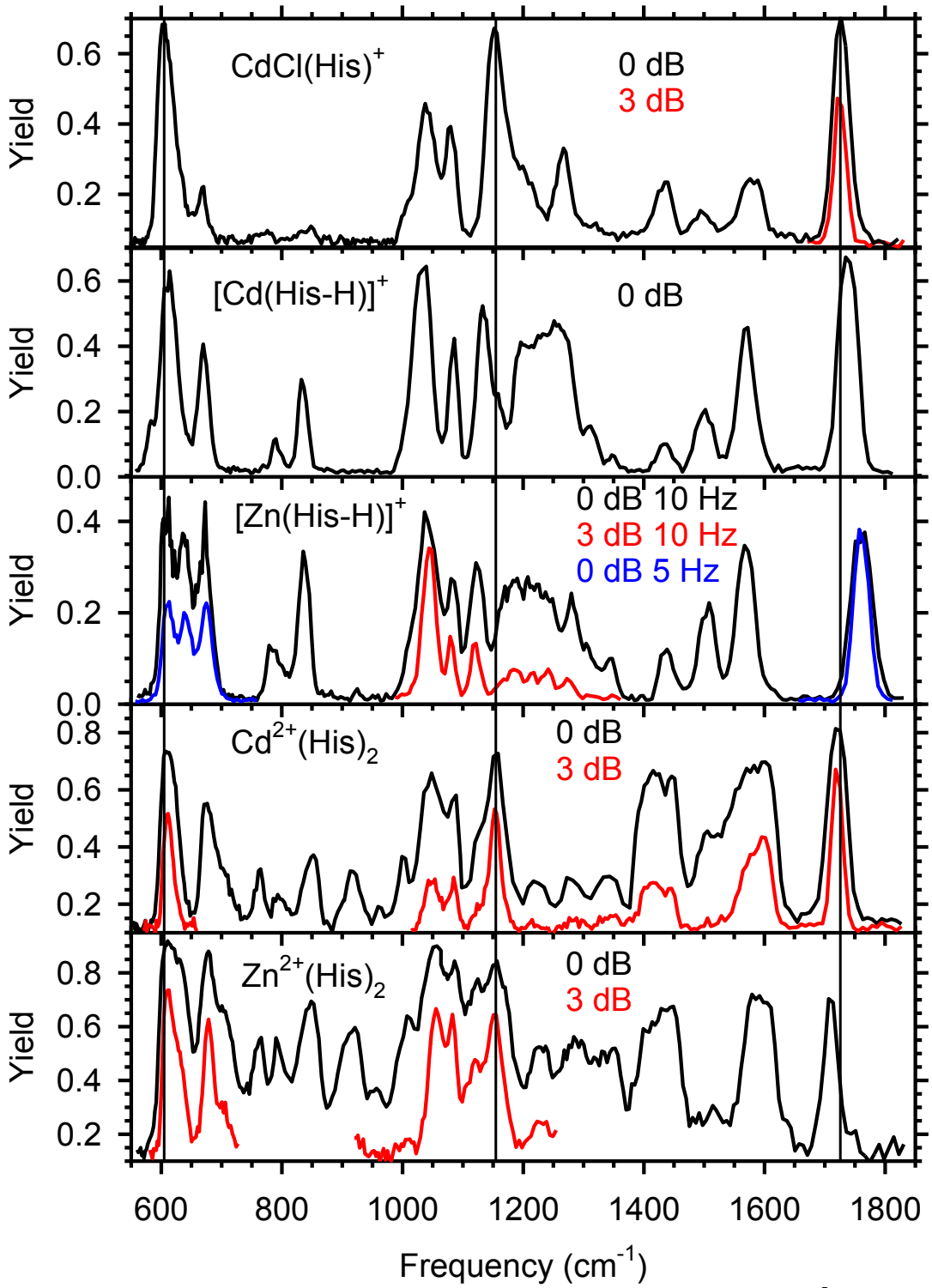

Figure 8.3. IRMPD spectra of $CdCl^+$(His), $[Cd(His–H)]^+$, $[Zn(His–H)]^+$, $Zn^{2+}(His)_2$, and $Cd^{2+}(His)_2$ complexes. Spectra taken with attenuated laser power (in decibels) or at reduced laser repetition rate are indicated in color. Solid lines at 610, 1155, and 1725 cm^{-1} are drawn to approximate the COH wagging, COH bending, and C=O stretch of $CdCl^+$(His), respectively.

Instead a sharp band at ~1120 cm^{-1} appears and is assigned as a $HN_{\alpha}CH$ bend. Both bands at ~1155 and ~1120 cm^{-1} are observed in the $Zn^{2+}(His)_2$ spectrum, whereas the $Cd^{2+}(His)_2$ has the band at ~1155 cm^{-1} and a shoulder on the red side of this band at 1120 cm^{-1}. This strong band at 1155 cm^{-1} suggests the presence of at least one CS ligand in the dimer spectra, whereas the band at 1120 cm^{-1} may demonstrate carboxylate character suggesting a salt-bridge conformation. The band at 1725 cm^{-1} in the $CdCl^{+}(His)$ spectrum is the C=O stretch of the carbonyl and shifts toward the blue for both the $[M(His–H)]^{+}$ spectra, red shifts for the $Zn^{2+}(His)_2$ spectrum, and remains for the $Cd^{2+}(His)_2$ spectrum. These shifts will be discussed in more detail along with the remaining bands in the spectra when compared to theory in the sections below.

Comparison to Theory: $CdCl^{+}$(His). Figure 8.4 shows the experimental IRMPD action spectrum along with calculated IR linear absorption spectra and relative 298 K free energies (at the B3LYP and MP2(full) levels) for the lowest-energy structures of $CdCl^{+}(His)$. For the most part, the calculated IR spectra of complexes having the same metal binding sites are very similar such that a comparison with the lowest energy conformer of each type of His coordination is sufficient for identification. It should be remembered that the experimental IRMPD intensities are not always reproduced by the calculated one-photon linear absorption spectrum, but the relative intensities between bands often offer a good qualitative comparison to experiment. As mentioned above, the most intense and distinctive bands are the carbonyl stretch at ~1725 cm^{-1} and COH bending at ~1155 cm^{-1}. The positions and large intensities of both bands in the experimental spectrum suggest that there is a significant population of a CS structure.

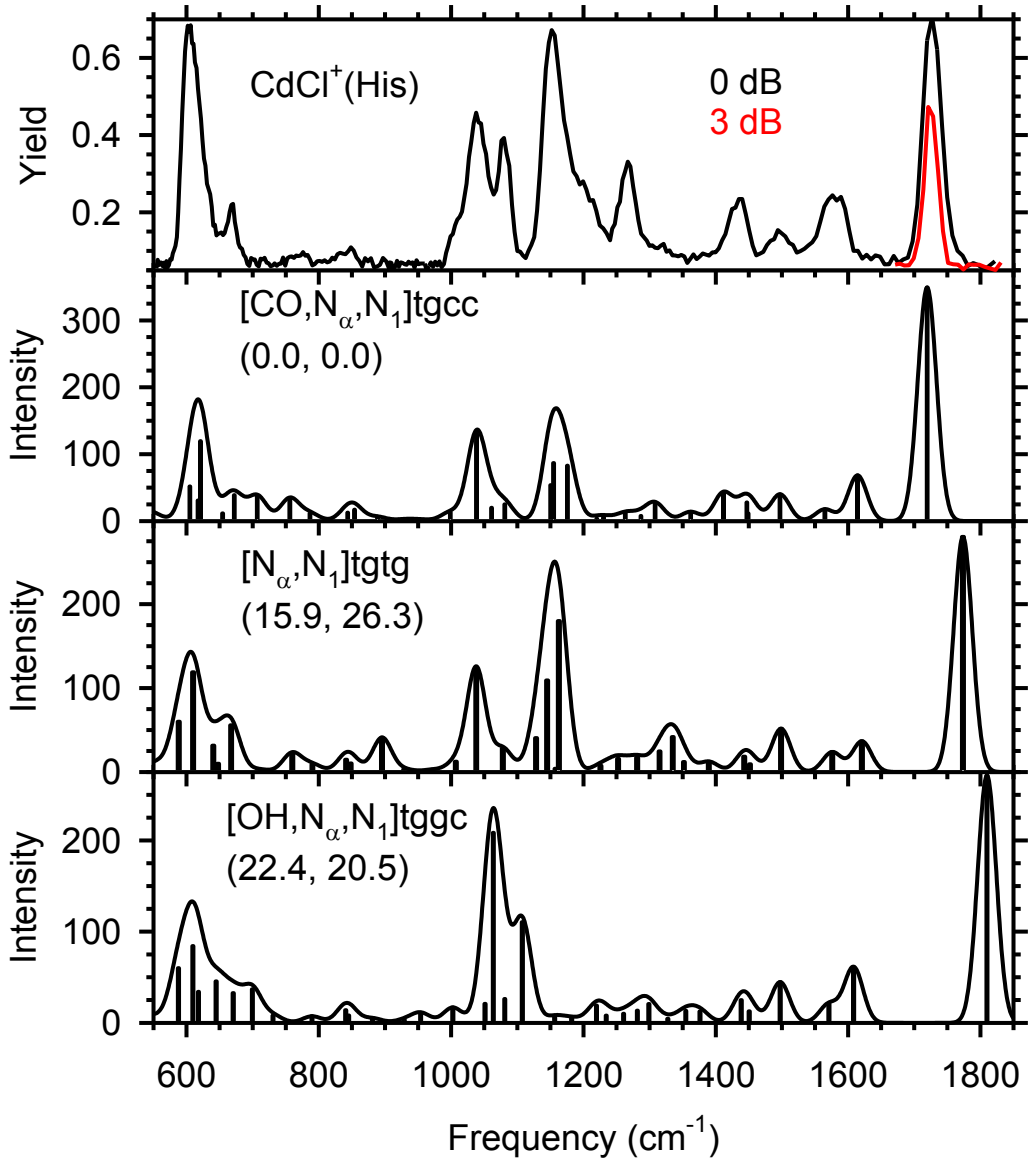

Figure 8.4. Comparison of the experimental IRMPD spectrum of $CdCl^+$(His) with IR spectra of six low-energy conformers predicted at the B3LYP/Def2TZVP level. A spectrum taken with attenuated laser power (in decibels) is indicated in color. Relative 298 K free energies from Table 8.1 are given in parenthesis calculated at the B3LYP and MP2(full) levels using a Def2TZVPP basis set.

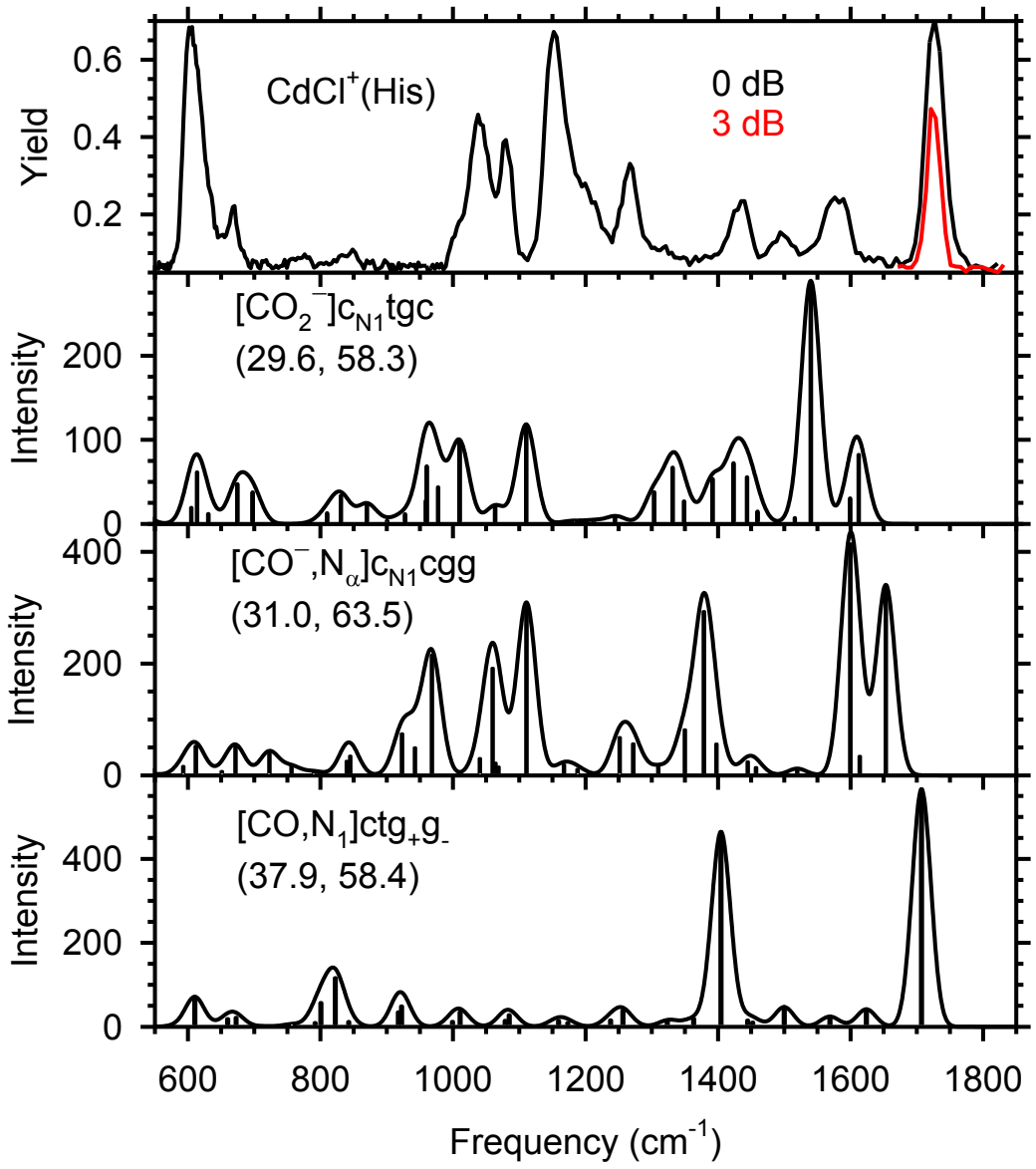

Figure 8.4. Continued

The [CO,N_α,N_1] structure is by far the lowest in energy and, for an equilibrium distribution of complexes at 298 K, should comprise more than 99% of the reactant ions. The predicted C=O band is located at 1720 cm^{-1}, in excellent agreement with experiment. For comparison, this band for Ca^{2+}(His) is located at ~1680 cm^{-1}. The blue shift of the C=O band in the $CdCl^+$(His) system as compared to the similarly sized Ca^{2+} ion is likely a consequence of the Cl^- spectator ion, which induces longer M–O coordination to the $CdCl^+$ and therefore less perturbation of the C=O stretch. The C=O stretching band is by far the most diagnostic when comparing the spectra of the higher energy structures. This experimental band does not agree in position or shape to the predicted spectra of the higher energy SB complexes, Figure 8.4. The predicted CO_2^- asymmetric stretch (ν_{asym}) in the [CO_2^-]c_{N1}tgc SB complex is at 1549 cm^{-1}, much lower in frequency than the C=O stretch of CS complexes, a shift seen previously[15] between similarly coordinated complexes of His. The ν_{asym} of the CO_2^- is intrinsically lower in frequency than the C=O stretch. The ν_{asym} of the coordinated CO^- in the [CO^-,N_α] complex is at ~1600 cm^{-1}, higher in frequency than the ν_{asym} of the CO_2^-, also in agreement with previous calculations by Dunbar et al. on Ba^{2+}(His) and Ca^{2+}(His).[15] Although there is no signature salt-bridge band predicted by theory, the $CdCl^+$(His) spectrum has little to no salt-bridge characteristics based on comparisons to the individual calculated spectra of the SB complexes. Therefore, it is unlikely that a SB complex is formed in the experiment.

The predicted C=O stretches of the other CS complexes have shapes similar to experiment, but do not agree in position (although this could be an artifact of the scaling factor chosen here), Figure 8.4. Although the C=O stretch of the [CO,N_1] complex

agrees within 15 cm^{1}, the remaining bands are in poor agreement with experiment. In the complexes where the metal is not coordinated to the carbonyl, [N_α,N_1] and [OH,N_α,N_1], the two C=O stretches are both blue shifted from experiment by 50 – 90 cm^{-1}. If we change the scaling factor applied to the predicted spectra such that this band agrees with experiment (requiring values of 0.927 – 0.945), then the lower frequency bands will be in poor agreement. Overall, the tridentate [CO,N_α,N_1] conformers provide the best agreement with experiment for the C=O stretch.

As mentioned above, the band at 1155 cm^{-1} is indicative of a CS structure because it involves the free OH motions of the carboxylic acid and therefore is not observed in any of the SB structures, Figure 8.4. This band is also shifted to lower frequencies in the [OH,N_α,N_1] complex. In the GS complex, the intense band at ~1155 cm^{-1} is primarily a result of the COH bending mode with contributions of $HN_\alpha CH$ and HN_3CH bending motions. There are additional intense bands in the spectrum that are identified as the NH_2 wagging at ~1040 cm^{-1} and COH wagging at ~610 cm^{-1}, but there are also contributions from wagging of the imidazole ring and a rocking motion of the NH_2 group. A side band of this main peak is centered at ~670 cm^{-1} and corresponds to a similar mode, namely the HNC wagging of the N_3 in the imidazole side chain. Both bands predicted for the [CO,N_α,N_1] GS conformer agree nicely with experiment in both position and relative intensity. The experimental band at ~1585 cm^{-1} is believed to be the NH_2 bending motion and the predicted peak of the GS is shifted to higher frequencies by ~25 cm^{-1} from experiment. This deviation has been observed previously,[41,44-47] and is believed to be a consequence of strong anharmonic effects. The remaining bands in the 1250 – 1500 cm^{-1} are different movements along the backbone and side chain of the amino acid.

Overall, the large bands at ~1725, 1155, 1040, 670, and 610 cm^{-1} are each in excellent agreement with the predicted vibrations of the [CO,N_α,N_1] complex in positions and band shapes. This overall agreement suggests that this complex is predominately formed in the experiment and that the vibrational scaling factor applied here is accurate.

There are two peaks in the experimental spectrum that are not reproduced with high fidelity in the predicted spectrum of the [CO,N_α,N_1] GS at ~1080 and 1270 cm^{-1}. The first may be an imidazole ring in-plane CH bending mode, as assigned on the basis of condensed-phase IR spectra of imidazole and histidine.[48,49] A small contribution from these modes are observed in the predicted spectrum, but the experimental peak is more intense than predicted by theory in any of the calculated spectra, Figure 8.4. This phenomenon has also been reported previously by Prell and coworkers for the H^+(HisArg) system, who found a similar sharp band at 1080 cm^{-1} that was not reproduced by theory.[20] Assignment of this band as the neutral imidazole was confirmed by the addition of a second proton to form H_2^{2+}(HisArg), where the band in question decreases substantially as the imidazole is believed to be protonated thereby altering its frequencies. The second unassigned band at 1270 cm^{-1} could be the ring stretch of the imidazole.[49] Given the large number of bands from 500 – 1500 cm^{-1} in the condensed-phase spectra of imidazole[49] and histidine,[48] as well as inconsistent matching to the IRMPD spectra, exact assignment of this as well as the other minor bands in the region measured for the experimental spectra is difficult. The lack of these two bands in the theoretical spectra is not surprising given that predicted vibrational frequencies are calculated using the harmonic oscillator approximation. As observed above, this multiple-photon experimental spectrum can lead to substantial shifts in bands with strong anharmonic

tendencies such that these experimental bands could be shifted or the result of an overtone not calculated in the theoretical linear absorption spectrum. Likewise, the predicted intensity of strongly anharmonic modes can deviate substantially from experiment.

[M(His–H)]$^+$. Comparing the experimental spectrum of [Cd(His–H)]$^+$ to the predicted spectra of the low-energy structures, there is good agreement with that of the [CO^-,N_α,N_1]-H_{CO}ggc GS, Figure 8.5a. Here the major and minor bands discussed above are predicted well in peak position and relative intensities are reasonable as well. This structure of the [CO^-,N_α,N_1]–H_{CO}ggc GS is similar to that determined to be the GS for the CdCl(His)$^+$ complex, except the carboxylic acid is de-protonated and there is no spectator Cl^- ion. This allows the metal to be closer in distance to each coordination site, which will most likely be reflected in the position of certain diagnostic bands like the C=O stretch, as discussed in detail below.

The peak intensities of all the bands below 1600 cm^{-1} are smaller relative to the band at 1740 cm^{-1} in the predicted GS spectrum, whereas they appear much more intense in experiment. This is because the experimental spectra presented in this chapter have not been corrected for the gradual decrease of laser power toward the blue edge of the spectra (up to 20 mJ per macropulse in this region). Once power corrected, the intensity of the C=O stretch increases (by a factor of about 2.2) and the intensity of the lower frequency bands relative to the C=O stretch agrees well with that predicted in the GS spectrum. We have chosen not to power correct experimental spectra for this chapter because shapes and positions of the minor lower frequency bands are then more easily examined.

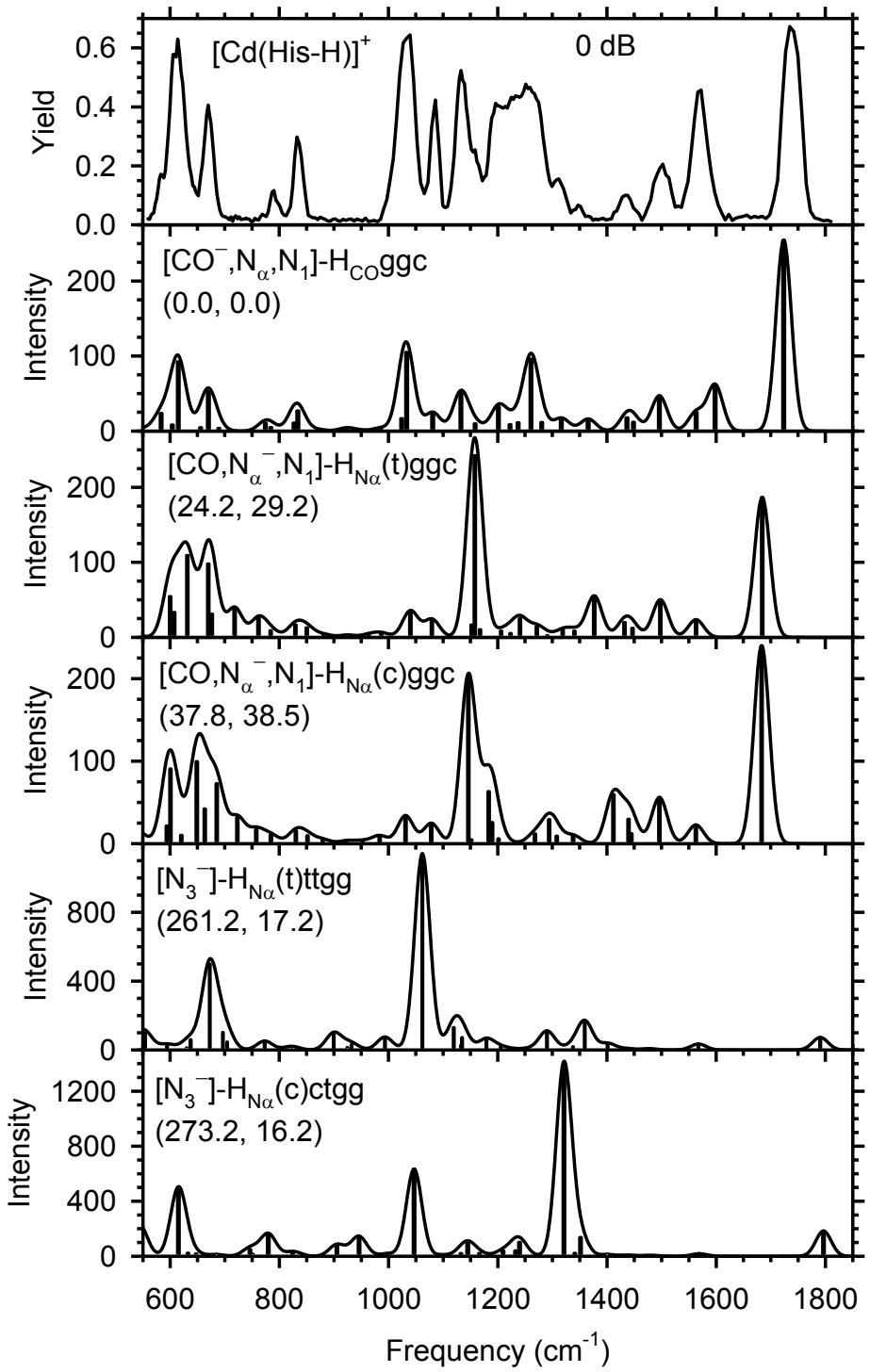

Figure 8.5. Comparison of the experimental IRMPD spectra of $[Cd(His–H)]^+$ and $[Zn(His–H)]^+$ with IR spectra of selected low-energy conformers predicted at the B3LYP/Def2TZVP and B3LYP/6-311+G(d,p) levels. Spectra taken with attenuated laser power (in decibels) or at reduced laser repetition rate are indicated in color. Relative 298 K free energies from Table 8.1 are given in parenthesis calculated at the B3LYP and MP2(full) levels.

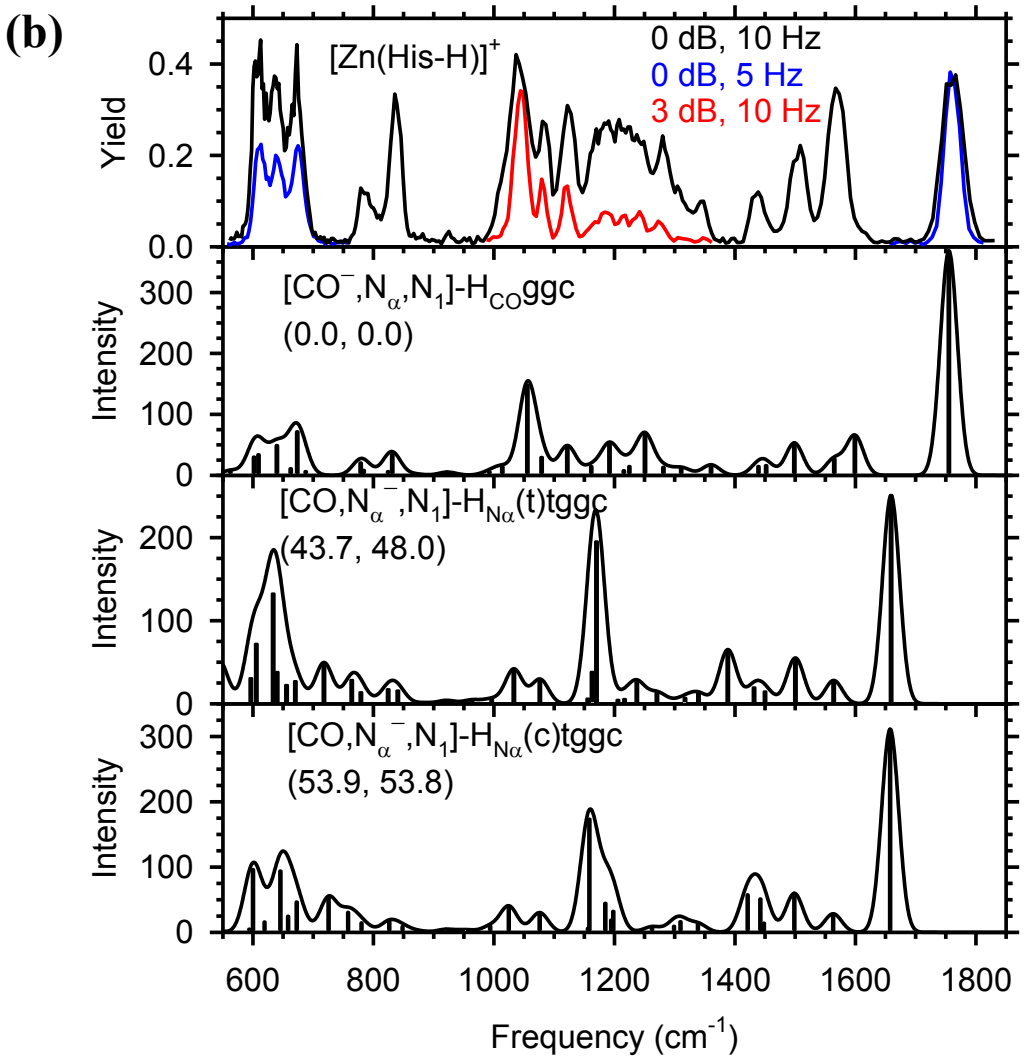

Figure 8.5. continued

The $[Cd(His–H)]^+$ spectrum is similar to that of the $CdCl^+$(His) complex over the wavelength range examined here, Figure 8.3. One subtle difference with respect to the two spectra is in the increased intensity of the minor bands in the deprotonated complex. Specifically, the experimental band at 610 cm^{-1} decreases relative to the band at 670 cm^{-1} because there is no COH wagging contribution in the deprotonated complex. This peak is predicted at 614 cm^{-1} for the $[CO^-,N_\alpha,N_1]$-H_{CO}ggc GS and comprises the wagging of the imidazole side chain along with the NH_2 rocking motion, which were minor contributions to this band discussed above. The peak at 670 cm^{-1} corresponds to the HNC wag of N_3 in the side chain in both species. Also, two bands at 790 and 835 cm^{-1} appear, which were only hinted at in the $CdCl^+$(His) spectrum. These two bands are C-C stretches and CH_2 rocking motions along the backbone causing the coordinated oxygen and alpha amino groups to stretch closer to the metal ion. The shapes, positions, and relative intensity of these two bands are only reproduced in the tridentate complex when the deprotonation occurs on the carboxylic acid terminus forming the $[CO^-,N_\alpha,N_1]$-H_{CO}ggc GS, Figure 8.5a. Deprotonation at N_α broadens these bands considerably and relative intensities are poorly reproduced. The $[Cd(His–H)]^+$ spectrum also has a sharp band at 1130 cm^{-1} and a broad band from 1200 – 1275 cm^{-1}. The band at ~1130 cm^{-1} is the $HN_\alpha CH$ bend, which is red shifted by ~25 cm^{-1} from the peak in the $CdCl^+$(His) spectrum where it was attributed primarily to the COH bend, along with contributions from the $HN_\alpha CH$ bend, as discussed above. The decrease in intensity and 25 cm^{-1} red shift in band position can be expected from the absence of the COH bend and a long range attractive interaction between the proton on the alpha amino group and the oxygens of the carboxylate. Interestingly, there is a small mode observable in the predicted

spectra at ~1155 cm^{-1}, assigned to the HN_3CH bending motion. This motion is also present though unresolved from the COH wag in the $CdCl^+$(His) spectrum, but is unaffected by the CO_2^- moiety formed by deprotonation. The broad band from 1200 – 1275 cm^{-1} includes the symmetric stretch (ν_{sym}) of CO_2^- at 1260 cm^{-1}, as well as other bends and twists along the backbone and side chain. This assignment agrees with previous vibrations assigned[14] to the Phe–H ligand in the $[Zn(Phe)(Phe–H)]^+$ complex. The small peaks at ~1300 and 1350 cm^{-1} are predicted in the theoretical spectrum of $[CO^-,N_\alpha,N_1,]$-H_{CO}ggc to be stretches of the ring and CH movements, also in agreement with the Phe–H assignments. The three bands from 1400 – 1600 cm^{-1} are also in relatively good agreement with the predicted spectrum, especially if the NH_2 umbrella motion at 1600 cm^{-1} is red shifted somewhat experimentally because of the anharmonic effects noted above.

The most surprising difference between the $[Cd(His–H)]^+$ and $CdCl^+$(His) spectra is that the ν_{asym} of the CO_2^- blue shifted by ~20 cm^{-1} from the C=O stretch in the $CdCl^+$(His) spectrum. One might expect a red shift of this stretching band in the $[Cd(His–H)]^+$ spectrum because of the carboxylate character in addition to the fact that the CO^- is coordinated 0.371 Å closer to the Cd^{2+} compared to the distance of the CO to $CdCl^+$. In the $[CO^-,N_\alpha,N_1,]$-H_{CO}ggc GS, this molecular motion consists primarily of the stretch of the uncoordinated oxygen of the carboxylate group, whereas in the $CdCl^+$(His) complex, this band corresponds to the coordinated oxygen of the carbonyl. This band position and movement of the CO_2^- is in agreement with the behavior observed in the $[Zn(Phe)(Phe\text{-}H)]^+$ system (experimental CO_2^- ν_{asym} = 1736 cm^{-1})[14] and also agrees with the predicted spectrum of the calculated GS, Figure 8.5a.

Looking at the two predicted spectra of higher-energy tridentate complexes where the alpha amino group is deprotonated, Figure 8.5a, the main C=O stretch feature consists of the movement of the metal-coordinated carbonyl group such that it is red-shifted from experiment by ~55 cm^{-1}. The other bands of these predicted spectra are also in poor agreement with experiment in band position and relative intensity. Thus, these conformations do not appear to be formed experimentally, agreeing with the calculated relative energetics, Table 8.1. Figure 8.5a also shows the [N_3] complexes, which are only 16 – 17 kJ/mol higher in 298 K free energy than the GS at the MP2(full) level. Comparing these spectra to experiment there is an immediate and obvious disagreement from the lack of a major C=O stretch. Instead the predominant bands in the predicted spectra result from wagging motions of the COH at ~1320 cm^{-1} and $CN_{\alpha}H$ at ~1055 cm^{-1}. The major differences between the two linear absorption spectra of the [N_3] complexes come from the differences in the hydrogen bonding network and orientation of the alpha amino group described in the section above.

The $[Zn(His–H)]^+$ spectrum is very similar to its Cd counterpart, Figure 8.3. As for $[Cd(His–H)]^+$, the Zn[CO^{-},N_{α},N_1]-H_{CO}ggc GS is in excellent agreement with the experimental spectrum, Figure 8.5b. The ν_{asym} of the CO_2^{-} agrees in both position and shape to the GS. Different from the Cd system, the $[Zn(His–H)]^+$ spectrum has three low frequency bands at ~605, 640, and 670 cm^{-1}. The positions of these bands agree within 5 cm^{-1} to three similarly shaped bands in the theoretically predicted spectrum of [CO^{-},N_{α},N_1]-H_{CO}ggc. Specifically, the predicted band at 610 cm^{-1} consists of the wagging and bending of the imidazole side chain, the frequency at 642 cm^{-1} is the $N_{\alpha}H_2$ rock, and the peak at 673 cm^{-1} is the HN_3C wag. Differences in the splitting of these

bands compared to the Cd system are most likely because of the tighter coordination of the Zn ion to His–H, as reflected in the smaller coordination distances. The remainder of the bands are similar to those discussed above for $[Cd(His\text{-}H)]^+$; and similar to the Cd system, the high energy isomers of $[Zn(His–H)]^+$ do not agree with experiment, Figure 8.5b. As a whole, the experimental spectra of the monomeric species agree very well with the spectra of the calculated GS conformers, which are overwhelmingly favored by the relative energetics at all three levels of theory for all three systems.

$Cd^{2+}(His)_2$. Up until this point the spectral comparisons and relative energetics of the monomeric species consistently demonstrate a preference for the tridentate binding of a charge solvated His and a tridentate His–H (with a de-protonated carboxylic acid terminus) to Cd and Zn. Comparing the experimental spectrum of $Cd^{2+}(His)_2$ to the $CdCl^+(His)$ spectrum, the position of the C=O stretch is fairly similar at ~1720 cm^{-1}, Figure 8.3, most likely a consequence of at least one similarly coordinated charge solvated ligand. The similar position of the C=O stretch compared to the $CdCl^+(His)$ complex also suggests that the coordination to the CS carbonyl is relatively long in the dimer complex probably because of the increased crowding around the metal, as discussed above. The $Cd^{2+}(His)_2$ spectrum also has a large peak at ~1150 cm^{-1}, indicative of the carboxylic acid free OH motion, which is also consistent with CS character. However, as mentioned above, the dimeric spectrum has broadening on the red side of this peak at ~1120 cm^{-1} (much smaller intensity relative to the peak at 1150 cm^{-1} in the 3 dB spectrum). There is no such broadening in the $CdCl^+(His)$ experimental spectrum, but there are bands at ~1110 cm^{-1} in the predicted spectra of the SB structures calculated for this reactant, namely the complexes containing the $[CO_2^-]$ and $[CO^-,N_\alpha]$ ligands, Figure

8.6. The position of this broadening at 1120 cm^{-1} is similar to the $HN_{\alpha}CH$ bending mode discussed above for the $[Cd(His–H)]^+$ spectrum, a spectrum with carboxylate characteristics. In comparison to the CS $CdCl^+(His)$ spectrum, the peaks from 1400 – 1600 cm^{-1} in the $Cd^{2+}(His)_2$ spectrum are much broader and have grown in intensity relative to the C=O stretch, which is suggestive of contributions from SB conformers. In addition, there are bands in the 1200 – 1400 cm^{-1} range, also similar to the $[Cd(His–H)]^+$ spectrum. There are new bands at 760, 925, 965, and 1005 cm^{-1}, which were not observed in the CS spectrum of $CdCl^+(His)$, Figure 8.4, or the spectrum of $[Cd(His–H)]^+$, Figure 8.5. Finally, the shapes and positions of the bands in the $Cd^{2+}(His)_2$ spectrum are similar to those reported in the IRMPD spectrum of $Cd^{2+}(Trp)_2$, which was assigned as a CS/SB conformation by Dunbar et al.[19] These authors observed similar, subtle changes between the monomer and dimer spectra of Trp complexed with Cd and assigned a CS and CS/SB configuration to these two spectra, respectively. On the basis of these observed changes in the experimental spectrum of the dimeric species and comparisons to the reported spectra in the literature, one of the His ligands is in a CS formation while the other is possibly SB, but contributions from CS/CS structures cannot be rejected yet.

The C=O stretch of the predicted spectrum of the C_2 symmetric $[CO,N_{\alpha},N_1]$tgcc/$[CO,N_{\alpha},N_1]$tgcc complex agrees best with experiment in both band position and shape, Figure 8.6a. The remaining predicted bands are also in relatively good agreement in peak position, although the intense contribution of the C=O stretching band obscures the smaller peaks. Obviously, there is poor agreement in the relative intensities between the C=O stretch and the lower frequency bands, in part because the gradually changing laser power is not accounted for or possibly by contributions of a SB

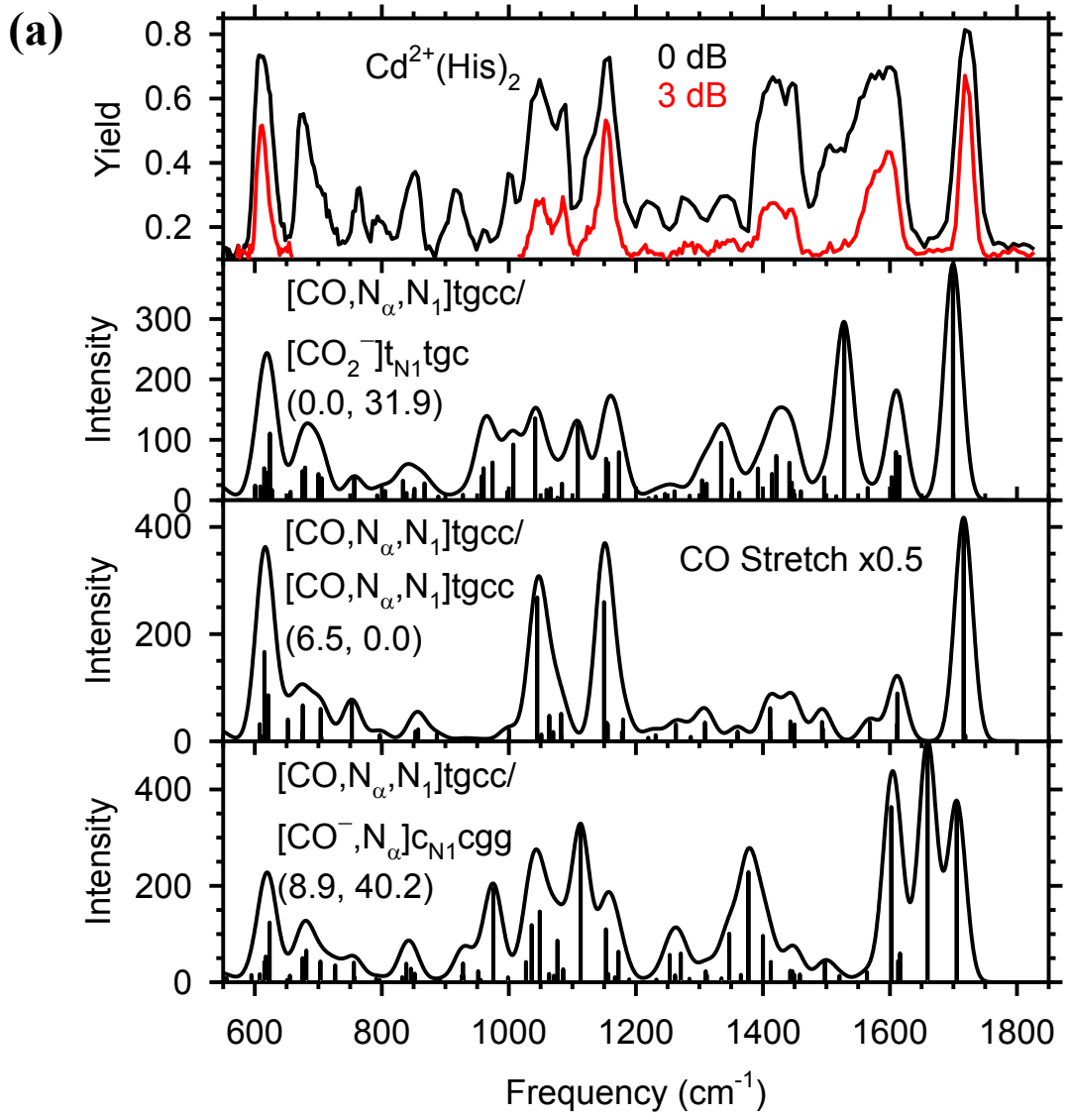

Figure 8.6. Comparison of the experimental IRMPD spectra of $Cd^{2+}(His)_2$ and $Zn^{2+}(His)_2$ with IR spectra of selected low-energy conformers predicted at the B3LYP/Def2TZVP and B3LYP/6-311+G(d,p) levels. Relative 298 K free energies from Table 8.2 are given in parenthesis calculated at the B3LYP and MP2(full) levels. A spectrum taken with attenuated laser power (in decibels) is indicated in color. The predicted C=O stretch is scaled by 0.5 for the $[CO,N_{\alpha},N_1]/[CO,N_{\alpha},N_1]$ conformer of $Cd^{2+}(His)_2$ and $Zn^{2+}(His)_2$.

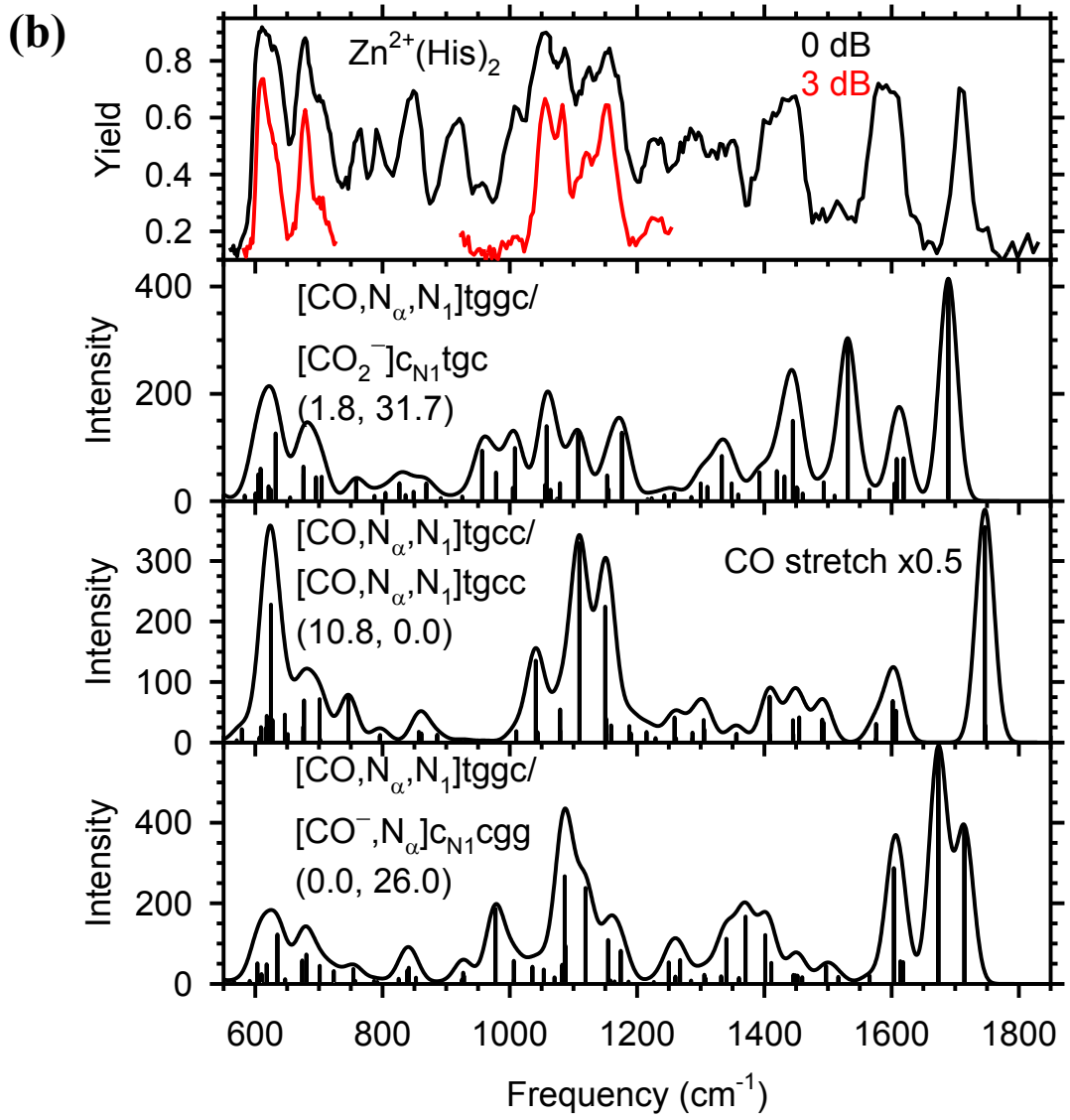

Figure 8.6. continued

conformer as discussed below. Therefore, we have scaled the C=O stretching band in the CS/CS predicted spectrum by a factor of 0.5 to better simulate the experimental spectrum (uncorrected for laser power) and to more clearly see the lower frequency bands. This allows for the clear identification of the band at 760 cm^{-1}, which is a OCOH bend, and is present in all CS/CS or CS/SB spectra. Because of the complexity of this dimer system, there is a large number of bands and there is no single mode diagnostic of a SB ligand. However, as suggested by the comparisons of experimental spectra above, there are no bands in the CS/CS spectrum at ~925 or 960 cm^{-1} and the large broad experimental bands in the range of 1200 – 1650 cm^{-1} are not reproduced with high fidelity. However, comparison of the 0 and 3 dB spectra shows that the C=O stretching band is easily saturated, such that the relative intensities between this band and those from 1200 – 1650 cm^{-1} in the 3 dB spectrum agree well with predicted relative intensities of the CS/CS MP2(full) GS. In addition, this CS/CS conformer has no predicted vibrational modes at 1120 cm^{-1}, a mode that may be indicative of some carboxylate characteristics, as discussed for the $[Cd(His–H)]^+$ spectrum. The $[CO,N_\alpha,N_1]$tgcc/$[CO,N_\alpha,N_1]$tgcc complex is the MP2(full) GS, but is 4.4 – 6.5 kJ/mol higher in 298 K free energy at the DFT levels, Table 8.2.

The DFT GS is a CS/SB complex, $[CO,N_\alpha,N_1]/[CO_2^-]$, which is higher in MP2(full) 298 K free energy by 32 kJ/mol. Comparing the predicted spectrum of this CS/SB complex to experiment, the C=O stretching band of the CS ligand is red shifted from experiment by ~20 cm^{-1}, peaking at 1700 cm^{-1}. The ν_{asym} stretch of the coordinated CO_2^- group peaks at 1527 cm^{-1}, in good agreement with the experimental shoulder ~1520 cm^{-1}, although the predicted intensity of this stretch is much higher than what is found

experimentally. Additionally, there are predicted bands that involve the motion of the proton involved in the salt-bridge between the N_1 and N_α groups from ~920 – 1010 cm^{-1} and at 1110 cm^{-1}. These bands reproduce the position of those found in the experiment within 3 – 20 cm^{-1}, although again the relative intensities are not well predicted.

The remaining bands from 1200 – 1600 cm^{-1} are difficult to assign as both predicted GS spectra have vibrational modes here. However, these bands in the CS/CS spectrum are very low in intensity relative to the predicted COH wagging, NH_2 wagging, COH bending, and C=O stretching peaks at 610, 1045, 1150, and 1716 cm^{-1}, respectively. More intense broad bands are found in the DFT GS CS/SB spectrum, similar to experiment, Figure 8.6a, suggesting possible contributions of this conformer to the experimental spectrum. The positioning of these bands is slightly off from experiment, which could be a result of large anharmonic affects in this region, as discussed above. The lower frequency bands at ~610 and 675 cm^{-1} are reproduced with either predicted spectrum, although the relative intensity between these two bands is predicted slightly better using the CS/SB conformer. This is because the band at 610 cm^{-1} decreases in intensity from the lack of the COH wagging motion in the SB ligand (as seen in the $[Cd(His–H)]^+$ spectrum) and the HNC band at 675 cm^{-1} grows in intensity because of the additional wagging movements of the protonated N_1 and N_3 in the side chain. The predicted spectrum of the $[CO,N_\alpha,N_1]$tgcc/$[CO^-,N_\alpha]c_{N1}$cgg complex is also given in Figure 8.6a, but the three intense and sharp bands at ~1600 (proton movement between the N_1 and CO^- and NH_2 bends), 1660 (ν_{asym} of the coordinated oxygen in the CO_2^-), and 1705 cm^{-1} (C=O stretch) do not agree well with experiment.

Overall it appears that the experimental spectrum has bands unique to at least one CS ligand, but also has bands indicative of a ligand with a SB structure, which can be described by the predicted spectrum of the $[CO,N_{\alpha},N_1]/[CO_2^-]$ DFT GS. The latter assignment is in agreement with that made by Dunbar et al.[19] for $Cd^{2+}(Trp)_2$; however, the main C=O stretching band is best described by the $[CO,N_{\alpha},N_1]/[CO,N_{\alpha},N_1]$ MP2(full) GS, which also predicts most of the other bands reasonably well. Given that the levels of theory disagree as to which complex is the GS and DFT predicts relatively close energetics between these two structures, it is difficult to make an unambiguous assignment of one particular complex to the $Cd^{2+}(His)_2$ spectrum. A combination of the CS/CS and CS/SB structures probably would reproduce the observed spectrum the best.

$Zn^{2+}(His)_2$. Comparing the $Cd^{2+}(His)_2$ spectrum to that of $Zn^{2+}(His)_2$ there are obvious similarities with slight differences in the spectral signatures, Figure 8.3. Notably, the C=O stretching band has shifted from ~1720 cm^{-1} in the Cd^{2+} spectrum to ~1710 cm^{-1} in the Zn^{2+} spectrum, implying a closer coordination of the carbonyl in the CS ligand to the Zn^{2+}. The width of this peak also decreases slightly from 23 to 17 cm^{-1}, but this could be a consequence of saturation, which unfortunately was not collected at 3 dB attenuation. The experimental bands from 920 – 1010 cm^{-1} and ~1120 cm^{-1} are assigned above to the proton participating in the SB of the $[CO_2^-]$ complex. These bands are present in the spectrum and have also grown in intensity compared to the same peaks in the $Cd^{2+}(His)_2$ spectrum, although again this could be a consequence of saturation of the C=O stretch. The band at 1120 cm^{-1} is more clearly observed, compared to the low-frequency shoulder on the COH bending band observed for $Cd^{2+}(His)_2$. However, there appears to be less saturation of the major bands at 610, 1050, 1075, 1110, and 1150 cm^{-1}

in the $Zn^{2+}(His)_2$ system, i.e., the decrease in intensity between the 0 dB and 3 dB spectra is not as drastic as for $Cd^{2+}(His)_2$. Saturation may be more easily obtained with the CS/CS complex because there are two coordinating carbonyls. The COH bend remains at 1150 cm^{-1}, implying the presence of at least one His ligand with a CS structure. These observations suggest a similar structure or combination of structures being present in the $Zn^{2+}(His)_2$ complex as for $Cd^{2+}(His)_2$. This indicates that there are only small structural changes to the experimental reactant when Cd is substituted for Zn in the gas phase, in agreement with our assignments of similar structures to the monomeric species.

Looking at the predicted spectrum of the C_2 symmetric $[CO,N_\alpha,N_1]$tggc/$[CO,N_\alpha,N_1]$tggc complex, the predicted C=O stretch is located at 1747 cm^{-1}, a blue shift of ~37 cm^{-1} from the experimental peak at ~1710 cm^{-1}, Figure 8.6b. Such a blue shift is induced by the longer CO coordination to the metal, a result of the steric hindrance of these His ligands around the smaller zinc dication, as discussed above. Instead, there is a small feature in the experimental spectrum near 1750 cm^{-1} which may be a small contribution from this blue shifted C=O stretch of the CS/CS complex. The less chelated structures, including ones containing a SB His ligand, are favored by the relative DFT energetics.

However, the evidence for a CS/SB conformer is hardly conclusive based on spectral comparisons to theory. The predicted C=O stretch of the carbonyl in the CS ligand of the $[CO,N_\alpha,N_1]$tggc/$[CO_2^-]$ complex is again red shifted from the experimental spectrum by ~20 cm^{-1}, similar to what was found for the corresponding structure of $Cd^{2+}(His)_2$. Additionally, this complex is no longer the DFT GS, instead the $[CO,N_\alpha,N_1]$tggc/$[CO^-,N_\alpha]$ is 2 – 3 kJ/mol lower in 298 K free energy at the B3LYP and

B3P86 levels. The predicted spectrum of this GS is again in relatively poor agreement to experiment. The large ν_{asym} of the CO_2^- at ~1673 cm^{-1} is split with the C=O stretch of the CS ligand at ~1714 cm^{-1} and has no match in the experimental spectrum. To try to achieve better spectral comparisons for this system, optimization and frequency calculations were performed on these $Zn^{2+}(His)_2$ complexes at the B3LYP/Def2TZVP level anticipating that the size consistent basis set may better describe this system. However, the resulting structures and vibrations were similar to those using the 6-311+G(d,p) basis set. Finally, CS/CS and CS/SB structures were rebuilt to try and change distances from the coordination sites to the metal, to better fit the band positions of the C=O and CO_2^- ν_{asym} stretches in the experimental spectrum, but during the optimization steps these structures returned to the low-energy structures already presented here. Less chelated CS/CS, CS/SB, and SB/SB conformers were calculated and the spectra of higher-energy structures were compared to experiment, however, none offer better agreement to the IRMPD spectrum. Perhaps a more extensive conformational search is required.

From these comparisons to the predicted spectra and from the ambiguous relative energetics, it seems that conventional theoretical calculations struggle with predicting structural parameters and vibrational modes in this complicated two-ligand system featuring a small highly charged metal. Given that the experimental spectrum of $Zn^{2+}(His)_2$ is similar to the $Cd^{2+}(His)_2$ spectrum, it seems that similar structural assignments of the $Zn^{2+}(His)_2$ complex can be made based on the spectral comparisons outlined for the $Cd^{2+}(His)_2$. Dunbar et al.[19] assigned a CS/SB structure as the GS for both the $Zn^{2+}(Trp)_2$ and $Cd^{2+}(Trp)_2$ spectra, where the CS/SB coordination is somewhat

similar to the $[CO,N_{\alpha},N_1]/[CO_2^-]$ complex discussed above. Each metal is coordinated similarly although in the Trp system the metal is coordinated to the aromatic ring instead of the N_1 of the imidazole ring as in the His system. Our comparisons as well as the MP2(full) energetics suggest that the CS/CS $[CO,N_{\alpha},N_1]/ [CO,N_{\alpha},N_1]$ structure may be a major contributor as well.

Conclusion

The role of the metal in the conformational dependence of histidine was investigated by measuring the IRMPD action spectra of monomeric histidine, deprotonated histidine, and dimeric histidine in the region of 550 – 1800 cm^{-1} for complexes with $CdCl^+$, Cd^{2+}, and Zn^{2+}. Comparison of these experimental spectra with IR spectra calculated at the B3LYP/6-311+G(d,p) and B3LYP/Def2TZVP levels of theory identified the conformations likely present in the experiment. The monomeric species are unambiguously assigned as tridentate complexes of histidine to the metal. Specifically, for the $CdCl^+$(His) system, the amino acid forms a charge solvated configuration coordinated to the carbonyl, N_1 of the imidazole side chain, and to the alpha-amino group in a $[CO,N_{\alpha},N_1]$tgcc fashion. This assignment is clear from the strong C=O stretch at ~1720 cm^{-1} and the obvious presence of the free OH motion of the COH bend at ~1150 cm^{-1}. Through comparisons to the other monomeric spectra and to theory, it is found that the Cl^- spectator ion has little effect on the experimental spectrum with the possible exception of the position of the C=O stretching band resulting from the longer coordination to the CO and lower overall charge transfer. The $[M(His–H)]^+$ spectra are very similar for both Cd^{2+} and Zn^{2+} and the structures identified as the primary component of both spectra had a deprotonated carboxylic acid terminus resulting

in a [CO,N_α,N_1]configuration. Minor differences in the splitting and position of certain bands between the spectra of $[Zn(His–H)]^+$ and $[Cd(His–H)]^+$ are observed. Structural differences of these two complexes are also minor and the small differences in the experimental spectra were most likely the result of the tighter coordination of the smaller Zn^{2+} metal. These spectral assignments agree with the assigned ground states calculated by all three levels of theory.

In contrast, the dimeric spectra of $Cd^{2+}(His)_2$ and $Zn^{2+}(His)_2$ were less conclusive partly because of the large size and complexity of these systems. Both experimental spectra have a large number bands making it difficult to definitively assign one configuration versus another. In addition, the calculated relative energetics disagree on the most stable configuration. The DFT levels favor a CS/SB binding of the two histidines, whereas MP2(full) strongly favors a CS/CS symmetric complex. The presence of at least one CS ligand is clear, as both spectra have strong bands resulting from the COH bend and C=O stretch typical of a CS configuration. The $Cd^{2+}(His)_2$ spectrum agrees fairly well with a 6-coordinate CS/CS complex, although there are bands not accounted for in the predicted spectrum as well as discrepancies in the relative intensities. Comparisons to theoretically predicted spectra show that the identification of a SB ligand in the presence of a CS ligand is not straightforward. In the experimental spectra, there are small peaks from 900 – 1010 cm^{-1}, the growth of a peak at 1120 cm^{-1}, and broad bands in the 1350 – 1600 cm^{-1} range, which all suggest the presence of a SB ligand. The exact identification of the CS/SB configuration rests heavily on the detailed matching of the predicted spectra to experiment in regions that were shown to have strong anharmonic tendencies. Future IRMPD studies on these metals with imidazole are

probably warranted to make unambiguous assignments of these bands, given that as theory is clearly not adequately describing some of these frequencies using simple harmonic oscillator methods.

Even without precise structural assignment of the $Zn^{2+}(His)_2$ and $Cd^{2+}(His)_2$, it seems that the spectra of both are quite similar to one another in agreement, with comparisons between the $[Zn(His–H)]^+$ and $[Cd(His–H)]^+$ spectra. Perhaps histidine is not susceptible to severe structural changes when replacing zinc with cadmium, as found for carbonic anhydrase, which comprises three His residues and is now believed[11] not to be affected by the replacement with a Cd^{2+} ion. Perhaps having more or different ligands bound to the metal is necessary to understand the toxicological affects of the cadmium ion and to better mimic its other biological states (e.g., zinc fingers where the metal is complexed by one or two histidine residues in addition to two or three cysteines). Future work could include the addition of solvent molecules like water or methanol, using less complicated amino acids like cysteine (to avoid the side chain affects on the spectra seen here), or including more amino acids as typically found physiologically (e.g., $Zn^{2+}(His)_2(Cys)_2$).

References

(1) Pavletich, N. P.; Pabo, C. O. *Science* **1991**, 809.

(2) Fairall, L.; Schwabe, J. W. R.; Chapman, L.; Finch, J. T.; Rhodes, D. *Nature* **1993**, *366*, 483

(3) Berg, J. M.; Shi, Y. *Science* **1996**, *271*, 1081.

(4) Mackay, J. P.; Crossley, M. *Trends Biochem. Sci.* **1998**, *23*, 1.

(5) Iuchi, S.; Kuldell, N. *Zinc Finger Proteins From Atomic Contact to Cellular Function*; Kluwer Academic/Plenum Pubslishers: New York, 2005.

(6) Spiro, T. G. *Zinc enzymes*; J. Wiley: New York, 1983.

(7) Hartwig, A.; Asmuss, M.; Blessing, H.; Hoffmann, S.; Jahnke, G.; Khandelwal, S.; Pelzer, A.; Burkle, A. *Food Chem. Toxicol.* **2002**, *40*, 1179.

(8) Asmuss, M.; Mullenders, L. H. F.; Eker, A.; Hartwig, A. *Carcinogenesis* **2000**, *21*, 2097.

(9) Salomons, W.; Förstner, U.; Mader, P. *Heavy metals : problems and solutions*; Springer-Verlag: Berlin ; New York, 1995.

(10) Fergusson, J. E. *The heavy elements : Chemistry, environmental impact, and health effects*, 1st ed.; Pergamon Press: Oxford ; New York, 1990.

(11) Price, N. M.; Morel, F. M. M. *Nature* **1990**, *344*, 658.

(12) Predki, P. F.; Sarkar, B. *J. Biol. Chem.* **1992**, *267*, 5842.

(13) Berezovskaya, Y.; Armstrong, C. T.; Boyle, A. L.; Porrini, M.; Woolfson, D.; Barran, P. E. *Chem. Comm.* **2011**, *47*, 412.

(14) Polfer, N. C.; Oomens, J.; Moore, D. T.; von Helden, G.; Meijer, G.; Dunbar, R. C. *J. Am. Chem. Soc.* **2006**, *128*, 517.

(15) Dunbar, R. C.; Hopkinson, A. C.; Oomens, J.; Siu, C. K.; Siu, K. W. M.; Steill, J. D.; Verkerk, U. H.; Zhao, J. F. *Journal of Physical Chemistry B* **2009**, *113*, 10403.

(16) Citir, M.; Hinton, C. S.; Oomens, J.; Steill, J. D.; Armentrout, P. B. **2011**, in preparation.

(17) Kimura, E. *Acc. Chem. Res.* **2001**, *34*, 171.

(18) Marino, T.; Russo, N.; Toscano, M. *J. Amer. Chem. Soc.* **2005**, *127*, 4242.

(19) Dunbar, R. C.; Steill, J. D.; Polfer, N. C.; Oomens, J. *J. Phys. Chem. A* **2009**, *113*, 845.

(20) Prell, J. S.; O'Brien, J. T.; Steill, J. D.; Oomens, J.; Williams, E. R. *J. Am. Chem. Soc.* **2009**, *131*, 11442.

(21) O'Brien, J. T.; Prell, J. S.; Berden, G.; Oomens, J.; Williams, E. R. *Int. J. Mass Spectrom.* **2010**, *297*, 116.

(22) Dunbar, R. C.; Polfer, N. C.; Oomens, J. *J. Am. Chem. Soc.* **2007**, *129*, 14562.

(23) Sousa, S. F.; Fernandes, P. A.; Ramos, M. J. *J. Amer. Chem. Soc.* **2007**, *129*, 1378.

(24) Duchackova, L.; Steinmetz, V.; Lemaire, J.; Roithova, J. *Inorg. Chem.* **2010**, *49*, 8897.

(25) Duchackova, L.; Schroder, D.; Roithova, J. *Inorg. Chem.* **2011**, *50*, 3153.

(26) Valle, J. J.; Eyler, J. R.; Oomens, J.; Moore, D. T.; van der Meer, A. F. G.; von Heldon, G.; Meijer, G.; Hendrickson, C. L.; Marshall, A. G.; Blakney, G. T. *Rev. Sci. Instrum.* **2005**, *76*, 023103.

(27) Polfer, N. C. J. O. *Phys. Chem. Chem. Phys.* **2007**, *9*, 3804.

(28) Oepts, D. v. d. M., A.F.G.; van Amersfoort, P.W. . *Infrared Phys. Technol.* **1995**, *36*, 297.

(29) Frisch, M. J.; Trucks, G. W.; Schlegel, H. B.; Scuseria, G. E.; Robb, M. A.; Cheeseman, J. R.; Scalmani, G.; Barone, V.; Mennucci, B.; Petersson, G. A.; Nakatsuji, H.; Caricato, M.; Li, X.; Hratchian, H. P.; Izmaylov, A. F.; Bloino, J.; Zheng, G.; Sonnenberg, J. L.; Hada, M.; Ehara, M.; Toyota, K.; Fukuda, R.; Hasegawa, J.; Ishida, M.; Nakajima, T.; Honda, Y.; Kitao, O.; Nakai, H.; Vreven, T.; Montgomery, J., J. A. ; Peralta, J. E.; Ogliaro, F.; Bearpark, M.; Heyd, J. J.; Brothers, E.; Kudin, K. N.; Staroverov, V. N.; Kobayashi, R.; Normand, J.; Raghavachari, K.; Rendell, A.; Burant, J. C.; Millam, J. M.; Iyengar, S. S.; Tomasi, J.; Cossi, M.; Rega, N.; Millam, J. M.; Klene, M.; Knox, J. E.; Cross, J. B.; Bakken, V.; Adamo, C.; Jaramillo, J.; Gomperts, R.; Stratmann, R. E.; Yazyev, O.; Austin, A. J.; Cammi, R.; Pomelli, C.; Ochterski, J. W.; Martin, R. L.; Morokuma, K.; Zakrzewski, V. G.; Voth, G. A.; Salvador, P.; Dannenberg, J. J.; Dapprich, S.; Daniels, A. D.; Farkas, O.; Foresman, J. B.; Ortiz, J. V.; Cioslowski, J.; Fox, D. J. Gaussian 09, Revision A.02; Gaussian Inc.: Pittsburgh, PA, 2009.

(30) Becke, A. D. *J. Chem. Phys.* **1993**, *98*, 5648.

(31) Ditchfield, R.; Hehre, W. J.; Pople, J. A. *J. Chem. Phys.* **1971**, *54*, 724.

(32) Weigend, F.; Ahlrichs, R. *Phys. Chem. Chem. Phys.* **2005**, *7*, 3297.

(33) Andrae, D.; Haeussermann, U.; Dolg, M.; Stoll, H.; Preuss, H. *Theo. Chem. Acc* **1990**, *77*, 123.

(34) Schuchardt, K. L.; Didier, B. T.; Elsethagen, T.; Sun, L. S.; Gurumoorthi, V.; Chase, J.; Li, J.; Windus, T. L. *J. Chem. Inf. Model.* **2007**, *47*, 1045.

(35) Dunbar, R. C.; Polfer, N. C.; Oomens, J. *J. Amer. Chem. Soc.* **2007**, *129*, 14562.

(36) Perdew, J. P. *Phys. Rev. B* **1986**, *33*, 8822.

(37) Möller, C.; Plesset, M. S. *Phys. Rev.* **1934**, *46*, 618.

(38) Bauschlicher, C. W., Jr.; Maitre, P. J. *J. Phys. Chem.* **1995**, *99*, 3444.

(39) Heaton, A. L.; Bowman, V. N.; Oomens, J.; Steill, J. D.; Armentrout, P. B. *J. Phys. Chem. A* **2009**, *113*, 5519.

(40) Citir, M.; Stennett, E. M. S.; Oomens, J.; Steill, J. D.; Rodgers, M. T.; Armentrout, P. B. *Int. J. Mass Spectrom.* **2010**, *297*, 9.

(41) Carl, D. R.; Cooper, T. E.; Oomens, J.; Steill, J. D.; Armentrout, P. B. *Phys. Chem. Chem. Phys.* **2010**, *12*, 3384.

(42) Wilson, R. G.; Brewer, G. R. *Ion Beams with Applications to Ion Implantation*; Wiley: New York, 1973.

(43) Citir, M.; Stennett, E. M. S.; Oomens, J.; Steill, J. D.; Rodgers, M. T.; Armentrout, P. B. *Int. J. Mass Spectrom.* , in press.

(44) Armentrout, P. B.; Rodgers, M. T.; Oomens, J.; Steill, J. D. *J. Phys. Chem. A* **2008**, *112*, 2248.

(45) Rodgers, M. T.; Armentrout, P. B.; Oomens, J.; Steill, J. D. *J. Phys. Chem. A* **2008**, *112*, 2258.

(46) Oomens, J. M., D.T.; Meijer, G.; von Helden, G. . *Phys. Chem. Chem. Phys.* **2004**, *6*, 710.

(47) Sinclair, W. E. P., D.W. . *J. Chem. Phys.* **1996**, *105*, 7942.

(48) Carlson, R. H.; Brown, T. L. *Inorg. Chem.* **1966**, *5*, 208.

(49) Cordes, M. d. N. D.; Walter, J. L. *Spectrochimica Acta* **1968**, *24A*, 237.